Magnetic Resonance Imaging as a Tool to Study Gas-Liquid Taylor Flows

Vom Fachbereich Produktionstechnik

der

UNIVERSITÄT BREMEN

zur Erlangung des Grades

Doktor-Ingenieur

genehmigte

Dissertation

von

M.Sc. Philip Kemper

Gutachter: **Prof. Dr.-Ing. Jorg Thöming**
Universität Bremen
Prof. Dr.-Ing. Michael Schlüter
Technische Universität Hamburg

Tag der mündlichen Prüfung: **27.11.2023**

Zusammenfassung

Die Motivation dieser Dissertation liegt in der Zusammenführung der zwei großen Forschungsbereiche der Magnetresonanztomographie (MRT) und der chemischen Reaktionstechnik. Das Hauptinteresse gilt dabei der Untersuchung von gas-flüssig Taylor-Strömungen mittels MRT. Für die Optimierung chemischer Prozesse ist die Wechselwirkung zwischen lokaler Strömung und chemischer Reaktion besonders entscheidend, da durch die zugrundeliegenden Strömungsfelder Verweilzeitvariationen auftreten können, welche die Produktselektivität und Ausbeute erheblich beeinflussen. In dieser Arbeit wird die Langzeitbeobachtung einzelner Blasen unter definierten und reproduzierbaren Strömungsbedingungen durch Taylor-Strömungen ermöglicht. Herkömmliche optische Messmethoden erlauben die Untersuchung von Strömungsfeldern und des Stofftransports. Sie sind jedoch auf die Zugabe von Tracer-Partikeln oder Farbstoffen angewiesen, welche starke Auswirkungen auf die zu untersuchenden Systeme ausüben können. Die nicht-invasive MRT Messung von Strömungsfeldern und Reaktionsprodukten widmet sich diesem Problem. Dabei stellen Echtzeitmessungen in nichtstationären und schnellfließenden Reinsystemen, bei gleichzeitig scharfer Abbildung und hoher Auflösung, die größte Herausforderung dar. Drei Forschungsziele zur Untersuchung von gas-flüssig Taylor-Strömungen mittels MRT werden definiert und erfolgreich beantwortet.

Zu Beginn stellt sich die Frage, ob die Untersuchung von gas-flüssig Taylor-Strömungen in Reinsystemen und unter realen Strömungsbedingungen möglich ist. Experimentelle MRT Untersuchungen sind anspruchsvoll. Am Anfang stehen die Entwicklung eines komplexen Strömungsaufbaus mit definierter Strömungsdynamik, die Konstruktion eines geeigneten Resonators mit angemessenem Signal-Rausch-Verhältnis und der Optimierung einer Pulssequenz zur schnellen Strömungsuntersuchung innerhalb des Aufbaus. Basierend auf dieser Grundlage wird die zugrundeliegende Strömung innerhalb des Aufbaus erfolgreich mit MRI und 2C-2D PIV untersucht. Ein qualitativer Vergleich verdeutlicht die gute Übereinstimmung zwischen beiden Methoden. Dabei deuten die Ergebnisse auf eine stationäre, aber nicht rotationssymmetrische Strömung im Inneren der Kapillare hin.

Als nächstes wird die Möglichkeit der Untersuchung reaktiver Strömungen adressiert. Exakte und korrekte Messungen fordern dazu weitere Verbesserungen bezüglich des Strömungssetups und der Messspule. Für eine optimale Leistung wird ein Birdcage-Resonator entwickelt und hinsichtlich seiner Feldhomogenität bei unterschiedlicher Beladung untersucht. Ein direkter Vergleich zu einer kommerziellen Spule zeigt die uneingeschränkte Funktionalität der Spule auf.
Mittels MRT Bildgebung wird der Stofftransport von O_2-Einzelblasen in N_2-gesättigtem Wasser erfolgreich über die zeitliche Blasenlängenabnahme im nichtreaktiven System aufgezeigt.

Für die Untersuchung reaktiver Strömungen wird die Oxidation von Fe^{II}(EDTA) zu Fe^{III}(EDTA) als eine geeignete Reaktion ermittelt, welche die anspruchsvollen Anforderungen der MRT Experimente erfüllt. Der Stofftransport von O_2-Einzelblasen in N_2-gesättigtem Wasser mit unterschiedlichen Fe^{II}(EDTA)-Konzentrationen wird durch die zeitliche Blasenlängenabnahme aufgezeigt. Das entstehende Reaktionsprodukt wird unter Verwendung von Inversionsmessungen erfolgreich im Wake der Taylor-Blase durch den Anstieg des MR-Signals visualisiert. Zusätzlich ist der zeitliche Reaktionsverlauf durch den Rückgang der Signalintensität verfolgbar.

Als letzte Frage stellt sich, ob die MRT-Daten mit einem physikalischen Modell der zeitlichen Blasenlängenabnahme in nicht-reaktiven und reaktiven Taylor-Strömungen korreliert werden können. Der Flüssigkeitsfilm zwischen der Taylor-Blase und der Kapillarwand ist hauptverantwortlich für den stattfinden Stofftransport. Um das 2D-Konzentrationsprofil des Films zu erhalten wird die zugrundeliegende Diffusions-Konvektions-Reaktions-Gleichung numerisch in einem diskretisierten Bereich unter Verwendung der Finite-Differenzen-Methode (FDM) gelöst. Die vereinfachten Annahmen der numerischen Lösung werden validiert und die Auswirkungen der physikalischen und Diskretisierungsparameter auf die berechneten Ergebnisse werden untersucht und bewertet. Die experimentellen MRT-Daten werden erfolgreich, mit den für verschiedene Filmdicken berechnet FDM-Ergebnissen, verglichen. Die Validität der vom Modell angenommenen Flüssigkeitsfilmdicke wird diskutiert.

Die in dieser Arbeit erfolgreich entwickelten Werkzeuge und Methoden bieten ein großes Potenzial und tragen zu einem tieferen Verständnis der Taylor-Strömungen in gas-flüssig Systemen bei. Der grundlegende Vorteil der MRT Messtechnik gegenüber herkömmlichen optischen Messmethoden liegt in der nicht-invasiven Untersuchung reiner Systeme, selbst unter optisch unzugänglichen Bedingungen. Die Durchführung räumlich aufgelöster in-*operando* Messungen zur Bestimmung von Strömungsfeldern und der Konzentrationen beteiligter Reaktionskomponenten durch die hier entwickelten Werkzeuge und Methoden wird das Verständnis und die Verbesserung realer Systeme maßgeblich unterstützen.

Abstract

This thesis is motivated by combining the two major research fields of magnetic resonance imaging (MRI) and chemical reaction engineering. Here, the main interest lies in investigating gas-liquid Taylor flows using MRI. The interaction of local flow dynamics and chemical reaction is especially crucial for chemical process optimization since residence time variations from the underlying flow fields can significantly impact the product's selectivity and yield. Here, Taylor flows allow for the prolonged observation of single bubbles under defined and reproducible flow conditions. Conventional optical measurement techniques enable the investigation of flow and mass transport, relying on adding tracers or fluorescent dyes, which can greatly impact the systems under investigation. MRI addresses this issue by performing non-invasive measurements of flow dynamics and reaction products. The key challenge is the real-time acquisition of sharply depicted and well-resolved MR images in non-stationary and fast-flowing pure systems. Three main research questions on investigating gas-liquid Taylor flows by MRI come up and are successfully answered.

The initial question arises whether MRI can evaluate gas-liquid Taylor flows in pure systems under real flow conditions. Experimental MRI studies are demanding. The first step is to develop a sophisticated flow setup with defined flow dynamics, a proper resonator with an adequate signal-to-noise ratio, and an optimized pulse sequence for fast flow investigation inside the setup. On this basis, the underlying flow inside the setup is successfully investigated using MRI and 2C-2D PIV. A qualitative comparison shows a good agreement between both methods and indicates a stationary but not rotationally symmetric flow inside the capillary.

The ability of MRI to analyze reactive flows is the next issue to be addressed. Further improvements of the flow setup and the MRI coil are needed for precise and correct measurements. A birdcage resonator is designed for optimum performance. The design is tested regarding field homogeneity under different loading conditions. A side-by-side comparison to a commercial coil demonstrates successful operation.
For non-reactive flows, mass transfer of single O_2 bubbles in N_2 saturated water is successfully demonstrated by MRI through the temporal decrease in bubble length.
For reactive flows, the oxidation of Fe^{II}(EDTA) to Fe^{III}(EDTA) is identified as a suitable reaction meeting the demanding requirements for MRI experiments. The temporal decrease in bubble length is employed to visualize mass transfer of single O_2 bubbles in N_2 saturated water with varying Fe^{II}(EDTA) concentrations. Inversion recovery measurements successfully reveal reaction product formation inside the Taylor bubble's wake by a considerable rise in MR signal with the ability to track the reaction's temporal progression by a decline in signal strength.

The final question to be answered is whether the MRI data can be correlated with a physical model of the temporal length decrease in non-reactive and reactive Taylor flows. The liquid film between the Taylor bubble and the capillary wall is the main contributor to mass transfer. The underlying diffusion-advection-reaction equation is numerically solved in a discretized domain using a finite difference method (FDM) to obtain the film's 2D concentration profile. The numerical solution's simplified assumptions are validated and the effects of physical and discretization parameters on the computed results are analyzed and assessed. The experimental MRI data are successfully compared to FDM results computed at various film thicknesses and are discussed regarding the validity of the model's best matching liquid film thickness.

The tools and methods successfully developed in this thesis offer great potential and contribute to a deeper understanding of gas-liquid Taylor flows. The fundamental advantage of MRI over conventional optical methods lies in the non-invasive measurement of pure systems, even in opaque environments. Thus, spatially resolved in-*operando* measurements of flow fields and local reaction component concentrations can be obtained so that the presented tools and methods will particularly aid in investigating, understanding, and improving real-world systems.

Acknowledgement

Between January 2018 and June 2023, this thesis was developed at the Center for Environmental Research and Sustainable Technology (UFT) at the University of Bremen. Funding for the project was provided by the German Research Foundation (DFG) as a part of the Priority Programme "Reactive Bubbly Flows" (SPP 1740).

After this long journey, I can reflect on over five exciting years filled with unique events, enjoyable discussions, and amazing colleagues from various scientific fields who became good friends. Obviously, there were not just enjoyable times to look back on. Moments of uncertainty regarding the project's successful completion surfaced several times after exhausting weeks of measuring with unsatisfying results. These were the moments at which I would have preferred to just quit and do something else. However, on these occasions, it was more important than ever to return to the drawing board with fresh bravery and embark on a new plan. As giving up was never an option for me, the project was completed successfully and interesting insights were gained. The support of many people has encouraged me in my efforts, for which I would like to express my gratitude.

First and foremost, I would like to thank my supervisor and first reviewer, Prof. Dr.-Ing. Jorg Thöming without whom this scientific journey would not have been possible. I am very grateful for the support, the fruitful discussions and the encouragement of my work. Your backing has helped me overcome challenges that at first seemed unsolvable.

I want to express my gratitude to Prof. Dr.-Ing. Michael Schlüter for accepting my thesis as a second reviewer right away and for taking his time to read and review my work. I also appreciate his dedicated and successful coordination of the "Reactive Bubbly Flows" Priority Program.

I am thankful to Dr.-Ing. Ulrich Mießner for his support and the countless discussions about fluid dynamics and Taylor flows. The valuable PIV measurements could only be conducted thanks to his encouragement. In retrospect, the interesting bachelor's and master's theses you offered me paved the way and set the direction of my scientific career, for which I am more than thankful. Our chats about music and life are also something I greatly value.

I am grateful to Dr. Ekkehard Küstermann for his patient assistance and the MR scanner operation, even during long evenings of MRI measurements. His knowledge and ideas in the field of MRI have greatly aided and advanced this thesis. Our pleasant and intense conversations about cars, people and politics made the long days enjoyable, which I greatly value.

I want to thank PD Dr. rer. nat. habil. Wolfgang Dreher for his help and support with all MRI-related questions. His profound knowledge allowed us to quickly tackle problems and progress.

I want to thank Dr.-Ing. Benjamin Besser for always taking his time to critically discuss the scientific aspects of my work over a cup of coffee.

I want to thank all of my wonderful former and present coworkers of the CVT group for the many valuable conversations, the encouragement, and of course, all the fun we had at work and during our seminar trips. Having such a supportive and accommodating work group is rare and invaluable.

I want to thank my mum and my grandparents for their unwavering support and for encouraging my early interest in science and technology. An apology from my end for all the torn-apart electrical devices to learn more about their functions is also due at this time.

Finally, I want to thank my partner, soulmate, and most important person in my life, Sven, for his infinite love and understanding. Your patience and positive mindset always cheer me up, even on the toughest days.

List of publications

Papers

- **P. Kemper**, E. Küstermann, W. Dreher, T. Helmers, U. Mießner, B. Besser, J. Thöming, *Magnetic Resonance Imaging for Non-invasive Study of Hydrodynamics Inside Gas-Liquid Taylor Flows*, Chemical Engineering & Technology, 44(3) (2021), 465-476
- **P. Kemper**, J. Thöming, E. Küstermann, *Tailored birdcage resonator for magnetic resonance imaging at 7 T using 3D printing*, HardwareX, 12 (2022), e00326

Book contributions

- **P. Kemper**, E. Küstermann, W. Dreher, J. Thöming, *Experimental Investigation of Local Hydrodynamics and Chemical Reactions in Taylor Flows Using Magnetic Resonance Imaging*, In: M. Schlüter, D. Bothe, S. Herres-Pawlis, U. Nieken (eds) Reactive Bubbly Flows. Fluid Mechanics and Its Applications, vol 128. Springer, Cham. (2021)

Conference talks

- **P. Kemper**, U. Mießner, E. Küstermann, W. Dreher, J. Thöming, *3D Magnetic Resonance Imaging: Set-up for Measuring Local Mass Transfer in Taylor Flows*, 2nd International Workshop FERMaT, (2018) Hamburg, Germany
- **P. Kemper**, W. Dreher, E. Küstermann, J. Thöming, *Magnetic Resonance Imaging: Spatially resolved experimental analysis of mass transfer on Taylor bubbles by means of NMR*, Annual Meeting on Reaction Engineering in Corporation with the Subject Division Multiphase Flows, (2019) Würzburg, Germany

Conference posters

- **P. Kemper**, E. Küstermann, U. Mießner, J. Thöming, *Magnetic resonance imaging (MRI) of reactive multiphase flows*, 26th International Congress of Chemical and Process Engineering, CHISA (2022) Prague, Czech Republic

Contents

1 Introduction

1.1 Introduction and motivation

Gas-liquid reactions have turned into a key component of modern industry. Processes including oxidation, hydrogenation, chlorination, and the absorption of CO_2 and NO_x from exhaust gases are based on the principle of mass transfer from the gaseous to the liquid phase, commonly followed by a chemical reaction [1–4]. Efforts are continuously focused on optimizing these processes regarding selectivity and yield, particularly since raw material and energy costs have lately risen rapidly [5]. Additionally, the focus is increasingly turning towards a more sustainable and environmentally friendly production.
Industrial processes often employ large bubble columns or gas-sparged tanks due to their ease of control and large output capacity. Thus, selectivity, yield, and mass transfer coefficients are mostly quantified globally over the entire process or individual unit operations by analyzing the product stream at the outlet. Models and equations for estimating these large-scale processes are available [6]. However, an in-depth understanding of the local transport phenomena and concentration fields is mandatory for specific efficiency enhancement. Especially when it comes to chemical reactions, the underlying flow field inside the specific device or process is critical. Flow and reaction are superimposed and their interaction influences local product distributions and residence times [7]. These phenomena are difficult to reproduce and investigate in conventional reactors due to the complex nature and limited optical accessibility of bubble swarms. Rather than investigating bubble swarms [8], single bubbles rising in large columns [9] or emulating bubble swarm effects in large setups [10], it is more convenient to carry out lab scale experiments of single bubbles in a system of reduced complexity.
Such measurements enable the assessment of various parameters and allow conclusions to be drawn, contributing to an in-depth understanding of processes inside large-scale systems. Further, downsizing also provides advantages on selectivity and yield in manufacturing fine chemicals and pharmaceuticals due to highly defined and precisely controllable process parameters. For this reason, such setups are considered in this work.

Taylor flows

Taylor flows are particularly suitable for this approach, as they enable reproducible and well-defined process conditions over a range of length scales. Fig. 1.1 schematically illustrates a Taylor bubble with all its crucial parameters. In cylindrical capillaries, Taylor flows are characterized by elongated bullet-shaped bubbles consisting of a cylindrical body with an

elongated half-sphere forming the front cap and a compressed half-sphere forming the rear cap. The specific flow conditions determine the shape of the caps. A thin, well-defined liquid film of uniform thickness σ_{film} separates the bubble from the capillary wall. If a train of bubbles is present, the single Taylor bubbles are separated by the so-called slugs. For this reason, the flow regime is also called segmented or slug flow. [11]

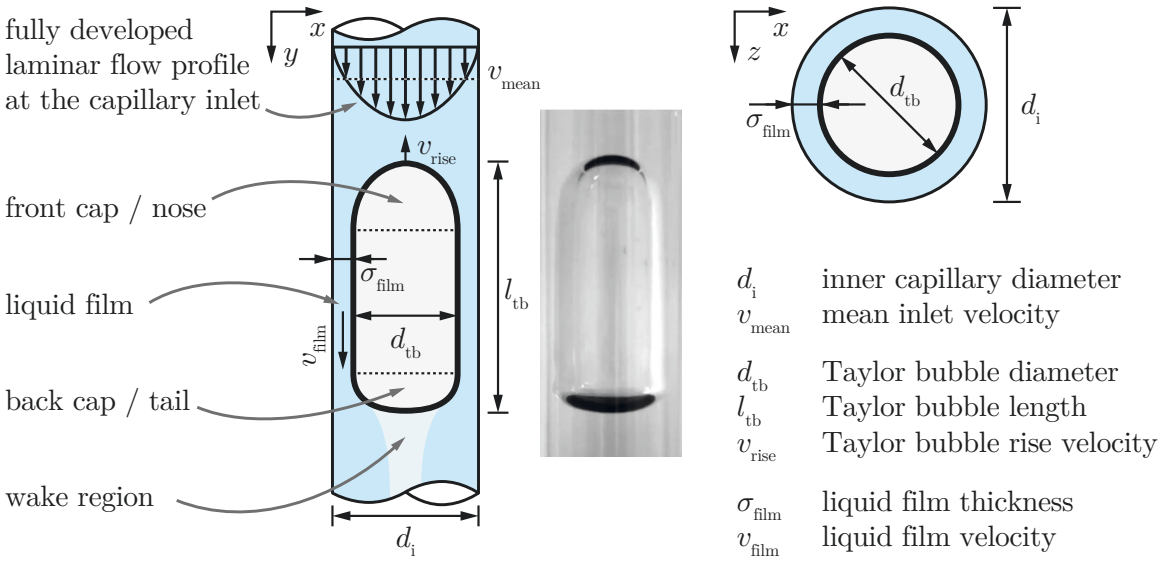

Fig. 1.1.: Schematic representation of a Taylor bubble inside a cylindrical capillary. Essential parts of the Taylor bubble are named and crucial describing parameters are listed. The system is depicted from the side view (x, y-plane) and by a horizontal cut through the center of the bubble and the capillary (x, z-plane). A photograph of an air bubble in acetonitrile at $d_{\text{i}} = 5.0\,\text{mm}$ is shown as a reference.

Research has long been devoted to the understanding and application of Taylor flows in various scales. Numerous experimental studies of multiphase flows were carried out in capillary setups inside small channels focusing on flow dynamics [12–18], mass transfer and chemical reactions [19–24]. Due to the well-defined conditions, the behavior of mass transfer and flow dynamics of these systems is moreover studied by numerical simulations within certain limits [25–30].

The multiphase flows discussed in all of these publications can be characterized and classified primarily using three dimensionless quantities. At first, the Reynolds number Re classifies the existing flow regime as a measure of the ratio between inertial and viscous forces [31]:

$$Re = \frac{\rho_{\text{liq}}\, v\, d_{\text{i}}}{\eta_{\text{liq}}} \tag{1.1}$$

The inertial term consists of the liquid phase density ρ_{liq}, the fluid's flow velocity v and the inner diameter of the capillary d_{i}. The viscous term solely consists of the dynamic viscosity of the fluid η_{liq}. Especially in pipes with larger d_{i}, the critical value of $Re_{\text{crit}} < 2040 \pm 10$ [32]

can easily be exceeded, causing a transition from the laminar to turbulent flow regime as the viscous forces can no longer dissipate flow disturbances. In capillaries and microchannels of small inner diameter d_i, the Reynolds number is typically in the laminar range.

In small geometries, however, the balance of the acting forces changes considerably. Compared to large pipes, the influence of gravitational forces decreases, whereas surface tension forces gain importance. Their ratio is described by the dimensionless Eötvös number (also found in literature as Bond number Bo) [31]:

$$Eo = \frac{(\rho_\mathrm{liq} - \rho_\mathrm{gas})\, g\, d_\mathrm{i}^2}{\sigma_\mathrm{surf}} \tag{1.2}$$

The Eötvös number relates the density difference of both phases $(\rho_\mathrm{liq} - \rho_\mathrm{gas})$, the gravitational acceleration g and the capillary's inner diameter d_i to the surface tension σ_surf of the gas-liquid system. Bretherton [33] demonstrated in first experiments that at $Eo < 3.37$ no buoyancy-driven bubble rise occurs since the surface tension forces dominate the gravitational forces. Later, the critical value was adjusted to $Eo < 4$ by further experimental work of White and Beardmore [34]. For an air-water system, this means that buoyancy-driven bubble rise only occurs within capillaries with an inner diameter of at least $d_\mathrm{i} = 5.5\,\mathrm{mm}$.

The dimensionless capillary number Ca describes the ratio of viscous forces to surface tension forces at the gas-liquid interface, which is useful for characterizing the bubble geometry. Ca is defined as [15]:

$$Ca = \frac{\eta_\mathrm{liq}\, v}{\sigma_\mathrm{surf}} \tag{1.3}$$

Both caps adopt the identical shape of perfect hemispheres for very small values of $Ca \to 0$. The characteristic bullet shape of the Taylor bubble forms with increasing Ca. The capillary number is often used to approximate the film thickness, which is particularly important for mass transport processes. Giavedoni and Saita [35] demonstrated by numerical simulations that a larger Ca corresponds to a thicker film [15].

In studies dealing with hydrodynamics or bubble shape, these three dimensionless parameters are often combined to the Morton number Mo [36]:

$$Mo = \frac{Eo\, Ca^2}{Re^2} = \frac{(\rho_\mathrm{liq} - \rho_\mathrm{gas})\, g\, \eta_\mathrm{liq}^4}{\sigma_\mathrm{surf}^3\, \rho_\mathrm{liq}^2} \tag{1.4}$$

It represents a further measure for describing the emerging bubble shape, which is more often used in numerical studies rather than in classical experimental investigations.

The previously mentioned dimensionless numbers enable the classification of the underlying flow dynamics and allow an estimation of how the flow field behaves in the wake region directly behind the bubble. The flow inside the wake is of major importance and interest, especially regarding chemical reactions, since recirculations can result in different, sometimes

significantly longer residence times τ. The residence time, in turn, will significantly impact the selectivity of chemical reactions. The emerging wake structures are often investigated and visualized by optical measurement methods. Particle image velocimetry (PIV) is one of the most commonly used methods for flow visualization. In this process, fluorescent particles are dispersed in the liquid phase, following the fluid's streamlines, and can be tracked optically. Particle fluorescence is induced by a pulsed or a high-power continuous wave laser. Subsequently, the emitted signal is captured with a precisely timed high-speed camera. The displacement of tracer particle ensembles can then be converted into a velocity vector by the exact knowledge of the temporal interval between two subsequent images [37]. Open source tools such as PIVlab [38] for Matlab are available for data evaluation and reconstruction of the flow field.

PIV is an established method often used for flow analysis in small channels and microchannels [15, 39]. Only a limited number of publications exist on PIV investigations of gas-liquid flows in small vertical capillaries [14, 18, 23].
Kastens et al. [23] investigated the wake structures of CO_2 bubbles in an aqueous system under countercurrent flow conditions within different capillary diameters of $d_\mathrm{i} = 6 - 8\,\mathrm{mm}$. The increase in diameter led to a change in the wake structure. For $d_\mathrm{i} = 6\,\mathrm{mm}$, no vortex was present and the flow followed the contour of the rear bubble cap. At $d_\mathrm{i} = 7\,\mathrm{mm}$, a ring vortex was observed, leading to a fluid recirculation behind the bubble. Unsteady vortices occurred at $d_\mathrm{i} = 8\,\mathrm{mm}$, resulting in a chaotic three-dimensional back mixing.

While PIV sheds light on the local flow fields, it does not provide information on mass transfer. However, technologies such as (planar) laser-induced fluorescence ((P)LIF) enable the experimental investigation of mass transfer [21, 40]. The technique is based on a fluorescent dye's excitation and absorption at a specific wavelength. Following excitation, the dye emits light of variable intensity, depending on several inhibitors like dissolved molecular oxygen or pH variations, also known as fluorescence quenching. [40]
Kastens et al. [23] employed an additional LIF system in their previously mentioned PIV investigations of wake structures inside capillaries of various diameters. Fluorescein was chosen as a dye whose fluorescence intensity reduces with decreasing pH values. This fluorescence quenching allows the dissolved and dissociated CO_2 concentration to be detected due to the pH change. The concentration fields obtained by LIF are in good agreement with the underlying flow fields of the PIV measurements inside the wake.

For the fundamental estimation of mass transport processes during reactions, it is sufficient to measure the volume decrease of a Taylor bubble by a time series of images [20]. In addition, these images can also provide information about product formation and removal when using a color-changing reaction and illumination at different wavelengths. By doing so, Kexel et al. [24] demonstrated the influence of fluid dynamics on the selectivity and yield of a consecutive competitive gas-liquid reaction in a methanol solution. Nitric oxide (NO) is transported from

the bubble into the liquid phase and reacts to an intermediate mononitrosyliron compound (MNIC) and a dinitrosyliron compound (DNIC). A change in the capillary diameter from $d_\mathrm{i} = 4\,\mathrm{mm}$ to $d_\mathrm{i} = 5\,\mathrm{mm}$ resulted in a better mixing due to turbulent vortices inside the wake. Consequently, more intermediate product MNIC with higher selectivity was formed. The capillary with $d_\mathrm{i} = 4\,\mathrm{mm}$ showed a laminar wake structure and had a longer residence time of the fluid inside the liquid film due to lower rise velocities, resulting in the predominant formation of DNIC.

All of these various optical measurement techniques have become the standard for investigating different characteristics of multiphase flows, as they are relatively easy to implement and apply. However, they rely on adding either tracer particles (PIV) or dyes (LIF) to reveal the specific underlying flow dynamics or mass transport processes, making them invasive by contaminating the system under investigation. Additionally, optical accessibility is mandatory, which renders measurements in opaque systems impossible.

Magnetic resonance imaging

These challenges can be faced using nuclear magnetic resonance (NMR) based imaging (MRI). MRI enables non-invasive and slice-selective multidimensional imaging of pure systems, even in opaque setups. The advantage of MRI over other tomographic methods, such as X-ray tomography [22, 41], is the ability to encode additional information in the complex NMR signal [42]. Thus, conclusions about diffusion coefficients, chemical composition or flow velocities can be drawn. Since the discovery of NMR in the 1920s, the technology has greatly advanced. Initially aimed at medical applications, MRI has gained popularity in many fields of engineering and research over the past decades due to its versatility. Nowadays, MRI evolved into an indispensable tool for chemical process engineering and fluid dynamics. [42]

The work by Gladden et al. [43] summarizes and compares different pulse sequences and their application to velocity imaging. EPI (echo-planar imaging) and spiral imaging sequences are particularly suitable for transient systems due to their fast acquisition times. However, they are sensitive to spatial or temporal fluctuations of the magnetic field B_0, such as coil inhomogeneities or susceptibility changes at phase boundaries. In comparison, RARE (rapid acquisition with relaxation enhancement) sequences benefit from higher spatial resolution but are often too slow for transient systems. Gradient echo based sequences such as FLASH (fast low angle shot) feature high robustness and decent acquisition times, mainly due to the use of small flip angles, however, at the cost of lower signal-to-noise ratios (SNR). The choice of the suited sequence is always related to the specific application.

For example, an ultra-fast sequence (SEMI-RARE) was developed by Sederman et al. [44] to investigate static and flowing systems. They successfully measured a parabolic flow profile of a single-phase flow inside a $d_\mathrm{i} = 3\,\mathrm{mm}$ capillary with a flow velocity of $u = 22\,\mathrm{mm\,s^{-1}}$ using a

time-of-flight measurement. Additionally, an air-water train flow was tested, giving first hints on the motion inside the liquid slug. However, due to the slice selectivity of the sequence, the signal decreased in flows with toroidal nature as the non-excited liquid from out of plane moved into the imaging slice.

Another approach to ultra-fast imaging was presented by Tayler et al. [45]. They used a spiral imaging sequence to quantify bubble size distributions and bubble shapes in high voidage bubbly flows up to $22\,\%$. A column of $d_\mathrm{i} = 31\,\mathrm{mm}$ and $l = 2000\,\mathrm{mm}$ was used. Susceptibility matching between air and water was performed using a $16.86\,\mathrm{mM}$ dysprosium chloride solution to minimize off-resonance effects at the gas-liquid interfaces. Suppression of the susceptibility artifacts by dysprosium chloride enabled measurements, but the added salt potentially led to a stabilizing effect on the bubbles.

Benders et al. [46] utilized the change of the magnetic state during the oxidation of a diamagnetic copper(I) complex to a paramagnetic copper(II) complex to determine the reaction product behind a freely rising oxygen bubble with sufficient contrast. Longtime measurements were realized by using a highly viscous medium of polyethylene glycol and acetonitrile ($\eta_\mathrm{liq} = 800\,\mathrm{mPa\,s}$), resulting in bubble rise velocities in the range of $0.14\,\mathrm{mm\,s^{-1}} - 0.5\,\mathrm{mm\,s^{-1}}$. The slow movement and long residence times were necessary as the oxidation of the [Cu(btmgp)I] complex takes $4\,\mathrm{s} - 5\,\mathrm{s}$ at room temperature [47].

Although numerous publications exist on the application of MRI to various gas-liquid systems, the explicit use of MRI on non-reactive and reactive Taylor flows is lacking. There are no known publications at the time of writing that compare MRI results from mass transfer in gas-liquid Taylor flows with simplified mass transfer models.

Investigating gas-liquid systems under real flow conditions is particularly challenging since these highly dynamic systems require very short measurement times and fast data acquisition to prevent motion blurring. Further, a sufficiently high resolution and a good signal-to-noise ratio are necessary to interpret the data. Ultra-fast methods for dynamic systems are scarce. Often these fast sequences are sensitive to coil inhomogeneities or susceptibility changes at the gas-liquid interface. Static and dynamic B_0 field fluctuations will induce artifacts [43, 48]. Thus, fast sequences are often applied to steady-state or relatively motionless systems or rely on additional chemicals for susceptibility matching.

1.2 Objective

Detailed knowledge of the present flow field is essential for process optimization in dynamic systems. Since flow fields and chemical reactions are superimposed, significant variations in local concentrations and residence times can occur. Classical optical methods offer limited

possibilities to investigate these local interactions between flow and reaction in pure systems. This work aims to combine the two comprehensive research fields of multiphase flows and magnetic resonance imaging in a proof of principle study by developing tools and methods for non-invasive measurements of pure gas-liquid Taylor flows.

Based on the aforementioned variety of available and promising publications in the field of MRI and multiphase flows, three challenging questions that motivate this work arise:

- "*Can MRI be used to study gas-liquid Taylor flows under real flow conditions, even in a pure system?*"
- "*Is it possible to investigate reactive gas-liquid Taylor flows by MRI and can the arising reaction product be visualized?*
- "*Can the experimental MRI data be verified by a simplified model that physically describes pure and reactive mass transfer by the time-dependent change in bubble length?*

Several steps have to be addressed successively to answer these research questions:

The first challenge is to design and build a sophisticated flow setup that meets the MR scanner's dimensional and material requirements. The most challenging part is establishing a homogeneous and uniform flow within a vertically aligned glass capillary inside the confined space of the horizontal bore scanner. A vertical flow setup enables long-term measurements of single bubbles over several minutes by holding buoyancy-driven Taylor bubbles in place using a countercurrent flow. A complex fluid supply and optimum use of the scanner's bore space are required. For this reason, constructing a tailor-made MR resonator around the sophisticated flow setup is necessary. Test measurements have to be performed to demonstrate the coil's and flow setup's correct operation. The setup has to be regularly adapted and improved throughout the project to address arising issues.

The second challenge is the development of a suitable MR pulse sequence for non-invasive real-time measurement of the flow field in the vicinity of the Taylor bubble. The development involves modifying existing pulse sequences to achieve a balance between high resolution, good SNR and fast data acquisition with minimal motion blurring. The collected MR datasets have to be compared to PIV measurements acquired inside the same setup to provide a conclusion about the correctness and accuracy of the MR sequence.

The third challenge addresses the second research question: the investigation of chemical reactions in gas-liquid Taylor flows. Following the successful completion of the first two steps, a suitable chemical gas-liquid reaction has to be identified. The requirements are stringent: a fast reaction rate is crucial due to short residence times in the system; a sufficient relaxation time contrast between reactant and product is mandatory so that their difference can be measured in real-time by MRI; safe and simple handling during preparation and experimentation is desirable in terms of safety.

The temporal bubble length decrease is experimentally determined for non-reactive and reactive Taylor flows using MRI with standard pulse sequences. T_1 contrast measurements of the reaction system are performed to visualize the temporal product distribution inside the bubble's wake. T_1 contrast measurements are favorable since fast sequences have an inherent T_1 weighting.

To address the final research question, the experimental MRI data of non-reactive and reactive Taylor flows are compared to a simplified numerical model that physically describes the given problem of two-sided mass transfer without and with a superimposed chemical reaction. The numerical model must be developed and tested before evaluating the MRI data.

1.3 Structure of this thesis

Chapter two addresses the theoretical background of NMR and MRI. The physical principle of NMR, basic pulse sequences, and the MR hardware are explained. Besides that, a particular focus is placed on the design of measurement coils, especially birdcage resonators, since the resonator design is crucial for this work.

Chapter three deals with the specific demands placed on the MRI experiments. A variety of different topics are addressed. The two main flow setups for different approaches are discussed in detail from the hydrodynamic standpoint. From the MRI side, this chapter provides details on both developed MR resonators and the adapted pulse sequence. A suitable reaction system for the investigation of reactive Taylor flows is highlighted.

Chapter four is devoted to the findings of the non-invasive Taylor flow characterization by MRI. The flow inside the Taylor bubble's wake is studied using the MRI pulse sequence proposed in this work. Identical PIV measurements were conducted to identify the flow field inside the wake region. Results from both methods are compared and discussed.

Chapter five focuses on the validation and characterization of the volumetric birdcage resonator for MRI at $7\,\mathrm{T}$. The coil's performance is evaluated at low and high loading conditions. Further, an image quality comparison with a commercial resonator is carried out.

Chapter six covers the development of a simple model for the computation of two-sided mass transport in non-reactive and reactive Taylor flows. First, the assumption to simplify the Taylor bubbles geometry as a cylinder is validated using the penetration theory. Next, two-sided mass transfer between the gas and liquid phases is modeled using a mathematical framework based on the two-film theory. Finally, a differential equation, solved numerically using the finite difference method (FDM), is used to incorporate the reaction term into the model. Thus, it is possible to compute the temporal change in bubble length for both reactive

and non-reactive systems. The effects of various parameters on the computed results are evaluated and discussed.

Chapter seven is devoted to the experimental MRI studies of reactive Taylor flows. Initially, the length decrease of non-reactive Taylor bubbles is examined. The data is utilized to identify the best fit between experiments and computations by adjusting the liquid film thickness of the proposed model. Results are discussed regarding the correctness of the chosen liquid film thickness. The inversion recovery method for visualization of Taylor flows with a superimposed chemical reaction is explained. Numerical computations and experimental MRI results of reactive Taylor flows with various reactant concentrations are compared. Further, the explained inversion recovery method reveals the arising reaction product inside the bubble's wake.

Chapter eight concludes the findings of this thesis. A perspective for future research is provided.

2 The principle of magnetic resonance imaging

The origin of today's sophisticated MRI measurement technology dates back to the early 1920s. The German physicists Stern and Gerlach proved experimentally that the spatial orientation of angular momentum shows a quantized behavior [49, 50]. During the 1930s, Rabi et al. used this finding to study the behavior of molecules in interaction with magnetic fields [51, 52]. Finally, in 1946, Bloch and Purcell used the knowledge of the early quantum mechanical concepts and developed it into a measurement technique [53, 54]. They demonstrated the phenomenon of nuclear magnetic resonance (NMR). Magnetic nuclei absorb and emit radio frequency (RF) energy when placed in a magnetic field. The energy was absorbed only at nuclei-specific frequencies. This resonance frequency varies for different nuclei at constant magnetic field strength. In 1952 they were rightly awarded the Nobel Prize in Physics for their discoveries. Twenty-seven years after the findings of Bloch and Purcell, a new milestone was reached. Lauterbur and Mansfield laid the foundation for modern days magnetic resonance imaging (MRI) in 1973 [55]. They hypothesized and demonstrated that when a spatially varying magnetic field is applied, the nuclei's spatial resonance frequency changes. As a result, the position of the emitting nuclei can be localized. Since then, MRI has become one of the most important and indispensable tools for medical diagnostics. MRI has recently gained popularity in many other fields of research, including chemical engineering, due to its enormous potential.

This chapter addresses the theoretical principles of NMR and MRI to put the developed methods, hardware, and results of this thesis into context. Since MRI is a highly complex subject, some of the following topics are presented in a simplified form so that they are sufficient for a complete understanding of this work.

For a detailed and comprehensive explanation, the interested reader is referred to the following literature on the subject, which covers the theory in its entirety:

- *Magnetic Resonance Imaging - Physical Principles and Sequence Design* - Robert W. Brown et al. - 2014 [56]
- *MRI at a Glance* - Catherine Westbrook, 2015 [57]
- *MRI from Picture to Proton* - Donald W. McRobbie et al., 2017 [48]
- *NMR Imaging in Chemical Engineering* - Siegfried Stapf and Song-I Han, 2006 [58]

2.1 Physical background

The MR measurement procedure can be summarized easily in principle. Initially, the specimen is placed inside the scanner, where it is excited by short RF pulses. In response to the excitation, the sample emits an RF signal which is recorded and reconstructed to obtain the actual image. The reality, however, quickly reveals the complexity of this seemingly straightforward procedure. The principles of NMR will be addressed next. In order to keep things simple, only the behavior of individual protons is explained at the quantum mechanical level. The classical vector model is used to illustrate the interaction of a group of nuclei.

2.1.1 NMR

A closer look at the abbreviation NMR (nuclear magnetic resonance) directly reveals the essential aspects of the method. Magnetic fields interact with the nuclear spins of molecules inside a sample. Resonance is achieved as soon as the system is excited with radio frequency (RF) pulses, matching the precessional frequency of the nuclear spins. The excitation results in an RF response of the system, containing information about the sample. [56]

Nuclear spin is an intrinsic property of subatomic particles in the form of angular momentum and is described by the spin quantum number I, which can only adopt quantized values ($I = 0, +1/2, +1, \dots$). A net spin ($I \neq 0$) is required for a nucleus to exhibit MR activity, which applies to nuclei with odd mass numbers (sum of protons and neutrons). Hydrogen ^{1}H is considered to be the prevalent nucleus for MR experiments (often termed as ^{1}H NMR or proton NMR). Being composed of only one proton ($I = 1/2$), hydrogen offers the highest gyromagnetic ratio γ and has a natural abundance of almost $100\,\%$. Other nuclei commonly found in the literature include ^{13}C, ^{19}F, ^{23}Na, ^{31}P, however, this work focuses solely on ^{1}H NMR. [57, 58]

The angular momentum of nuclei can only adopt a finite number of $2I + 1$ spin states ranging from $-I$ to $+I$. Thus, the hydrogen atom ($I = 1/2$) can be found in two different energy states. In the low energy or spin-up state $+1/2$, the nuclei will align parallel to the external magnetic field B_0. In the high energy or spin-down state $-1/2$, the nuclei have sufficient energy to oppose the external magnetic field, resulting in an alignment anti-parallel to B_0.

The spin states are degenerated in the absence of a magnetic field B_0, meaning they all have equal energy levels. However, energy levels will separate when exposed to a magnetic field $B_0 > 0$. This phenomenon is referred to as the Zeeman effect or Zeeman splitting. The

resulting energy difference ΔE between the quantized states is proportional to the magnetic field strength B_0 and can be described as [48]:

$$\Delta E = \frac{h}{2\pi}\gamma B_0 \tag{2.1}$$

Where γ is known as the gyromagnetic ratio, which is a nuclei-specific constant (for ^{1}H: $\gamma = 2.67 \times 10^8\,\mathrm{rad\,s^{-1}\,T^{-1}}$ or $\frac{\gamma}{2\pi} = 42.57\,\mathrm{MHz\,T^{-1}}$ [57]), B_0 is the magnetic field strength and h is Planck's constant ($h = 6.626 \times 10^{-34}\,\mathrm{J\,s^{-1}}$ [57]). Fig. 2.1 schematically illustrates a Zeeman diagram for hydrogen nuclei.

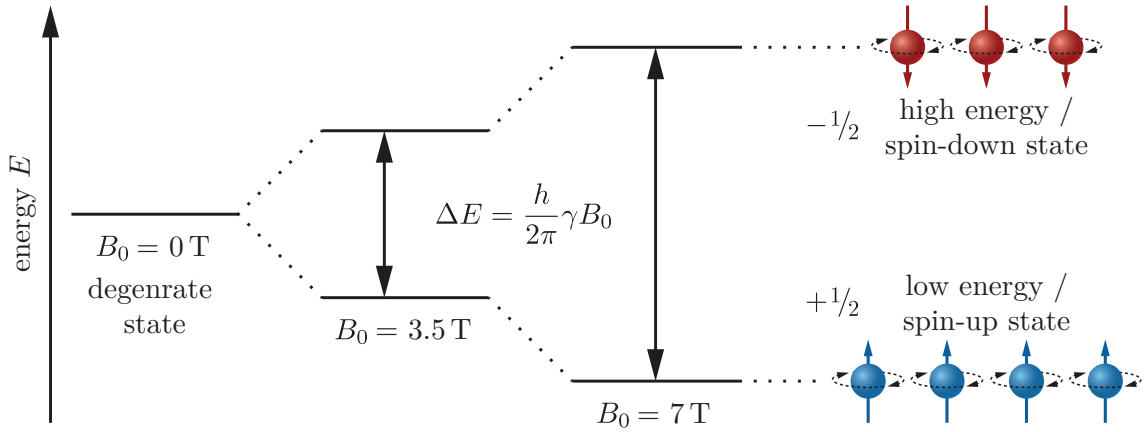

Fig. 2.1.: Zeeman diagram of ^{1}H nuclei. The energy difference ΔE between the lower energy state $+1/2$ and the higher energy state $-1/2$ is shown at different magnetic field strength B_0. A transition between the two stable states occurs by absorption or emission of a photon with the exact energy ΔE. The low energy state $+1/2$ is slightly more occupied than the high energy state $-1/2$, as illustrated by the spins on the right. Inspired by [56–58].

From a thermodynamic point of view, the low energy state $+1/2$ is populated with a slightly higher probability. The population difference between the two energy states $\frac{N_{-1/2}}{N_{+1/2}}$ at thermal equilibrium can be predicted by the Boltzmann distribution [58]:

$$\frac{N_{-1/2}}{N_{+1/2}} = \exp\left(-\frac{\Delta E}{k_\mathrm{B}T}\right) \tag{2.2}$$

where k_B refers to the Boltzmann constant ($k_\mathrm{B} = 1.381 \times 10^{-23}\,\mathrm{J\,K^{-1}}$ [57]) and T to the temperature. Assuming a magnetic field strength of $B_0 = 7\,\mathrm{T}$ at a temperature of $T = 298\,\mathrm{K}$, the calculated population difference is as small as $0.0048\,\%$. Although this difference seems very small at first, the vast number of molecules inside the specimen ($1\,\mathrm{mL}$ water corresponds to about 3.35×10^{22} H_2O molecules) contributes to the measurable net signal. The equilibrium net magnetization vector M_0, also known as net magnetization vector (NMV), is aligned parallel to the main magnetic field B_0 and increases with higher field strength of B_0.

The external magnetic field interacts with the spin of each individual proton, creating a torque that results in a movement known as precession. The magnetic moments of protons follow a circular path around the same axis as the B_0 field, as illustrated in Fig. 2.2 a) for a single ^{1}H nucleus. This movement is often compared to a gyroscope's wobbling motion.

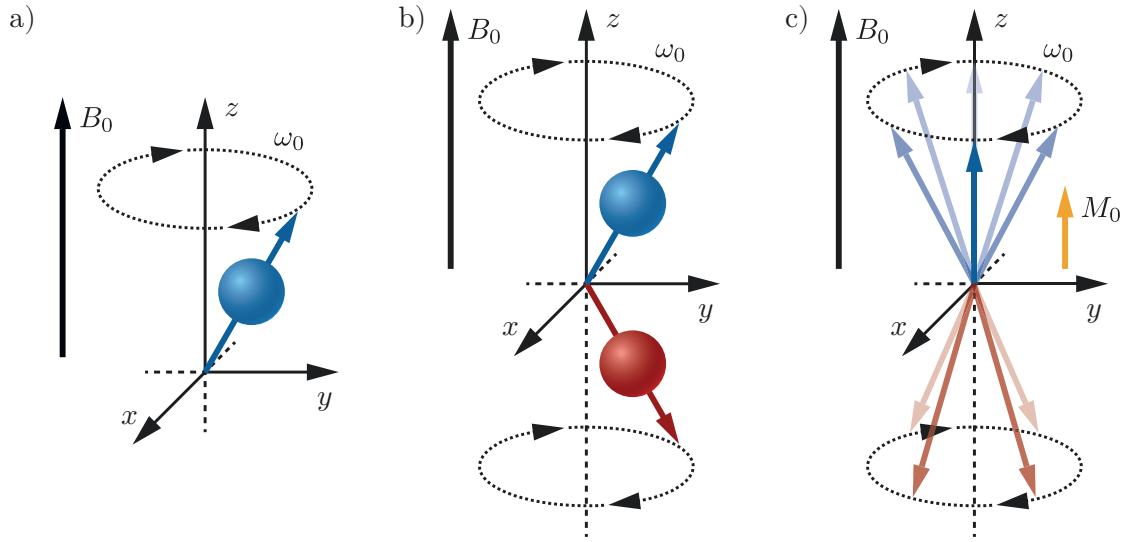

Fig. 2.2.: a) Precession of a single hydrogen nucleus around the magnetic field B_0. b) Two hydrogen nuclei in a parallel (blue) and anti-parallel (red) quantum spin state precess on the same circular path with identical ω_0. c) Protons of a spin ensemble behave like a single spin but are randomly oriented on their precessional path. The higher populated up-spin state results in an equilibrium net magnetization vector M_0, parallel to the B_0 field. Inspired by [48, 57].

The frequency of precession is proportional to the strength of the B_0 field and is also referred to as the Larmor frequency ω_0 [48]:

$$\omega_0 = \gamma B_0 \tag{2.3}$$

The precession movements of multiple nuclei are out of phase while being at rest, which is the case, for instance, when a sample has been placed inside the MR scanner's magnetic field. Despite moving at the same Larmor frequency ω_0, their magnetic moments are randomly arranged, either parallel or anti-parallel to B_0 (Fig. 2.2 b)). As a result, the equilibrium net magnetization vector M_0 precisely aligns with the external magnetic field B_0 (Fig. 2.2 c)).

2.1.2 MR signal

The equilibrium net magnetization vector M_0 of a spin ensemble has a measurable magnetization in the range of μT [48], which is up to six orders of magnitude smaller compared to the MR scanner's static magnetic field (here $B_0 = 7\,\mathrm{T}$). This signal is so small that it is practically impossible to measure it directly when the system is at rest. In order to produce a clearly

detectable signal, the system must be driven out of equilibrium, which is accomplished by using a second magnetic field.

Applying a radio frequency (RF) field of very short duration (referred to as an RF pulse) at the same frequency as the Larmor frequency ω_0 induces resonance. This field is always referred to as the B_1 field. The spins absorb energy and phase coherence is established, meaning all spins point to the identical location on the precessional path. As a result, the longitudinal magnetization is tilted. This tilting motion into the transverse plane resembles a spiral trajectory in a laboratory frame of reference (fixed x, y-plane) because the net magnetization vector M still precesses around B_0 with ω_0. Fig. 2.3 a) depicts the resulting spiral motion.

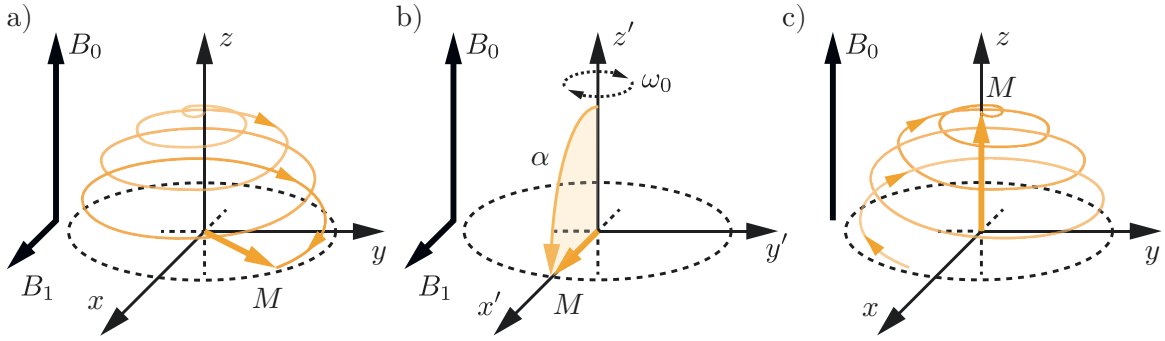

Fig. 2.3.: Illustration of spin motion during RF excitation by a B_1 field. a) The spin follows a spiral path into the transverse plane in a fixed reference coordinate system (x, y, z). b) In a reference frame (x', y', z') rotating at ω_0, the tilting can be simply described by the flip angle α. c) Following B_1 excitation, longitudinal magnetization is restored during relaxation. Again the spin motion resembles a spiral path in a fixed reference coordinate system. The hemispherical illustration shows an idealized representation in which T_1 and T_2 are practically of similar size. The spiral path's incline is much steeper in reality. Inspired by [48].

A rotating frame of reference is helpful for a simplified presentation, as shown in Fig. 2.3 b). The x', y'-plane of the coordinate system is assumed to rotate around the z'-axis with the Larmor frequency ω_0. Thus, in the rotating frame of reference, the precession around B_0 is suppressed, and the effect of B_1 can be observed independently. The deflection of M is defined by the flip angle α, which is mainly affected by the RF pulse's field strength B_1 and its pulse duration t_p [48]:

$$\alpha = \gamma B_1 t_\mathrm{p} \tag{2.4}$$

Excitation with a $90°$ pulse results in a maximum transverse magnetization perpendicular to the B_0 field. The system will undergo relaxation immediately after the RF excitation stops. In the laboratory frame of reference, M will recover to its equilibrium state following a spiral path, as illustrated in Fig. 2.3 c). Longitudinal magnetization M_z is restored while transverse magnetization M_{xy} decays. Both processes are described by a respective time constant, T_1 and T_2 (or more precisely, T_2^*), which are specific for different materials and are essential

parameters in NMR and MRI. These time constants are referred to as relaxation times and are further elaborated in the following section.

2.1.3 Relaxation times

In general, the time dependency of the net magnetization vector $M(t)$ is given by the cross product of the net magnetization vector M and the magnetic field strength B [58]:

$$\frac{dM}{dt} = \gamma M \times B \tag{2.5}$$

The Bloch equations (details can be found in [48, 56, 57]) are used to describe the temporal change of magnetization during excitation and relaxation for both the longitudinal magnetization $M_z(t)$ and the transverse magnetization $M_{xy}(t)$, depending on their time constants, T_1 and T_2 [48]:

$$M_z(t) = M_0\left(1 - \exp\left(\frac{-t}{T_1}\right)\right) \tag{2.6}$$

$$M_{xy}(t) = M_0\left(\exp\left(\frac{-t}{T_2}\right)\right) \tag{2.7}$$

The recovery of the net magnetization vector M_0 along B_0 is described by T_1 relaxation. The absorbed energy from the previously applied RF pulse is released by the spins when they flip back from high to low energy states through a process known as spin-lattice relaxation. Fig. 2.4 illustrates the time-dependent signal recovery of longitudinal magnetization M_z. After at least five times T_1, M_z is regarded as fully recovered.

T_2 (or more precisely, T_2^*) relaxation describes the decay of the net magnetic vector M_0 in the transverse plane due to spin dephasing. The RF excitation caused the system to achieve precessional coherence. As a result of spin-spin interactions, this coherence is quickly lost after excitation stops. Fig. 2.5 illustrates the time-dependent signal decay of transverse magnetization M_{xy}. It takes at least five times T_2 to consider M_{xy} as fully decayed.
Local magnetic field inhomogeneities contribute to spin dephasing, which can be compensated specifically by spin-echo pulse sequences. This combined dephasing caused by T_2 spin-spin interactions and field inhomogeneities is referred to as T_2^* decay. [57]

T_2 relaxation always happens faster and is shorter than T_1 relaxation. Full T_2 decay often occurs in a few hundred milliseconds, whereas total T_1 recovery typically takes several seconds. Both relaxation times heavily depend on the sample media and substance and are independent of each other, except that $T_1 \geq T_2 \geq T_2^*$. [48]

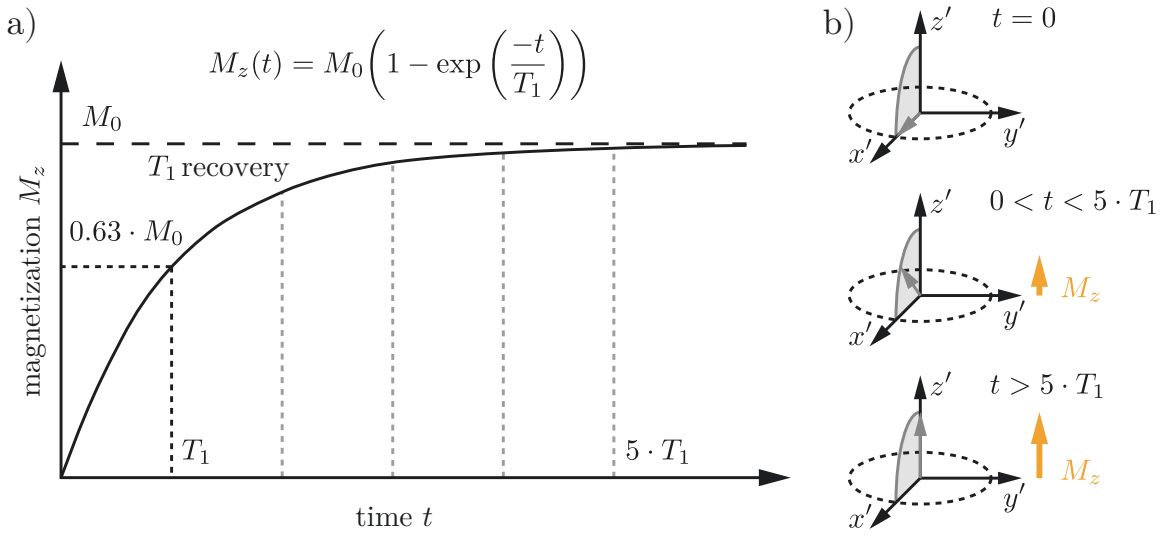

Fig. 2.4.: a) Recovery of longitudinal magnetization M_z. T_1 relaxation occurs due to energy transfer between the spins and the surrounding lattice. Full recovery is assumed after at least five times T_1. b) The recovery of M_z at different T_1 times is shown in a simplified form using a rotating frame of reference (x', y', z'). Inspired by [48, 57].

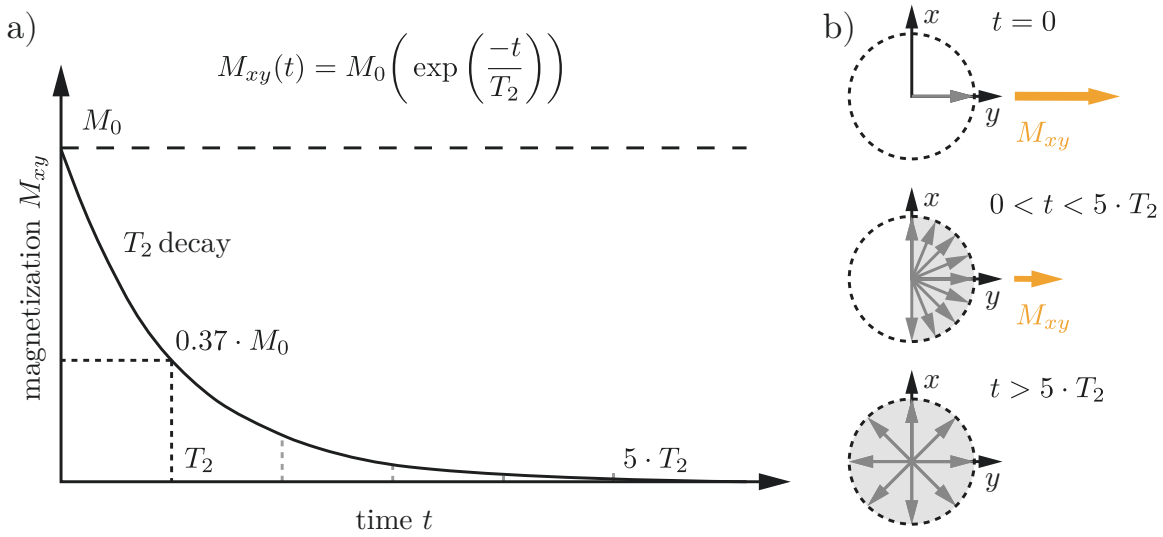

Fig. 2.5.: a) Decay of transverse magnetization M_{xy}. T_2 relaxation results from spin-spin interactions. It takes at least five times T_2 to assume full decay. b) The decay process of M_{xy} is illustrated at different T_2 times in the x, y-plane. Inspired by [48, 57].

2.1.4 Imaging

This work employs NMR to generate multidimensional images of the system under investigation, a technique known as magnetic resonance imaging (MRI). The required tools to acquire and process spatial data are briefly explained below.

Field gradients

MRI is based on the application of magnetic field gradients G superimposed over the scanner's static B_0 field, allowing for the spatial allocation of spins via a uniform and location-dependent change in their precession frequency ω [48, 58]:

$$\begin{aligned} \omega(x) &= \gamma(B_0 + (x\,G_x)) \\ \omega(y) &= \gamma(B_0 + (y\,G_y)) \\ \omega(z) &= \gamma(B_0 + (z\,G_z)) \end{aligned} \tag{2.8}$$

The product of the gradient vector and the corresponding position vector extends the static B_0 field. Application of the three different field gradients G_x, G_y, G_z enables three possible types of spatial encoding:

- **Slice selection**

  Slice selection is accomplished by altering the resonance frequency ω along the gradient direction. Different regions can be selectively excited as the Larmor frequency varies along the gradient position. The thickness of the selected slice is determined by the gradient strength G_{SS} and the RF bandwidth (BW) and RF pattern of the excitation pulse. Thin slices can be achieved by employing steep gradients or a narrower bandwidth. Hardware constraints mainly limit the steepness of the gradients. When choosing a narrower BW, there is always a trade-off between slice thickness and excitation duration. Thinner slices with a narrow BW require a longer RF pulse duration and vice versa. After selecting a slice, a two-dimensional in-plane localization has to be performed. For 3D image acquisition, the slice selection gradient can be paired with a phase encoding gradient for spatial slice selection. [48]

- **Phase encoding**

  The phase encoding gradient G_{PE} alters the magnetic field strength along one spatial direction, consequently changing the nuclei's precessional speed and phase. When the gradient G_{PE} is turned off, all nuclei revert to their original Larmor frequency while keeping their individual phase angles. The nuclei are thus phase encoded as a result. [48]
  Steeper phase encoding gradients result in a larger phase shift and, as a result, increased spatial resolution. Typically, the gradient is applied after RF excitation and before signal readout. Applying G_{PE} along the sample's shortest axis benefits acquisition times. [57]

- **Frequency encoding**

  Consequently, frequency encoding is applied in the second spatial direction along the longer sample axis. By modifying the strength of the magnetic field and consequently the nuclei's precessional frequency, the frequency encoding gradient G_{FE} causes a continuous frequency

shift of the nuclei along the axis of application. The frequency location and amplitude can be determined, providing spatial information about the sample. Because the gradient is applied during signal acquisition, it is commonly called the readout gradient. A reduced field of view (FOV) results from steeper frequency encoding gradients. [57]

k-space

All data from the entire field of view is incorporated into the measured signal in MRI. The spatially encoded signal is captured and recorded into the so-called k-space, comparable to a 'raw data space,' according to McRobbie et al. [48]. The k-space data contains frequency (horizontal axis) and phase (vertical axis) information about the measured signal, with the resolution defined by the number of frequency and phase encoding steps. This data is present in the spatial frequency domain and must be converted to an actual image using an inverse fast Fourier transform (IFFT), schematically illustrated in Fig. 2.6. The number of phase encoding and frequency encoding steps specifies the resolution of the k-space, resulting in data acquisition at defined sampling points. Although the matrices of the spatial frequency domain and the actual image are identical in size, the individual points of the k-space do not directly correspond to the respective pixels of the image. Data from the center of the k-space contains low-frequency information and contributes to noise and image contrast. The surrounding data contains high-frequency information and provides details on the edges and borders of the image, thus contributing to a sharp depiction of the image. The IFFT produces an image by converting phase and frequency information contained in the k-space into signal intensities of single voxels. Voxels are three-dimensional volume elements employed in MRI instead of pixels, as even 2D data from a single slice possess a particular thickness. [48, 57]

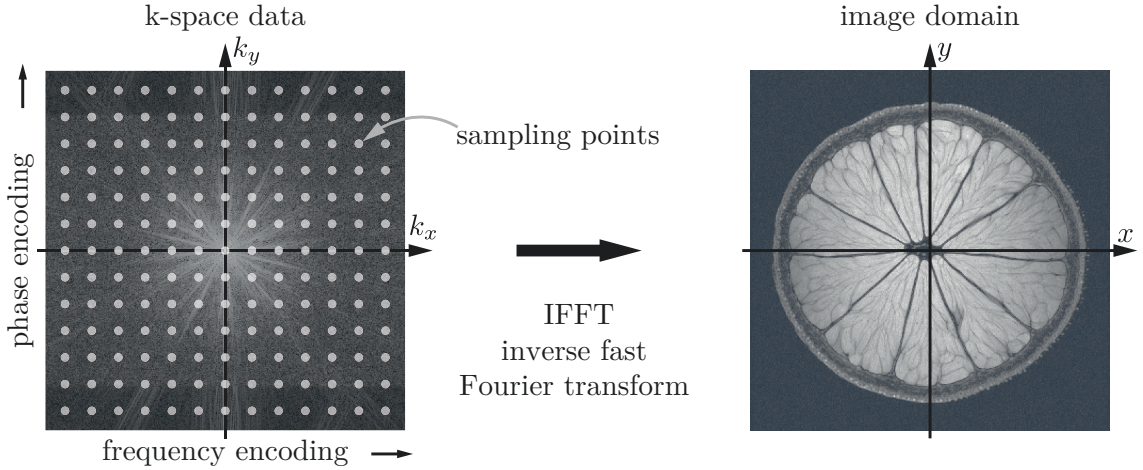

Fig. 2.6.: Schematic representation of the k-space data and the actual image resulting from the inverse fast Fourier transform. Discrete sampling points are defined by the number of frequency and phase encoding steps along the k-space axis k_x, k_y. IFFT results in a 2D image in the x, y-plane. Inspired by [48, 57].

Signal-to-noise ratio

In order to assess the performance of the MR system, the signal-to-noise ratio (SNR) is an important characteristic. The SNR is frequently used to evaluate the imaging quality of pulse sequences or hardware components, such as different resonators. It measures how well the system's noise and the sample's signal can be distinguished. Quantification requires two regions of interest (ROI) inside an image, one representing the signal and the other the background noise. The noise must be evenly distributed across the entire image or the distribution must be known to correctly compare the two ROIs. [59]

The SNR for the above mentioned two-region technique is computed as follows [59]:

$$\mathrm{SNR} = \frac{\mathrm{mean(signal\ ROI)}}{\mathrm{mean(noise\ ROI)}} \left(\sqrt{\frac{2}{\pi}} \right)^{-1} \tag{2.9}$$

The mean value of the signal ROI is divided by the mean value of the noise ROI. In magnitude images, the multiplicative correction factor is needed to account for the Rayleigh distribution of background noise [59, 60].

2.1.5 Pulse sequences

The three distinct gradients ($G_{\mathrm{SS}}, G_{\mathrm{PE}}, G_{\mathrm{FE}}$) required for spatially resolved 3D imaging are addressed in Sec. 2.1.4. To obtain spatially resolved k-space data, however, it is not sufficient to simply switch the gradients on and off. Since MRI is a time-sensitive process, it requires exact timing of the individual gradients, excitation pulses, and readout cycles, as well as accurate adjustment of the respective field strengths. So-called pulse sequences specify this precisely timed procedure and all of its parameters. Numerous pulse sequences are available, each suited for investigating specific samples or processes. Only the sequences relevant to this work are briefly described in this chapter.

The structure of such a pulse sequence is illustrated in Fig 2.7, using the example of a basic gradient-echo MR sequence.

Gradient echo

Initially, magnetic resonance is induced by RF excitation. For gradient echo sequences, the flip angle α (see Eqn. 2.4) is typically set below $90°$, which is controlled by the duration and magnitude of the chosen RF excitation pulse. A simultaneously applied slice selection gradient G_{SS} limits RF excitation to a slice of specified thickness. The position and orientation of G_{SS} can be specified freely, but typically a solely transversal (x, y), coronal (x, z), or sagittal (y, z)

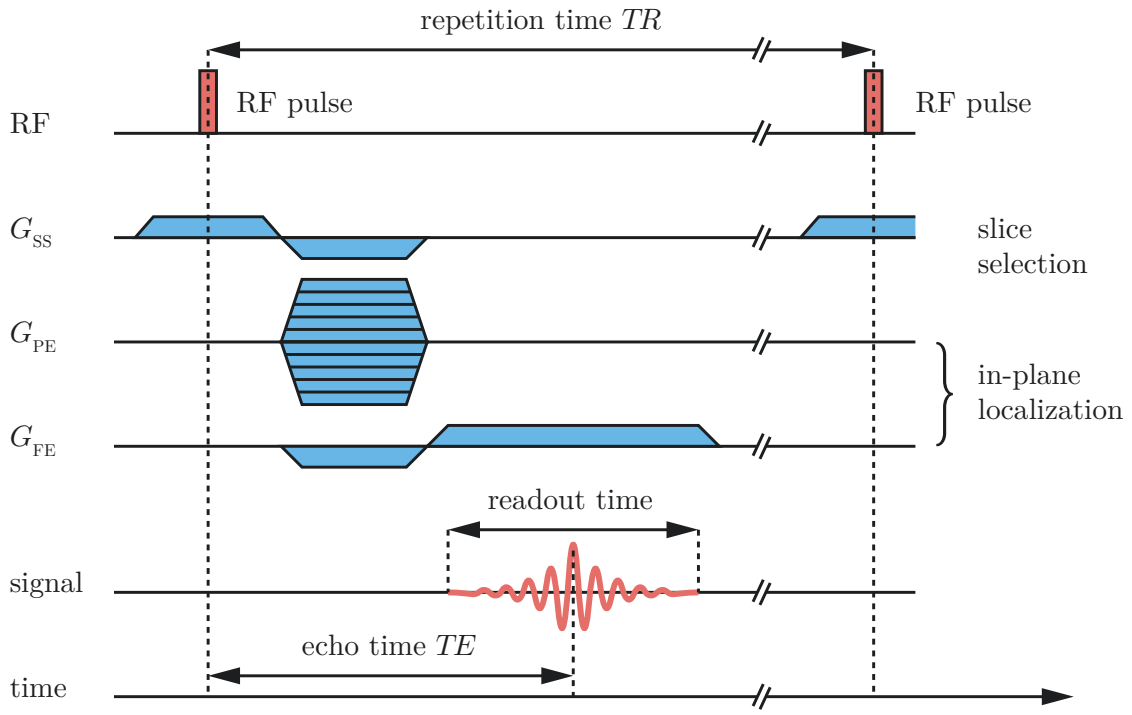

Fig. 2.7.: Schematic representation of a basic gradient echo pulse sequence. RF excitation with precise timing of the distinct gradients (G_{SS}, G_{PE}, G_{FE}) enables the measurement of spatially resolved data. The shown times are not to scale. Image according to [48, 57].

plane is chosen. In-plane localization is accomplished by combining phase and frequency encoding gradients. The phase encoding gradient G_{PE} is applied orthogonal to the slice selection gradient G_{SS} to achieve phase encoding. Only the frequency encoding or readout gradient G_{FE} is active during signal acquisition. The repetition time TR defines the length of an entire excitation and readout cycle. This cycle is repeated until the entire k-space dataset is obtained. The phase encoding gradient G_{PE} is modified at each repetition to extract spatial information. This modification is commonly illustrated by a set of multiple lines inside the schematic pulse sequence representation (see G_{PE} in Fig. 2.7). By selecting small flip angles α, relaxation time is lowered, and hence TR is reduced. However, fast measurements with short TR come at a cost. Due to the relationship of $M_{xy} = M_z \sin\alpha$, small flip angles α result in a significantly reduced signal-to-noise ratio. The echo time TE describes the period between RF excitation and echo signal acquisition, measured from center to center, as indicated in Fig. 2.7. As a result of lacking inhomogeneity compensation, gradient echos might contain susceptibility artifacts and increased noise. The total scan time of the image is defined by the product of the repetition time, the number of phase encoding steps, and the number of total averages. The FLASH sequence (fast low-angle shot) is one of the most commonly applied gradient echo sequences because of its fast scan times and good SNR. [48, 57]

Inversion recovery

The inversion recovery (IR) sequence is a spin echo sequence variant often employed to null the signal of distinct materials or substances. IR pulse sequences are highly sensitive to changes in T_1 relaxation times. An initial $180°$ pulse inverts the longitudinal magnetization from $+M_z$ to $-M_z$. Positive magnetization $+M_z$ recovers over time based on the T_1 relaxation rate, which varies, for example, depending on biological tissue composition or the number and amount of dissolved substances in chemical products. Fig. 2.8 illustrates the inversion process. The inversion time TI refers to the amount of time that elapses between the inversion pulse and the imaging sequence. When TI is set to the zero-crossing time of a specific tissue or substance $TI = T_1(M_z = 0)$, no signal from that sample is acquired in the imaging sequence. [48, 57]
The TI at the zero-crossing point will be referred to as TI_{zero} in the results section (see Sec. 7.2).

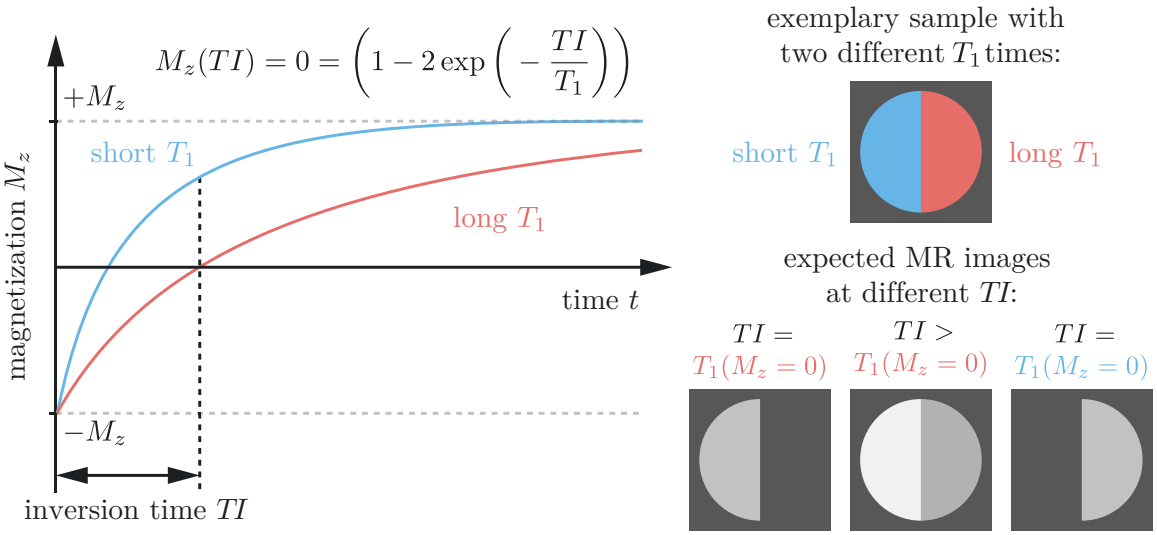

Fig. 2.8.: Schematic representation of an inversion recovery pulse sequence. In case of a sufficiently large T_1 difference between two samples or chemical substances, the signal of one of the two components can be canceled by a specific selection of TI. The expected MR images based on different TI selections are illustrated on the right. Inspired by [48, 57].

The mathematical relationship between TI and T_1 is described as [48]:

$$M_z(TI) = 0 = \left(1 - 2\exp\left(-\frac{TI}{T_1}\right)\right) \tag{2.10}$$

Rearranging the equation gives the relationship of $TI = 0.6931 \times T_1$, which is useful as TI can be selectively adjusted to suppress a signal of a substance with known T_1 or a TI measurement series can be utilized to determine a substance's T_1 value. Full relaxation is mandatory to

determine T_1 by inversion recovery measurements. Thus, the repetition time TR must be set to at least five times T_1 (see Sec. 2.1.3, Fig. 2.4).

2.2 MR hardware in general

At first sight, an MR scanner appears to be a self-contained device capable of performing measurements simply by placing a sample inside and following a measurement routine. A deeper glance, however, reveals the system's complexity, particularly concerning its hardware. The interaction of various components is what defines the scanner as such. It becomes apparent that the scanner is not self-contained and that some of its hardware components are interchangeable and can be adapted to specific needs.
This section describes the hardware of the MR system, which is based on the physical concepts provided in Sec. 2.1. Since coil development is an important aspect of this work, the requirements of various coils will be discussed in detail in Sec. 2.3.

Fig. 2.9 schematically illustrates a cross-sectional cut through the MR scanner, in which the approximate location of the individual hardware components are indicated in different colors. A borehole provides access to the center of the scanner, which is used to load the RF coil and sample into the system. The experimental periphery can be placed on the table in front of the bore. The magnet and shim coils are encapsulated inside the scanner and are not meant to be exchanged. The gradient coil is mounted inside the system and may be replaced if it fails. The scanner's coordinate system is used as a reference throughout the entire work.

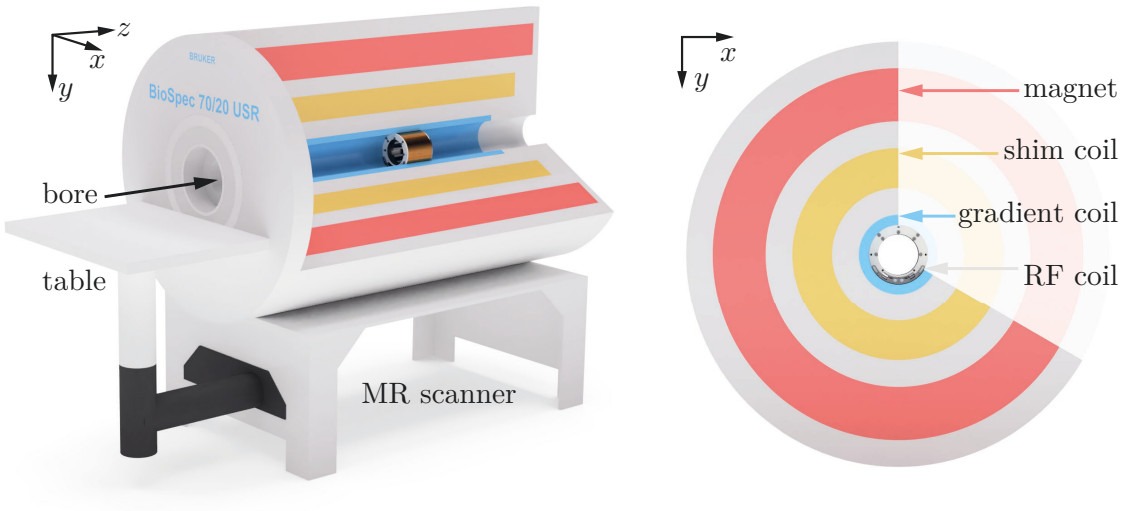

Fig. 2.9.: Schematic cutaway (not to scale) along the scanner to illustrate the internal hardware of the 7 T horizontal bore Bruker BioSpec 70/20 USR system used in this work. A vertical cross-section in x, y-direction reveals the radial arrangement of the individual components.

Fig. 2.10 depicts a substantially simplified interconnection of the single hardware components with the corresponding periphery.

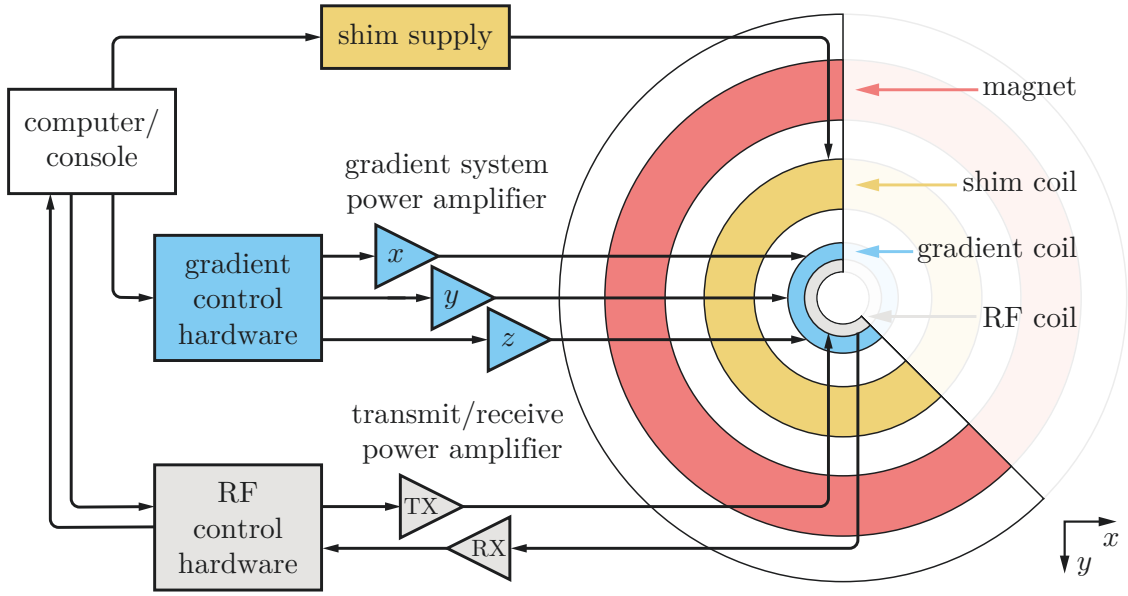

Fig. 2.10.: Simplified illustration of interconnections between the scanner's different hardware components and the corresponding periphery.

A computer, also called the console, controls the entire system. Dedicated hardware, such as high-power amplifiers, is needed to drive the various coils inside the MR scanner. A more detailed description of the individual components follows below.

Magnet

The magnet is at the heart of every MR system. It defines the scanner's fixed magnetic field strength B_0, which cannot be changed. Since electromagnets (such as coils) are more affordable and portable than permanent magnets, they are frequently utilized to generate the static magnetic field B_0, particularly in larger systems. However, the operating cost of traditional electromagnets is a considerable disadvantage. Large amounts of electrical energy are required to generate a magnetic field, as most energy dissipates as heat. Superconducting magnets are employed in systems with field strengths greater than $0.3\,\mathrm{T}$ [57]. The coil's wire consists of a special niobium-titanium (NbTi) alloy, which experiences superconducting characteristics below $7.7\,\mathrm{K}$ [48]. As the material's resistance approaches virtually zero, electrical energy is no longer dissipated as heat. Supercooling is achieved by submerging the coil in liquid helium at a temperature of $4.0\,\mathrm{K}$ [48]. A superconducting magnet has cheap operating expenses since no additional energy is needed to sustain the strong magnetic field. As a result, the magnet is always active in its supercooled state. On the other hand, the

investment costs are enormous due to the superconducting alloys and the complex cooling system. [57]

A horizontal bore Bruker BioSpec 70/20 USR scanner with a magnetic field strength of $7\,\mathrm{T}$ is used in this study. The B_0 field points along the scanner's bore.

Shim

Magnetic field homogeneity is essential for the MR system to guarantee proper operation. The distances between the individual coil windings of the superconducting magnet directly influence the resulting field strength. Coils with uniformly spaced windings along the full scanner length would be necessary to generate a homogeneous field. However, from a technical standpoint, implementing equidistant windings is practically impossible, resulting in local field strength fluctuations inside the scanner. The so-called shims address this problem. Cryogenic and room temperature shims are distinguished. Like the superconducting magnet, the cryogenic shim coils are charged and stay engaged in their supercooled state. They are located close to the scanner's magnet, submerged in liquid helium. Cryo-shims are employed to compensate for the magnet's inhomogeneities. Additionally, passive shims of small iron plates are placed close to the magnet, serving the same purpose. Room temperature shims correct inhomogeneities caused by the measurement coils and the samples' susceptibility differences. These shims consist of an arrangement of numerous and permanently driven coils. The precision of the shim system varies amongst MR scanners, with a higher order indicating better accuracy along the given direction (e.g., z^2 is more accurate than z). Shim coils used in the Bruker BioSpec 70/20 USR system are: $x, y, z, z^2, x^2 - y^2, zx, zy, xy$. 'Shimming' is the term used to describe the process of matching fields controlled by the console. [48, 57, 58]

Gradients

Acquiring spatially resolved data relies on selective modification of the local magnetic field (see Sec. 2.1.4). Another coil arrangement inside the MR scanner, the gradient system, achieves this field modification. Three different gradient coils are provided for spatial modification in x, y, z-direction. The gradient system is installed into the magnet's bore and securely attached to the scanner. However, it can be changed if electrical over-currents destroy it during measurement, which is rare but not excluded. For this reason, the gradient coil configuration is not submerged in liquid helium, meaning that the coils heat up quickly under load, which is why heat has to be dissipated via water cooling. The isocenter is defined by the middle of the gradient system that corresponds to the magnet's center. Depending on the polarity and amplitude of the gradients, the magnetic field intensity either increases or decreases from this zero point. Aside from the coils, the gradient system relies on complex

peripheral hardware. A dedicated power amplifier supplies the necessary electrical current to each gradient coil. Adequate cooling must also be provided for the periphery. The gradient control hardware, responsible for each coil's exact timing and amplitude, drives the amplifiers. The hardware is computer controlled by the console. [48, 57]

RF coil

RF coils are among the key elements of the MR system as they are interchangeable and can often be tailored to specific experiments via various design possibilities. At first, a transmitter coil excites the nuclei with RF pulses which induce magnetic resonance. Following excitation, the generated MR response signal must be captured with a receiver coil to obtain data from the system for image reconstruction. In simple applications, often, one coil is sufficient for both sending the RF excitation and receiving the MR signal. Such coils are referred to as transceiver coils. Nevertheless, two or more different coils can be utilized for sending and receiving, depending on the complexity of the setup and experiment. In medical applications, complex coil arrays are a typical solution. Simple transceiver coils come in a wide range of shapes and sizes, which will be covered in depth in the upcoming section (see Sec. 2.3).

The coil and the specimen of interest are placed inside the scanner's bore, ideally at the isocenter of the gradient system where the field is most homogeneous. Either the entire sample is surrounded by a resonator or a very localized coil is used. As with gradient coils, complex peripheral hardware is required to drive the RF system. A high-power amplifier is necessary for RF excitation to supply enough energy to generate magnetic resonance. The signal must be amplified, digitized, and processed within the receive chain. When using a single transceiver coil, dedicated RF control hardware is required for communication between the RF system and the console, as well as for precise control of signal transmission and reception. [48, 57]

2.3 Coil design

RF coils come in different shapes, sizes, and complexity levels, often tailored to suit a particular application. Highly sophisticated and optimized resonators are typically purchased from third parties, especially in the field of medical research. However, for specific applications in chemical reaction engineering, it is often sufficient to employ a rather basic coil design and adapt it to the problem under investigation. Although simple resonators can be developed and built with little material effort, they require an in-depth knowledge of RF technology. A significant part of the design depends heavily on know-how and prior experience in coil fabrication, as stated by Mispelter et al. [61].

Doty et al. [62] categorized MR probes regarding their size by calculating the product fd of the operating frequency f and the coil diameter d. They are referred to as mid-range coils for an fd ranging from $2\,\mathrm{MHz\,m} - 30\,\mathrm{MHz\,m}$. Resonators with $fd < 2\,\mathrm{MHz\,m}$ are classified as micro-coils, whereas those with $fd > 30\,\mathrm{MHz\,m}$ are simply denoted as large coils. All sources of loss caused by the coil, the capacitors, the shielding, the sample, and the transmission lines are significant in mid-range coils, as used throughout this thesis, and contribute to the total resonator performance.

This section focuses on the design guidelines and pitfalls of MR coils, particularly for the loop-gap resonator and the birdcage resonator employed in this thesis. The in-depth work on NMR probeheads by Mispelter et al. [61] is highly recommended, as it offers valuable information for the interested reader and coil-building enthusiast.

The probe's function is to convert an oscillating RF current into an oscillating magnetic field at the system's Larmor frequency ω_0 and vice versa. NMR probes are typically a conductive structure that forms an electrical resonant circuit composed of an inductive part L and a capacitive part C. In its most basic form, a LC resonant circuit consists of one inductor, generally the coil's wire, and one capacitor. The circuit's resonant frequency is determined as [63]:

$$f_0 = \frac{1}{2\pi\sqrt{LC}} \tag{2.11}$$

Frequency tuning is one crucial requirement to achieve a properly functioning resonator, as the coil's resonant frequency has to match the MR system's Larmor frequency. A frequency adjustment is accomplished by adapting component values or changing geometrical parameters during the design phase.
Impedance matching is the second important aspect that determines the performance of a resonator. A lossless energy transfer between both devices is achieved by matching the probe's impedance to the impedance of the MR periphery, which is usually $50\,\Omega$. Only a perfectly tuned and matched resonator absorbs the system's total energy, resulting in maximum performance. Fig. 2.11 illustrates the basic electrical circuit of a resonator. It includes a variable tuning capacitor C_{tune} and an inductive coil L_{coil}. Impedance matching to the MR hardware at $50\,\Omega$ is archived either via capacitive coupling (Fig. 2.11 a)) or inductive coupling (Fig. 2.11 b)). The former approach connects the probe directly to the hardware through a variable impedance matching capacitor C_{match}. The latter incorporates a second coil L_{pickup}, often known as the pickup coil or coupling loop, linked to the hardware via a variable impedance matching capacitor C_{match}. For the inductive coupling scheme, impedance matching is performed by picking up a small part of the resonator's magnetic flux. The physical distance between both coils changes the mutual inductance $\widehat{M}$, which is adjusted until a purely resistive part of $50\,\Omega$ is obtained. [63]

A vector network analyzer (VNA) is the most convenient instrument to analyze the coil on the workbench and make necessary adjustments to the hardware during the design

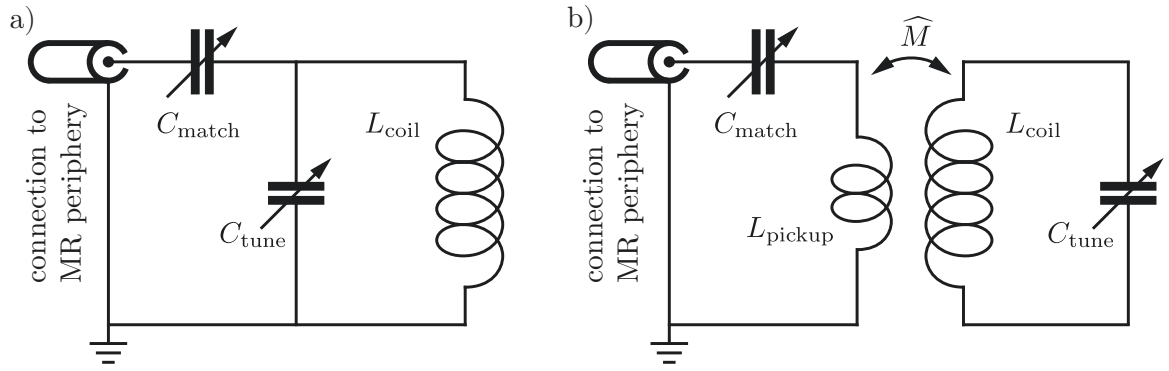

Fig. 2.11.: Basic electrical circuit of a resonator and its connection to the MR periphery. a) The capacitive coupling scheme connects the LC resonator directly to the MR periphery via an impedance matching capacitor C_{match}. b) Inductive coupling uses a pickup coil L_{pickup} which partly samples the signal of the LC resonator. The physical distance between both coils varies the mutual inductance $\widehat{M}$ and is adjusted for impedance matching. Illustration according to [63].

and manufacturing process. A VNA can immediately determine the reflection coefficient Γ and other critical network parameters, which is highly beneficial for direct troubleshooting. Because VNAs are very expensive and thus not commonly accessible to people, the coil design can also be directly tested, tweaked, and matched inside the MR system. However, troubleshooting and on-the-fly component changes will become far more complicated. The so-called 'wobble' function is accessible on most MR consoles, allowing the reflection coefficient Γ to be examined in a narrow range around the coil's supposed operating frequency.

Fig. 2.12 a) illustrates different coupling conditions for a capacitive coupled resonator. This representation looks similar to the one obtained using the 'wobble' function on the MR console. All the energy will be reflected when the coil is far off resonance ($\Gamma = 1$). As soon as the probe starts to resonate near ω_0, energy is absorbed and the reflection coefficient decreases ($\Gamma < 1$). Depending on the frequency position relative to ω_0, the coil is said to be over- or under-coupled. A perfectly tuned and matched resonator absorbs the total energy ($\Gamma = 0$) at the system's Larmor frequency ω_0, resulting in optimal performance.

Since the probe is sensitive to different loadings and materials, final tuning must be performed inside the MR scanner with the sample placed inside the resonator. The standard tuning procedure is illustrated in Fig. 2.12 b) and Fig. 2.12 c). At first, the probe's resonance frequency is adjusted to ω_0. Subsequently, impedance matching is carried out until a minimum reflection of ideally $\Gamma = 0$ is achieved (Fig. 2.12 b)). Since tune and match parameters mutually influence each other, the frequency must be re-tuned to ω_0 in a further step (Fig. 2.12 c)). This process is then repeated until an optimum result is obtained. Perfect tuning may not always be attainable depending on the resonator's design and specific application. In such a situation, the best possible configuration is set for measurements. [61, 63]

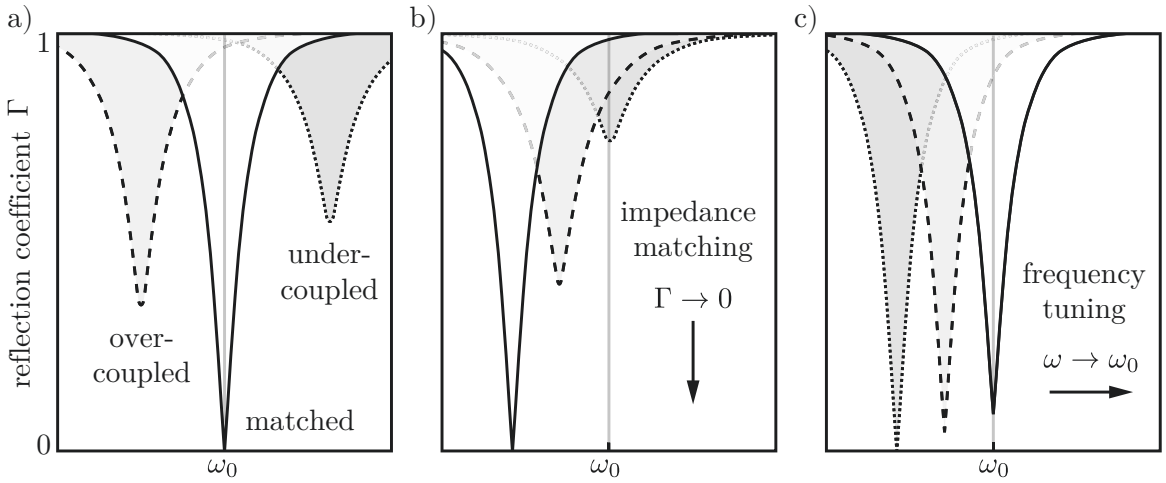

Fig. 2.12.: a) Different coupling conditions, similar to those obtained when using the 'wobble' function on the MR console. A perfectly tuned coil oscillates at the system's Larmor frequency ω_0. The reflection coefficient Γ becomes zero as the total RF energy is absorbed. Over- or under-coupling, shown for a capacitive coupling scheme, occurs when the probe is not perfectly matched. The RF energy is partly reflected, decreasing the overall efficiency of the probe. b) Starting from resonance at ω_0, impedance matching reduces the amount of reflected energy and lowers the probe's resonance frequency. c) Frequency readjustment results in a slight increase of reflected energy. The impedance matching and frequency tuning process is repeated until an ideal operating condition is obtained. Illustration according to [61, 63].

A sphere represents the theoretically ideal resonator geometry in terms of field homogeneity and sensitivity. This concept, however, is highly limiting for real-world applications since the ideal sample would have to be spherical as well. Moreover, the sample would have to be surrounded by the coil, rendering it inaccessible. For this reason, a cylindrical coil design is typically preferred for real-world applications, as the design is realizable and the sample remains accessible. [64]

Coils are categorized in two ways, according to their B_1 field orientation regarding the center axis of the cylindrical resonator. A distinction is made between axial and transverse resonators. The experimental requirements and the accessibility of the sample are critical considerations for choosing an appropriate coil design.

Axial resonators

A theoretically ideal axial resonator is defined by an indefinitely long cylinder with a homogeneous electrical current running tangentially on its surface, resulting in a perfectly uniform magnetic field inside the cylinder along its axis. The so-called solenoid coil comes close to this ideal scenario as long as its length is substantially greater than its radius. The solenoid coil is constructed of a single wire wrapped equidistantly spaced around a cylinder. [64]

Geometrical constraints and self-resonance, however, work against the exceptional homogeneity and sensitivity of the solenoid. Self-resonance emerges when the conductor's length l approaches the system's wavelength [48]:

$$\lambda = \frac{\widehat{c}}{\sqrt{\epsilon_\mathrm{r}}\, f} \tag{2.12}$$

$\widehat{c} = 2.997\,924\,58 \times 10^8\,\mathrm{m\,s^{-1}}$ [61] denotes the speed of light and ϵ_r the relative permittivity of the medium or sample inside the coil (for air $\epsilon_\mathrm{r} \approx 1.0$, for water $\epsilon_\mathrm{r} \approx 80$) [48]. Self-resonance can result in standing waves, weakening the signal due to interference. Consequently, this coil is typically only used for small samples at low frequencies [61]. The shape of the coil can pose an issue as the B_1 field runs along the axis of the solenoid, which is oriented orthogonal to the scanner's bore. As a result, the sample cannot be accessed or modified while the resonator is inserted into the MR scanner. Problems regarding the B_0 field homogeneity can be encountered and the bore space is not effectively used when utilizing a solenoid coil. [61]

A so-called Helmholtz pair can improve sample accessibility. In this design, the solenoid coil is simplified by two parallel circular loops that provide the best homogeneity when spaced at a distance equal to their radius. [61]

When it is sufficient to examine only a specific area near the surface of a sample, such as looking at a rodent's brain rather than the entire body, the solenoid coil can be simplified to one single turn. This design represents the so-called surface coil. The probe's diameter is easily adjustable to the region of interest (ROI). Although the axial homogeneity is fairly low, the surface coil features a high sensitivity. The resonator can also be operated as an array of multiple coils to cover a larger surface area. [64]
Surface coils are usually operated in receive-only mode. Homogeneous excitation is accomplished with a body coil operated in transmitter mode. [62]

The loop-gap resonator is another frequently used design. Here, a cylindrical copper sleeve is interrupted along its length by one or more gaps. Chip capacitors connect the separated copper surfaces by bridging the gaps. The construction of a loop-gap resonator is straightforward. However, it is crucial to notice that the current density on the surface is not homogeneous and increases significantly towards both ends of the resonator. Despite this, a homogeneous magnetic field is obtained in the coil's center. [61]

Transverse resonators

In an ideal transverse resonator, a sinusoidal current distribution running along the surface of an infinitely long cylinder creates a homogeneous magnetic field inside the cylinder perpendicular to its axis. This theoretical consideration cannot be achieved in reality. Various

designs, however, attempt to approximate this ideal current distribution. Among the early concepts are the slotted tube and the Alderman-Grant resonator, in which a pair of opposing conductive copper sheets is used to accomplish the desired current distribution.

The main advantage of transverse resonators over axial resonators is that the axes of the coil and the scanner's bore are aligned. This design enables full sample access even when the resonator is installed inside the MR scanner. Additionally, transverse resonators efficiently utilize the entire bore space. Increasing the number of parallel conductors improves the sinusoidal field approximation of the transverse resonator. Due to its appearance, the resulting structure is known as the birdcage (BC) resonator. [64]
Given its complexity and importance for this study, the following sub-section is devoted to the design of the birdcage resonator.

The birdcage resonator

Hayes et al. [65] introduced the birdcage resonator for high-field head and body imaging in 1985. Since then, the design has been widely adopted and is found in various MRI applications. It is the preferred coil type when a high magnetic field homogeneity and a good SNR are required [62, 63]. However, these benefits are countered by the increased complexity of construction and tuning.

In general, a birdcage is a transverse resonator constructed from multiple conductors distributed equidistantly around a cylinder's surface and joined by two end rings, one on each side. The conductors are called rungs or legs and typically come in an even number of segments N_{leg}. Depending on the application, the lumped capacitors can be arranged at different positions of the BC structure to form the resonant LC circuit. A distinction can be made between three different types, as illustrated in Fig. 2.13.

The capacitors are placed on each leg (C_{leg}) in the low-pass (LP) design (Fig. 2.13 a)). As this BC type involves the fewest components, it is the most common one used for simple self-built resonators.
The capacitors are symmetrically distributed on both end rings (C_{er}) at the positions between the legs for the high-pass (HP) configuration (Fig. 2.13 b)). Compared to the low-pass resonator, this design needs twice as many capacitors.
The third configuration is the so-called band pass (BP) or hybrid design (Fig. 2.13 c)). It combines the placement of capacitors on the legs and both end rings. The ratio of $C_{\text{leg}}/C_{\text{er}}$ determines the characteristic behavior of the BP resonator, acting as an LP for $C_{\text{leg}}/C_{\text{er}} \to 0$ or as an HP for $C_{\text{leg}}/C_{\text{er}} \to \infty$. The capacitance distribution reduces propagation effects, which can benefit high-frequency applications. [66]

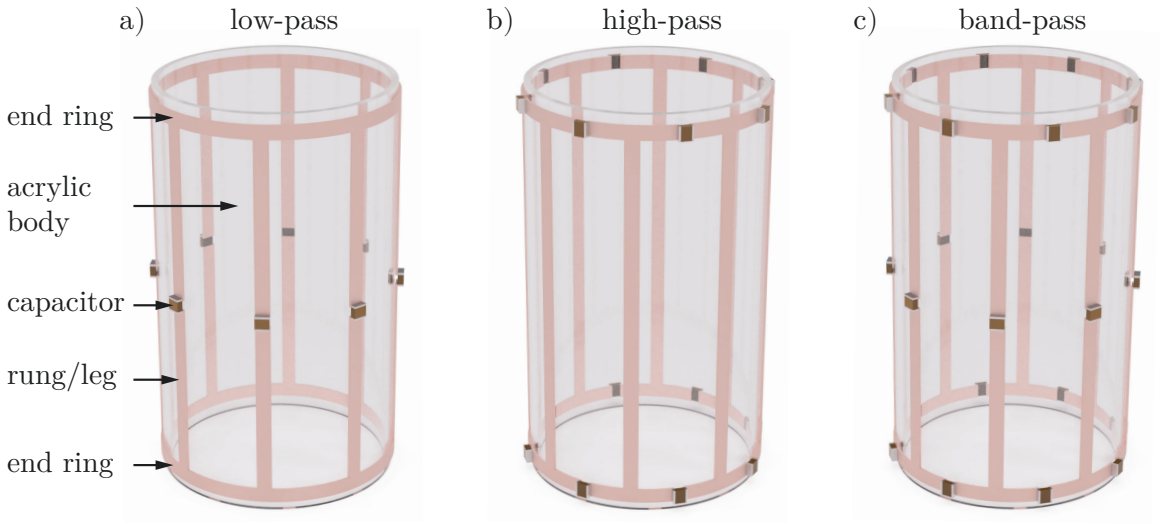

Fig. 2.13.: Rendering of an $N_{\text{leg}} = 8$ BC, demonstrating the placement of capacitors on the resonant structure for different filter configurations. In the low-pass configuration a), capacitors are placed at the legs, whereas for the high-pass design b), capacitors are located on both end rings. The band-pass design c) combines the arrangement of capacitors on all legs and both end rings.

The structure of the birdcage resonator results in the coexistence of several resonant modes k_{res} occurring at different frequencies. In general, $k_{\text{res}} = N_{\text{leg}}/2$ resonant modes can be determined for a resonator with an even number of legs N_{leg}. The $k_{\text{res}} = 1$ mode is most interesting for probe design since it approaches the cosine current distribution. In a low-pass BC, the $k_{\text{res}} = 1$ mode is found at the lowest frequency of all occurring modes, whereas at the high-pass design, the $k_{\text{res}} = 1$ mode is encountered at the highest frequency. [61]
It should be noted that two additional modes occur in the HP design, created by Helmholtz resonance of the two end rings. They are called co- and anti-rotational modes and are located in the HF region of the resonance spectrum. [67]

When it comes to the physical structure of the BC resonator, one of the most important parameters is the number of legs N_{leg}. The best field homogeneity inside the resonator is accomplished by ideally approximating the cosine current distribution, which becomes more accurate as N_{leg} increases.

According to Mispelter et al. [61], the field amplitude ζ and thus, the magnetic field strength, increases slightly with larger numbers of N_{leg} in the resonator's center. While a four-legged BC shows a $\zeta = 0.707$, a resonator with infinite legs approaches the maximum field amplitude of $\zeta = 0.785$. $N_{\text{leg}} = 12$ results in $\zeta \approx 0.775$. The homogeneous field extends towards the edge of the coil as N_{leg} increases, allowing the resonator's volume to be used more efficiently. They also show that a higher number of legs ($N_{\text{leg}} = 128$ vs. $N_{\text{leg}} = 12$) is beneficial in terms of current errors as they are averaged out more evenly. On the other hand, the tuning range of

the coil is reduced with increasing N_{leg}. A 16-leg BC has about half the tuning range compared to an 8-leg BC [62].

Small BC resonators tend to exhibit a tuning shift of up to $8\,\%$ between the empty and the fully loaded state [62]. In addition, capacitor losses can have a major impact at small dimensions, such that increasing the number of legs degrades the coil quality [68]. A segmentation of conductors with lengths greater than $\lambda/8$ (see Eqn. 2.12) by several equally distributed capacitors is recommended to avoid propagation effects when working with larger coils at high frequencies [63]. It is known from the saddle coil design that the magnetic field is maximized for a resonator's length-to-diameter ratio of $l/d = \sqrt{2}$, with optimum coil homogeneity being attained at $l/d = 1.661$ [61].
As stated by Mispelter et al. [61], the low-pass BC design is preferred for either low frequencies $f \leq 200\,\text{MHz}$ or when only a moderate number of legs $N_{\text{leg}} \leq 12$ is used. According to Doty et al. [62], in a small, closely shielded BC resonator, at least 12 rungs are needed for adequate B_1 homogeneity when relying on a large uniform ROI. Depending on the resonator's diameter and length, as well as its configuration (LP, HP, BP), a compromise between the required field homogeneity and the construction complexity, mainly defined by the number of rungs N_{leg}, has to be made.

A shield around the resonator is recommended to protect the coil from external RF interference and sensitive equipment from the resonator's RF radiation. Coil efficiency improves by reducing radiation losses. Furthermore, it lowers capacitive coupling effects between the resonator and the surrounding metallic parts of the gradient system (close to the bore wall), which often cause parasitic currents in unshielded setups. [63, 64]
The shield can be constructed of plain copper foil. However, using either a mesh or segmented foil stripes is advisable to prevent the buildup of Eddy-currents [64]. The resonance frequency of the shield can be tuned to a specific range to avoid overlapping with the resonator's frequency, achievable by a slotted shield interconnected via capacitors [61].
It is important to remember that the resonance frequency of a shielded resonator increases when compared to an unshielded coil due to a decrease in probe inductance. Another critical factor is the shielding ratio, defined by the shield-to-coil diameter relationship $d_{\text{shield}}/d_{\text{coil}}$. The magnetic field amplitude inside the resonator is higher in an unshielded coil than in a closely shielded coil. As the ratio of $d_{\text{shield}}/d_{\text{coil}}$ decreases, so does the magnetic field amplitude.
According to Mispelter et al. [63], the field will primarily concentrate in the narrow region between the shield and the rungs of a closely shielded BC resonator with a ratio of $d_{\text{shield}}/d_{\text{coil}} = 1.2$. Changing the ratio to $d_{\text{shield}}/d_{\text{coil}} = 1.5$ significantly increases the magnetic field intensity inside the resonator. Consequently, the shield-to-coil diameter ratio should be chosen as large as possible during the design phase.

The birdcage resonator can be connected to the external MR hardware via a capacitive or an inductive coupling scheme (see Fig. 2.11). Both methods are commonly applied but have

their specific advantages and drawbacks.
Inductive coupling is likely the simplest method of connecting the BC to the external hardware. For this, a rectangular coupling loop is placed between the resonating structure and the shield. In the case of a perfectly symmetrical resonator, the loop can be arbitrarily positioned along the circumference. Impedance matching is performed by physically adjusting the distance between the coupling loop and the resonant BC structure. If this is not practicable due to space constraints, impedance matching can also be accomplished by a variable capacitor C_{match} attached to the coupling loop.
Capacitive coupling is commonly utilized for so-called quadrature excitation. The birdcage can be interfaced from two ports with a 90° phase shift when built with fourfold symmetry. The required RF power is halved, while the SNR is increased by a factor of $\sqrt{2}$. [65]
However, a resonator in quadrature operation is considerably more complex to tune and match. It has to be considered that the perfect cosine distribution is most likely disrupted as a direct electrical load is applied to the coil via the directly soldered connections [61].

Precise determination of the needed capacitors for a specific geometry is critical for achieving resonance in homogeneous $k_{\text{res}} = 1$ mode. Mispelter et al. [61] provide basic equations for calculating the inductance values of the legs and end rings. Furthermore, the mutual inductance between all segments must be taken into account.
The capacitors can be calculated in several ways. By determining the impedance matrices for all components, every practical application can be represented using the birdcage theory [67, 69, 70]. The underlying complex linear equations can be solved numerically. Alternatively, simplified analytical solutions are available [71].
Another approach is to use full-wave 3D electromagnetic simulation software during the design process to estimate critical parameters. Programs like CST MICROWAVE STUDIO (Dassault Systèmes, France), XFdtd (Remcom Inc., USA), or HFSS (Ansys Inc., USA) are often utilized for this approach. Simulations provide a decent performance estimation before building the resonator and possible design weaknesses can be eliminated beforehand. However, these programs are generally costly and require powerful computing hardware.
From the coil builder's standpoint, Chin et al. [72] provided an elegant and straightforward solution for calculating BC resonators. Their software *Birdcagebuilder* allows the user to enter the BC's specific geometry parameters and estimates the required capacitor values. Additionally, the resonator's configuration (LP, HP, BP), the number of rungs N_{leg}, and the shield diameter d_{shield} can be set. The program is easy to use and provides a proper initial estimation of the required values. The Java-based code was recently ported to Python3 for cross-platform compatibility and is accessible via GitHub under the name *pyBirdcagebuilder* [73].

With the details of the birdcage theory explained above, the *pyBirdcagebuilder* [73] is utilized to determine an appropriate design based on various geometric parameters and readily available capacitor values. The calculated values are given in the appendix (see App. C.2).

3 Specific demands on the MRI experiments regarding the research questions

This chapter addresses the various specific demands placed on MRI experiments. Two flow setups for different experimental approaches are discussed from a hydrodynamic aspect. From the MRI side, this chapter elaborates on the developed MR resonators for the two different flow setups. Further, the adapted pulse sequence developed for fast flow measurements is explained. Finally, a suitable reaction system is presented that fulfills the MRI experiment's stringent requirements and can thus contribute to answering one of the main research questions.

3.1 Hydrodynamics and flow setup

The first major challenge had to be addressed right from the beginning of the project: designing and building a sophisticated and MRI-compatible flow setup to generate the vertically oriented buoyancy-driven Taylor flow. One of the most important requirements was to hold a Taylor bubble stable within a countercurrent flow to accomplish long measurement times. This fixation enables observing the bubble dissolution process and the temporal progression of chemical reactions. Numerous different flow configurations were built, tested, and adjusted. Here, only the two most relevant configurations are discussed.

Measurements had to be realized in a horizontal bore Bruker BioSpec 70/20 USR (Bruker Biospin MRI GmbH, Germany) MR scanner of limited height. The maximum inner diameter of the scanner's bore is reduced from $d = 133\,\mathrm{mm}$ to $d = 116\,\mathrm{mm}$ by the magnetic field gradient insert BGA12S2 (maximum gradient strength of $441\,\mathrm{mT\,m^{-1}}$).

To induce buoyancy-driven bubble rise, the Eötvös number (see Chap.1, Eqn.1.2) had to exceed $Eo > 4$. As a pure air-water system was chosen, Eo was only adjustable by the flow setup's capillary diameter d_i. The inner capillary diameter thus provided the first design constraint of the experiment. Glass capillaries with integer diameters in the range of $5.0 - 8.0\,\mathrm{mm}$ were readily available. To provide an overview, Eo numbers were calculated at finer intervals of $0.5\,\mathrm{mm}$ for various inner diameters d_i and are listed in Tab.3.1.

As previously mentioned, only capillaries with integer diameter values were available. Thus, at least $d_\mathrm{i} = 6.0\,\mathrm{mm}$ is required for the occurrence of buoyancy-driven bubble rise. The

Tab. 3.1.: Eötvös numbers calculated according to Eqn. 1.2 for various capillary diameters d_i. Physical properties of an air-water system at $T = 293\,\mathrm{K}$ were taken from Stephan et al. [74]: $\rho_\mathrm{water} = 998.21\,\mathrm{kg\,m^{-3}}$, $\rho_\mathrm{air} = 1.189\,\mathrm{kg\,m^{-3}}$, $\sigma_\mathrm{surf} = 72.74\,\mathrm{mN\,m^{-1}}$, $g = 9.81\,\mathrm{m\,s^{-2}}$.

d_i	$5.0\,\mathrm{mm}$	$5.5\,\mathrm{mm}$	$6.0\,\mathrm{mm}$	$6.5\,\mathrm{mm}$	$7.0\,\mathrm{mm}$	$7.5\,\mathrm{mm}$	$8.0\,\mathrm{mm}$
Eo	3.36	4.07	4.84	5.68	6.59	7.56	8.61

influence of the buoyancy force grows as the diameter increases. As a result, a higher rise velocity occurs, and therefore, more energy has to be introduced into the system by the applied countercurrent flow to keep the bubble spatially fixed. Consequently, residence times shorten and Re (see Eqn. 1.1) and Ca (see Eqn. 1.3) increase. With higher rise velocities, inertia increases, and thus, flow disturbances are dissipated less strongly by the fluid's viscosity. Vortices or irregular flow patterns are formed as the increase in inertial force directly changes the bubble's wake structure. Kastens et al. [23] observed this behavior in an air-water system inside glass capillaries of similar diameters.

Regarding the flow inside the capillary, the laminar hydrodynamic entrance length $l_{h,\mathrm{lam}}$ is critical. It specifies the length after which a completely parabolic flow profile has developed and the flow dynamics within the pipe remain constant in the case of laminar flow. $l_{h,\mathrm{lam}}$ is calculated as a function of Re and the capillary diameter d_i [75]:

$$l_{h,\mathrm{lam}} \approx 0.058\, d_\mathrm{i}\, Re \tag{3.1}$$

Based on this knowledge, the rise velocities v_rise of Taylor bubbles were experimentally estimated in preliminary tests by a temporal image series in two capillaries of $d_\mathrm{i} = 6.0\,\mathrm{mm}$ and $d_\mathrm{i} = 7.0\,\mathrm{mm}$ within an air-water system. Tab. 3.2 summarizes the corresponding results.

Tab. 3.2.: Calculated dimensionless numbers and entrance length for two capillary diameters d_i using experimentally obtained rise velocities. Physical properties of an air-water system at $T = 293\,\mathrm{K}$ were taken from Stephan et al. [74]: $\rho_\mathrm{water} = 998.21\,\mathrm{kg\,m^{-3}}$, $\rho_\mathrm{air} = 1.189\,\mathrm{kg\,m^{-3}}$, $\sigma_\mathrm{surf} = 72.74\,\mathrm{mN\,m^{-1}}$, $g = 9.81\,\mathrm{m\,s^{-2}}$, $\eta_\mathrm{water} = 1.0016\,\mathrm{mPa\,s}$.

d_i	$6.0\,\mathrm{mm}$	$7.0\,\mathrm{mm}$
v_rise	$5.3\,\mathrm{mm\,s^{-1}}$	$21.0\,\mathrm{mm\,s^{-1}}$
Re	31.69	146.5
Eo	4.84	6.59
Ca	7.30×10^{-5}	2.89×10^{-4}
Mo	2.57×10^{-11}	2.57×10^{-11}
$l_{h,\mathrm{lam}}$	$11.03\,\mathrm{mm}$	$59.48\,\mathrm{mm}$

When the larger capillary is compared to the smaller one, the rise velocity increases nearly fourfold, forming a different flow pattern inside the Taylor bubble's wake. The findings agree with those of Kastens et al. [23]. An almost sixfold increase in the hydrodynamic entrance

length $l_{h,\mathrm{lam}}$ occurs. As a result of the limited height, the bore space cannot be used properly with such a long entrance length. Consequently, the smaller diameter of $d_\mathrm{i} = 6.0\,\mathrm{mm}$ is chosen for the experimental investigations.

In order to develop a parabolic flow profile within the calculated entrance length, the flow at the capillary inlet must be applied evenly. Even minor variations of the local inlet velocities from a perfectly downward-directed flow result in a distortion of the flow field inside the capillary. Ideally, the fluid would be supplied evenly from a stationary basin above the capillary. Technically, this is not realizable due to the constrained dimensions inside the MR scanner. Numerous flow distributors were designed and tested to ensure fluid enters the capillary as evenly as possible.

Prior to construction, the characteristics of single-phase flows in various flow distributor geometries were simulated using Ansys FLUENT. The CFD (computational fluid dynamics) simulations greatly assisted the design process. The main focus was to estimate the expected flow pattern inside the inlet region and the capillary. The simulation results are shown in the following sub-chapters of the two individual flow setups. The pressure-velocity coupling of the flow field was computed with the SIMPLE scheme in Ansys FLUENT. Residuals were set to 1×10^{-6}. The following discretization schemes used are: gradient = least squares cell-based, pressure = second order, momentum = second order upwind, turbulent kinetic energy and turbulent dissipation rate = first order upwind.

3.1.1 Setup A: Investigation of flow dynamics by MRI and PIV

Several design revisions resulted in the flow distributor for comparing hydrodynamics inside a $d_\mathrm{i} = 6.0\,\mathrm{mm}$ capillary by MRI and PIV measurements. As stated in the previous section (see Sec. 3.1), the task was to establish a steady and homogeneous flow inside the setup. Unfortunately, this setup's resulting flow pattern was not rotationally symmetrical. Nevertheless, an advantage was taken of the encountered hydrodynamics as they allowed for a specific distinction between the flow's front view (x, y-plane) and side view (y, z-plane).

A vertically aligned borosilicate glass capillary of $d_\mathrm{i} = 6.0\,\mathrm{mm}$ and $l = 80\,\mathrm{mm}$ was mounted between two holders machined from polyoxymethylene (POM). Fig. 3.1 a) illustrates a schematic cross-sectional view of the flow setup. Besides the MRI requirements, the setup was designed to be housed in a glass box for PIV measurements. The glass box enables refractive index matching, which is necessary to gain unrestricted optical access to the flow setup. Therefore, the space between the glass box and the capillary could be filled with a refractive index matching liquid (water/glycerin mixture). Fig. 3.1 b) shows a photo of the flow setup with the surrounding glass box constructed from four microscope slides. Detailed information on the PIV experiments is given in the appendix (see App. B).

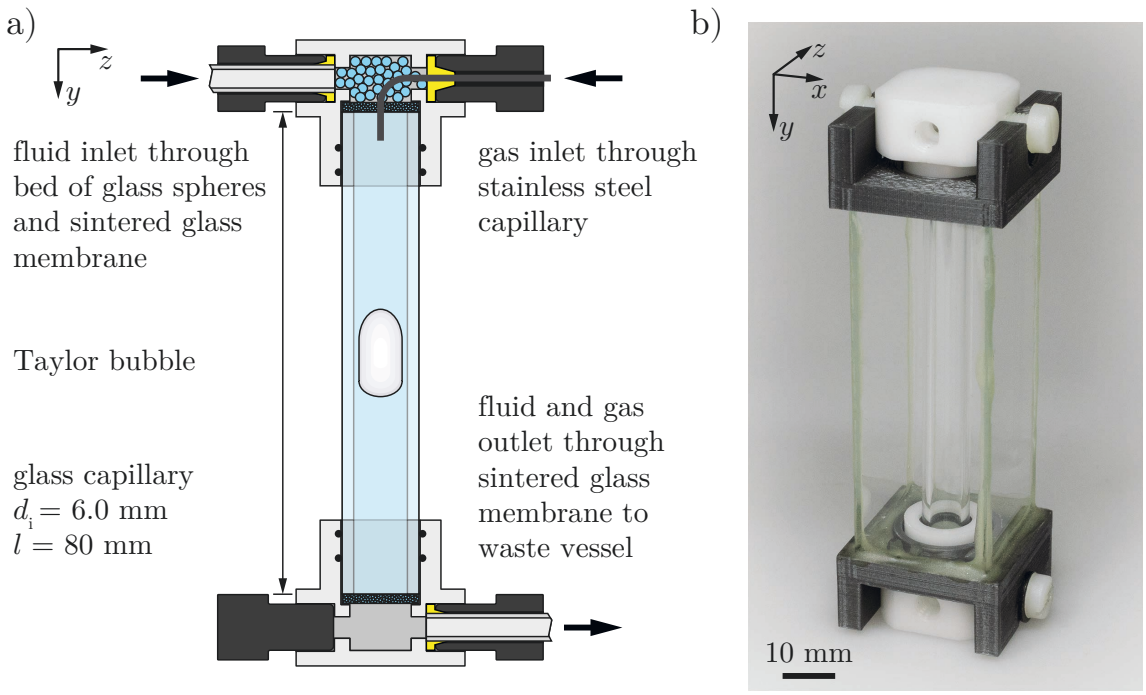

Fig. 3.1.: a) Schematic cross-sectional view of the flow setup for hydrodynamic investigations by MRI and PIV. The capillary is mounted in-between two flow distributors. b) Photo of the flow setup surrounded by a glass box for refractive index matching during PIV experiments.

The fluid entered horizontally at the upper end of the setup and was diffused into the vertical direction by a packed bed of glass spheres (sphere diameter $d = 1.4\,\mathrm{mm}$) placed inside the top holder. A fine-pored glass membrane (ROBU Glasfilter-Geräte GmbH, Germany; pore diameter $d = 160\,\mu\mathrm{m} - 250\,\mu\mathrm{m}$ retained the spheres within the top holder and acted as a follow-up flow straightener directly in front of the glass capillary. The same type of glass membrane was built into the bottom holder to establish a minor counterpressure, thus helping to stabilize the flow. Most of the flow is guided solely in the vertical direction, yet, the horizontally imprinted flow velocity partly persists and a relatively constant swirling of the fluid occurs at the capillary's entrance.

Fig. 3.2 a) illustrates the CFD results of the occurring swirling motion at the inlet due to the flow deflection inside the top holder. Four cross-sectional planes of the flow distribution are shown at different capillary positions, where the inlet is denoted as $\Delta l = 0\,\mathrm{mm}$. A distinct flow distortion is visible, which reduces along the capillary. Fig. 3.2 b) shows the flow profiles in x and z-direction at different capillary positions Δl, compared to a parabolic flow profile at $v_{\mathrm{mean}} = 5.3\,\mathrm{mm\,s^{-1}}$. In both directions, an asymmetrical behavior is visible at the inlet $\Delta l = 0\,\mathrm{mm}$. After $\Delta l = 15\,\mathrm{mm}$, the profiles almost approach the parabolic profile. However, a minor deviation remains visible in z-direction.

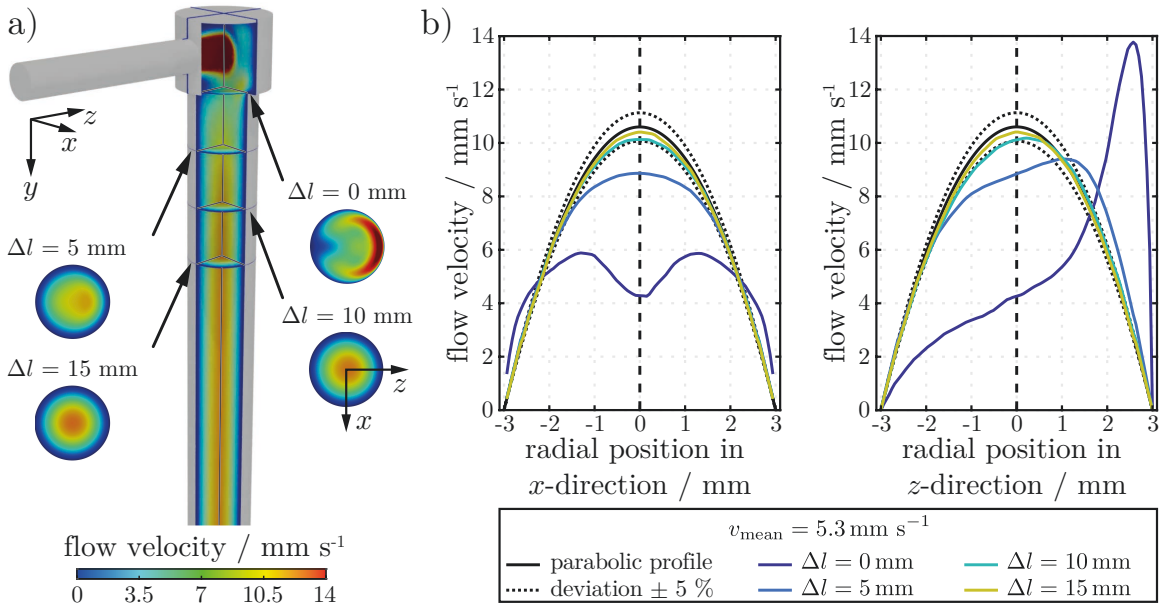

Fig. 3.2.: a) Cutaway of the initial flow setup, showing the color-coded velocity magnitude inside the flow distributor and along the capillary. The velocity profiles inside the capillary are examined at four horizontal planes beginning at the capillary inlet $\Delta l = 0\,\mathrm{mm}$. b) Plots along x and z-direction show the extracted velocity profiles in comparison to the computed parabolic flow profile with $v_{\mathrm{mean}} = 5.3\,\mathrm{mm\,s^{-1}}$.

The gas phase was manually injected with a gas-tight syringe directly into the glass tube by a $^1/_{16}$" stainless steel capillary through the top of the setup. The syringe was flushed at least three times with the particular gas drawn from a gas cylinder directly before injection into the setup. The gas-carrying capillary to the flow setup was also purged with the respective gas phase. High-performance liquid chromatography (HPLC) fittings were used to create gas-tight connections. Fluid was supplied pulsation-free from a pressurized vessel via $^1/_8$" fluorinated ethylene propylene (FEP) capillaries with low gas permeability. A gas bottle of N_2 pressurized the vessel, with pressure indicated by a gauge. A manually controlled needle valve enabled liquid flow regulation. After leaving the flow setup, a waste vessel with additional temperature indication collected the liquid phase. Gaseous components were directed into the fume hood. Fig. 3.3 shows the schematic diagram of the gas and liquid supply.

3.1.2 Setup B: Investigation of mass transfer and chemical reactions

A homogeneous rotationally symmetrical flow is critical for mass transfer investigations with and without superimposed chemical reaction. Furthermore, the Taylor bubble has to be approached with a fully developed laminar flow profile to obtain comparable results. Since the liquid film between the bubble and the capillary wall is the main contributor to mass transfer,

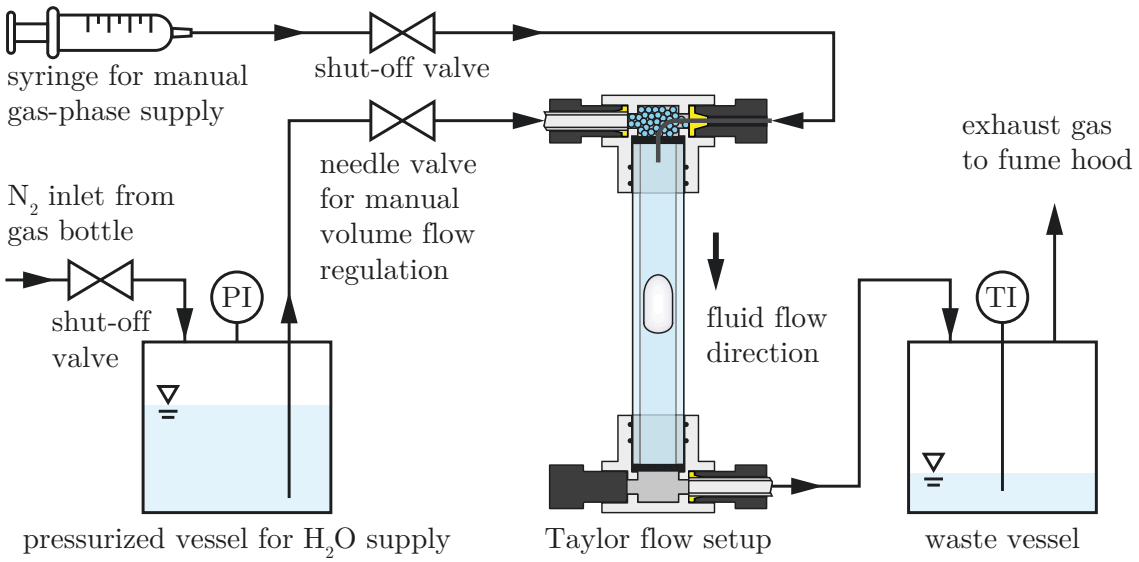

Fig. 3.3.: Schematic diagram of the gas and liquid supply for the MRI and PIV flow experiments.

a defined and uniform fluid supply is crucial. The calculated values from Tab. 3.2 apply here as well, since again, a water-air system in a capillary of $d_\mathrm{i} = 6.0\,\mathrm{mm}$ is investigated.

The challenge was to transform the high-speed horizontal flow entering from the setup's side into a purely vertical downward flow with no horizontal velocity components as encountered in the previously explained flow setup (see Sec. 3.1.1). For this reason, a flow distributor was designed, which, due to its complex internal structure, could only be manufactured from epoxy resin by DLP (digital light processing) printing. Fig. 3.4 a) illustrates the schematic cross-sectional view of the flow setup. In this design, the capillary had to be shortened to $l = 50\,\mathrm{mm}$ since the flow distributors at the top and bottom occupied more height than in the inital design.

Fig. 3.4 b) illustrates a cutaway rendering and a Fig. 3.4 c) shows a photograph, revealing the flow distributor's internal structure. This design solely relied on the concept of a uniform and symmetrical flow distribution by the 3D printed structure. Since well-considered flow guidance was crucial for the resulting fluid distribution, the internal layout of the setup had been manually optimized by CFD simulations prior to manufacturing.

Uniform fluid distribution was accomplished by symmetrically splitting the fluid orthogonal to its flow direction. This splitting operation was repeated until separation into eight equally-sized volume flows was achieved. The eight independent fluid flows were distributed around the capillary in a rotational symmetric ring shape. Recombination of the fluid flow occurred on its guided way through a meandering structure and resulted in a uniform inflow at the capillary's inlet.
Fig. 3.5 a) illustrates the CFD results of the meandering motion inside the upper flow dis-

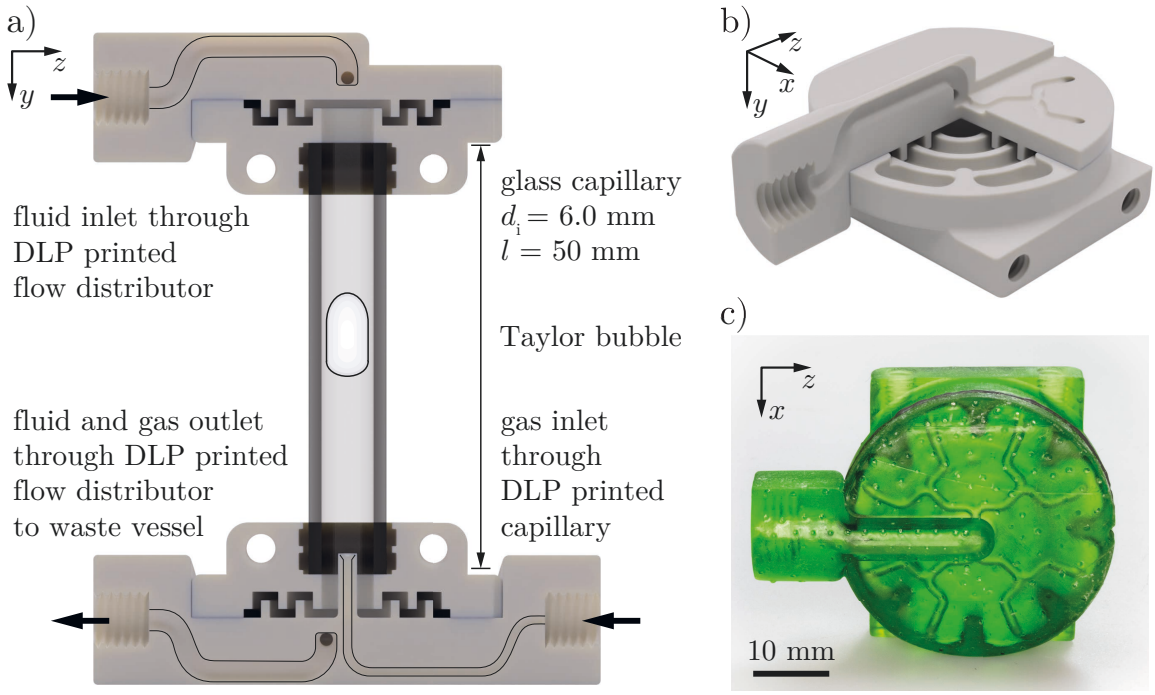

Fig. 3.4.: a) Schematic cross-sectional view of the flow setup for reactive and non-reactive mass transfer experiments. The capillary is mounted in between two DLP printed flow distributors. b) Cutaway rendering through the upper flow distributor, revealing the complex internal flow routing. c) Photo of the semi-translucent DLP printed top flow distributor, showing the same flow routing.

tributor and the uniform inflow into the capillary. The flow distribution is shown in four cross-sectional planes at different capillary positions, where the inlet is denoted as $\Delta l = 0\,\mathrm{mm}$. All four planes show a rotationally symmetrical flow profile. Fig. 3.5 b) shows the flow profiles in x and z-direction at different capillary positions Δl, compared to a parabolic flow profile at $v_{\mathrm{mean}} = 5.3\,\mathrm{mm\,s^{-1}}$. As the flow has not yet fully developed, a minor compression of the profile is apparent at the inlet $\Delta l = 0\,\mathrm{mm}$ in both directions. The flow approaches the parabolic profile after $\Delta l = 5\,\mathrm{mm}$.

As in the first flow setup (see Sec. 3.1.1), the gas phase was manually injected into the glass tube with a gas-tight syringe. As previously, the syringe was flushed at least three times with the particular gas, which was drawn from a gas cylinder directly before injection into the setup. The gas-carrying capillary to the flow setup was also purged with the respective gas phase. The gas phase was supplied from below by a capillary printed into the bottom holder to avoid a disruption of the uniform flow distribution at the inlet. A rotary pump delivered fluid from a Schott flask into the flow setup. Manual voltage control from a laboratory power supply was used for volume flow regulation. The reactive liquid was permanently kept under an unpressurized inert nitrogen atmosphere, supplied from a gas bottle, to avoid any contact with air. The remaining atmospheric air inside the Schott flask was displaced by the N_2 layer above

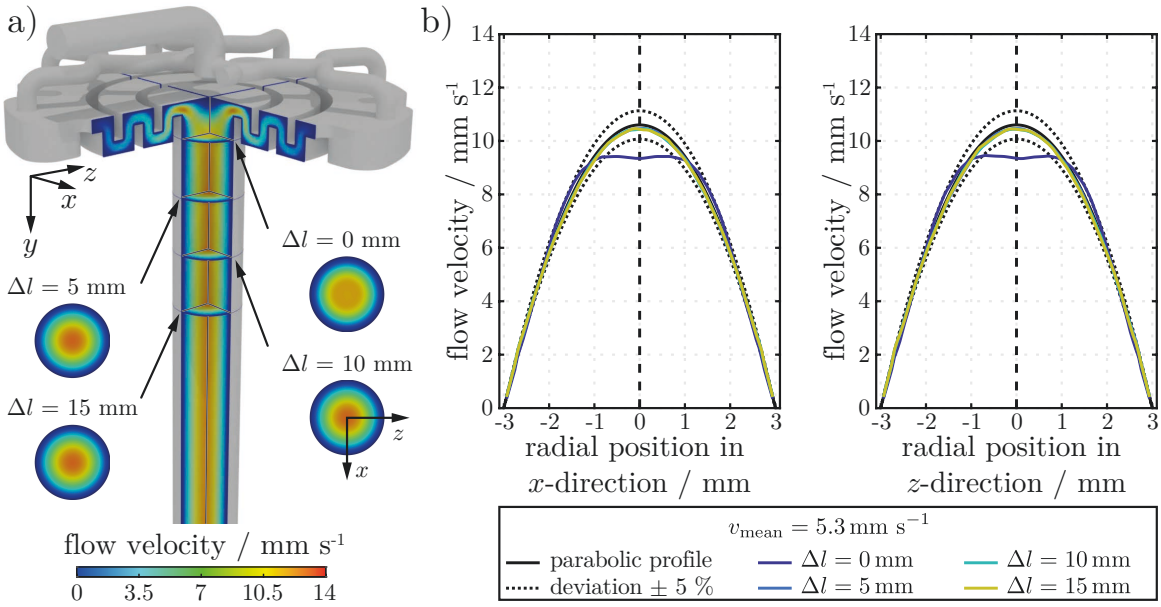

Fig. 3.5.: a) Cutaway of the enhanced flow setup, showing the color-coded velocity magnitude inside the flow distributor and along the capillary. The velocity profiles inside the capillary are examined at four horizontal planes beginning at the capillary inlet $\Delta l = 0\,\mathrm{mm}$. b) Plots along x and z-direction show the extracted velocity profiles in comparison to the computed parabolic flow profile with $v_{\mathrm{mean}} = 5.3\,\mathrm{mm\,s^{-1}}$.

the liquid phase. Fluid supply from a pressurized vessel would have been disadvantageous for mass transfer studies since the increased pressure inside the vessel would have caused the inert gas to be more soluble inside the liquid phase. 1/8" FEP capillaries with low gas permeability and HPLC fittings were used for gas and liquid supply. As before, a waste vessel with additional temperature indication collected the liquid phase from the flow setup, with gaseous components being directed into the fume hood. Fig. 3.6 shows the schematic diagram of the gas and liquid supply.

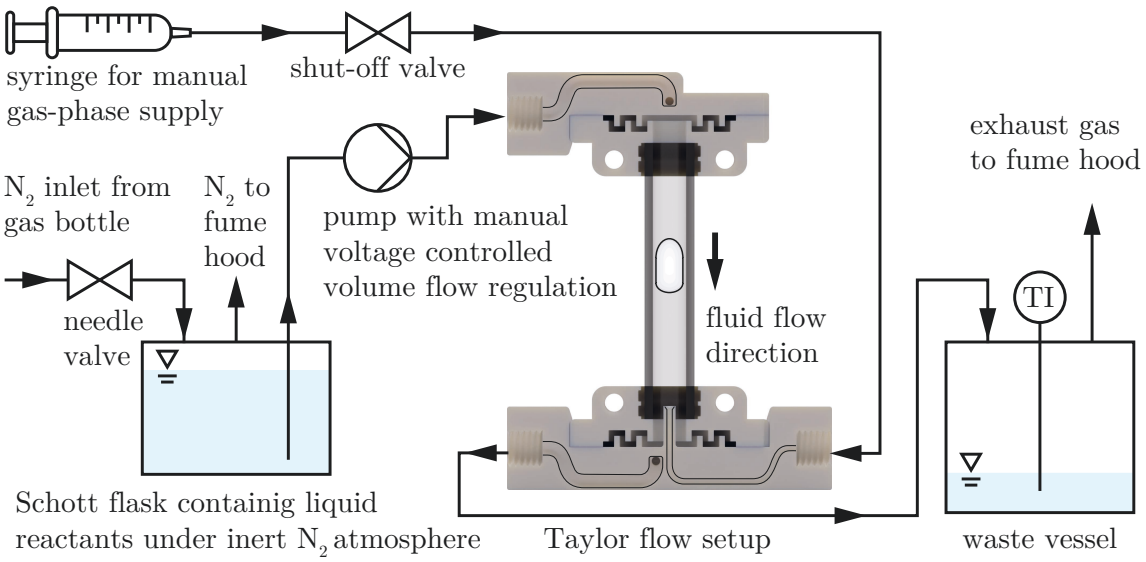

Fig. 3.6.: Schematic diagram of the gas and liquid supply for the non-reactive and reactive mass transfer experiments.

3.2 MRI hardware

Aside from a clearly defined flow, precise positioning of the flow setup inside the MR scanner is mandatory. Further, a resonator tailored to the experimental flow setup is required for signal excitation and data acquisition. In addition to the tailored coil, a suitable pulse sequence adapted to the experiment is also necessary. The following section addresses these crucial points.

Many requirements were placed on the hardware regarding precision and MR material compatibility. The scanner's magnetic field attracts ferromagnetic metals, prohibiting their use in the design. Non-ferromagnetic metals, such as stainless steel or aluminum, should be avoided as they cause homogeneity problems by locally altering the magnetic field. 3D printed polymers and machined plastic parts were thus primarily utilized for the design. The MR measurements do not require optical access. However, an optical fiber endoscope (Hinze Optoengineering GmbH, Germany) with a digital camera (Grasshopper FLIR Systems Inc., USA) was integrated into the setup for in-process monitoring of the flow setup inside the scanner's bore. The bubble position could thus be observed and controlled in real-time from the experimental room. A dovetailed guide mounted to the table in front of the scanner allowed for precise insertion and positioning of the flow setup inside the bore.

Again, a distinction is made between the two different setups.

3.2.1 Setup A: Investigation of flow dynamics by MRI and PIV

Since it was initially unknown how the flow setup and the coil design would evolve, a modular design was favored as it provided flexibility. For this, a sturdy PTFE (polytetrafluoroethylene) base plate was designed that supported all of the components of the MRI setup. Fig. 3.7 shows the final assembly of the modular PTFE base plate with all the necessary components.

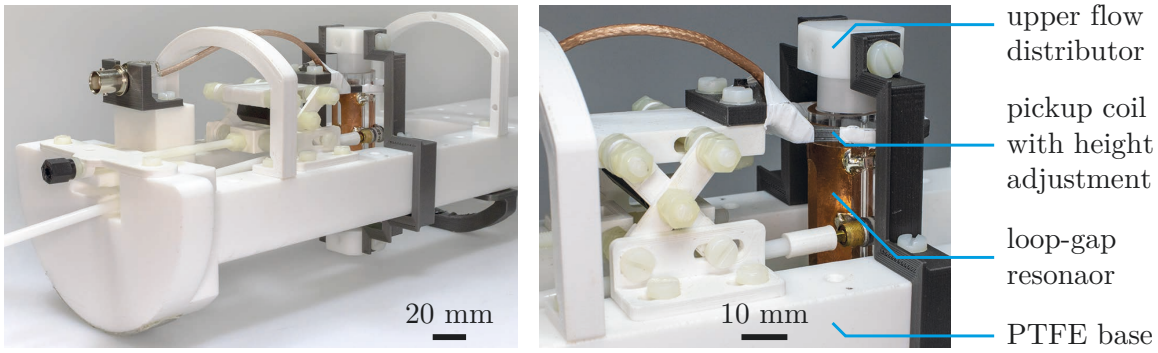

Fig. 3.7.: Final assembly of the setup for comparing MRI and PIV measurements showing all important components. All parts are securely mounted to the PTFE base plate that is inserted into the MR scanner during the experiments.

The capillary is mounted inside the two flow distributors attached to the PTFE base through 3D-printed holders. The loop-gap resonator encloses the glass capillary and is held in position by the flow distributors. A height-adjustable pickup coil is positioned above the resonator and connects to the MR periphery by a BNC connector. The semicircular sliding plate for insertion into the scanner and the two turning rods for impedance and frequency tuning are located on the left. The optical fiber endoscope for in-process monitoring is not depicted here but can be mounted on the right-hand side directly in front of the capillary.

Resonator

The simple loop-gap resonator was built through trial and error without previous MRI coil design experience. Initial prototypes were constructed from copper tape adhered to the plastic bodies of single-use syringes to determine the required capacitance for the coil. These preliminary tests resulted in a more sturdy version, subsequently built onto a piece of acrylic tubing. Fig. 3.8 shows the loop-gap resonator from the front and side view. Both images depict the prototype on the left and the sturdy version on the right.

The resonator consisted of two copper stripes and six capacitors, five of which had fixed values and one variable capacitor for frequency tuning. The capacitance was distributed uniformly along the resonator by placing the capacitors evenly over its entire length. Grooves were cut into the copper foil to gain optical access to the flow setup for the endoscope. Frequency

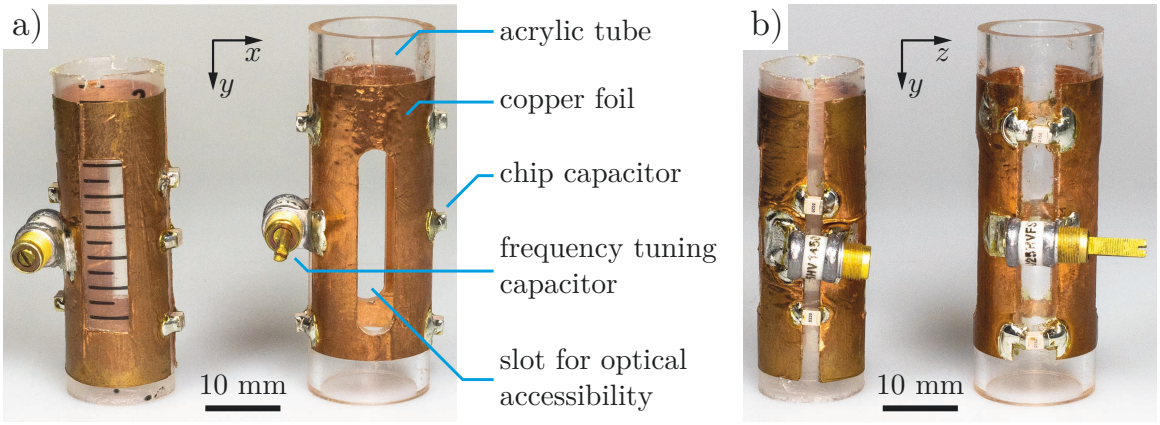

Fig. 3.8.: Front view a) and side view b) of the loop-gap resonator. Each image shows the initial prototype for testing on the left and the final sturdy version on the right.

tuning was possible while inserted into the MR system through the scanner's bore. Detailed information regarding dimensions and capacitor values is provided in the appendix (see App. C.1).

The loop-gap resonator was inductively coupled (see Sec. 2.3) to the MR periphery by a one-turn coupling loop positioned above the resonator. In this design, impedance matching was accomplished by adjusting the vertical distance between the single-turn pickup loop and the loop-gap resonator. A mechanical scissor-lift mechanism was constructed, which enabled height adjustment of the pickup loop while being inserted into the scanner.

High sensitivity is achieved because the resonator closely surrounds the capillary. However, the sample's close proximity to the coil also has a negative effect: the capacitors strongly influence the local signal intensity. This change in intensity is strongest in the vicinity of the capacitors but also propagates into the sample because of its proximity. Fig. 3.9 shows a field map of the resonator to visualize the signal intensity changes. T_1 weighted intensity data of the loop-gap resonator were acquired inside a capillary filled with pure water. A pronounced increase in signal intensity is visible towards the resonator's ends ($y = 5\,\mathrm{mm}$ and $y = 45\,\mathrm{mm}$, indicated by horizontal dotted lines) in the front view (Fig. 3.9 a)) and in the side view (Fig. 3.9 b)). A cross-sectional view of the intensity at the resonator's center ($y = 25\,\mathrm{mm}$) is shown in Fig. 3.9 c). Besides the minor signal increase near the static and the variable capacitor, the signal is evenly distributed in the x, z-center plane.

The coil itself causes the observed changes. The field fluctuations are of static nature and can be removed to a certain extent after the measurement. However, the overall performance of the resonator suffers from these field changes. As a result, the SNR decreases. When chemical reactions are measured with the coil, for example, by T_1 relaxation measurements, the field variations pose a major problem. They will lead to incorrect results since the sample is also

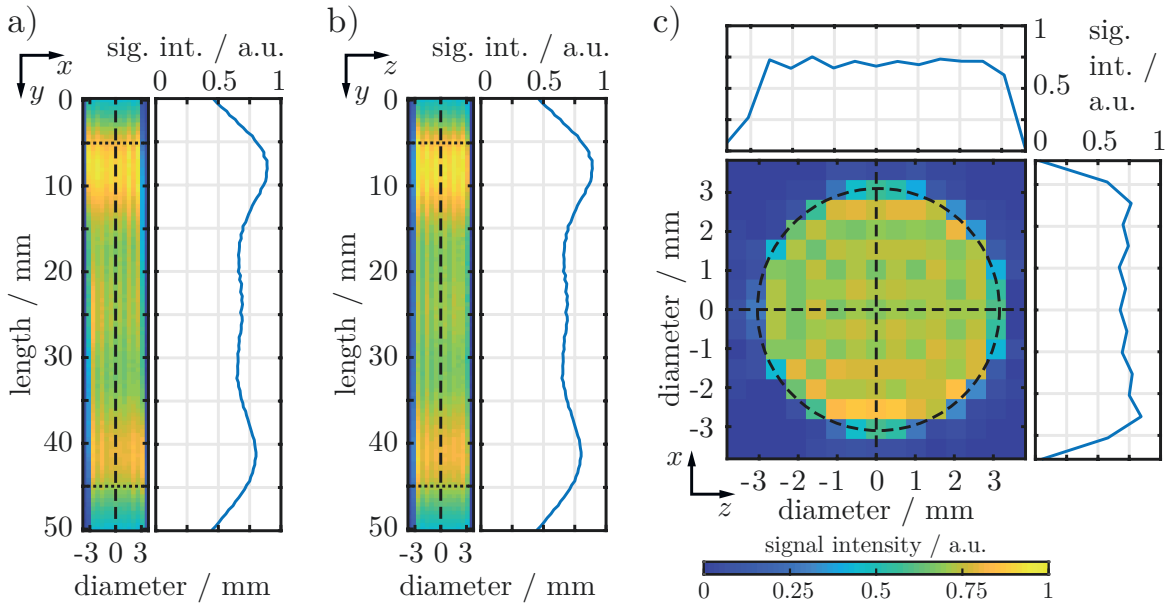

Fig. 3.9.: T_1 weighted intensity plots of the loop-gap resonator measured inside a capillary filled with pure water. The signal distribution is shown inside the x, y-center plane (front view) a) and inside the y, z-center plane (side view) b). A cross-sectional view along the x, z-center plane is shown in c). A signal increase is visible close to the static and the variable capacitors.

excited with the same non-ideal field. Due to the locally varying excitation and the transport of the liquid over time, it is no longer possible to conclude the measured intensities.

3.2.2 Setup B: Investigation of mass transfer and chemical reactions

The MRI setup used for investigating mass transfer and chemical reaction experiments is much more evolved than the one presented previously. Since the requirements for the MRI setup regarding flow distribution and resonator performance were precisely defined by previous experiments, they could be directly transferred into a more streamlined design. Fig. 3.10 a) shows the final version of the shielded birdcage resonator, loaded with the Taylor flow setup.

The flow setup discussed in Sec. 3.1.2 is securely mounted and adjusted in a rigid insert inside the birdcage resonator, which can be easily removed for manual capillary cleaning and precise adjustment without disassembling the entire setup. Fig. 3.10 b) depicts the respective insert. The coil is connected to the MR periphery by a BNC cable. Variable capacitors, accessible from the left side through the back of the scanner's bore, enable frequency tuning and impedance matching. The optical fiber endoscope for in-process monitoring is not depicted here but can be mounted on the right-hand side in front of the resonator assembly.

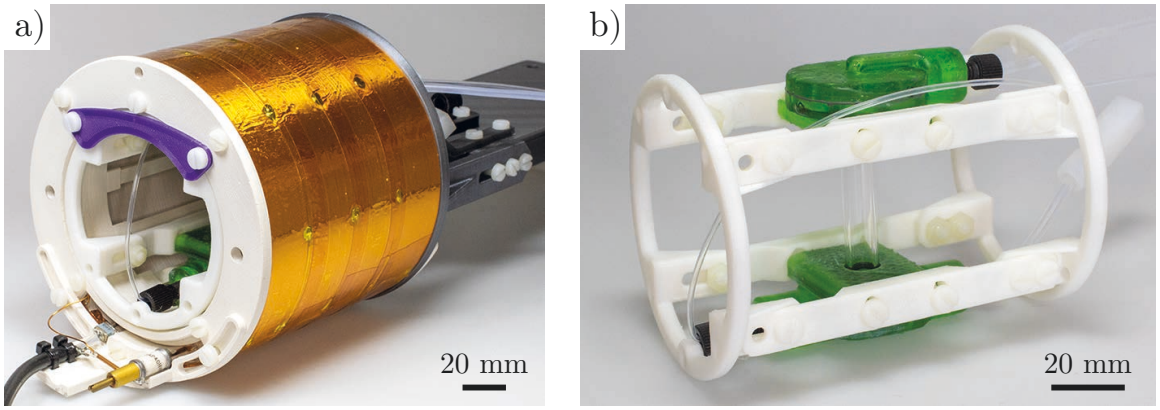

Fig. 3.10.: a) Final assembly of the setup for mass transfer and chemical reaction experiments loaded into the tailored birdcage resonator. b) The flow setup is sturdily mounted on an insert within the streamlined BC assembly which is placed inside the MR scanner during the experiments.

Resonator

A birdcage was the resonator of choice for mass transfer and chemical reaction studies since it offers a highly uniform magnetic field. The available commercial coils at the MR scanner facility were designed for biomedical samples with a corresponding range of loadings. As a result, accurate tuning and matching were not achievable for the flow setup. Additionally, the bore space could not be fully utilized due to the limited height inside the resonators. These issues were addressed with an inductively connected low-pass birdcage with twelve rungs tailored around the given flow setup. The resonator design was published open-source with detailed assembly instructions [76] so other researchers can replicate it.
A photograph of the constructed $N_{\text{leg}} = 12$ low-pass design is illustrated in Fig. 3.11 a). In Fig. 3.11 b), a 3D rendering visualizes the internal structure, which is hidden behind the shield in the actual photograph. The resonant structure consists of the rungs and end rings. It holds the chip capacitors as well as the variable capacitors for frequency tuning (similar to Sec. 2.3, Fig. 2.13). Detailed information regarding dimensions and capacitor values is provided in the appendix (see App. C.2).

The following illustration and evaluation are based on the already published results of the MRI birdcage resonator (Kemper et al. [76]). The text and illustrations have been adapted to match the style of this work.

Deviations in the coil's B_1 field constitute a significant source of error in quantitative imaging. Taking T_1 contrast measurements as an example, local deviations in the B_1 field will affect the results due to the caused intensity variations. A B_1 map provides information about the fluctuations and can be used to correct the data later. The double angle method [77] was used to calculate the B_1 field inside the resonator by taking two identical T_1 intensity

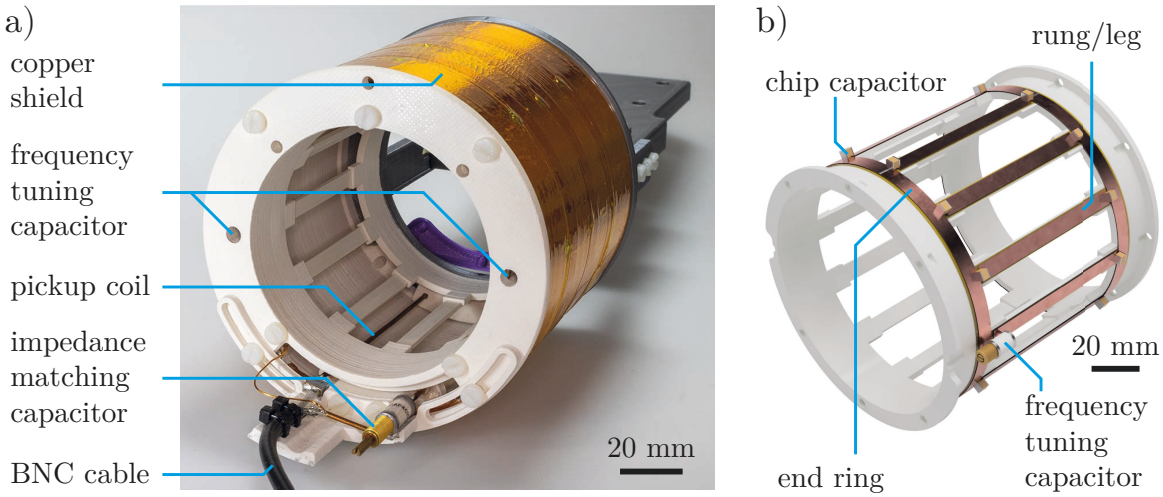

Fig. 3.11.: a) Photograph of the unloaded low-pass birdcage resonator with $N_{\text{leg}} = 12$. b) A 3D rendering visualizes the internal resonant structure, hidden by the copper shield.

measurements at two different flip angles. Here, $\alpha_1 = 30°$ and $\alpha_2 = 60°$ were set. Given that no T_1 dependency exists and complete recovery has occurred after TR, the percentage deviation from $\alpha_1 = 30°$ can be determined. Fig. 3.12 shows the resulting B_1 maps in the front and top center plane inside the resonator.

In the front view (Fig. 3.12 a)), local deviations near the center were in the range of $\pm 5\,\%$. The value increased rather steadily with further distance from the resonator's center. However, substantial flip angle deviations were observed close to the rungs since the circulating currents contributed locally to the magnetic field. The same effect was also evident in the center plane of the top view (Fig. 3.12 b)). Additionally, the deviation increased towards both ends of the resonator, visible as a gradient in z-direction.

As the normally-distributed probability density distributions were analyzed, the influence of the field of view became evident. When the values for the complete FOV in the x, y-plane of $d_{\text{i}} = 83\,\text{mm}$ were compared to a reduced FOV of $d_{\text{i}} = 60\,\text{mm}$, a decrease of the standard deviation σ by more than a factor of three was observed.

A similar behavior applied to the x, z-plane: Reducing the FOV of the resonator from $(90 \times 90)\,\text{mm}$ to $(40 \times 60)\,\text{mm}$, a reduction of σ by more than a factor of three was calculated. The mean value μ decreased in both cases as the field maxima near the rungs were excluded from the calculations due to the smaller FOV. This decrease implies that the specimen should ideally not occupy the entire coil volume to keep the B_1 field uniform over the full sample size. The B_1 maps shown in Fig. 3.12 are in good agreement with similar BC resonators found in literature, and thus, the resonator can be considered working.

Chap. 5 gives an in-depth review of the validation and characterization of the volumetric birdcage resonator based on the published results by Kemper et al. [76].

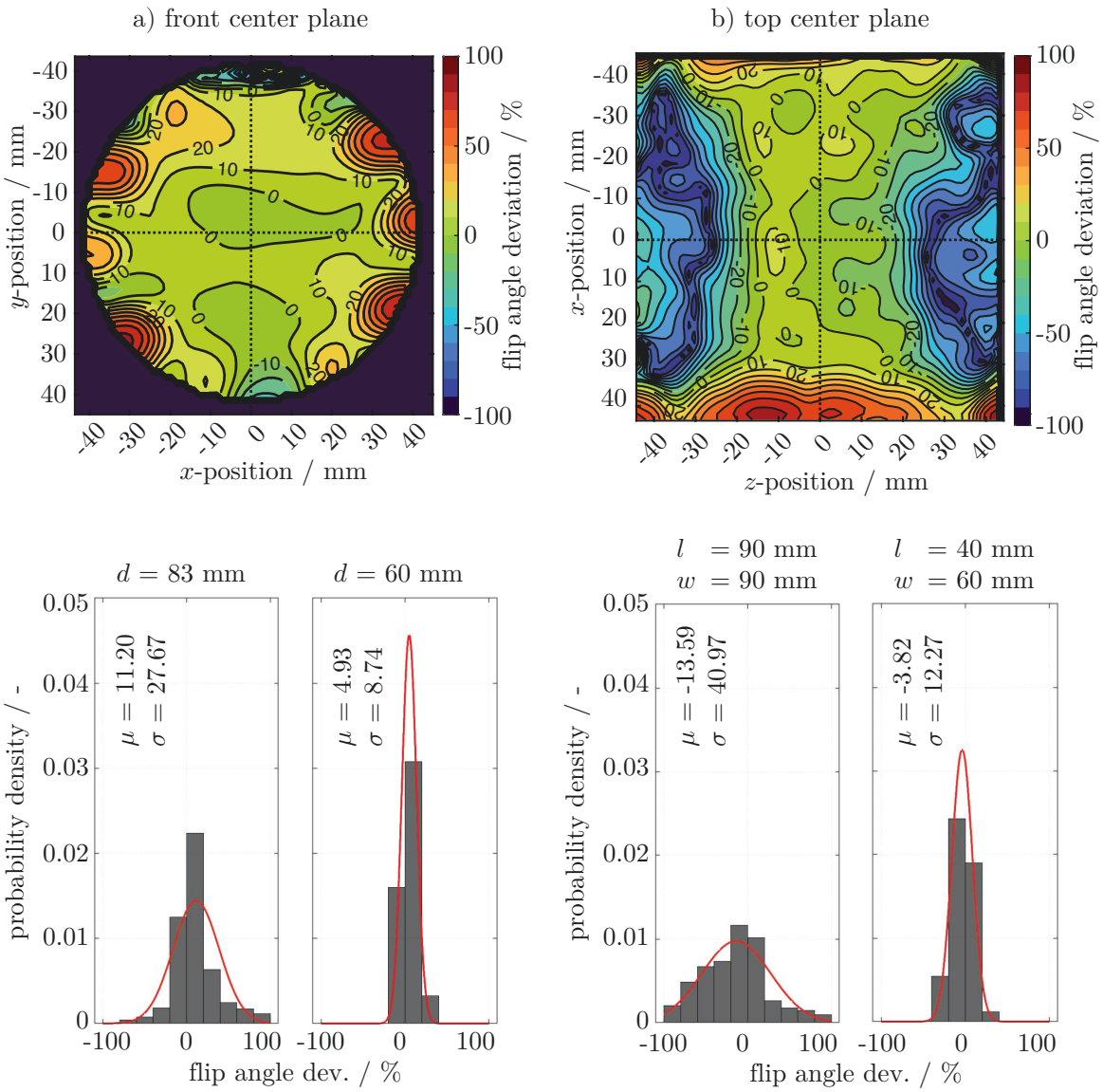

Fig. 3.12.: B_1 field maps of the BC resonator, obtained using the double angle method [77]. Percentage deviation from the reference flip angle of $\alpha_1 = 30°$ is shown in the front a) and top b) center planes of the resonator. Below both field maps, two probability density plots describe the flip angle deviation distribution for the complete FOV (left) and a narrower FOV (right) in each case. The mean value μ and the standard deviation σ are given within the plots. MRI sequence parameters: 2D FLASH sequence, $\text{FOV}_{\text{front}} = (90 \times 90)\,\text{mm}$, $\text{FOV}_{\text{top}} = (180 \times 90)\,\text{mm}$, spatial resolution $= (1.406 \times 1.406)\,\text{mm}$, slice thickness $= 2.0\,\text{mm}$, $TE = 4.0\,\text{ms}$, $TR = 6000\,\text{ms}$, flip angle $\alpha_1 = 30°$ and $\alpha_2 = 60°$. Image based on Kemper et al. [76].

3.3 Pulse sequence

The adapted, robust, and rapid MR pulse sequence for time-resolved flow mapping is explained below.

The following illustration and explanation are based on the already published results of the MRI sequence for the non-invasive study of gas-liquid Taylor flows by Kemper et al. [78]. The text and illustrations have been adapted to match the style of this work.

Fig. 3.13 illustrates a simplified diagram of the MR pulse sequence for time-resolved flow mapping.

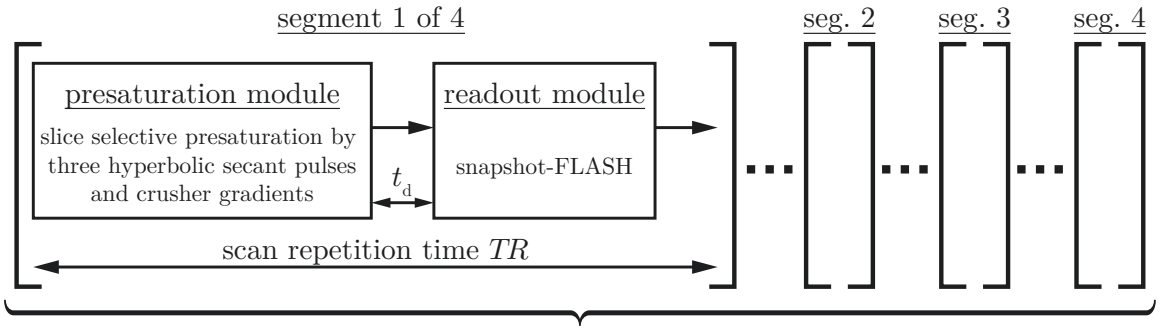

Fig. 3.13.: Simplified diagram of the MR pulse sequence for flow mapping. One MR image is acquired in four single segments, each with a scan repetition time of $TR = 250\,\mathrm{ms}$, to counteract motion blurring. This results in a $1\,\mathrm{Hz}$ recording rate. A variable delay time t_d separates the presaturation and readout module for flow mapping. Image based on Kemper et al. [78].

Data was acquired within the capillary's center plane. First, a presaturation module nulled the signal generated by the water protons in the respective measurement plane. A snapshot-FLASH sequence performed signal acquisition [79] after a specified delay time t_d. During the delay time, unsaturated water protons were flushed into the measurement plane, which contributed to the measurable MR signal as they replaced the previously presaturated protons. Here, the saturation of the protons refers to the removal of their longitudinal magnetization. A signal increase is observed for longer t_d, as more unsaturated protons can enter the measurement plane over time. The same effect can also be observed with increasing flow velocities at a fixed t_d. By setting long delay times, T_1 relaxation of non-exchanged protons will also contribute to the MR signal to a limited extent.

A standard FISP sequence from ParaVision 5.1 was extended by the presaturation module and the variable delay time t_d to create the described MRI sequence. A fourfold segmentation of the image acquisition inside the pulse sequence minimized motion blurring. A further increase in readout time was achievable by using a partial Fourier acceleration factor of up to 1.5 for each segment. The scan repetition time of a single segment was adjusted to $TR = 250\,\mathrm{ms}$, which resulted in a recording rate of $1\,\mathrm{Hz}$. Here, TR limited the variable delay time to approximately $t_\mathrm{d} < 200\,\mathrm{ms}$ per segment. Three slice selective $90°$ hyperbolic secant pulses with subsequent crusher gradients were used for presaturation, which had a total duration of $13.46\,\mathrm{ms}$. The field of view mainly influenced readout time. The sequence performed well

with a slice thickness of $2.0\,\mathrm{mm}$ and an in-plane resolution of $(0.5 \times 0.5)\,\mathrm{mm}$ with the FOV set to $(42 \times 16)\,\mathrm{mm}$. The signal readout was done parallel to the flow in y-direction. Here, pulses used an image bandwidth of $200\,\mathrm{kHz}$, an echo time of $TE = 0.811\,\mathrm{ms}$ and an echo position of $30\,\%$.

The flow was characterized along the capillary's center line from the x, y-plane and the orthogonally oriented y, z-plane at different t_d using the sequence described above. The results of the time-resolved flow mapping are discussed in Chap. 4.

3.4 Chemical reaction system

In order to investigate chemical reactions inside the flow setup by MRI, a suitable gas-liquid reaction has to be identified. The demands on the reactive system are manifold:
A reaction system is required that provides sufficient MR contrast between the reactant and the product so that they can be distinguished from each other. In addition, fast reaction rates are necessary as the residence times in the system are very short. The fluid leaves the capillary after only a few seconds and must therefore react directly upon contact with the gas phase. Furthermore, the chemicals should pose as little risk as possible since work is carried out in an uncontained system. In this context, safety and practical benefits must be evaluated. Finally, the reaction should use commonly available chemicals. Complex syntheses with low yields are not an option here, as larger quantities are required for the experiments.

A wide range of contrast agents is available for medical MRI diagnostics. Contrast is generated by the interaction between the water protons and the contrast agent, which reduces T_1 and/or T_2 relaxation times [80]. Mostly, chelated gadolinium complexes such as Gd(DTPA) (diethylene triaminepentaacetic acid) are intravenously injected for contrast enhancement to diagnose breakdowns in the blood-brain barrier, tumors, or infectious diseases [57].
Chelation ensures the complex's high thermodynamic stability and inertness within the human body, preventing toxicity. The chemistry of the metal complex is altered to achieve selective binding and activation by specific proteins. Various chelated metal complexes, such as cobalt, manganese, or iron, are utilized. [80]

Additionally, redox-activated contrast agents are particularly interesting. Their contrast can be switched on or off after contact with oxygen. Tsitovitch et al. [81] presented a cobalt complex that loses its MRI activity after exposure to oxygen. However, this complex is intended for biologically relevant investigations at body temperature and reacts rather slowly, as demonstrated by a change in absorbance over a time of $190\,\mathrm{min}$.

Wang et al. [82] introduced a redox-activated iron complex. The proposed Fe^{2+}-PyC3A complex oxidized rapidly to Fe^{3+}-PyC3A upon contact with H_2O_2. Absorbance measurements

revealed the rapid formation of Fe^{3+} in a matter of seconds. It was possible to achieve a ten- to fifteen-fold increase in relaxivity between Fe^{3+}/Fe^{2+}. Unfortunately, synthesizing the Fe^{3+}-PyC3A complex is rather cumbersome.

Iron-based reaction system in aqueous solution

The oxidation reaction of iron offered a promising starting point for a potential reaction system. Metal complexes developed as MRI contrast agents are subject to strict regulations regarding biological compatibility and safety, which often makes sophisticated syntheses of highly specific compounds unavoidable. These stringent requirements, however, do not apply to this work since no biological studies have been conducted. Thus, a simple iron-based reaction system is sufficient for the MRI experiments and is outlined below.

Dietrich et al. [83] performed MRI measurements of pure ferrous (Fe^{2+}) and ferric (Fe^{3+}) chloride solutions with different concentrations up to $10\,\mathrm{mM}$ to demonstrate the change in relaxation rates. Fe^{3+} showed a significantly increased transverse relaxation rate ($1/T_2^*$) over Fe^{2+}. The relaxation rate increased linearly with concentration for both iron species. The susceptibility of both species behaved similarly, which is an important point that helps to avoid susceptibility artifacts.

Balcom et al. [84] demonstrated the propagation of a reaction front inside a polyacrylamide gel cylinder during Fe^{2+} to Fe^{3+} oxidation. For $1\,\mathrm{mM}$ Fe^{2+} inside the water-polyacrylamide gel, inversion recovery measurements showed $T_1 = 1100\,\mathrm{ms}$ for Fe^{2+} and $T_1 = 75\,\mathrm{ms}$ for Fe^{3+}. The large difference in T_1 relaxation times results in high image contrast between both iron species. Sodium bromate was used as an oxidizer. The reaction was diffusion limited by the gel to enable a time-dependent propagation of a reaction front through the sample.

Based on the previously discussed literature, the oxidation reaction of Fe^{2+} is suited for MRI experiments regarding image contrast, leaving the reaction speed the next critical aspect. Short residence times inside the experimental setup require an instantaneous reaction upon contact with oxygen. The reaction can be accelerated by adding a chelating agent like EDTA (ethylenediaminetetraacetic acid). A metal complex is created, which stabilizes the ferric species and prevents precipitation following oxidation. [85]

Iron chelates are discussed in numerous articles due to their applicability to gas-scrubbing processes. For NO absorption from flue gas, aqueous Fe^{II}(EDTA) solutions are frequently utilized [86, 87]. However, this absorption process is affected by other components in the flue gas. Primarily, molecular oxygen leads to undesired oxidation of Fe^{II}(EDTA) to Fe^{III}(EDTA). As a result, the overall efficiency of the scrubbing process decreases since Fe^{III}(EDTA) cannot bind NO. [88]
Due to this negative effect on process efficiency, different studies [88–91] examined the

kinetics of the oxidation reaction. This knowledge is used for the reaction system required in this work.

Previous studies have shown that there is evidence of possible side reactions in addition to the oxidation itself. However, the nature and number of these possible side reactions are still not fully understood. They seem to be promoted by higher oxygen contents and low pH values [88]. The overall reaction of the iron chelate with oxygen is given as [88]:

$$O_2 + 4Fe^{II}(EDTA) + 2H_2O \rightarrow 4Fe^{III}(EDTA) + 4OH^- \tag{3.2}$$

Gambardella et al. [88] provided valuable information on the kinetics of the oxidation reaction.
The kinetic constant was determined to be $k_{12} = 5.3 \times 10^3\,\mathrm{e}^{-4098/T}\mathrm{m}^6/(\mathrm{mol}^2\mathrm{s})$ with a first-order reaction in O_2 and a second-order reaction in $Fe^{II}(EDTA)$. At pH $= 7$, temperature dependency of k_{12} is valid in a range of $298\,\mathrm{K} < T < 328\,\mathrm{K}$.

Mass transfer studies of freely rising bubbles have been conducted using the reaction of $Fe^{II}(EDTA)$ and NO [9, 92]. The rapid color change upon contact with the gas phase was successfully used to track the reaction product and estimate mass transfer.
The use of NO was discarded in this thesis since experiments are carried out in an open system. Even low concentrations of nitric oxide pose significant health risks (Indicative Occupational Exposure Limit Values of $2\,\mathrm{ppm}$ over $8\,\mathrm{h}$ [93]), which outweigh the advantages of the NO reaction.

The oxidation reaction of $Fe^{II}(EDTA)$ has been successfully used to conduct MRI experiments of reactive Taylor flows in this thesis. A detailed instruction on the $Fe^{II}(EDTA)$ complex preparation is given in the appendix (see App. A).

Copper-based reaction system in organic solution

The [Cu(btmgp)I] system (copper - bis(tetramethylguanidino)propylene) utilized by Benders et al. [46] for the MRI visualization of reactive bubbly flow has been considered as a possible alternative reaction system. They demonstrated that the reaction product generated sufficient contrast behind a freely ascending bubble. NMR activity was achieved by a change of the magnetic state during the oxidation of a diamagnetic copper(I) complex to a paramagnetic copper(II) complex. The reaction system relies on the organic solvent acetonitrile as the liquid phase, which alters the fluid dynamics and the acting forces. By changing the solvent viscosity, the reaction system can be adapted to the setup to a certain extent.
Benders et al. [46] used a highly viscous medium of polyethylene glycol and acetonitrile ($\eta_{\mathrm{liq}} = 800\,\mathrm{mPa\,s}$). Consequently, the resulting bubble rise velocities were in the range of $0.14\,\mathrm{mm\,s^{-1}} - 0.5\,\mathrm{mm\,s^{-1}}$. This severe slowdown was necessary to obtain sufficiently long

residence times inside the experimental setup since the complete oxidation of the [Cu(btmgp)I] complex takes $4\,\mathrm{s} - 5\,\mathrm{s}$ at room temperature, as shown by Schurr et al. [47]. Another drawback is that there is hardly any experimental data on this reaction system concerning bubbly flows. Thus, comparability with other experiments is not possible. The synthesis of the [Cu(btmgp)I] complex is highly sophisticated [94]. The substance was, therefore, externally prepared and provided for our experiments in small quantities by the Institute of Inorganic Chemistry, RWTH Aachen, Germany.

The [Cu(btmgp)I] system underwent preliminary testing, but the performance requirements for sufficient contrast and fast reaction speed were not met in pure acetonitrile. Relaxation times were determined in pure acetonitrile as $T_1 = 6.35\,\mathrm{s}$ and in acetonitrile with $10\,\mathrm{mM}$ [Cu(btmgp)I] after oxidation as $T_1 = 4.92\,\mathrm{s}$. Because of the small T_1 difference, the contrast between the product and the reactant is low. As a result of the long T_1 and consequently TI times, a sufficiently long residence time inside the setup is required to suppress the reactant signal by using the inversion recovery method. Thus, the reaction was only considered as a possible backup solution.

4 Non-invasive flow characterization of Taylor flows by MRI

Results shown in this chapter are published by Kemper et al. [78]. The text and illustrations have been adapted to match the style of this work.

The findings of the hydrodynamic investigations of Taylor flows by MRI are examined in this chapter. Experiments were performed with the initial flow setup (see Sec. 3.1.1) and the corresponding MRI hardware with the loop-gap resonator (see Sec. 3.2.1). At first, a closer look is taken at the results obtained by the adapted pulse sequence for non-invasive MRI flow measurements (see Sec. 3.3). After that, the data of the PIV flow investigations performed inside the same setup will be evaluated. Lastly, both methods are compared with each other.

4.1 MRI flow characterization

The wake region of pure N_2 bubbles held stationary in a countercurrent flow of ultra-pure water was measured with the adapted snapshot-FLASH sequence from Sec. 3.3. The liquid phase was degassed and stripped with pure N_2 to suppress mass transfer completely. Datasets were collected in the center planes of the front view (x, y-plane) and side (y, z-plane) view with varying delay times t_d. The delay time describes the time between slice selective presaturation and readout, during which water molecules can be exchanged between the saturated in-plane molecules within the desired slice thickness and the non-excited molecules from the surrounding liquid. A longer t_d or a higher flow velocity is associated with an increased exchange of molecules. The impact of increasing t_d on the signal intensity within the bubble's wake is visualized in Fig. 4.1. Three exemplary chosen delay times from averaged MRI intensity images are shown for both center planes.

The intensity images of the front view show two distinct maxima towards the capillary walls near the back cap of the bubble. In contrast, the side view reveals a focused intensity increase centered directly behind the bubble. Here, longer delay times lead to higher signal intensities, especially in regions with a higher flow velocity. This increase is caused by unsaturated water molecules, meaning those with full longitudinal magnetization, that enter the measurement slice and thus contribute to the MR signal. The purpose of the presaturation module is to

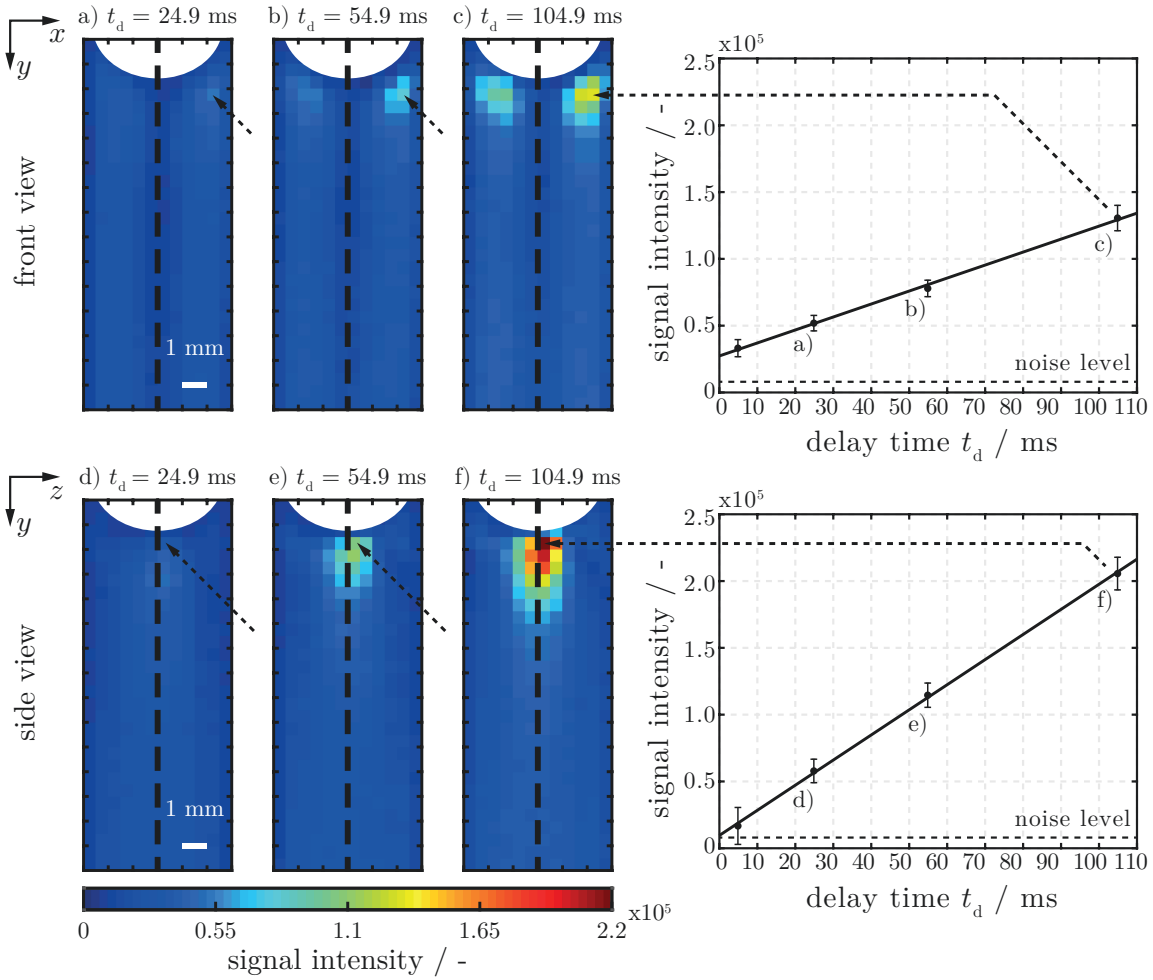

Fig. 4.1.: Averaged MRI signals inside the bubble's wake. The effect of different delay times on the signal is shown in the x, y-plane (a)-c)) and in the y, z-plane (d)-f)). The time-dependent increase in averaged signal intensity is plotted at different t_d at a fixed position, indicated by dashed arrows, regarding the highest signal intensity at the longest t_d for each view. The back cap has been manually added as a visual reference to distinguish between the flow field and the bubble. MRI sequence parameters: spatial resolution $= (0.5 \times 0.5)\,\mathrm{mm}$, slice thickness $= 2.0\,\mathrm{mm}$. Image based on Kemper et al. [78].

suppress the detectable magnetization of the water molecules within the measuring plane by removing the longitudinal magnetization, or in other words, by saturating the protons.

The different intensity profiles of both views indicate that the flow is not rotationally symmetric. If this were the case, identical patterns should have been observed inside the wake, similar to those measured by Kastens et al. [23]. In the flow setup utilized here (see Sec. 3.1.1, Fig. 3.1), the fluid is supplied from the side, deflected downward in a very confined space, and thus imprinted with a lateral velocity component that cannot be fully removed due to an insufficient entrance length. Nevertheless, this asymmetric but still stationary flow field

benefits the validation of the MRI method. Systematic errors can thus be ruled out since the two measurement planes can be precisely distinguished.

Next to the intensity maps, Fig. 4.1 depicts the signal intensity increase over the delay time t_d. The plot only shows the linear progression for the voxel of the highest intensity, as indicated by an arrow. A steeper slope is observed in the side view, which is caused by a higher amount of liquid entering the measuring plane than in the front view, and thus, a stronger signal is generated. Even short t_d allow for a distinction between signal and background noise. Thus, fast measurements are possible. However, short delay times also lead to a considerably lower signal intensity, which causes a decreased SNR. Tab. 4.1 lists the calculated SNR values (see Eqn. 2.9).

Tab. 4.1.: Number of images and calculated SNR (see Eqn. 2.9) for the processed MR data.

x, y-plane / front view				
delay time t_d	$4.9\,\mathrm{ms}$	$24.9\,\mathrm{ms}$	$54.9\,\mathrm{ms}$	$104.9\,\mathrm{ms}$
number of images N_img	44	32	31	33
SNR	3.7	4.4	5.2	6.9
y, z-plane / side view				
delay time t_d	$4.9\,\mathrm{ms}$	$24.9\,\mathrm{ms}$	$54.9\,\mathrm{ms}$	$104.9\,\mathrm{ms}$
number of images N_img	58	33	30	43
SNR	3.4	4.4	5.7	8.2

For a typical snapshot flash sequence with 32 phase encoding steps, about $TR = 58\,\mathrm{ms}$ are needed to complete the signal readout. The readout time inevitably leads to a distortion of the data, comparable to the motion blurring of a photograph, caused by the constantly moving fluid and the dynamic nature of the system.

In order to contain the problem of blurred data, the readout time had to be reduced drastically. Here, a partial Fourier acceleration factor of 1.5 was used for asymmetrical k-space truncation. Rather than acquiring the complete signal, the recording was divided into four sequential segments to make the data robust against flow-related artifacts. The segments were read in succession, allowing for a $TR = 8.5\,\mathrm{ms}$ per segment. This almost sevenfold reduction in TR decreases the influence of flow-related image artifacts. Physically, the readout time cannot be prevented, and thus all intensity measurements are affected marginally by flow-related artifacts. However, this influence is only noticeable at short t_d and loses impact as the delay time t_d increases.

Fig. 4.2 depicts the voxel-wise evaluation of the signal intensity in the bubble's wake measured from the side view. The distance from the bubble is increased along the centerline in seven

increments of one voxel at a time, starting after the maximum intensity. The linear regressions are color-coded according to their corresponding voxel intensity at $t_d = 104.9\,\mathrm{ms}$.

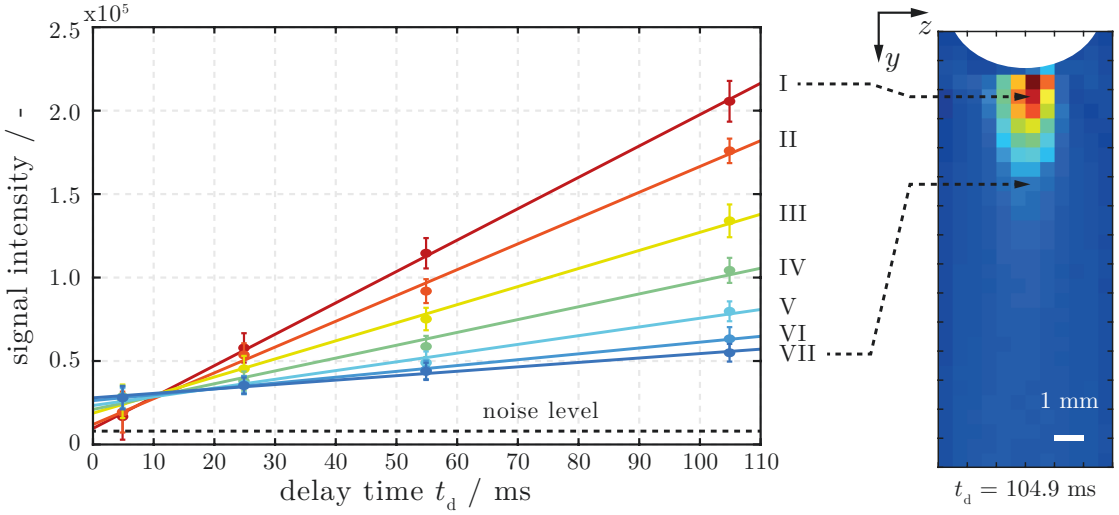

Fig. 4.2.: Signal intensities inside the bubble's wake region plotted along the centerline within the y, z-plane. The voxel-wise increase in distance from the bubble's rear cap is denoted from I-VII. The respective positions are indicated by arrows in the MRI image (identical image as in Fig. 4.1 f)). Image based on Kemper et al. [78].

If sufficiently long delay times are chosen, the signal will likely reach a maximum intensity value since the flow has replaced all saturated water molecules inside the measurement plane by surrounding water molecules with full longitudinal magnetization. A maximum signal is generated as a result. However, this limit was not yet reached here.

The present flow pattern can explain the flattening slope of the regressions with increasing distance from the bubble. The radial flow component is strongest close to the bubble as the liquid partly follows its contour. Thus, more molecules are carried into the measuring plane. With increasing distance, the fluid strives to flow downwards the capillary. Consequently, the radial component, and thus, the inflow into the measuring plane, decreases. The slope indicates how much fluid enters the measuring plane in a defined time and can accordingly be interpreted as a measure of velocity. A shallow slope and associated low signal intensity indicate a low radial flow velocity and vice versa. The linear increase in intensity over time observed here further indicates a simple downward flow in the wake region without back mixing or unsteady vortices.

4.2 PIV flow characterization

As can be seen from the MRI measurements, there is a non-rotationally symmetrical flow due to the flow setup used. Hence, PIV measurements were performed in the same flow setup to

verify the MRI data. Fig. 4.3 shows the results of the PIV flow analyses. Again, images were acquired in the capillary's x, y and y, z-center planes.

All $N_{\text{img}} = 1200$ single frames are used to calculate the mean image (Fig. 4.3 a),d)) in which the underlying flow field can already be guessed from the particle trajectories. The dark spot in the upper left corner of the mean images results from the bubble interface attenuating the laser light entering from the right. Despite the visible attenuation, the particles can be evaluated in this range since they are sufficiently fluorescent to be detected.

The flow fields obtained by the ensemble correlation algorithm are plotted for both sides. The trajectories represent the flow within the given 2D plane. In addition, the velocity of the axial and radial components is separately shown and color-coded. Significant differences exist in the present flow patterns between the two measurement planes. In both views, a downward flow originates near the bubble in the axial direction. It strikes that a source of flow originates behind the bubble in the side view (Fig. 4.3 e),f)). The out-of-plane fluid carried into the observed cross-section explains the origin of this source. The arising flow field can be described as axisymmetrical in the y, z-plane.
Examining the radial velocities, the fluid originating directly behind the bubble becomes evident through flow components directed towards the capillary wall (Fig. 4.3 f)). The radial velocities observed in the side view (Fig. 4.3 f)) are up to one order of magnitude smaller than those in the front view (Fig. 4.3 c)). In contrast to that, the radial velocity components in the front view are pointing towards the capillary's center line (Fig. 4.3 c)). Here, the flow leaves the film region with a higher velocity on the right side close to the bubble's rear cap. As a result, the fluid does not flow off axisymmetrically but is shifted slightly to the left.

Similar to the MRI results, a symmetrical and uniform flow in the bubble's wake is not observed either. As already concluded from the MRI measurements, no back mixing or vortices are present within the wake region.

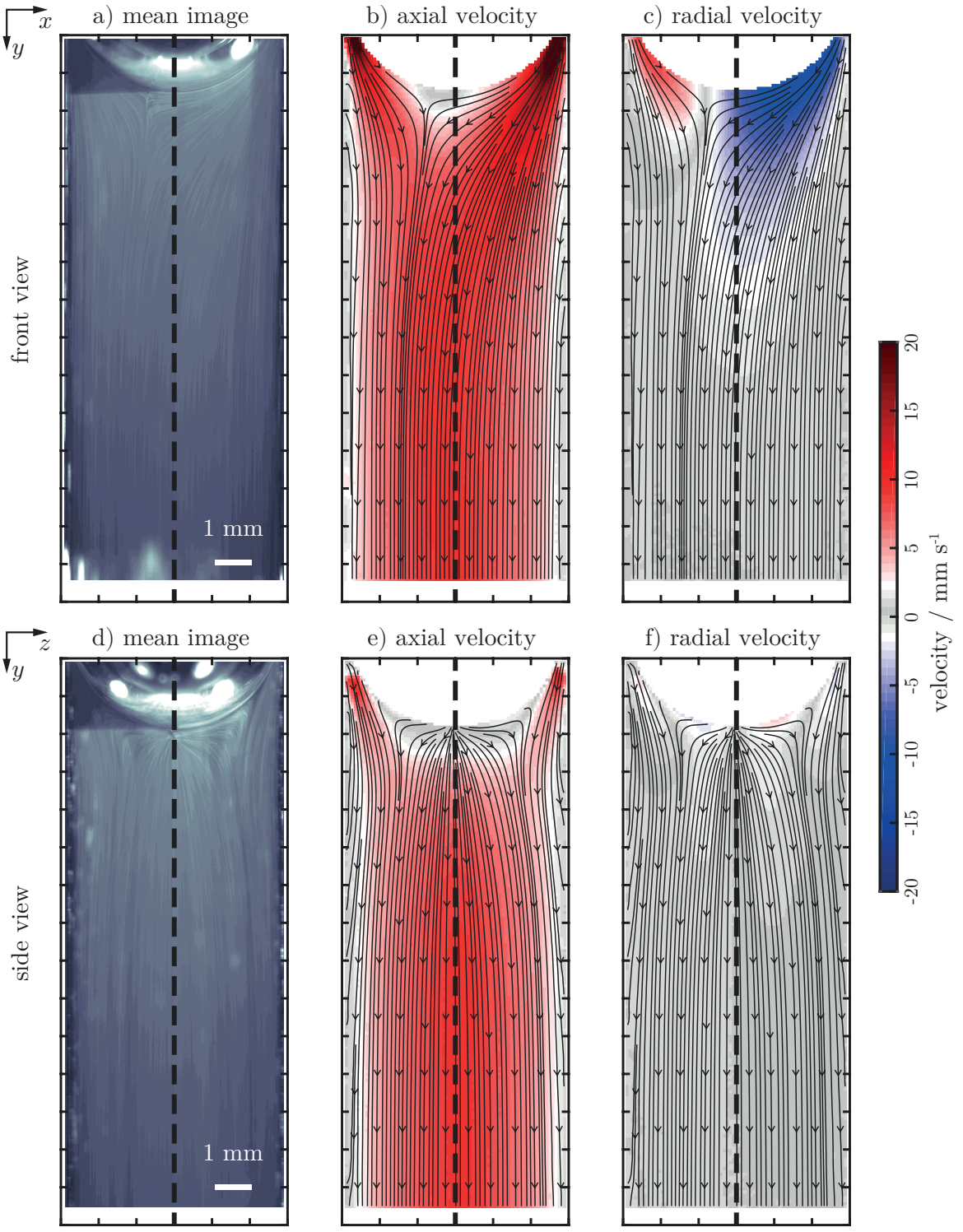

Fig. 4.3.: Results of the PIV analyses in the x, y-plane (a)-c)) and in the y, z-plane (d)-f)). $N_{\text{img}} = 1200$ shifted and stacked frames were used to calculate the mean image. The sharply visualized bubble cap indicates a precisely operating cap tracking algorithm. The white streaks in the mean image, formed by the signal of the single particles, provide an early indication of the underlying flow field. Streamlines indicate the computed 2D in-plane flow direction of the 3D flow field. The partial velocity magnitude is color-coded in axial and radial directions. Image based on Kemper et al. [78].

4.3 Comparison of MRI and PIV flow fields

MRI and PIV were used to analyze the flow fields inside the setup. However, a direct comparison between them is impossible since both methods consider different phenomena. While the PIV measurements directly represent the flow velocities within the 2D measurement plane by tracking the particle movement, the MRI results provide information about the flux into the measurement plane by an increase in signal intensity.
Comparability is achieved by calculating the divergence of the 2D PIV vector field, which represents the flux into and out of the measurement plane. As the proposed MRI method can solely represent the flux entering the measurement plane, only the positive divergence values of the PIV results are used as they reflect the flux into the cross-sectional plane. Because of the high resolution and accuracy of the data provided by numerous single images, PIV is well-suited as a reference method for the MRI data of the underlying hydrodynamics.
Fig. 4.4 compares the calculated divergence and the MRI data from both views. Here, the data was normalized between zero and one concerning the maximum value of each method occurring within the side view (Fig. 4.4 c)-d)). The similarity of the data among each other is striking. Both methods show the stationary and asymmetric flow field without back mixing or vortices in the wake region. Two regions of increased flux are revealed in the front view (Fig. 4.4 a)-b)). The area to the right of the bubble shows a higher intensity for both methods. A clear intensity peak behind the bubble is observed in the side view (Fig. 4.4 c)-d)). This region of high flux propagates along the center line of the capillary while the signal intensity attenuates.

In contrast to the PIV measurements, the area near the phase boundary layer can only be resolved to a limited extent with the MRI method. In addition, the thickness of the measurement slices differs between the two methods. In PIV, the slice thickness is specified by the depth of field of the optical setup. Here, the DOF was calculated to be $0.725\,\mathrm{mm}$ (see App. B). In MRI, the slice thickness can freely be adjusted for each measurement. However, the thickness is restricted to the lower end by the maximum gradient strength of the MR hardware. The thinner the slice, the stronger the gradients have to be. Here, a minimum thickness of $2.0\,\mathrm{mm}$ was obtained. Thinner measurement slices would increase the spatial resolution, and thus, more detail of the flow field can be recovered.

The gas phase varied between both methods. N_2 was used during MRI experiments, whereas PIV measurements were carried out using air. In both cases, the liquid phase was saturated with the corresponding gas to prevent mass transfer. Due to that fact and that both gases have similar physical properties, the influence of the different gas phases can be ruled out.

The relationship between the MRI and PIV data can be easily understood without computing the divergence by simply looking at the corresponding center planes in 3D space, as depicted in Fig. 4.5. The 3D illustration in Fig. 4.5 a) is composed from the results presented in

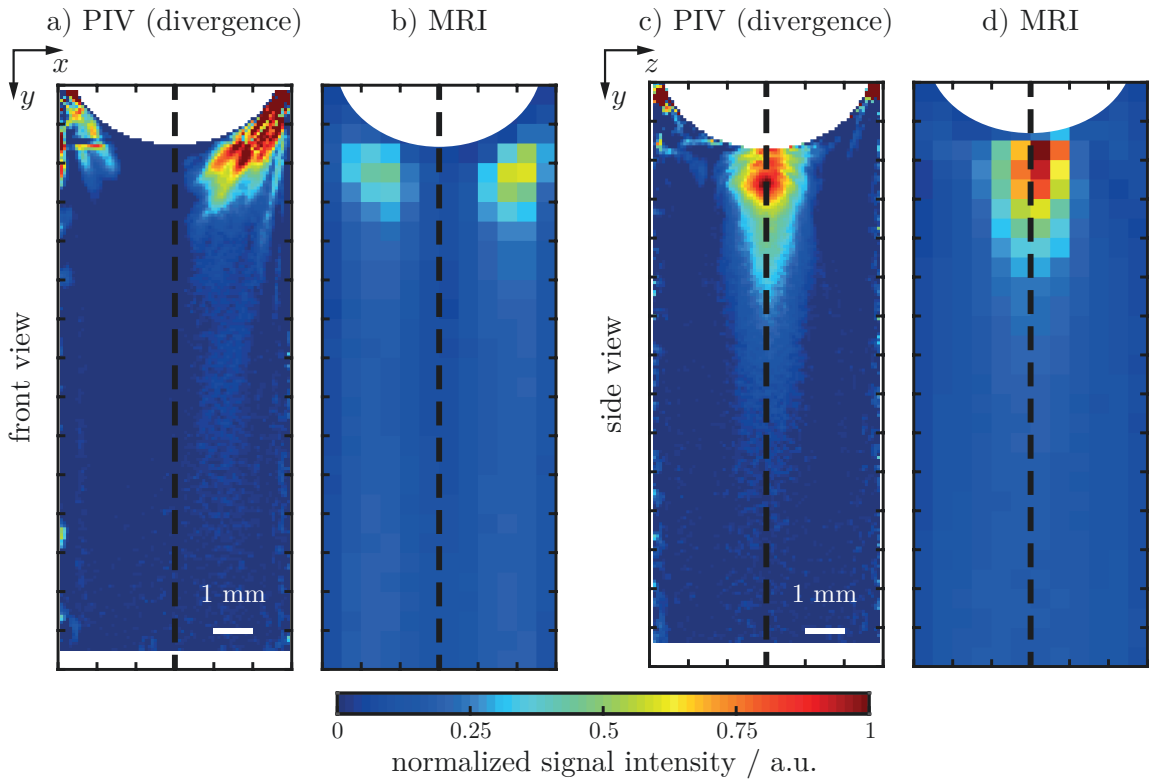

Fig. 4.4.: Resulting PIV and MRI images are compared in the x, y-plane (a)-b)) and in the y, z-plane (c)-d)). The divergence of the PIV flow field was computed to compare the two approaches directly. Solely positive divergence values were mapped, showing the flow into the measurement plane to match the MRI data. The signal intensities from each method's bubble wake (c)-d)) were adjusted to their highest value for a more straightforward comparison. Image based on Kemper et al. [78].

Fig. 4.1 f) and Fig. 4.3 c). Fig. 4.5 b) consists of the previous results coming from Fig. 4.1 c) and Fig. 4.3 f).

Fig. 4.5 a) demonstrates fluid transport into the capillary's center, shown by the PIV measurements inside the x, y-center plane. This flow is measured using the proposed MRI method inside the y, z-center plane and is indicated by an increase in the MRI signal intensity. Fig. 4.5 b) demonstrates the opposite behavior. The PIV flow field inside the y, z-center plane reveals a fluid flow from the capillary's center towards its wall. As a result, no unsaturated protons flow into the x, y-center plane where MRI measurements are performed. Thus, there is no measurable increase in signal strength within this region.

A qualitative comparison of the calculated divergence from PIV data with the MRI results shown in Fig. 4.4 revealed a good agreement with striking similarities. For quantification, the normalized intensity profiles along the side view's center line (Fig. 4.4 c),d)) are compared and shown in Fig. 4.6.

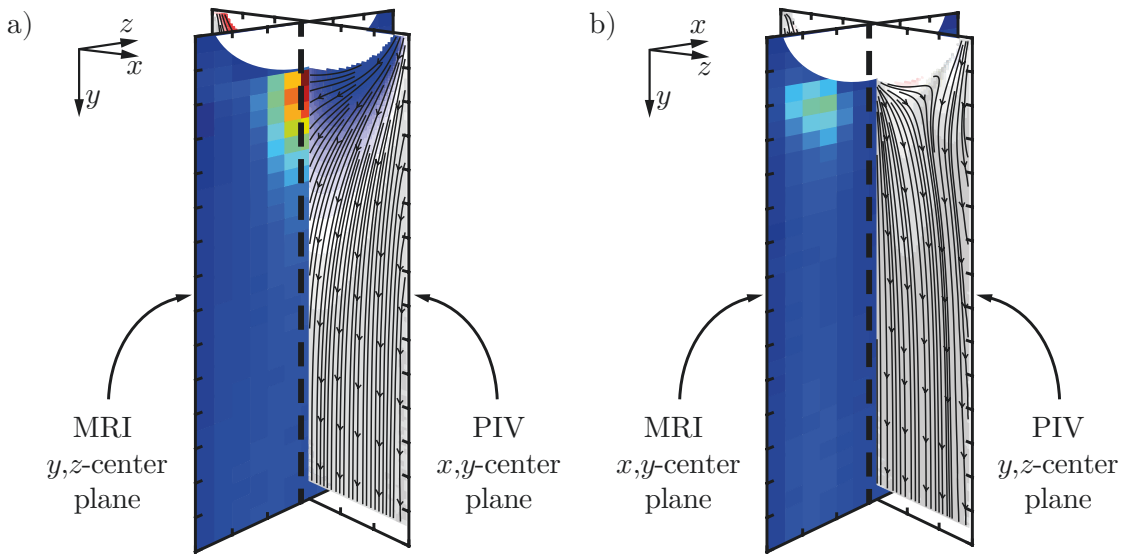

Fig. 4.5.: Comparing PIV and MRI data in 3D space. Flow fields measured inside the PIV center planes are in good agreement with the corresponding MRI intensity data. a) Saturated protons are flushed into the MRI y, z-center plane and are indicated by a higher signal intensity. b) Fluid flows towards the capillary wall so that no unsaturated protons are flushed into the MRI x, y-center plane where consequently, no signal is generated.

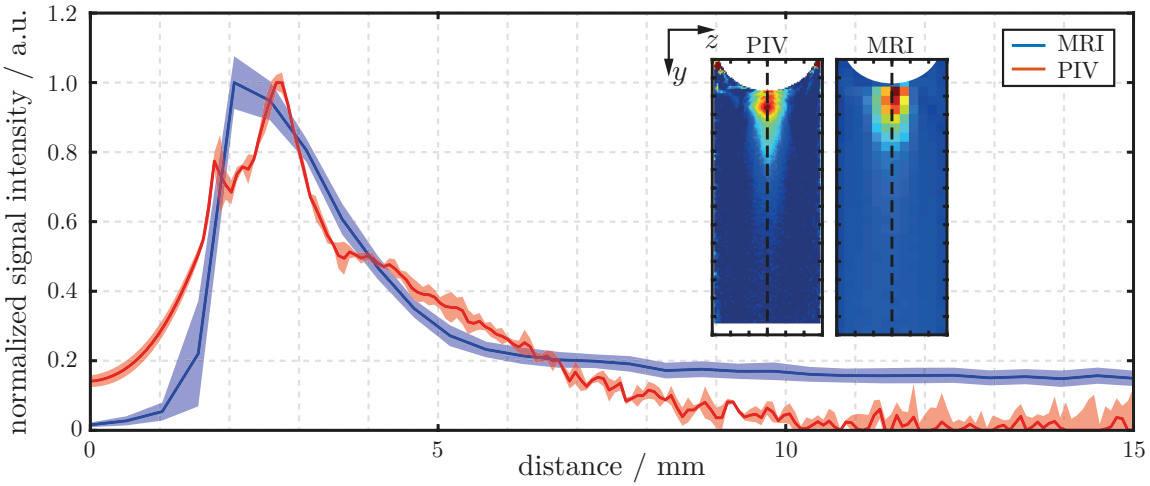

Fig. 4.6.: Normalized MRI ($t_\mathrm{d} = 104.9\,\mathrm{ms}$) and PIV intensity profiles inside the y, z-plane (side view) from along the capillary's center line as shown by the insets (see vertical dashed lines in Fig. 4.4 c)-d)). The standard deviation corresponds to $N_\mathrm{img} = 43$ MRI images and three calculated PIV correlation images. Image based on Kemper et al. [78].

The plotted divergence data was computed from the resulting correlation image of the PIV ensemble analysis. For statistical data evaluation, the ensemble correlation approach was performed with the same 1200 particle images but this time divided into three individual sets of 400 frames each. Three correlation images were obtained for calculating the divergence

from which the standard deviation was determined. The resulting curves in Fig. 4.6 are aligned with each other regarding the position of the phase boundary layer.

A uniform deviation of the MRI signal is noticeable in the wake region. This deviation attributes to the relatively coarse spatial resolution of $0.5\,\mathrm{mm}$, which leads to a systematic deviation when matching the intensity maxima. The phase boundary can move in the sub-voxel range where the position cannot be precisely determined. Thus, the locally measured intensity in the adjacent voxels will be slightly affected. The resolution of the PIV data is about six times higher with a pixel size of $0.08\,\mathrm{mm}$. As a result, the datasets match more precisely when overlaid, reducing the deviation, particularly near the bubble. However, the PIV data shows an increase in deviation with greater distance from the bubble. This more significant change in normalized signal intensity is caused by the divergence calculation derived from the vector field, which responds sensitively to minor changes.

The signal decreases similarly for both methods up to a distance of $6.5\,\mathrm{mm}$. The intensity increase, visible in the PIV measurements shortly after the bubble, cannot be detected by MRI due to the lower resolution. After a distance of $10.0\,\mathrm{mm}$, the calculated divergence approaches a value close to zero. In contrast, the normalized signal intensity of the MRI data remains at a constant value just below 0.2 since the water molecules within the measurement contribute to the signal and add up to a baseline intensity. In comparison, the MRI intensity is almost zero at a distance of less than $1.0\,\mathrm{mm}$. The N_2 bubble is located in this area and does not contribute to the ^{1}H NMR signal. Only the background noise of the MR system is measured.

4.4 Conclusion

The initial version of the countercurrent flow setup (see Sec. 3.1.1) successfully enabled long-term measurements of single Taylor bubbles inside an MR scanner of limited height. Images were successfully captured using the tailored loop-gap resonator (see Sec. 3.2.1) and the tweaked snapshot-FLASH pulse sequence (see Sec. 3.3). Temporal series of intensity images were recorded. Here, the SNR was improved by averaging the time-resolved images, albeit at the cost of losing temporal information. However, this was not important here since no mass transfer and resulting time-dependent changes in bubble size were investigated.

A qualitative comparison with ensemble correlated PIV data obtained in the identical setup revealed a good agreement between the two methods. An asymmetric but stable flow could be demonstrated due to the lateral fluid supply and the missing entrance length inside the flow setup. The particular flow field enabled a better comparison of the methods, as both views could be clearly distinguished. No vortices or back mixing were observed in the wake of the bubble.

The variable delay time t_d provides information on the time-dependent flux into the measurement plane. Spatial progression in stationary flows is mapped by multiple measurements with increasing t_d.

A direct qualitative comparison of the MRI data to the results of the ensemble correlation was possible after calculating the divergence of the 2D flow field obtained via PIV. Apparent similarities can be identified, and changes in the local flux are well represented by both methods and coincide with each other.

Although the spatial resolution of the MRI data is lower than that obtained by PIV, the proposed method enables the measurement in pure and even opaque systems.

5 Validation and characterization of the volumetric birdcage resonator for MRI at 7 T

Results shown in this chapter are published by Kemper et al. [76]. The text and illustrations have been adapted to match the style of this work.

A birdcage resonator is preferred for mass transfer and chemical reaction experiments as it provides a highly homogeneous magnetic field with a large sample volume of easy accessibility. The commercial coils available at the MR scanner are designed for biomedical samples with different loadings. Thus, accurate tuning and matching is not possible with the used sample and the bore space can not be fully utilized due to the limited height inside the resonator. An inductively coupled low-pass birdcage with twelve rungs is tailored around the given flow setup to address these problems [76]. The design is published open-source to be fully replicable by other researchers.

Performance tests of the coil are carried out under three distinct conditions, which are discussed in the following section. First, a bottle of rapeseed oil is placed inside the resonator to assess the image quality over the entire coil volume. Subsequently, the effect of a higher loading is investigated by measuring a water-filled ping pong ball. Finally, the imaging quality is highlighted through MRI images using a lime as a phantom. In addition, a qualitative image comparison with a commercially available coil is performed.

Detailed information regarding dimensions and capacitor values is provided in the appendix (see App. C.2).

5.1 Volumetric performance assessment

A simple way to find flaws in the design is to perform 3D measurements of a homogeneous specimen over the entire resonator volume. For initial measurements, a $1\,\mathrm{L}$ plastic bottle filled with rapeseed oil was inserted into the coil as demonstrated in Fig. 5.1 a). The advantage lies in a lower loading of the coil due to the approximately 20 times lower dielectric constant of rapeseed oil compared to water [95], which helps to reduce distortions and artifacts at the phase boundary. A FLASH sequence was used to acquire a 3D dataset of the phantom with an isotropic resolution of $1.0\,\mathrm{mm}$.

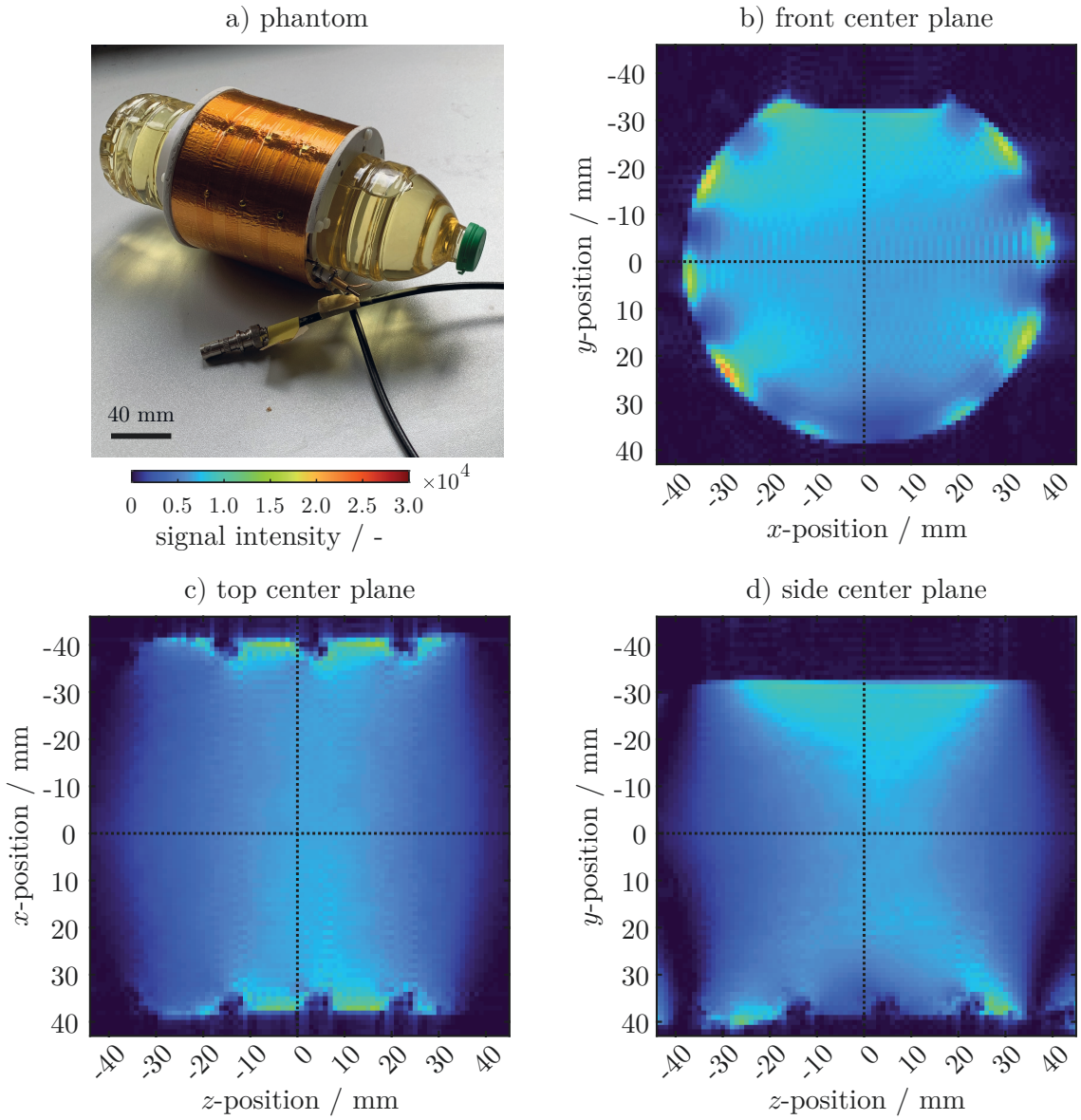

Fig. 5.1.: A plastic bottle filled with rapeseed oil a) is placed inside the BC resonator as a phantom for volumetric FLASH measurements. In b)-d), resulting T_1 weighted intensity images are depicted for all three center planes of the resonator. MRI sequence parameters: 3D FLASH sequence, field of view $= (128 \times 90 \times 90)\,\mathrm{mm}$, spatial resolution $= (1.0 \times 1.0 \times 1.0)\,\mathrm{mm}$, $TE = 4.0\,\mathrm{ms}$, $TR = 50\,\mathrm{ms}$. Image based on Kemper et al. [76].

Fig. 5.1 b)-d) shows the T_1 weighted intensity images of the rapeseed-filled plastic bottle phantom in all three center planes of the resonator. All perspectives indicate intensity fluctuations, especially close to the rungs of the coil. These changes are observed in all BC resonators since the field is locally affected by the electric currents flowing through the rungs. Near the oil surface, which is formed by the air contained in the bottle, an increase in signal intensity can be detected (Fig. 5.1 b),d)). The change in susceptibility between air and oil at the phase boundary causes this effect. It is also noticeable that local increases in

intensity occur in the vicinity of the capacitors, which is particularly pronounced in the side view (Fig. 5.1 d)). The legs and end rings were connected by capacitors located close to the z-positions of $\pm 30\,\mathrm{mm}$. The capacitance was split between two capacitors so that the local increase in intensity does not occur within the resonator's region of interest at the center of the leg. The uniform notches in z-direction (Fig. 5.1 c),d)) originate from the geometry of the oil-containing plastic bottle, which is visible in Fig. 5.1 a). The loss of intensity at the bottom of the specimen (Fig. 5.1 b)) is attributed to the position of the inductively coupled pickup loop. The coupling induces a load onto the resonator. Thus, a slight signal attenuation occurs, which is physically unavoidable.

Careful consideration of the coil design is essential when building an HF resonator. Fig. 5.2 illustrates the consequences of a somewhat trivial design decision that became apparent in an earlier coil prototype.

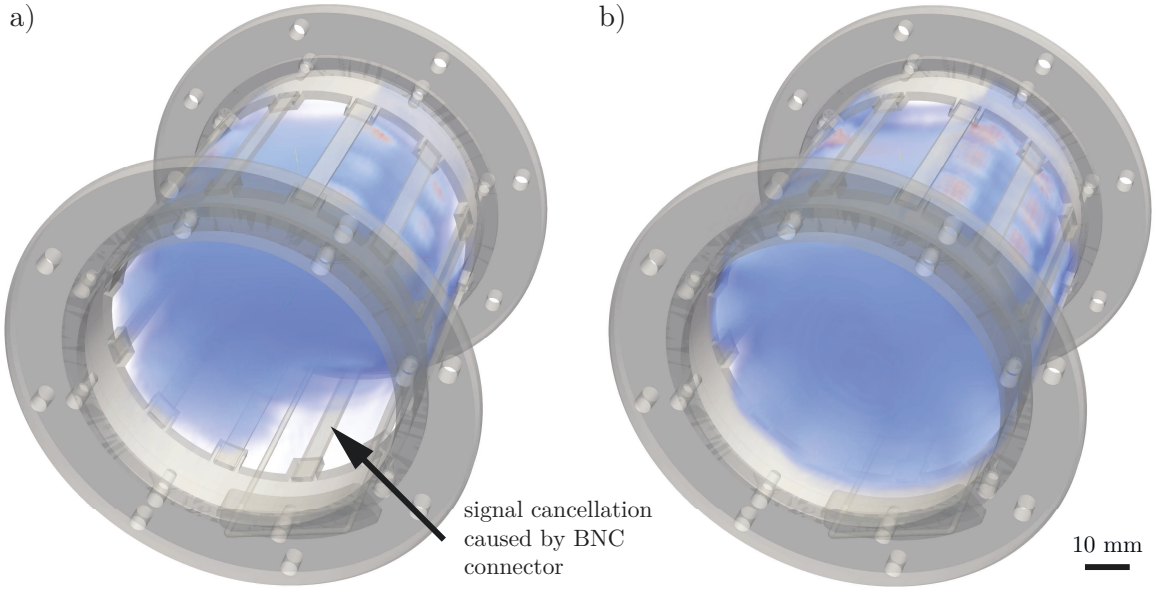

Fig. 5.2.: Comparing the field inside two almost identical birdcage resonators. A pickup loop interfaces the BC to the MR hardware. A static BNC connector is used in a), whereas in b), the cable is soldered directly onto the pickup loop, omitting the connector. For improved visualization, the measured volumetric FLASH data and the CAD model of the BC are overlaid. The presence of the BNC connector changes the field inside the resonator and results in a loss of signal in its immediate surrounding. This effect demonstrates the importance of proper design decisions on the overall resonator performance. Image based on Kemper et al. [76].

A BNC connector was soldered directly to the pickup loop for easier setup handling. The connector, however, strongly influenced the uniformity of the electromagnetic field inside the birdcage. Its slightly ferromagnetic properties caused distortion and signal cancellation in its vicinity (Fig. 5.2 a)). This error was not reduced by repeated shimming of the system. The problem was solved by omitting the connector and soldering the BNC cable directly to the pickup loop (Fig. 5.2 b)).

Deviations in the coil's B_1 field constitute a significant source of error in quantitative imaging. Taking T_1 contrast measurements as an example, local deviations in the B_1 field will affect the results due to the caused intensity variations. A B_1 map provides information about the fluctuations and can be used to correct the data later. The resulting B_1 maps (see Sec. 3.2.2, Fig. 3.12) are essential for correct data interpretation and were anticipated and discussed earlier in Sec. 3.2.2.

5.2 Performance of the BC under higher loading

The influence of a higher coil loading on the image quality of the BC was tested using a water-filled ping-pong ball with $d = 40\,\mathrm{mm}$ as a phantom. The ball was precisely placed inside the most homogeneous center region of the resonator, where 3D FLASH measurements with an isotropic resolution of $0.781\,\mathrm{mm}$ were performed.

Fig. 5.3 a) illustrates the resulting 3D representation of the water inside the ping-pong ball. An arrow indicates the seam that runs around the ball where the two sides of the sphere were fused together during manufacturing. The trapped air inside the ball is visible as an indentation near the top.

Significant susceptibility differences between water and air can often lead to distortions and artifacts at the phase interface. Thus, the phase interface is suitable for qualitatively evaluating the resonator. Fig. 5.3 b)-d) illustrates the three corresponding T_1 weighted intensity images of the center planes. None of the views show field distortions at or close to the gas-liquid phase boundary. However, the change in susceptibility resulted in a small intensity increase near the interface at the top of the ping-pong ball (Fig. 5.3 b)). The intensity varies slightly between the individual center planes. These minor changes are generally caused by the coil's unique profile and the higher loading of the water phantom.

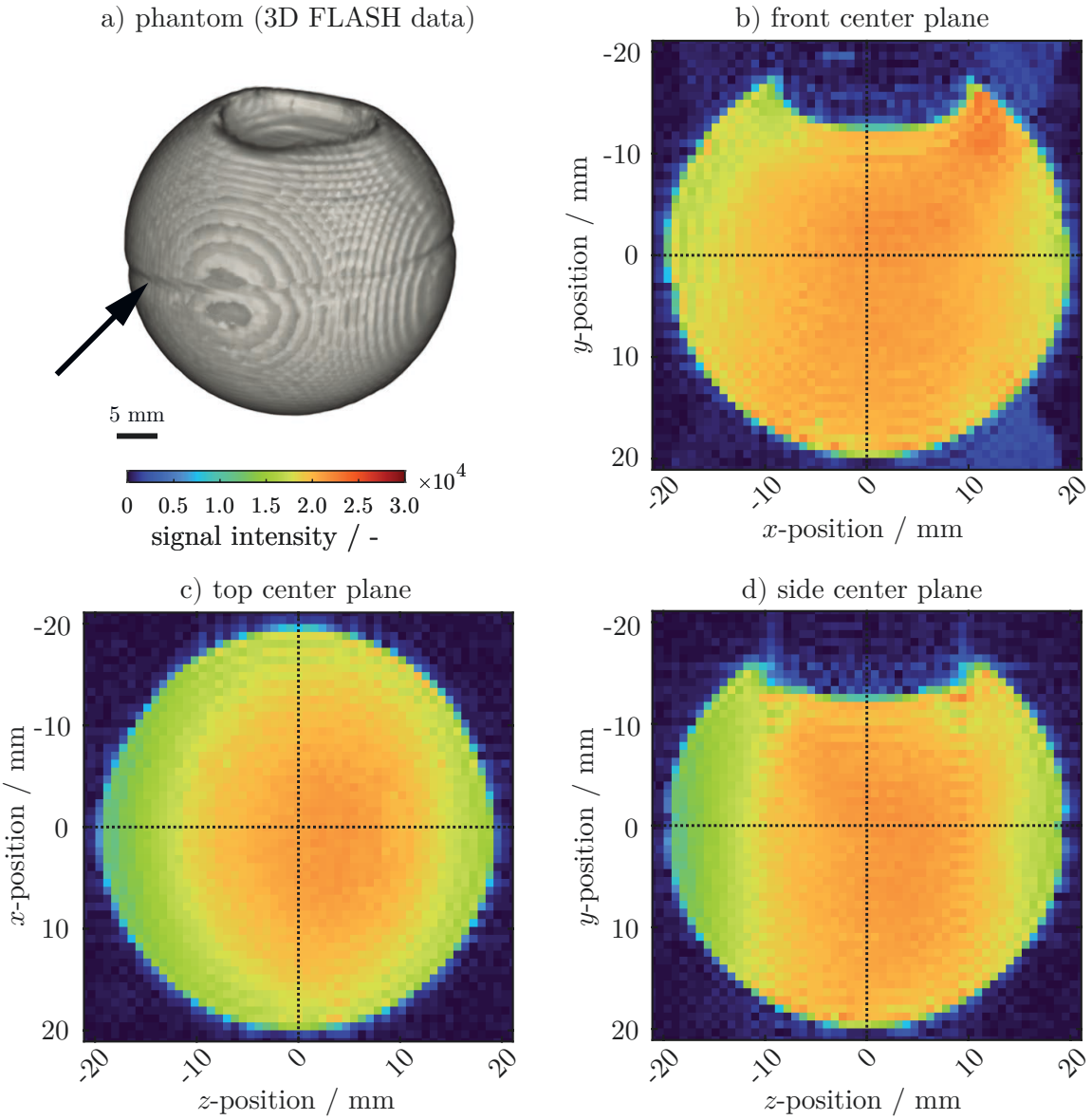

Fig. 5.3.: 3D FLASH measurements of a water-filled ping-pong ball with $d = 40\,\mathrm{mm}$ were used to assess the influence of higher loadings on the performance of the resonator. a) Shows the reconstructed 3D data. The arrow points towards the seam from the manufacturing process at which the ball is fused together. In b)-d), T_1 weighted intensity images of the sample are depicted for all three center planes of the resonator. The phase boundary between the water and the entrapped air inside the phantom is visible at the ball's top inside the front b) and side d) views. MRI sequence parameters: 3D FLASH sequence, field of view $= (50 \times 50 \times 50)\,\mathrm{mm}$, spatial resolution $= (0.781 \times 0.781 \times 0.781)\,\mathrm{mm}$, $TE = 2.0\,\mathrm{ms}$, $TR = 100\,\mathrm{ms}$. Image based on Kemper et al. [76].

5.3 Qualitative measurements and comparison to a commercial coil

The system's qualitative performance was assessed using a lime as a sample. Well-resolved 2D slices were acquired using a RARE sequence with a RARE factor = 2, a slice thickness of $3.0\,\mathrm{mm}$ and an in-plane resolution of $(0.117 \times 0.117)\,\mathrm{mm}$. Two different effective echo times of $TE = 8.8\,\mathrm{ms}$ and $TE = 44.0\,\mathrm{ms}$ were set for the RARE measurements. The effective echo times TE of the RARE sequence were calculated and given according to ParaVision 6.0.1. Identical measurements were performed with a commercial birdcage resonator (Bruker Linear Transmitter Coil, Part No T10720V3) to compare both systems directly. Fig. 5.4 illustrates the results of both resonators obtained at the two different effective echo times TE.

Structural differences are observed since precise repositioning of the lime was not possible between the measurements inside the different resonators.

The SNR was calculated using the mean intensity of the ROI (the lime) and the background noise level (see Eqn. 2.9). SNR deviation between the coils is well below $1\,\%$ and can therefore be considered equal. Compared to the effective $TE = 44.0\,\mathrm{ms}$, the signal intensity was higher at the effective $TE = 8.8\,\mathrm{ms}$.

The short echo time resulted in a more prominent representation of the skin, also known as epidermis [96]. The area between the skin and the segments, called albedo, was also more visible. At both echo times, the juice vesicles were well-defined inside the single segments of the fruit.

Qualitatively, no significant differences in the imaging quality of the lime were visible between both resonators. However, the local intensity distributions within the sample were somewhat different. The tailored birdcage resonator showed a horizontal intensity gradient with its maximum located at the sample's center. The same behavior was present within the commercial coil, however, the intensity gradient was vertically aligned. Different positioning of the pickup coil inside the Bruker resonator probably caused this behavior. Unfortunately, this assumption could not be verified by looking inside the Bruker BC since it was sealed.

For this test case, both coils behave equally well, which proves the functionality of the tailored BC resonator.

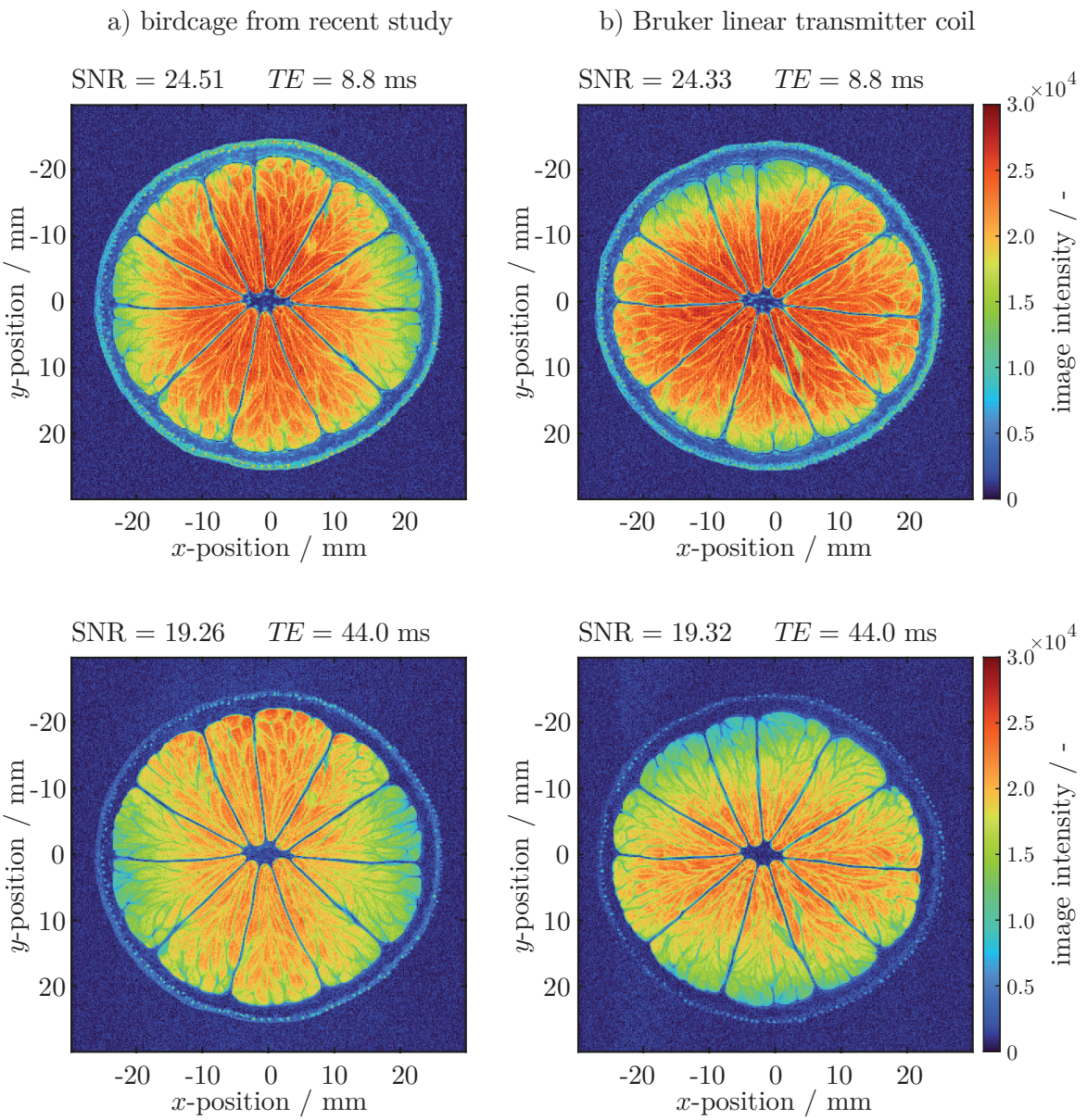

Fig. 5.4.: Comparing the proposed birdcage design a) with a Bruker Linear Transmitter Coil (Part No T10720V3) b). A lime served as a phantom for quality assessment. 2D RARE images were acquired at two different effective TE for both resonators. The ROI (lime) and background noise level were used to determine the SNR (see Eqn. 2.9), which is almost identical in both configurations. The fruit's structure is well resolved by both resonators. MRI sequence parameters: 2D RARE sequence, field of view = $(50 \times 50)\,\mathrm{mm}$, spatial resolution = $(0.117 \times 0.117)\,\mathrm{mm}$, slice thickness = $3.0\,\mathrm{mm}$, effective $TE = 8.8\,\mathrm{ms}$ and effective $TE = 44\,\mathrm{ms}$, $TR = 7500\,\mathrm{ms}$, RARE factor = 2, averages = 2. Image based on Kemper et al. [76].

5.4 Conclusion

The tailor-made inductively coupled linear birdcage resonator for MRI at 7 T was successfully validated and characterized. Three different conditions were tested to prove the BC's function and provide information about the quality of the magnetic field.

The homogeneity of the field was first examined under low loading conditions. For this, the resonator's entire volume was occupied with a plastic bottle of rapeseed oil, in which 3D FLASH measurements were performed. Minor field fluctuations were observed near the rungs and the pickup loop. The BC resonator's magnetic field variations were successfully represented by a B_1 field map using the same specimen, as anticipated and discussed earlier in Sec. 3.2.2, Fig. 3.12.

Next, the resonator's performance was assessed under high loading conditions, where it operated flawlessly. A water-filled ping-pong ball acted as a specimen and was depicted without distortions along the phase boundary.

Finally, the BC was qualitatively tested against a commercial Bruker resonator. MR images of a lime were acquired and compared in terms of SNR and visible image quality. Both coils performed equally well.

The resonator performed successfully under low and high loading conditions, such that experimental hydrodynamic investigations inside the given flow setup could be conducted in the upcoming step.

6 Modeling mass transfer of Taylor bubbles in non-reactive and reactive flows

In order to evaluate the experimental MRI data, a model is required that physically explains the influence of two-sided mass transfer without and with a superimposed chemical reaction on the resulting temporal change in Taylor bubble length. Such a modeling approach is described in detail in this chapter. The applied theories, assumptions, methods and results obtained with the models are reported and discussed here. An in-depth derivation with all necessary equations of the models is given in the appendix (see App. D) to avoid disrupting the reading flow.

At first, comparing the MRI results to a 2D rotational symmetric or a full 3D CFD simulation of the flow inside the setup may seem most convenient. In CFD, the curvature of the phase boundary is usually calculated from an initial state for interface capturing methods like volume of fluid (VOF). With these methods, the main issue is caused by the spurious or parasitic currents that arise during surface tension modeling by continuum surface force (CSF) models. At small capillary numbers $Ca \leq 0.03$, these currents significantly influence and inhibit a correct computation of the actual flow field [28]. High fluid velocity and small mesh spacing inside the liquid film result in particularly small calculation time steps in the range of $1 \times 10^{-7}\,\mathrm{s}$ or below in order to ensure numerical stability. As a result, an enormous number of computational steps are needed to simulate the given problem, and computing times can easily reach several weeks or longer. Hence, a simplified model with reasonable computational effort is required to draw conclusions about the measured MRI data.

The primary assumption for simplification is that the Taylor bubble can be approximated by a cylinder of the same length l_{tb}, at which mass transfer takes place solely over the cylinder's lateral surface and not over the two bases. This simplification results in an equal film thickness σ_{film} along the entire cylinder.
In the first step, the penetration theory is employed to determine the influence on mass transport caused by the geometric deviation between the cylinder approximation and the Taylor bubble's shape with two hemispherical caps. After that, the two-film theory is applied to model pure two-sided mass transfer. Finally, a numerical FDM simulation is employed to additionally consider the effect of a superimposed chemical reaction on mass transfer.

6.1 Calculation of liquid side mass transfer coefficient using the penetration theory

Higbie [97] developed the so-called penetration theory to describe the unsteady diffusion process on gas-liquid interfaces for short contact times. A fluid element attaches to the gas-liquid interface and changes its concentration by unsteady diffusion as it moves along the interface until it finally detaches. He assumes that small fluid elements of the liquid phase are in contact with the gas phase for a residence time τ, which is equal for all elements. According to Higbie [97], the liquid side mass transfer coefficient k_L can be expressed as:

$$k_L = 2\sqrt{\frac{D_{AB}}{\pi\tau}} \tag{6.1}$$

D_{AB} describes the liquid side diffusivity of a gas A inside a liquid B and τ stands for the contact time of the fluid element [98].

The total liquid side mass transfer coefficient of the Taylor bubble $k_{L,\text{tb}}$ and of the cylinder approximation $k_{L,\text{cyl}}$ are calculated with different residence times τ for the film and the cap region. Additionally, the surface ratio of the caps and the cylinder wall on the total surface area has to be taken into account for the Taylor bubble. For low Ca and small Eo numbers, the perturbations by the flow on the shape of the Taylor bubble, especially the caps, are small, and it is a valid assumption to approximate the shape as a cylinder with two hemispherical caps [33].
A detailed calculation of the total liquid side mass transfer coefficients is given in the appendix (see App. D.1).

Fig. 6.1 illustrates a schematic representation of the Taylor bubble and the approximated cylinder shape. The total surface area contributing to mass transfer is identical between the Taylor bubble's surface area (Fig. 6.1 a), red line) and the lateral surface area of the cylinder (Fig. 6.1 b), blue line). At the cap regions, the cylindrical geometry offers a 1.5 times higher volume than the Taylor bubble's hemispherical caps. Therefore, the amount of substance is always higher inside the cylinder at identical l_{tb}.

6.1.1 Results - penetration theory

To quantify the impact of the geometric variation resulting from the cylinder shape approximation, total liquid side mass transfer coefficients were calculated for a Taylor bubble $k_{L,\text{tb}}$ (see Eqn. 6.2 and Eqn. D.8) and a cylinder shape $k_{L,\text{cyl}}$ (see Eqn. 6.3 and Eqn. D.9) of same length l_{tb} over a range of various l/d ratios.

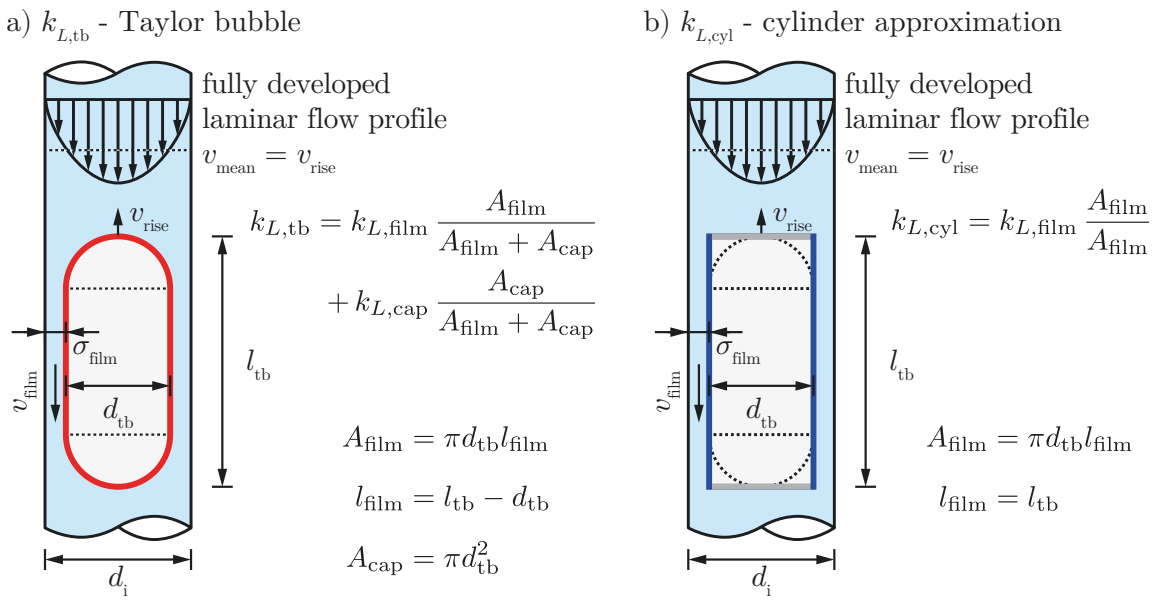

Fig. 6.1.: Schematic representation of the Taylor bubble shape a) and the cylinder approximation b) with the main variables. A detailed calculation is found in the appendix (see App. D.1).

$$k_{L,\mathrm{tb}} = k_{L,\mathrm{film}} \frac{A_{\mathrm{film}}}{A_{\mathrm{film}} + A_{\mathrm{cap}}} + k_{L,\mathrm{cap}} \frac{A_{\mathrm{cap}}}{A_{\mathrm{film}} + A_{\mathrm{cap}}} \tag{6.2}$$

$$k_{L,\mathrm{cyl}} = k_{L,\mathrm{film}} \frac{A_{\mathrm{film}}}{A_{\mathrm{film}}} = k_{L,\mathrm{film}} \tag{6.3}$$

To better visualize the influence of the bubble length, a representation of k_L over the dimensionless l/d ratio is chosen. In Fig. 6.2 a), k_L values for two different film thicknesses σ_{film} (solid / dotted lines) are shown as a function of l/d for the Taylor bubble (red lines) and the cylinder approximation (blue lines).

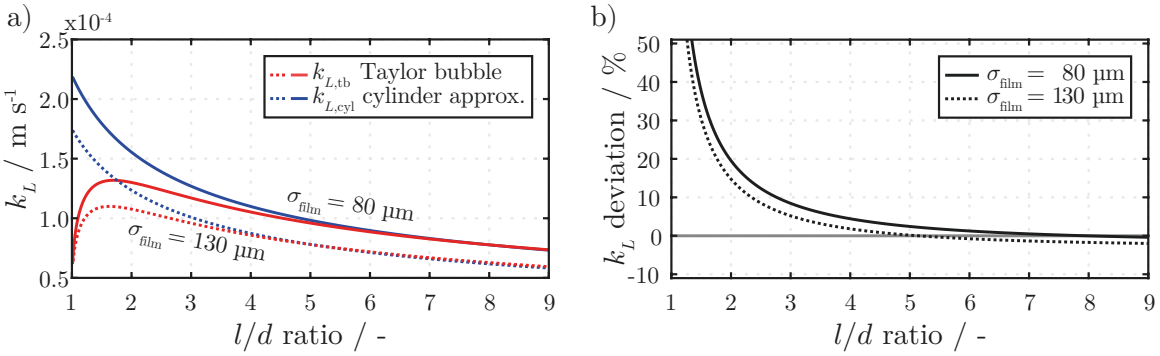

Fig. 6.2.: a) Influence of the liquid film thickness σ_{film} on the calculated liquid side mass transfer coefficients k_L for the Taylor bubble ($k_{L,\mathrm{tb}}$) and the cylinder approximation ($k_{L,\mathrm{cyl}}$). b) The percentage deviation between both calculations $(((k_{L,\mathrm{cyl}} / k_{L,\mathrm{tb}}) - 1) \times 100)$ increases with decreasing l/d. Results were calculated using $D_{\mathrm{O_2}} = 2.2 \times 10^{-9}\,\mathrm{m^2\,s^{-1}}$, $d_{\mathrm{i}} = 6.0\,\mathrm{mm}$, $v_{\mathrm{rise}} = 5.3\,\mathrm{mm\,s^{-1}}$.

Both film thicknesses compared here were carefully chosen for two reasons:
Firstly, Haghnegahdar et al. [99] experimentally determined a film thickness of approximately $\sigma_{\text{film}} = 130\,\mu\text{m}$ using X-ray tomography at similar hydrodynamic flow parameters (CO_2 Taylor bubble held in a countercurrent flow of ultrapure water inside a capillary of $d_{\text{i}} = 6.0\,\text{mm}$). Since MRI cannot resolve the film region, the experimentally determined value from Haghnegahdar et al. [99] is used as a first guideline. Secondly, the best agreement between the soon-to-be-described FDM model and our MRI experiments was found to be $\sigma_{\text{film}} = 80\,\mu\text{m}$. The MRI results are examined in detail in Chap. 7.

A higher film velocity v_{film} is found for thinner films (conservation of mass, see Eqn. D.3), and thus, the overall mass transport is enhanced as can be seen in Fig. 6.2 a) by increased k_L values between both σ_{film}. For long bubbles, the liquid side mass transfer coefficient is almost identical between both shapes. However, as the bubble length reduces, the two curves diverge increasingly from each other. Altered hydrodynamics at the Taylor bubble's caps cause this variation which gains in influence for smaller l/d ratios. The deviation between the Taylor bubble and the cylindrical approximation is highest at the lower limiting case of $l/d = 1$ (spherical bubble).

Fig. 6.2 b) illustrates the percentage deviation between both shapes as $(((k_{L,\text{cyl}} \,/\, k_{L,\text{tb}}) - 1) \times 100)$ over l/d. For the investigated film thicknesses, the deviation between the cylinder approximation and the Taylor bubble stays below $50\,\%$ for all $l/d >= 1.4$. The cylinder approximation overestimates k_L at small l/d. All values were calculated using the diffusion coefficient of oxygen $D_{O_2} = 2.2 \times 10^{-9}\,\text{m}^2\,\text{s}^{-1}$. In the case of nitrogen, lower k_L values will result for $D_{N_2} = 2.0 \times 10^{-9}\,\text{m}^2\,\text{s}^{-1}$. However, the percentage deviation between both shapes remains identical. The exactly calculated percentage deviations for different l/d ratios are listed in the appendix in Tab. D.1.

The next step is to create a simple model for solving the two-sided mass transfer problem, resulting in a time-dependent length decrease of the Taylor bubble. The penetration theory is used to calculate the necessary liquid side mass transfer coefficients for both shapes. In the following section, mass transport at the gas-liquid interface is modeled using the two-film theory.

6.2 Modeling of two-sided mass transfer with the two-film theory

The previously calculated k_L values are now incorporated into a mathematical framework to progressively determine the transport of O_2 out of and N_2 into the gas bubble. Mass transfer of oxygen and nitrogen across the gas-liquid interface can be described by the two-film theory

proposed by Lewis and Whitman [100]. Equilibrium between both phases at the gas-liquid interface without accumulation and the contribution of both films to the overall resistance for mass transfer is assumed [101]. Fig. 6.3 illustrates the concentration profiles of O_2 and N_2 over both phases.

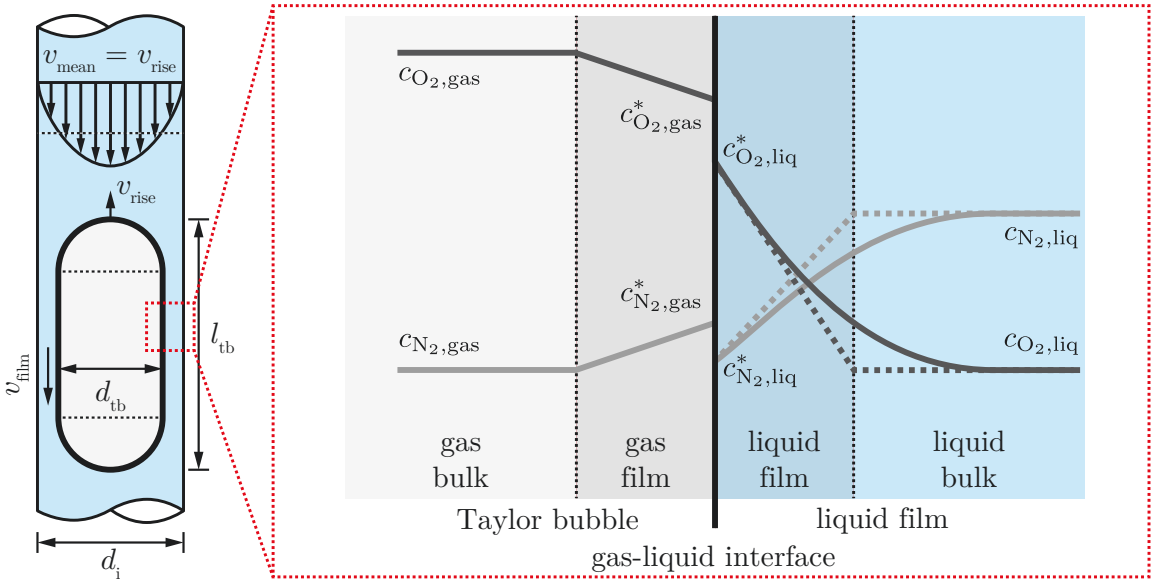

Fig. 6.3.: Two-film theory, showing the concentration profiles of O_2 and N_2 inside the gas and liquid phase under the assumption of pure oxygen inside the bubble and solely dissolved nitrogen inside the liquid phase.

The critical factor for mass transfer is the driving concentration gradient between the bulk concentrations of the gas phase $c_{i,\text{gas}}$ and the liquid phase $c_{i,\text{liq}}$. In the case of weakly soluble gases, the liquid phase is the main contributor to mass transport resistance at the gas-liquid interface. Therefore, the resistance inside the gas film becomes negligible so that $c^*_{i,\text{gas}} \approx c_{i,\text{gas}}$ applies for the gas phase, and only the liquid side mass transport has to be taken into account. The relation between the concentrations of both phases at the phase boundary can be expressed by Henry's law, again, only under the condition of weak solubility of the gas inside the liquid phase. Henry's law states that a component's dissolved mole fraction x_i is proportional to its partial pressure p_i in the gas phase ($p_i = x_i\, H_i^{px}$). [31, 75]

The liquid side mass transport of a species i equals the change in amount of substance n_i inside the bubble over time t [99, 102]:

$$\frac{dn_i}{dt} = -k_{L,i} A (c^*_{i,\text{liq}} - c_{i,\text{liq}}) \tag{6.4}$$

The transport of substance is defined by the liquid side mass transfer coefficient $k_{L,i}$, the total surface area A, and, most importantly, the concentration difference between both phases. The driving concentration gradient for liquid side mass transfer is the difference between the gas concentration at the phase interface $c^*_{i,\text{liq}}$ and the gas concentration inside the liquid

bulk $c_{i,\text{liq}}$ at a considerable distance away from the bubble. Mass transfer ceases when the concentration difference between the two phases approaches zero. Here, i denotes the respective components, O_2 and N_2. Assuming equilibrium with the atmosphere inside the bubble, the concentration at the gas-liquid interface $c^*_{i,\text{liq}}$ can be calculated using Henry's law [99, 102]:

$$c^*_{i,\text{liq}} = \frac{c_L p_0 x_i}{H_i^{px} - p_0 x_i} \tag{6.5}$$

where c_L describes the molar concentration of water ($c_L = 55.4 \times 10^3\,\text{mol}\,\text{m}^{-3}$), p_0 is the atmospheric pressure ($p_0 = 101\,325\,\text{Pa}$), H_i^{px} is Henry's law solubility constant (defined as partial pressure p / molar fraction x [103]) and x_i is the mole fraction of the respective gas. Eqn. 6.5 is also used to calculate the concentration of dissolved gas inside the liquid bulk $c_{i,\text{liq}}$ using the corresponding mole fraction of the dissolved gas. In our experimental studies, the liquid phase is degassed and stripped with pure nitrogen. The resulting initial concentrations at $T = 298\,\text{K}$ and $p_0 = 101\,325\,\text{Pa}$ are listed in 6.1. An in-depth calculation of the liquid side mass transport is given in the appendix (see App. D.2).

Tab. 6.1.: Initial concentrations at the gas-liquid interface $c^*_{i,\text{liq}}$ and inside the liquid bulk $c_{i,\text{liq}}$ for O_2 and N_2, determined by Eqn. 6.5. Values were calculated for $T = 298\,\text{K}$ and $p_0 = 101\,325\,\text{Pa}$ with Henry's law solubility constants from Tab. D.2, converted by Eqn. D.13.

	gas-liquid interface concentration		liquid bulk concentration	
component i	x_i	$c^*_{i,\text{liq}}$	x_i	$c_{i,\text{liq}}$
O_2	1	$1.2193\,\text{mol}\,\text{m}^{-3}$	0	$0\,\text{mol}\,\text{m}^{-3}$
N_2	0	$0\,\text{mol}\,\text{m}^{-3}$	1	$0.6524\,\text{mol}\,\text{m}^{-3}$

Eqn. 6.4 can now be used to solve the two-sided mass transfer of O_2 leaving and N_2 entering the bubble over a given time. The change of substance over time $\frac{dn_i}{dt}$ is solved iteratively for both gases, where t denotes the length of a single time step between recalculations. For clarity, this period is referred to as the update time Δt. Iterative calculation of n_i is performed in fixed steps of Δt, starting at $t = 0$. Thus, the desired end time t_{end} has to be a multiple of Δt. For the calculation, a perfect mixing of the gasses is assumed inside the bubble. Further, the concentration c_i and the amount of substance n_i inside the bubble are assumed to be constant between the update intervals Δt. A schematic representation of the iterative calculation is shown in Fig. 6.4.

6.2.1 Results - two-film theory

Unless otherwise stated, the following results were obtained by the previously described model using: $l/d = 4.0$, $\sigma_{\text{film}} = 80\,\mu\text{m}$, $T = 298\,\text{K}$, $d_\text{i} = 6.0\,\text{mm}$, $v_{\text{rise}} = 5.3\,\text{mm}\,\text{s}^{-1}$, $D_{O_2} = 2.2 \times 10^{-9}\,\text{m}^2\,\text{s}^{-1}$, $D_{N_2} = 2.0 \times 10^{-9}\,\text{m}^2\,\text{s}^{-1}$.

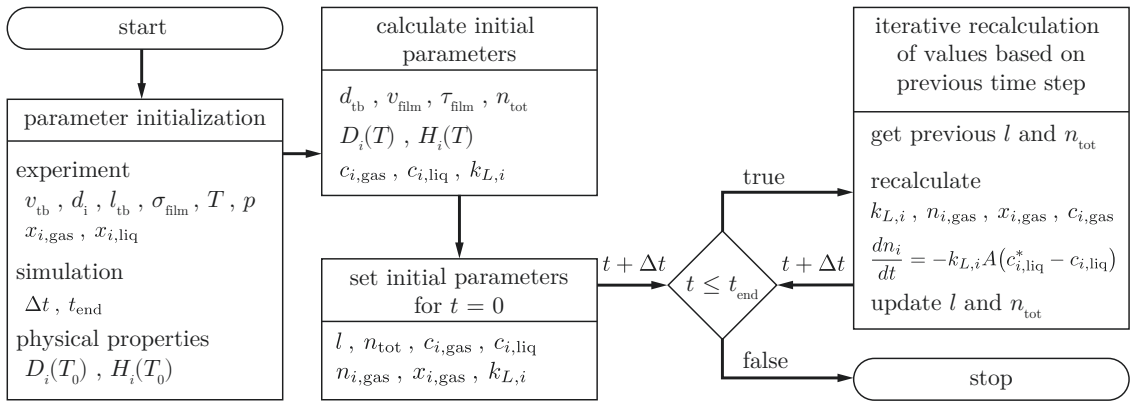

Fig. 6.4.: Simplified representation of the calculation of time-dependent variables using the two-film and penetration theory. See App. D.2 for a detailed description of all values.

Fig. 6.5 a) shows the change in the amount of substance n_i of both gases as a function of time. Based on the gases' different solubility and diffusion coefficients, more oxygen exits the bubble over one hour than nitrogen can enter. In contrast, when the mole fraction x_i is evaluated, as shown in Fig. 6.5 b), a shift from 1 to 0 takes place for O_2 and vice versa for N_2 across the whole period. This shift happens because the mole fraction x_i is determined using the temporally changing total amount of substance n_{tot} of both gases (see Eqn. D.14).

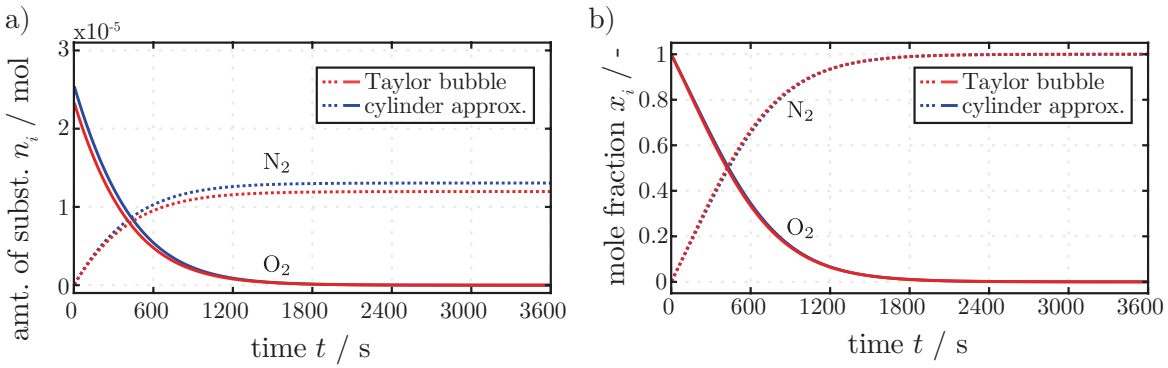

Fig. 6.5.: Temporal behavior of the amount of substance n_i a) and the mole fraction x_i b) inside the bubble for $l/d = 4.0$ and $\sigma_{film} = 80\,\mu m$. Oxygen is represented by the solid line and nitrogen by the dashed line.

The bubble's oxygen concentration acts as the driving force for two-sided mass transfer. Nitrogen uptake will stop as soon as all oxygen has been released because no driving concentration gradient is present. The slopes of the curves for both gases in Fig. 6.5 indicate this effect. The concentration difference is largest at $t = 0\,s$. Thus, the steepest slope is found at this point. As time progresses, the slopes flatten out and mass transfer decreases.

The cylindrical approximation shows an initially higher oxygen concentration at the beginning and respectively, a higher nitrogen concentration at the end due to the 1.5 times increased volume of the cylinder at the cap regions compared to the hemispherical caps of the Taylor

bubble. When looking at both components' respective mole fractions x_i, both shapes show an almost identical temporal progression.

For better comparability between different l/d ratios, the data is plotted as the normalized bubble length $l_{\mathrm{tb},t}/l_{\mathrm{tb},0}$, where the bubble's length at a given time t is compared to the initial length at $t = 0\,\mathrm{s}$.

The time-dependent change in normalized bubble length was investigated for this work's experimental upper and lower l/d limits of $l/d = 8$ and $l/d = 2$. Results are shown in Fig. 6.6 for a film thickness of $\sigma_{\mathrm{film}} = 80\,\mu\mathrm{m}$ a) and $\sigma_{\mathrm{film}} = 130\,\mu\mathrm{m}$ b).

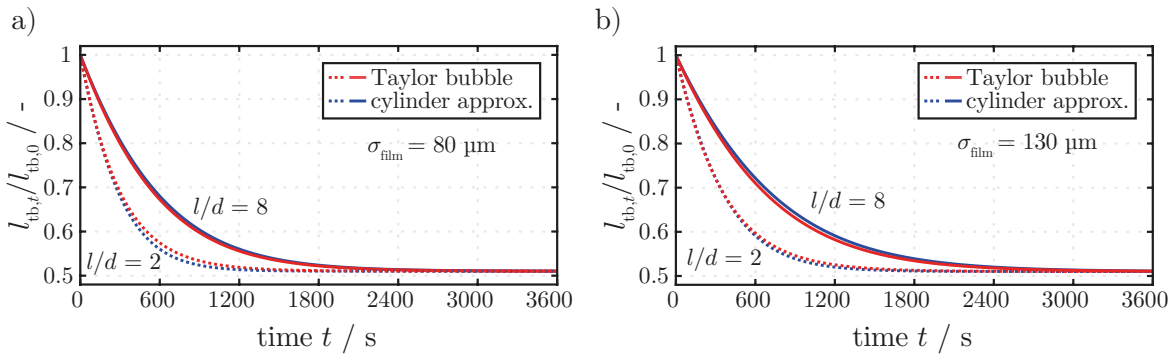

Fig. 6.6.: Change in normalized length $l_{\mathrm{tb,t}}/l_{\mathrm{tb,0}}$ of the Taylor bubble and cylindrical approximation over time. Two different liquid film thicknesses of $\sigma_{\mathrm{film}} = 80\,\mu\mathrm{m}$ a) and $\sigma_{\mathrm{film}} = 130\,\mu\mathrm{m}$ b) are illustrated.

A more rapid length decrease is evident for smaller l/d ratios caused by higher mass transfer coefficients $k_{L,i}$ due to shorter residence times τ. This behavior is identical for both film thicknesses. However, the slope of the length decrease is lower with thicker films as a direct result of lower film speeds and thus, higher residence times. Over time, the length decrease slows down until a stationary bubble size is reached.

Only a minor deviation in the temporal behavior is found between both models. At the lower limit of $l/d = 2$, the normalized bubble length decreases slightly faster for the cylindrical approximation. In contrast, at the upper limit of $l/d = 8$, the length decrease is slightly slower compared to the Taylor bubble. The influence of the geometric cap deviation is most dominant at the limiting case of $l/d = 1$ (sphere vs. cylinder). At this point, the largest deviation in volume ($V_{\mathrm{cyl}}/V_{\mathrm{tb}} = 1.5$) and thus, in the bubble's amount of substance n_i is present. The cap influence decreases with longer bubbles, which explains the shown behavior.

Even though the mass transfer coefficient k_L is overestimated, especially at small l/d (see Fig. 6.2), the deviation between both models is rather low. Due to the overestimation of k_L for both gases contributing to the two-sided mass transport, the influence on the length is largely canceled out.

The minimum and maximum deviation between both models is calculated as the percentage error:

$$E_{\%} = \left(\frac{\left(l_{tb,t}/l_{tb,0}\right)_{\text{cyl}}}{\left(l_{tb,t}/l_{tb,0}\right)_{\text{tb}}} - 1 \right) \times 100 \tag{6.6}$$

Resulting deviations for both film thicknesses and different l/d ratios are listed in Tab. 6.2. As can be seen from Tab. 6.2, the deviation between the approximated cylinder shape and the Taylor bubble lies in the range of $\pm 3.0\,\%$ for all l/d ratios between $l/d = 2$ to $l/d = 8$. Therefore, the cylindrical approximation of the Taylor bubble's shape can be considered valid.

Tab. 6.2.: The minimum deviations $\min(E_{\%})$ and maximum deviations $\max(E_{\%})$ between both geometries are calculated at two different film thicknesses by Eqn. 6.6.

	$\sigma_{\text{film}} = 80\,\mu\text{m}$		$\sigma_{\text{film}} = 130\,\mu\text{m}$	
l/d ratio	$\min(E_{\%})$	$\max(E_{\%})$	$\min(E_{\%})$	$\max(E_{\%})$
8.0	0.00 %	1.15 %	0.00 %	1.74 %
7.0	0.00 %	1.14 %	0.00 %	1.77 %
6.0	0.00 %	1.11 %	0.00 %	1.79 %
5.0	0.00 %	1.03 %	0.00 %	1.78 %
4.0	−0.01 %	0.87 %	0.00 %	1.69 %
3.0	−0.33 %	0.51 %	−0.01 %	1.38 %
2.0	−2.50 %	0.00 %	−1.35 %	0.44 %

Next, the influence of the l/d ratio and the oxygen diffusion coefficient D_{O_2} on mass transfer were investigated and are shown in Fig. 6.7.

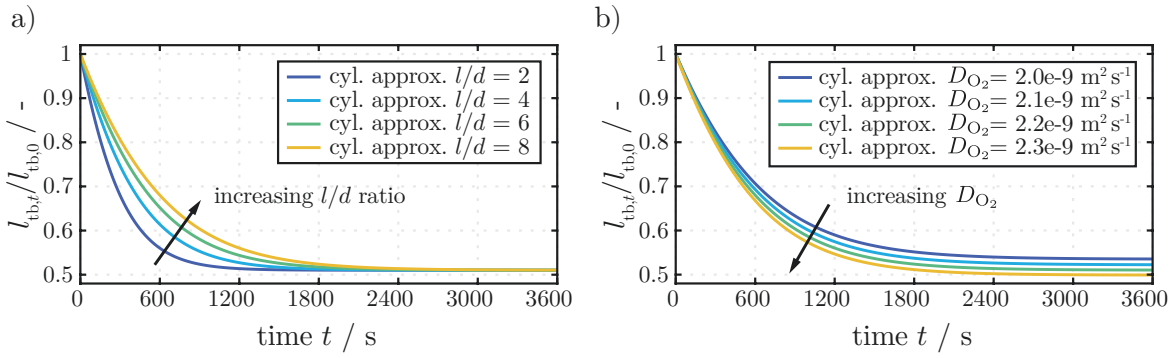

Fig. 6.7.: Influence of varying l/d ratios at fixed $D_{O_2} = 2.2 \times 10^{-9}\,\text{m}^2\,\text{s}^{-1}$ a) and varying diffusion coefficients D_{O_2} at fixed $l/d = 8$ b) on the normalized bubble length in case of the cylindrical approximation with $\sigma_{\text{film}} = 80\,\mu\text{m}$.

As previously demonstrated, the differences between both models are below $\pm 3.0\,\%$ (see Fig. 6.6 and Tab. 6.2), so that only the cylinder approximation is considered here. With

increasing l/d, the slope flattens, which results in a steady state length that is reached later. However, the normalized terminal bubble length is independent of l/d since only the liquid side mass transfer coefficients $k_{L,i}$ are lowered at greater length. However, the driving concentration gradient remains the same.

D_{O_2} was varied in the range of $2.0 \times 10^{-9}\,\mathrm{m^2\,s^{-1}}$ to $2.3 \times 10^{-9}\,\mathrm{m^2\,s^{-1}}$, as these values are found in literature [104]. The liquid side mass transfer coefficient k_{L,O_2} is enhanced with increasing D_{O_2} (see Eqn. D.6). Consequently, a steeper slope and a shorter normalized terminal bubble length are present. Increasing D_{N_2} will cause the opposite effect, resulting in a higher normalized terminal bubble length.

The previously described two-film theory works well in combination with the penetration theory for $k_{L,i}$ determination to estimate bubble shrinkage caused by liquid side mass transfer. However, the effect of a superimposed chemical reaction cannot be assessed. Next, the model is extended to include the reaction term for investigating two-sided mass transfer with a superimposed chemical reaction. The extended model is explained in the following section.

6.3 FDM model for two-sided mass transfer with superimposed chemical reaction

The oxidation reaction of Fe^{II}(EDTA) to Fe^{III}(EDTA) consumes the oxygen transferred from the bubble into the liquid film, resulting in a steeper concentration gradient that enhances mass transfer. The reaction is affected by both the local oxygen concentration and the Fe^{II}(EDTA) concentration inside the liquid phase and is described by a reaction rate r. A simple analytical solution of the present diffusion-advection-reaction problem inside the liquid film is no longer possible. Hence, the differential equation for describing the 2D concentration profile within the liquid film is solved numerically using a finite difference method (FDM).

It is important to emphasize that the objective of the proposed model is to estimate the temporal change in bubble length for non-reactive and reactive flows for later comparison with the MRI data. It is not the aim to provide a completely accurate description of the mass transport based on the real hydrodynamics around a Taylor bubble. The following assumptions and simplifications are made for the numerical solution:

- Shape approximation of the Taylor bubble as a cylinder of same length l_{tb} with mass transfer only taking place over the lateral surface area.
- The flow profile inside the liquid film is estimated as a plug flow with constant velocity v_{film} over the whole film thickness and along the bubble. Additionally, the horizontal velocity component of the flow in x-direction is zero ($u = 0$).

- The gases N_2 and O_2 are perfectly mixed within the bubble.
- In between the update intervals Δt, the concentration c_i and amount of substance n_i inside the bubble are constant. Thus, the film concentration reaches a steady state as soon as the film residence time τ_{film} (see Eqn. D.2) has been reached.
- The Fe^{II}(EDTA) concentration is assumed to remain constant along the film during the reaction.

Fig. 6.8 shows a schematic representation of the FDM model for calculating the two-dimensional concentration field inside the liquid film. The computation of the 2D concentration field relies on discrete mesh nodes inside the film region (Fig. 6.8 b)).

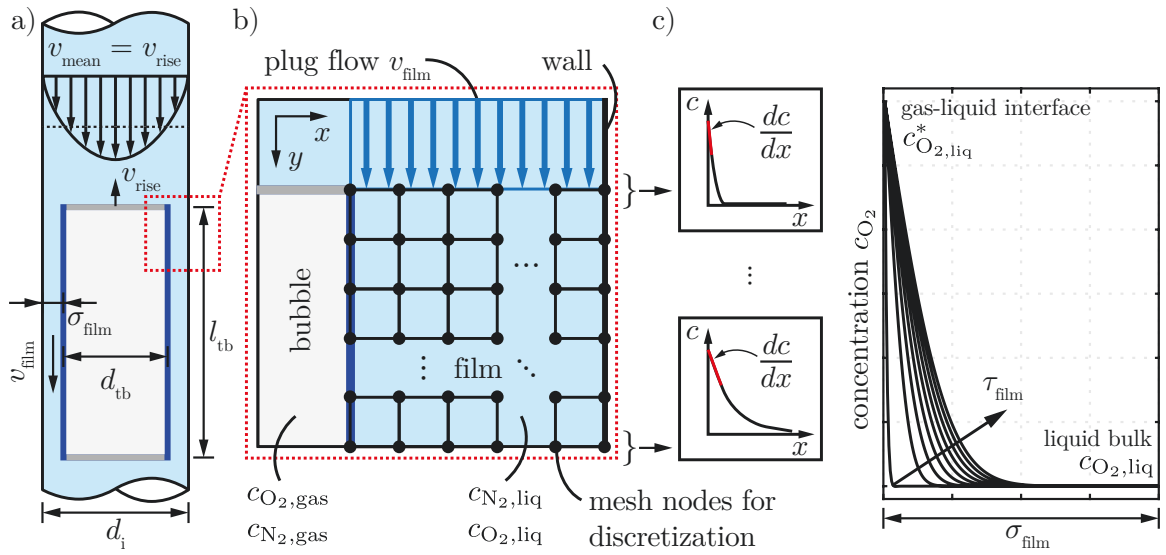

Fig. 6.8.: Schematic FDM model for calculating the 2D film concentration profile. The Taylor bubble's shape is approximated by a cylinder, with mass transfer only occurring over its lateral surface area a). Discrete mesh nodes inside the film are required for calculation using the finite difference method b). The quantity of transferred substance over time is calculated by computing the concentration gradients at the discrete mesh nodes along the phase boundary c). The transferred oxygen accumulates in the film in the absence of reactants, lowering the driving concentration gradient at the gas-liquid interface.

The steepest concentration gradient is found at the inlet of the liquid film, which corresponds to the front of the bubble. In the absence of reactants, the transferred oxygen species accumulates within the liquid film as it travels down the bubble, reducing the driving concentration gradient until it reaches the outlet of the liquid film at the bubble's rear. With increasing distance from the bubble's front and, correspondingly, a longer residence time τ, the driving concentration gradient decreases. The liquid film's τ dependent O_2 concentration profile is illustrated on the right in Fig. 6.8 c).

The mean concentration gradient inside the liquid film $\frac{dc_i}{dx}$ is determined along the phase boundary (y-direction) from the numerically calculated 2D concentration field. Knowing the

cylinder's lateral surface A_{film} over the entire film length and the diffusion coefficient D_i, the amount of substance n_i passing over the phase boundary after a defined time t can be calculated with Fick's first law of diffusion [105]:

$$\frac{dn_i}{dt} = -D_i \, A_{\text{film}} \frac{dc_i}{dx} \tag{6.7}$$

In the presence of an oxygen-consuming reaction, the concentration c_{O_2} is consequently reduced within the liquid phase, causing a steeper gradient $\frac{dc_{O_2}}{dx}$ and thus promoting O_2 mass transport out of the bubble.
The initial liquid phase concentrations of both gases at the interface and in the bulk are calculated identically to those used by the previously described two-film theory (see Sec. 6.2, Eqn. 6.5), listed in Tab. 6.1.

As indicated in Fig. 6.8, the liquid film region must be discretized to determine the mean liquid film concentration gradient along the bubble for mass transfer calculation with the numerical FDM method. Fig. 6.9 provides a more detailed visualization of the mesh discretization.

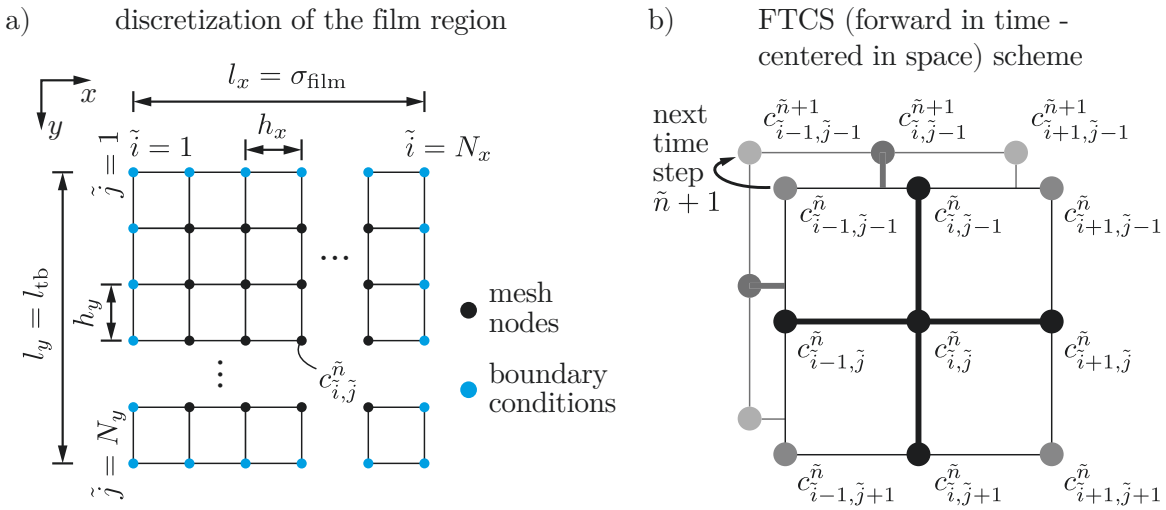

Fig. 6.9.: a) Illustration of the discretized domain with N_x and N_y nodes along both dimensions. The size of the domain is determined by the geometric conditions of the film region as $l_x = \sigma_{\text{film}}$ and $l_y = l_{\text{tb}}$. Node distance is calculated by h_x and h_y. Boundary conditions (indicated in blue) are assigned to the nodes around the domain's edges. b) Illustrated nodes of the FTCS scheme to numerically solve the given differential equation. The second-order centered calculation scheme relies on five known values at the actual time step $\tilde{n}$ to calculate the variable at the next time step $\tilde{n}+1$.

The spatial resolution and, thus, the accuracy of the discretization increases with a higher number of total mesh nodes N_x and N_y. The domain length l_x in x-direction is determined by the film thickness σ_{film}. In y-direction, the domain length l_y is defined by the bubble length l_{tb}.

The distances h_x and h_y between the nodes are constant in each direction and are calculated as:

$$h_x = \frac{l_x}{N_x - 1} \quad , \quad h_y = \frac{l_y}{N_y - 1} \tag{6.8}$$

Boundary conditions must be assigned to all the domain edges for a correct and stable solution.

Spatial control variables $\tilde{i}$ along x and $\tilde{j}$ along y, as well as a temporal control variable $\tilde{n}$ for each time step are defined for the discretization. The concentration $c_{\tilde{i},\tilde{j}}^{\tilde{n}}$ can now be calculated with respect to the control variables for the entire domain.

The two-dimensional concentration field inside the liquid film is described by a diffusion-advection-reaction partial differential equation (PDE):

$$\frac{\partial c}{\partial t} = \underbrace{D\left(\frac{\partial^2 c}{\partial x^2} + \frac{\partial^2 c}{\partial y^2}\right)}_{\text{diffusion}} \underbrace{-u\frac{\partial c}{\partial x} - v\frac{\partial c}{\partial y}}_{\text{advection}} \underbrace{+r}_{\text{reaction}} \tag{6.9}$$

A numerical solution of the proposed PDE is achieved by an explicit (forward) Euler scheme for temporal and a second-order centered spacing scheme for spatial discretization. The method is often called FTCS (forward in time, centered in space) in literature. The explicit Euler scheme enables the calculation of values at the next time step $\tilde{n}+1$ by using only known values from the actual time step $\tilde{n}$ (see Fig. 6.9 b)). [106, 107]

Discretization of the PDE (Eqn. 6.9)(formulations given by [107]: 1.3, 1.13, 5.18) results in the following mathematical formulation:

$$\begin{aligned}\frac{c_{\tilde{i},\tilde{j}}^{\tilde{n}+1} - c_{\tilde{i},\tilde{j}}^{\tilde{n}}}{\Delta t_{\text{step}}} = {} & \frac{D}{h_x^2}\left(c_{\tilde{i}+1,\tilde{j}}^{\tilde{n}} - 2c_{\tilde{i},\tilde{j}}^{\tilde{n}} + c_{\tilde{i}-1,\tilde{j}}^{\tilde{n}}\right) + \frac{D}{h_y^2}\left(c_{\tilde{i},\tilde{j}+1}^{\tilde{n}} - 2c_{\tilde{i},\tilde{j}}^{\tilde{n}} + c_{\tilde{i},\tilde{j}-1}^{\tilde{n}}\right) \\ & - \frac{u}{2h_x}\left(c_{\tilde{i}+1,\tilde{j}}^{\tilde{n}} - c_{\tilde{i}-1,\tilde{j}}^{\tilde{n}}\right) - \frac{v}{2h_y}\left(c_{\tilde{i},\tilde{j}+1}^{\tilde{n}} - c_{\tilde{i},\tilde{j}-1}^{\tilde{n}}\right) + r\end{aligned} \tag{6.10}$$

Rearranging yields the expression of the concentration for the next time step $\tilde{n}+1$:

$$\begin{aligned}c_{\tilde{i},\tilde{j}}^{\tilde{n}+1} = {} & c_{\tilde{i},\tilde{j}}^{\tilde{n}} + \frac{D\Delta t_{\text{step}}}{h_x^2}\left(c_{\tilde{i}+1,\tilde{j}}^{\tilde{n}} - 2c_{\tilde{i},\tilde{j}}^{\tilde{n}} + c_{\tilde{i}-1,\tilde{j}}^{\tilde{n}}\right) + \frac{D\Delta t_{\text{step}}}{h_y^2}\left(c_{\tilde{i},\tilde{j}+1}^{\tilde{n}} - 2c_{\tilde{i},\tilde{j}}^{\tilde{n}} + c_{\tilde{i},\tilde{j}-1}^{\tilde{n}}\right) \\ & - \frac{u\Delta t_{\text{step}}}{2h_x}\left(c_{\tilde{i}+1,\tilde{j}}^{\tilde{n}} - c_{\tilde{i}-1,\tilde{j}}^{\tilde{n}}\right) - \frac{v\Delta t_{\text{step}}}{2h_y}\left(c_{\tilde{i},\tilde{j}+1}^{\tilde{n}} - c_{\tilde{i},\tilde{j}-1}^{\tilde{n}}\right) + r\Delta t_{\text{step}}\end{aligned} \tag{6.11}$$

The reaction rate r is defined for a first-order reaction by the reaction rate constant k_r multiplied by the concentration c of oxygen if Fe^{II}(EDTA) is assumed to be constant. In the more general case, however, the utilized Fe^{II}(EDTA) to Fe^{III}(EDTA) oxidation reaction is first-order in oxygen and second-order in Fe^{II}(EDTA) [88] (see Sec. 3.4). Thus, the reaction rate is defined as:

$$r = -k_{12}\, c_{\mathrm{O_2}}\, c_{\mathrm{EDTA}}^2 = -k_{12}\, c_{\tilde{i},\tilde{j}}^{\tilde{\mathrm{n}}}\, c_{\mathrm{EDTA}}^2 \tag{6.12}$$

The temperature-dependent reaction rate constant is defined in the range of $298\,\mathrm{K} < T < 328\,\mathrm{K}$ as $k_{12} = 5.3 \times 10^3\, \mathrm{e}^{-4098/T} \mathrm{m}^6/(\mathrm{mol}^2\mathrm{s})$ [88]. Nitrogen undergoes no reaction inside the liquid phase. Consequently, the resulting reaction rate is $r = 0$.

Eqn. 6.11 can now be solved iteratively. To maintain stability during the calculation of the solution, the time step Δt_{step} must be chosen appropriately. The stability criteria for a 2D advection-diffusion equation solved by the FTCS method can be calculated by the von Neumann stability analysis. The solution for this exact problem was already investigated by Hindmarsh et al. [106]:

$$\begin{aligned} \Delta t_{\mathrm{step}} &\leq \frac{h_x^2 h_y^2}{2D\left(h_x^2 + h_y^2\right)} && \text{diffusion} \\ \Delta t_{\mathrm{step}} &\leq \frac{2D}{u^2 + v^2} && \text{convection} \end{aligned} \tag{6.13}$$

Numerical stability is retained by two factors that characterize the length of a single time step Δt_{step}. The first factor is the node distance h_x, h_y, which results from the overall domain resolution, defined by the number of mesh nodes N_x, N_y. The second factor are the velocity components u, v. Since there is no flow in the film direction (x-direction), u becomes zero. The film thickness specifies the flow velocity v along the bubble (see Eqn. D.3). Consequently, higher domain resolutions or higher flow velocities caused by thinner films result in a smaller Δt_{step} and thus increase the total number of calculation steps and computing time.

The smaller of both Δt_{step} values defines the stable time step used for the iterative calculation. Four values are calculated here because two different diffusion coefficients exist for O_2 and N_2. Δt_{step} is defined by the lowest of all four values multiplied by a factor of 0.95 to be on the safe side and maintain numerical stability.

Initial (I.C.) and boundary conditions (B.C.) for the calculation of the concentration field are required for the numerical solution and are defined in Eqn. 6.14. The domain is initialized at the time $t = 0$ by setting all of its values to the liquid phase concentration $c_{i,\mathrm{liq}}$ of the species i to be calculated. Fixed value boundary conditions (Dirichlet B.C.) are defined for the inlet and phase boundary of the domain. The capillary wall and outlet are set to zero gradient

boundary conditions (Neumann B.C.), which means that the flux at the boundaries is set to zero by adopting the calculated value from the previous spatial step close to the boundary.

$$
\begin{aligned}
&\text{I.C. domain:} && c_{i,\text{liq}} && \text{for} && c(x, y, t = 0) \\
&\text{B.C. film inlet:} && c_{i,\text{liq}} && \text{for} && c(x > 0, y = 0, t) \\
&\text{B.C. phase boundary:} && c_{i,\text{gas}} && \text{for} && c(x = 0, y, t) \\
&\text{B.C. film outlet:} && \left(\frac{\partial c_i}{\partial y} = 0\right) && \text{for} && c(x > 0, y = l_{\text{tb}}, t) \\
&\text{B.C. capillary wall:} && \left(\frac{\partial c_i}{\partial x} = 0\right) && \text{for} && c(x = l_{\text{film}}, y, t)
\end{aligned}
\tag{6.14}
$$

6.3.1 Results - FDM model

First, the impact of different numerical calculation parameters on the results must be examined. Critical factors are the grid resolution, defined by the number of mesh nodes N_x and N_y, as well as the update time Δt between the recalculations of the liquid film concentration profile.

A FDM calculation attempts to estimate the exact solution of a given problem numerically. Since no exact analytical solution for the examined partial differential equation (Eqn. 6.9) is given, it is challenging to assess the total accuracy of the calculated results obtained for different parameters. The problem presented here is relatively computationally intensive. The fact that the calculation steps build upon each other prevents parallelization. Thus, it is not possible to compute very fine grids or short update times in a reasonable amount of time. However, the influence of finer meshes and shorter update times can still be estimated by gradually halving the parameter of choice (e.g., results are calculated for $h, h/2, h/4, ...$ or $\Delta t, \Delta t/2, \Delta t/4, ...$) and looking at the maximum deviation between the refined calculations.

Here, the largest difference between two refinements is calculated by the maximum value of the absolute percentage error (similar to Eqn. 6.6):

$$
E_{\%,\text{max}} = \max \left| \frac{(l_{\text{tb},t}/l_{\text{tb},0})\text{refined}}{(l_{\text{tb},t}/l_{\text{tb},0})\text{initial}} - 1 \right| \times 100 \tag{6.15}
$$

In this equation, $(l_{\text{tb},t}/l_{\text{tb},0})\text{initial}$ refers to the initial solution, and $(l_{\text{tb},t}/l_{\text{tb},0})\text{refined}$ refers to the results computed with the refined parameter of choice. The calculated deviations between two computations are stated in the figures' legends below.

In the upcoming plots, the dashed line indicates the resulting length decrease calculated using the two-film theory combined with the penetration theory for the cylinder shape approximation in non-reactive systems (see Sec. 6.2). It is not reasonable to assess the overall accuracy between the FDM results and those based on the two-film and penetration theory, as both methods explain the investigated problem differently. Nevertheless, the results of both methods should approximately show a similar trend. Hence, the visualization is only provided to show the difference between the two approaches.

Unless otherwise stated, the upcoming results were calculated using: $l/d = 4.0$, $\sigma_{\text{film}} = 80\,\mu\text{m}$, $T = 298\,\text{K}$, $d_\text{i} = 6.0\,\text{mm}$, $v_{\text{rise}} = 5.3\,\text{mm}\,\text{s}^{-1}$, $D_{\text{O}_2} = 2.2 \times 10^{-9}\,\text{m}^2\,\text{s}^{-1}$, $D_{\text{N}_2} = 2.0 \times 10^{-9}\,\text{m}^2\,\text{s}^{-1}$.

First, the influence of the mesh resolution with uniform size ($N_x = N_y$) on the solution was investigated at a fixed update time step of $\Delta t = 100\,\text{s}$. Fig. 6.10 illustrates the results.

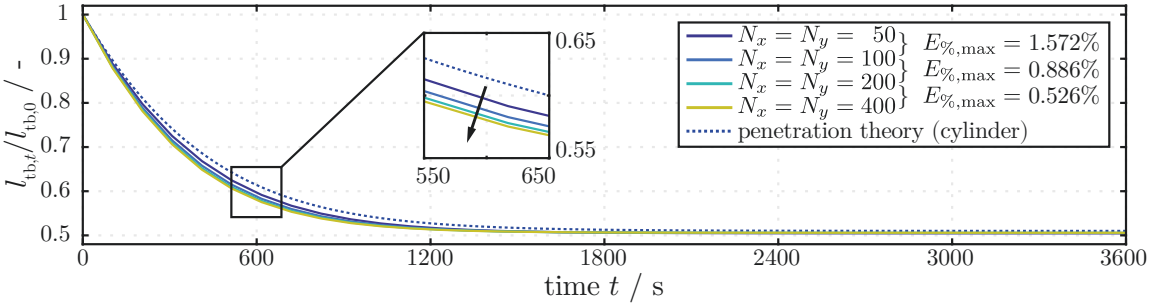

Fig. 6.10.: Influence of uniform mesh size refinement on the normalized bubble length varying over time at a fixed time step of $\Delta t = 100\,\text{s}$. Each refinement by a factor of two nearly halves the deviation between two subsequent computations.

The maximum percentage deviation decreases by slightly less than one-half for a twofold refinement of mesh resolution between the individual calculations. An increased slope is evident for finer meshes. It is mainly caused by the higher resolution in film direction and, thus, a better representation of the concentration gradient near the phase boundary. The calculation time was at least quadrupled in between the individual calculations.

Fig. 6.11 shows the effect of solely refining the mesh resolution N_y along the phase boundary of the Taylor bubble. With twice the resolution, the maximum percentage deviation decreases by slightly more than one-half, whereas the calculation time is almost doubled. The slope decreases slightly with finer mesh resolution, resulting from a more precise spatial representation of the concentration field along the phase boundary.

The impact of the update time Δt on the results was investigated at a fixed mesh resolution of $N_x = 200$ and $N_y = 400$ and is shown in Fig. 6.12. After doubling the temporal resolution, the maximum relative deviation between the respective calculations is reduced by more than $50\,\%$. A minor decrease in the slope is evident at higher temporal resolutions since the solution is

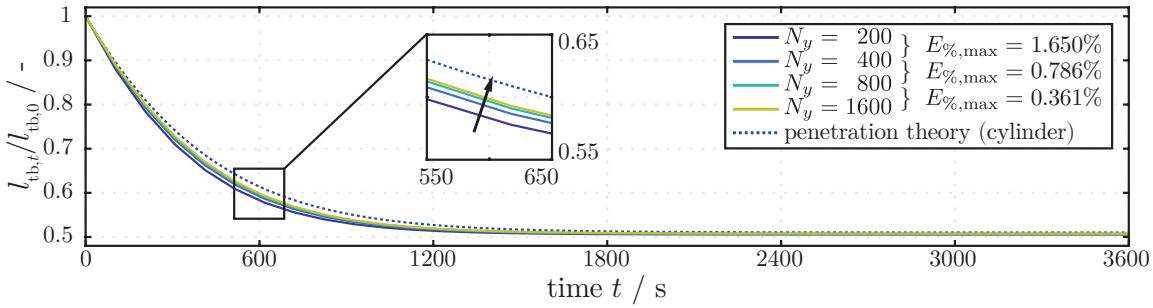

Fig. 6.11.: Influence of finer mesh resolution N_y at fixed $\Delta t = 100\,\mathrm{s}$ and $N_x = 200$ on the normalized bubble length varying over time. Each refinement by a factor of two reduces the deviation by more than $50\,\%$ between two subsequent calculations.

calculated more accurately for smaller Δt. Calculation time increases almost linearly with the number of time steps.

The results are of first-order accuracy for the mesh size h_x, h_y, and the update time Δt. As a result, doubling the respective parameter leads to an approximate halving of the deviation between the initial and refined calculation. Thus, the ideal solution would have a very fine mesh with a significantly higher number of nodes in y direction, ideally of uniform node spacing $h_x = h_y$, and a small update time Δt in the same order of magnitude as the film residence time τ_{film}.
As a compromise, the parameters had to be chosen such that the computing time remained within an acceptable range. Here, computing times below $24\,\mathrm{h}$ were considered tolerable. For this reason, a mesh resolution of $N_x = 200$ and $N_y = 400$ with an update time step of $\Delta t = 25\,\mathrm{s}$ was selected. It is to note that the total computation time is significantly influenced by the film thickness σ_{film}. Due to mass conservation, a thinner film consequently increases the flow velocity (see Eqn. D.3). To ensure numerical stability of the solution (see Eqn. 6.13), the iterative calculation time step Δt_{step} has to be reduced, which consequently increases the number of iterations and therefore also computation time.

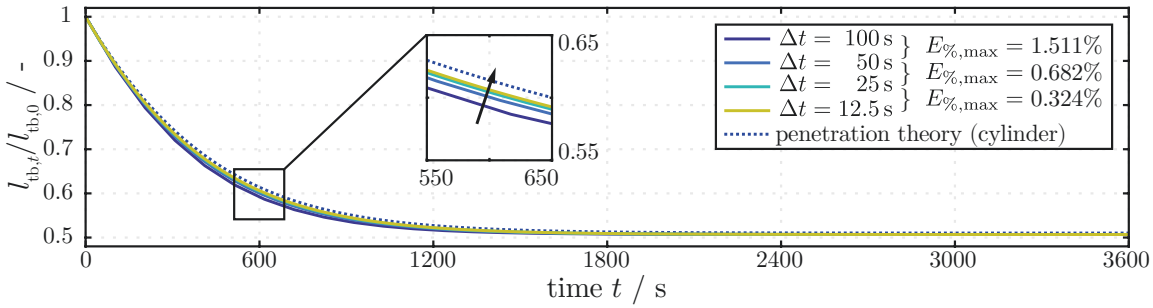

Fig. 6.12.: Effect of smaller time steps Δt on the results at a fixed mesh size of $N_x = 200$ and $N_y = 400$ nodes. Each Δt refinement by a factor of two reduces the maximum percentage deviation between two subsequent calculations by over $50\,\%$.

With the previously defined parameters for the FDM calculation, the effect of the Taylor bubble's l/d ratio on mass transfer was investigated and is shown in Fig. 6.13 a). The slope of the normalized bubble length flattens with increasing l/d ratio since the averaged mass transport decreases with longer bubbles. This observation agrees with the decreasing liquid side mass transfer coefficients k_L for larger l/d as calculated using the penetration theory illustrated in Fig. 6.2.

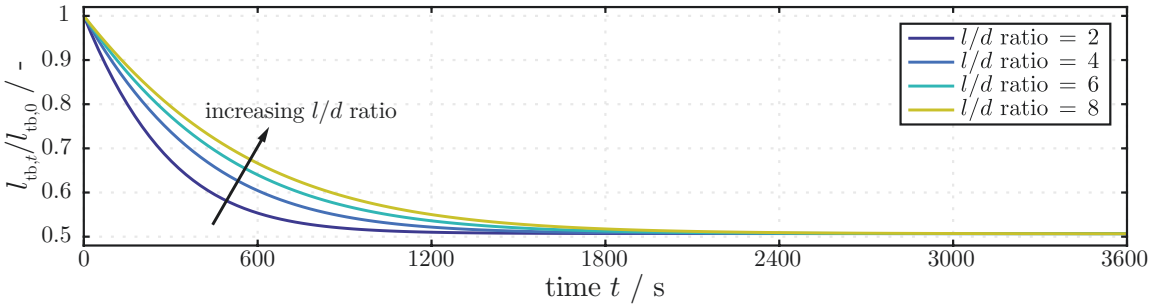

Fig. 6.13.: Influence of different l/d ratios on mass transfer expressed as normalized bubble length variation over time at a fixed mesh size of $N_x = 200$, $N_y = 400$ and an update time of $\Delta t = 25\,\mathrm{s}$.

In the presence of a superimposed chemical reaction, the Fe^{II}(EDTA) concentration plays an essential role regarding mass transfer. A higher reactant concentration results in a faster bubble length decrease as well as a shorter final bubble length, as indicated by Fig. 6.14. This behavior is attributed to the consumption of the transferred oxygen species by the dissolved Fe^{II}(EDTA). Consequently, mass transfer is promoted by a steeper concentration gradient along the phase boundary, which causes a faster temporal bubble length decrease as more oxygen is transferred. Since the reaction is second-order in Fe^{II}(EDTA) and first-order in O_2 [88], this effect is significantly pronounced with higher reactant concentration c_{EDTA} (see Eqn. 6.12). The reaction only marginally influences computation time.

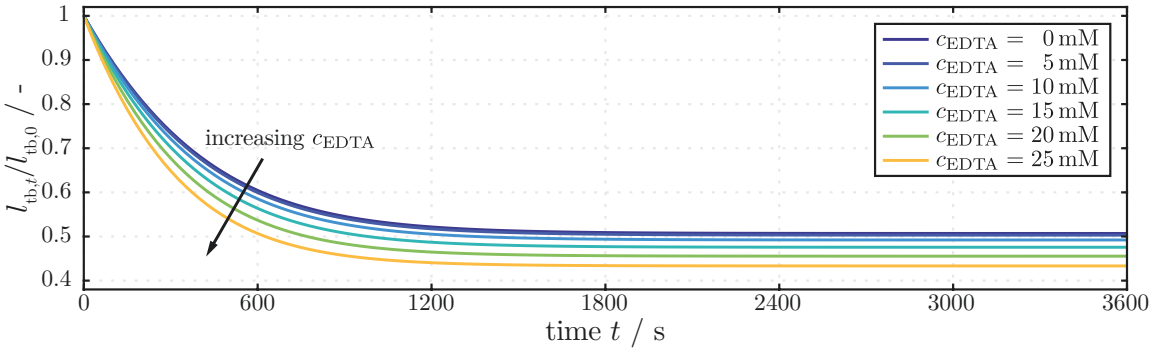

Fig. 6.14.: Influence of different c_{EDTA} concentrations on mass transfer of an $l/d = 4$ bubble at a fixed mesh size of $N_x = 200$, $N_y = 400$ and an update time of $\Delta t = 25\,\mathrm{s}$. Mass transfer is enhanced as the consumption of O_2 is promoted by higher Fe^{II}(EDTA) concentrations, which results in a steeper driving concentration gradient along the phase boundary.

Fig. 6.15 illustrates the film concentration profiles along an $l/d = 4$ bubble at the initial time step $t = 0\,\mathrm{s}$. The profile is shown as the percentage amount related to the initial O_2 concentration $c_{O_2} = 1.2193\,\mathrm{mol\,m^{-3}}$ at the gas-liquid interface and to the initial N_2 concentration $c_{N_2} = 0.6542\,\mathrm{mol\,m^{-3}}$ inside the liquid bulk (see Tab. 6.1). The concentration profiles of both gases were computed independently from each other. Oxygen diffuses from the bubble into the liquid phase, which is carried downstream by the flow and accumulates in the film along the phase boundary. Nitrogen, contrarily, diffuses from the liquid phase into the gas phase. Thus, the nitrogen concentration is depleted downstream close to the gas-liquid interface.

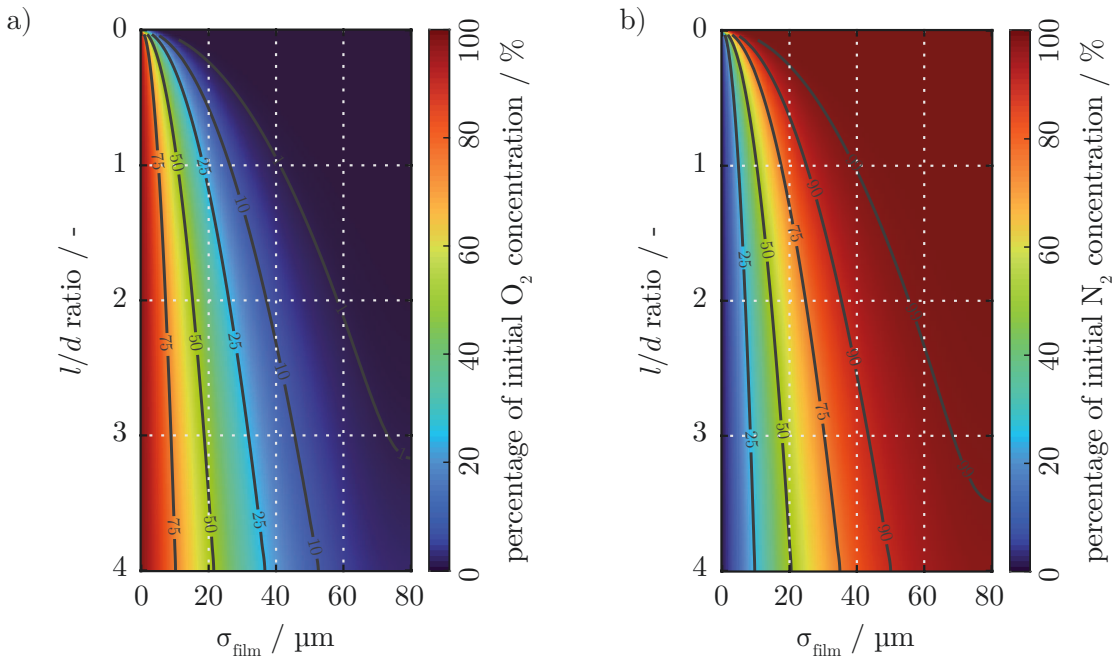

Fig. 6.15.: The liquid film concentration profiles along an $l/d = 4$ bubble at the first time step are illustrated as the enrichment of O_2 a) and depletion of N_2 b) inside the liquid film. The profiles are shown as the percentage amount related to the initial O_2 concentration at the interface a) and the initial N_2 concentration inside the liquid bulk b). The components are evaluated independently of one another. Initial concentrations are similar to those listed in Tab. 6.1.

When a chemical reaction is taking place, the consumption of oxygen will lower the local film concentration. Hence, the concentration profile will propagate less far into the film towards the capillary wall. The O_2 film concentration was computed for three distinct Fe^{II}(EDTA) concentrations to demonstrate the influence of the chemical reaction on the concentration profile.

Fig. 6.16 shows the absolute percentage deviation of the liquid film O_2 concentration between the reactive case at three different c_{EDTA}, related to the computed O_2 concentration field of pure mass transport.

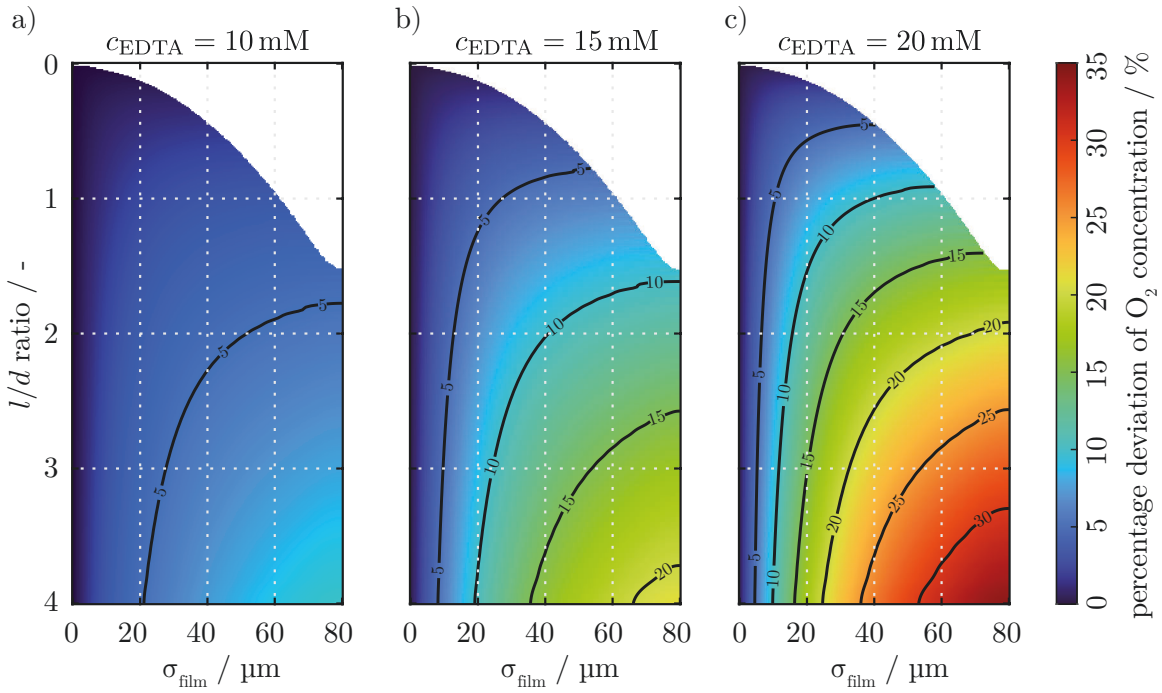

Fig. 6.16.: Calculated concentration profiles, showing the absolute percentage deviation of the liquid film O_2 concentration between the reactive and non-reactive case at three different c_{EDTA} concentrations a)-c). Computation was performed with an initial concentration of $c_{O_2} = 1.2193\,mol\,m^{-3}$ (see Tab. 6.1).

Here, all concentrations below $1 \times 10^{-4}\,mol\,m^{-3}$ have been masked to suppress noise from the numerical method in regions with no significant changes in concentration. The upper right corner is presented in white without a concentration profile since no oxygen could penetrate this area as advection from the flow overlays the diffusive transport towards the wall.

A step-wise increase of c_{EDTA} from $10\,mM$ (Fig. 6.16 a)) over $15\,mM$ (Fig. 6.16 b)) to $20\,mM$ (Fig. 6.16 c)) shows a significant growth of the absolute O_2 percentage deviation, compared to the non-reactive case. This strong increase between the steps can be explained by the quadratic influence of c_{EDTA} on the reaction rate r (see Eqn. 6.12).

The highest absolute percentage deviation is found in the lower right corner of all three concentration profiles. This position corresponds to the end of the bubble and the capillary wall, with a maximum distance from the phase boundary. The driving concentration gradient is lowest at this point, which means that the transport of fresh oxygen is most limited at this location. The reaction consumes the dissolved oxygen, which causes a higher absolute O_2 percentage deviation from the case of pure mass transport. It is evident that the reaction only partly consumes the dissolved oxygen at the three computed c_{EDTA} concentrations. Total consumption would be indicated by a $100\,\%$ deviation. A fast diffusive transport of dissolved oxygen is present near the gas-liquid interface, caused by the steep concentration gradient, which results in a rather low O_2 percentage deviation near the phase boundary.

6.4 Conclusion

A model for the characterization of mass transfer without and with a superimposed chemical reaction and the associated change in Taylor bubble length was successfully developed and examined within this chapter.

The shape of the Taylor bubble was first approximated as a cylinder of same length, with mass transfer solely taking place over the cylinder's lateral surface to simplify calculations and speed-up computation time. The penetration theory was applied to estimate how the cylinder shape approximation affects the mass transport compared to the Taylor bubble's geometry. The influence of the hemispherical bubble caps is most dominant for short bubbles. Hence, the strongest deviation of the liquid side mass transfer coefficient k_L between both shapes is found for small l/d.

In a subsequent step, the two-sided mass transport of O_2 and N_2 was modeled using the two-film theory, where only the liquid side mass transfer was investigated. Again, the penetration theory was employed to estimate the liquid side mass transfer coefficients k_L for both bubble shapes. With this method, the temporal change in bubble length could be calculated iteratively and gave an insight into how the l/d ratio or the diffusion coefficient influences mass transfer and the associated bubble length. Due to the two-sided mass transfer, the previously found k_L deviation at short bubbles largely cancels each other out.

Lastly, the effect of a superimposed chemical reaction on mass transport was examined. A numerical FDM method was used to solve the given differential equation of the diffusion-advection-reaction problem. In order to assess the model's accuracy, the impact of various numerical computation parameters, mainly the number of mesh nodes (N_x, N_y) and the update time (Δt), on the results were examined. After that, different influences on the computed concentration field within the film, including l/d, c_{EDTA}, and the flow profile, were successfully analyzed.

As a result, a model is provided to compare the change in bubble length observed by MRI in non-reactive and reactive Taylor flows.

7 MRI of reactive Taylor flows

The findings from the reactive and non-reactive Taylor flow experiments are discussed in this section. Measurements were performed using the optimized flow setup (see Sec. 3.1.2) and the improved birdcage resonator (see Sec. 3.2.2 and Chap. 5). Data interpretation is aided by the implemented FTCS algorithm (see Sec. 6.3).

Initially, non-reactive experiments were conducted with O_2 Taylor bubbles in N_2 saturated ultrapure water. The findings were used to describe pure mass transfer by the related decrease in bubble length. Experiments were repeated with varied Fe^{II}(EDTA) concentrations inside the liquid phase. Here, steeper O_2 concentration gradients near the gas-liquid interface resulted from the consumption of the transferred oxygen species by the oxidation reaction, which promoted mass transfer. The obtained MRI data were then compared to computations of the developed FDM mass transfer model. The model's results were discussed regarding the correctness of the chosen liquid film thickness. Additionally, MRI inversion recovery measurements visualized the reaction product, and the time-dependent signal decrease of the product could be shown.

7.1 Temporal Taylor bubble length decrease by two-sided mass transfer - non-reactive case

Pure O_2 Taylor bubbles were held in a countercurrent flow of N_2 saturated ultrapure water to determine the temporal length reduction caused by mass transport without superimposed chemical reaction. Each individual bubble was measured over an extended period until a quasi-stationary bubble length was obtained. Here, this condition was met after about half an hour.

Fig. 7.1 illustrates the resulting MRI images of two Taylor bubbles with different l/d ratios. A snapshot FLASH sequence without inversion recovery was employed for data acquisition. 600 images were continuously recorded with a $3\,\mathrm{s}$ time delay between each image. Here, the resulting bubble lengths are shown in three-minute increments. A fourfold bicubic interpolation was applied to refine the MRI Images for automatic intensity-based cap detection. All images were shifted to the same position regarding their detected front cap position.

The length decrease is fastest at the beginning and reduces over time until almost no change occurs. This effect is caused by both components' decreasing concentration gradients at the

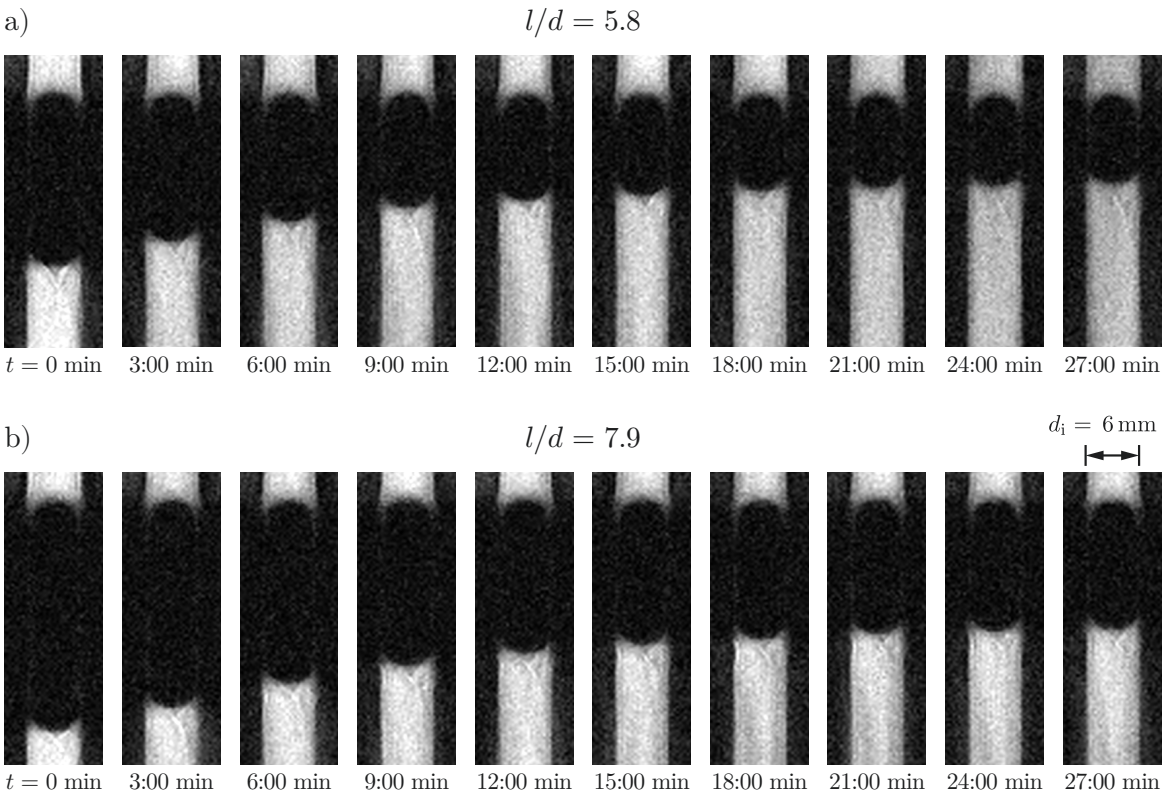

Fig. 7.1.: MRI time series of two single O_2 bubbles measured over approximately 30 minutes with a) $l/d = 5.8$ and b) $l/d = 7.9$. The shown images were enhanced by a bicubic interpolation with a factor of 4 to obtain a more precise shifting regarding their front cap position. MRI sequence parameters: inversion recovery off, spatial resolution $= (0.3125 \times 0.3125)\,\mathrm{mm}$, slice thickness $= 2.5\,\mathrm{mm}$, $TE = 0.71\,\mathrm{ms}$, $TR = 1.612\,\mathrm{ms}$, flip angle $\alpha = 24°$, scan repetition time $= 3000\,\mathrm{ms}$

gas-liquid interface during the experiment. A maximum concentration gradient between the gas and liquid phase in terms of O_2 and N_2 is present at $t = 0\,\mathrm{min}$. The mole fraction of oxygen inside the bubble lowers over time as nitrogen enters from the liquid phase due to two-sided mass transfer and dilutes the initially pure O_2 bubble. At the same time, the mole fraction of nitrogen inside the bubble rises. As a result, the driving concentration gradient between both phases lowers, and thus, the temporal length reduction of the Taylor bubble declines until reaching a quasi-stationary state.

It strikes for both cases of $l/d = 5.8$ (Fig. 7.1 a)) and $l/d = 7.9$ (Fig. 7.1 b)) that the bubble length has approximately halved over the course of half an hour. This behavior is explained by the nearly two-fold solubility difference between both gases (see Tab. D.2) and the resulting concentration gradients. Since diffusion coefficients of both components exhibit approximately the same magnitude (see Tab. 7.1), about twice as much oxygen can be released from the bubble as nitrogen can enter.

The averaged signal intensity at a defined distance from the front and back cap of the bubble fluctuates in a range of about $\pm 10\,\%$ and does not correlate with time. Intensity fluctuations are most likely related to the horizontal bubble movement and the resulting position inside the setup. The signal strength around the caps changes with bubble position due to minor B_1 inhomogeneities of the resonator (see Sec. 3.2.2, Fig. 3.12). A flow-related structure is barely visible inside the wake of both Taylor bubbles with different l/d ratios. This structure is explained by the inflow of spins from outside the measurement plane during data readout, similar to the developed method for MRI flow characterization explained in Chap. 4.

The mass transfer-related temporal length decrease shown in Fig. 7.1 was used as a reference to manually fit the FDM-based mass transfer model (see Sec. 6.3) by a step-wise adjustment of the liquid film thickness σ_{film}. The experimental and FDM discretization parameters used for the computation are listed in Tab. 7.1. The selected FDM parameters are discussed in detail in Sec. 6.3.

Tab. 7.1.: FDM discretization and experimental parameters for computation of the temporal bubble length reduction using the FDM-based model.

FDM discretization parameters	
number of nodes in film direction	$N_x = 200$
number of nodes along the bubble	$N_y = 400$
time step between recalculations	$\Delta t = 25\,\text{s}$
experimental parameters	
temperature	$T = 298\,\text{K}$
capillary diameter	$d_\text{i} = 6.0\,\text{mm}$
fluid velocity	$v_\text{rise} = 5.3\,\text{mm}\,\text{s}^{-1}$
diffusivity of O_2 in water	$D_{O_2} = 2.2 \times 10^{-9}\,\text{m}^2\,\text{s}^{-1}$
diffusivity of N_2 in water	$D_{N_2} = 2.0 \times 10^{-9}\,\text{m}^2\,\text{s}^{-1}$

Since literature specifies the diffusion coefficients of oxygen in water at $T = 298\,\text{K}$ in a range from $1.9 \times 10^{-9}\,\text{m}^2\,\text{s}^{-1}$ to $2.3 \times 10^{-9}\,\text{m}^2\,\text{s}^{-1}$ [104], different values were tested.
A higher oxygen diffusivity reduces the final bubble length at the quasi-stationary state, which has previously been shown by calculations using the two-film theory in Sec. 6.2, Fig. 6.7. Regarding the terminal bubble length, the best agreement between calculations and experiments was obtained with $D_{O_2} = 2.2 \times 10^{-9}\,\text{m}^2\,\text{s}^{-1}$.

The best fit between the experimental MRI data and the FDM calculations was achieved at a film thickness of $\sigma_{\text{film}} = 80\,\mu\text{m}$ (see Fig. 7.3). The method for determining the matching film thickness and its validity are discussed in detail in Sec. 7.1.1 and Sec. 7.1.2 following after the upcoming results.

Fig. 7.2 compares the temporal length decrease of the MRI data and the calculated results from the FDM model for $l/d = 5.8$ and $l/d = 7.9$. Results were computed with $\sigma_{\text{film}} = 80\,\mu\text{m}$. The experimental MRI data points correspond to the previously demonstrated measurements of temporal length decrease shown in Fig. 7.1. A good agreement between the experiments and simulation results is observed, with only the l/d ratio being adjusted to match the experiments.

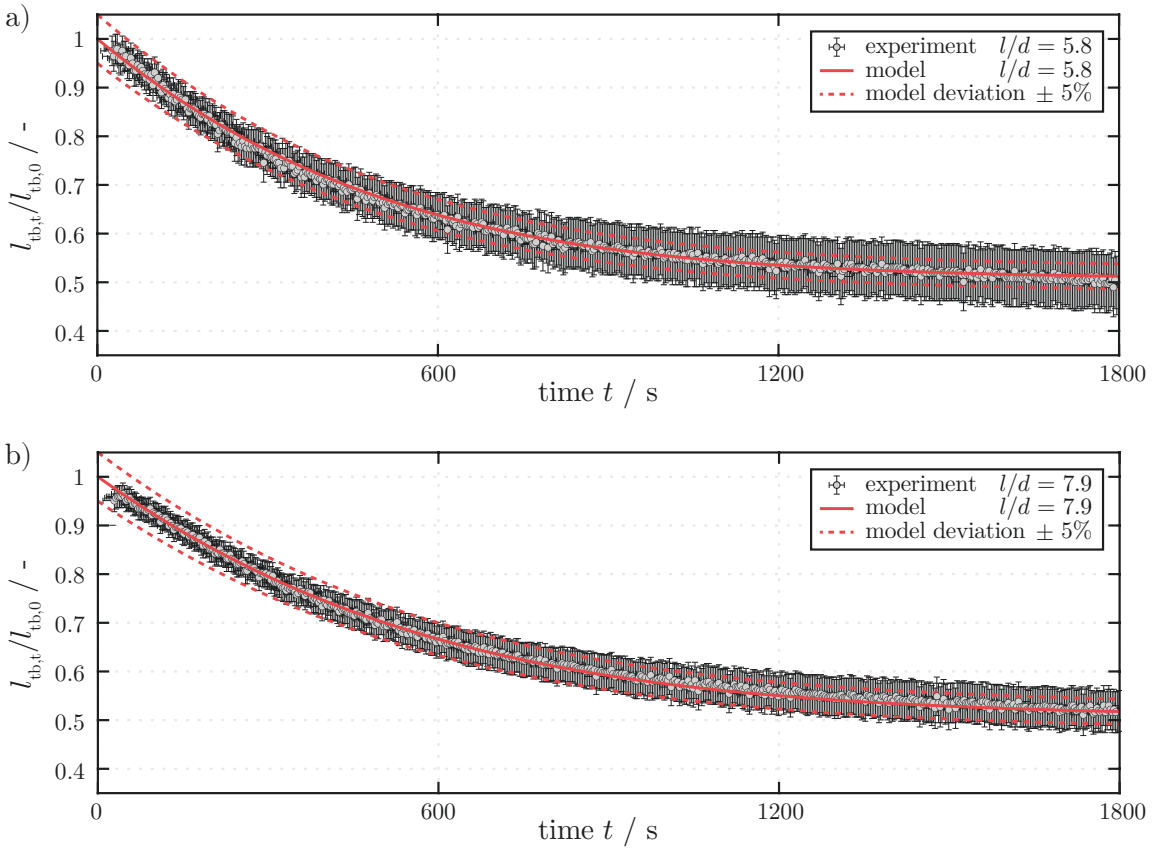

Fig. 7.2.: Comparison of MRI data and calculated results of normalized bubble length decrease over time. Two Taylor bubbles with a) $l/d = 5.8$ and b) $l/d = 7.9$ were measured over the course of $30\,\text{min}$ (see Fig. 7.1). $\sigma_{\text{film}} = 80\,\mu\text{m}$ and $D_{\text{O}_2} = 2.2 \times 10^{-9}\,\text{m}^2\,\text{s}^{-1}$ resulted in the best fit of the model.

The indicated error in normalized bubble length is related to the low resolution of the MR images and the automatic cap detection algorithm. Threshold-based edge detection is applied based on the high contrast between the bubble and the surrounding liquid. A fourfold bicubic interpolation of the MRI data allows for sub-voxel detection and helps to smooth out the length detection. Nevertheless, inaccuracies of ± 4 sub-voxels or ± 1 actual voxel per cap may occur, especially in the case of unavoidable bubble movement. The error sums up for both caps to ± 8 sub-voxels or ± 2 actual voxels, which corresponds to $0.625\,\text{mm}$. Therefore, the error in detected bubble length is less significant at larger l/d ratios and increases during the experiment as the bubble shrinks. It stays below $3\,\%$ at $l/d = 7.9$ and below $4\,\%$ at $l/d = 5.8$.

The temporal error is caused by the way experiments were conducted. A short time will elapse between bubble generation ($t = 0\,\mathrm{s}$), position adjustment inside the flow setup, and the subsequent start of the MRI data acquisition. This error of arbitrary size is considered by a deviation of the actual time step by $\pm 20\,\mathrm{s}$.

7.1.1 Determination of the liquid film thickness to fit the FDM model to the MRI data

X-ray tomography experiments by Haghnegahdar et al. [99] demonstrated a liquid film thickness for stationary CO_2 Taylor bubbles in water inside a circular $d_\mathrm{i} = 6.0\,\mathrm{mm}$ capillary of approximately $130\,\mu\mathrm{m}$ for $l/d > 2.3$. Since MRI cannot resolve the film region, an initial film thickness of $130\,\mu\mathrm{m}$ was chosen for the FDM calculations, which was subsequently reduced down to $70\,\mu\mathrm{m}$ in $10\,\mu\mathrm{m}$ steps. Fig. 7.3 a) shows the resulting temporal length reductions at different film thicknesses, compared to the experimental data of a $l/d = 5.8$ Taylor bubble (see Fig. 7.1 a) and Fig. 7.2 a)). The coefficient of determination R^2 was calculated for each film thickness to identify the best fit between the model and the experimental MRI data. Fig. 7.3 b) plots the calculated R^2 values over the various σ_film of the computed results. The best fit between the MRI experiments and FDM calculations is achieved for $\sigma_\mathrm{film} = 80\,\mu\mathrm{m}$ with $R^2 = 0.9963$.

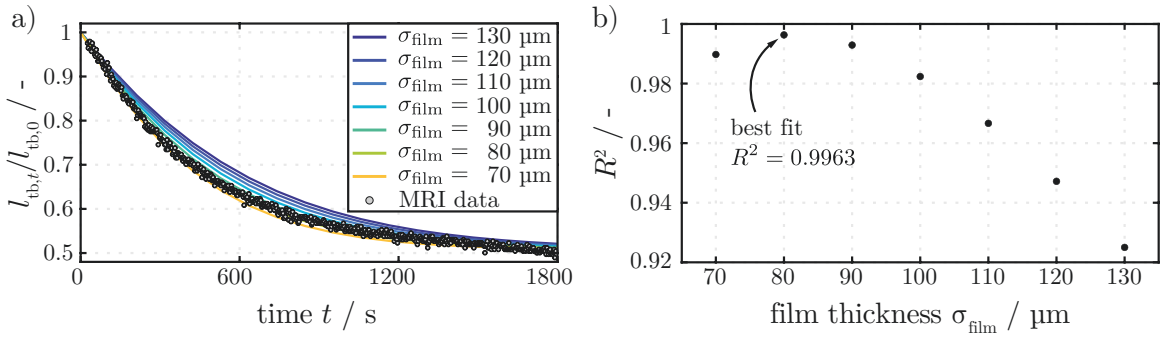

Fig. 7.3.: a) Plots of the temporal reduction in normalized bubble length computed with varying film thicknesses are compared to the MRI data of a $l/d = 5.8$ Taylor bubble (see Fig. 7.1 a)). b) Plotting the calculated coefficient of determination R^2 between the model and the MRI data over different film thicknesses reveals the best fit at $\sigma_\mathrm{film} = 80\,\mu\mathrm{m}$ with $R^2 = 0.9963$. Discretization parameters: $N_x = 200$, $N_y = 400$, $\Delta t = 100\,\mathrm{s}$

Experimental investigations of Taylor bubbles under similar hydrodynamic flow conditions were conducted by Haghnegahdar et al. [99] using X-ray tomography, where a film thickness of approximately $\sigma_\mathrm{film} = 130\,\mu\mathrm{m}$ was determined from the extracted contour of the bubble interface. The best agreement between the proposed numerical model and the MRI results shown here, however, was found to be at $\sigma_\mathrm{film} = 80\,\mu\mathrm{m}$ as demonstrated in Fig. 7.3.

This discrepancy in film thickness is explained by the deviation caused by the assumption of the liquid film velocity as a plug flow profile. This assumption was made to achieve a constant residence time τ_{film} over the entire film region, enabling faster computation of the complete 2D concentration field.

7.1.2 Effect of the plug flow approximation inside the liquid film on the computed FDM results

In the following, the effect of the plug flow approximation on film thickness is investigated. Therefore, the numerical code was adapted to a more realistic approach by computing the concentration profile using one-half of a parabolic velocity profile instead of a plug flow along the film to quantify the influence of this film velocity approximation. The velocity of the parabolic profile v_{p} is defined along the film in x-direction between the phase boundary $x = 0$ and the capillary wall $x = \sigma_{\text{film}}$ as:

$$v_{\text{p}}(x) = 2\, v_{\text{film}} \left(1 - \left(\frac{\sigma_{\text{film}}}{x} \right)^2 \right) \quad \text{for} \quad 0 \leq x \leq \sigma_{\text{film}} \tag{7.1}$$

A minimum velocity of zero exists at the capillary wall and a maximum of $2\, v_{\text{film}}$ is present at the gas-liquid interface. To correctly determine the concentration profile inside the liquid film, the liquid phase has to pass the complete domain (all discrete mesh nodes) along y-direction during computation. For this, the residence time of the computation τ_{compute} must be set to the lowest film velocity > 0, which equals the velocity one position before the capillary wall. As a result, computation times will rise unreasonably.

The influence of the ratio between τ_{compute} / τ_{film} on the parabolic flow profile and the plug flow is illustrated in Fig. 7.4 a). A logarithmic plot of the ratio over the dimensionless film thickness was chosen for computations using $N_x = 200$ mesh nodes in film direction. Here, the residence time of the plug flow τ_{film} is selected as the reference value. As correctly assumed for the plug flow, a constant ratio is observed, independent of the dimensionless film position, meaning that all fluid has passed the domain simultaneously after $\tau_{\text{compute}} = \tau_{\text{film}}$.

However, this is different for the parabolic profile. After the same residence time ratio of $\tau_{\text{compute}} = \tau_{\text{film}}$, just over $70\,\%$ of the fluid has passed the entire domain. Due to its lower flow velocity, the remaining fluid was not fully calculated up to the outlet. As a result, the calculated concentration profile is incomplete. The resulting deviation from a complete calculation becomes smaller with longer residence times. Here, the $N_x = 200$ mesh nodes would require a fifty times longer computational residence time for complete calculation, which will also increase the computation time by the same factor.
A compromise was made by using a residence time of $\tau_{\text{compute}} = 2\, \tau_{\text{film}}$ after which about $86\,\%$

of the liquid passed the entire domain during computation. The remaining $14\,\%$ are located towards the capillary wall with little to no significant impact on the calculated concentration profile, especially with larger film thicknesses, as the relevant mass transfer occurs near the gas-liquid interface.

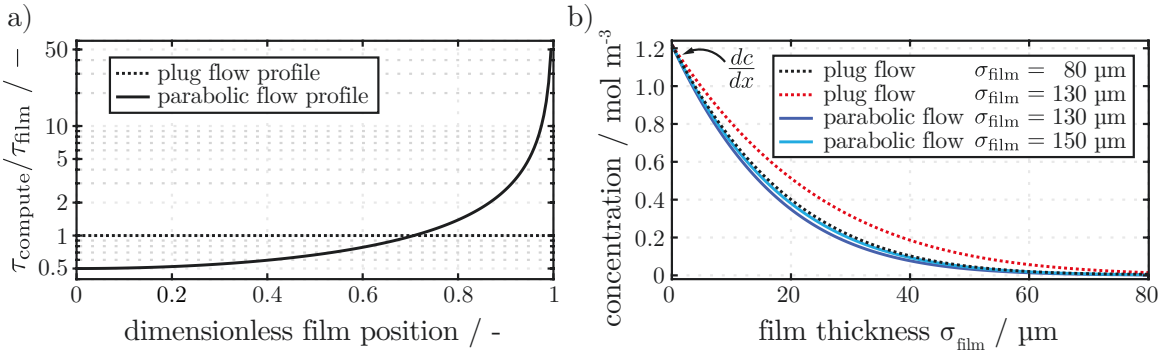

Fig. 7.4.: a) Residence time ratio along the dimensionless film position for the plug flow and parabolic flow profile. The manually defined residence time of the computation $\tau_{compute}$ is referenced to the residence time of the plug flow τ_{film}. b) Mean oxygen film concentrations inside the liquid film, compared for both flow profiles at different film thicknesses σ_{film}. Computation was performed with an initial concentration of $c_{O_2} = 1.2193\,\mathrm{mol\,m^{-3}}$ (see Tab. 6.1).

Fig. 7.4 b) compares the mean oxygen concentration profiles inside the film after the first full computation step of the 2D concentration field. The mean value was calculated along the bubble over the entire y-direction. Because of the changes in the flow profiles between the plug flow and the parabolic flow, the mean concentration profiles follow a slightly different trend. These differences, however, are too small to be seen here. The slope near the phase boundary is critical since it defines the driving concentration gradient dc/dx for mass transfer calculations (see Eqn. 6.7). A dc/dx difference of less than $8\,\%$ is achieved between the plug flow with $\sigma_{film} = 80\,\mu\mathrm{m}$ and the parabolic flow profile with $\sigma_{film} = 130\,\mu\mathrm{m}$ close to the gas-liquid interface. When the liquid film thickness for the parabolic flow profile increases to $\sigma_{film} = 150\,\mu\mathrm{m}$, the dc/dx deviation from the plug flow with $\sigma_{film} = 80\,\mu\mathrm{m}$ is further reduced to under $1\,\%$.

The effect of the two flow profiles on the calculated film thickness was demonstrated. As a result, an actual film thickness for the experimental investigations in the range of $\sigma_{film} = 130\,\mu\mathrm{m}$ to $150\,\mu\mathrm{m}$ can be assumed here, which is in good agreement to the $\sigma_{film} = 130\,\mu\mathrm{m}$ demonstrated by Haghnegahdar et al. [99].

7.2 Temporal Taylor bubble length decrease by two-sided mass transfer - superimposed chemical reaction

In this experimental study, Fe^{II}(EDTA) solutions of different concentrations were prepared according to the method described in the appendix (see App. A). The reactive Fe^{II}(EDTA) solutions were used as a liquid phase to study the temporal length reduction caused by mass transport with superimposed chemical reaction. Apart from the added iron complex, experimental conditions were chosen identical to those described in the previous section dealing with non-reactive two-sided mass transport (see Sec. 7.1). First, the process of employing the inversion recovery approach is explained in more detail in order to better understand the resulting data.

7.2.1 Inversion recovery method for reactant signal suppression

The MRI experiments shown here take advantage of the inversion recovery setting of the snapshot FLASH sequence to cancel out the signal of the unreacted Fe^{II}(EDTA) solution. A precise adjustment of the inversion time TI for the superimposed chemical reaction experiments is necessary to simultaneously visualize the reaction product and obtain spatial information of the bubble cap positions as both caps are only visible due to the contrast between the surrounding liquid and the gas phase.

The oxidation of Fe^{II}(EDTA) forms Fe^{III}(EDTA), which has a significantly lower T_1 relaxation time and thus contributes differently to the detectable MR signal. The inversion time TI is directly related to the T_1 relaxation time of the investigated substance (see Eqn. 2.10) as $TI = 0.6931 \times T_1$. For this reason, T_1 and, consequently, TI of the liquid phase are reduced with increasing Fe^{II}(EDTA) concentration and vary between different experiments. The inversion time of the Fe^{II}(EDTA) solution is determined by a series of single images with successively increased TI values.

The best approximation of TI is found when the entire liquid phase signal of the unreacted Fe^{II}(EDTA) is suppressed so that the measured signal intensity is only dominated by noise. This state is referred to as TI_{zero} in the following. Fig. 7.5 illustrates the results of inversion time determination inside a $10\,\text{mM}$ Fe^{II}(EDTA) solution. The corresponding values are listed in Tab. 7.2.

The flow setup was rinsed with fresh reactant and flow was switched off right before acquiring the TI images shown in Fig. 7.5 b). A signal decrease is evident in the MRI intensity images during the subsequent increase of TI in steps of $50\,\text{ms}$. The lowest signal is found at $TI_{\text{zero}} = 250\,\text{ms}$ after which intensity is regained for increasing TI. This behavior becomes

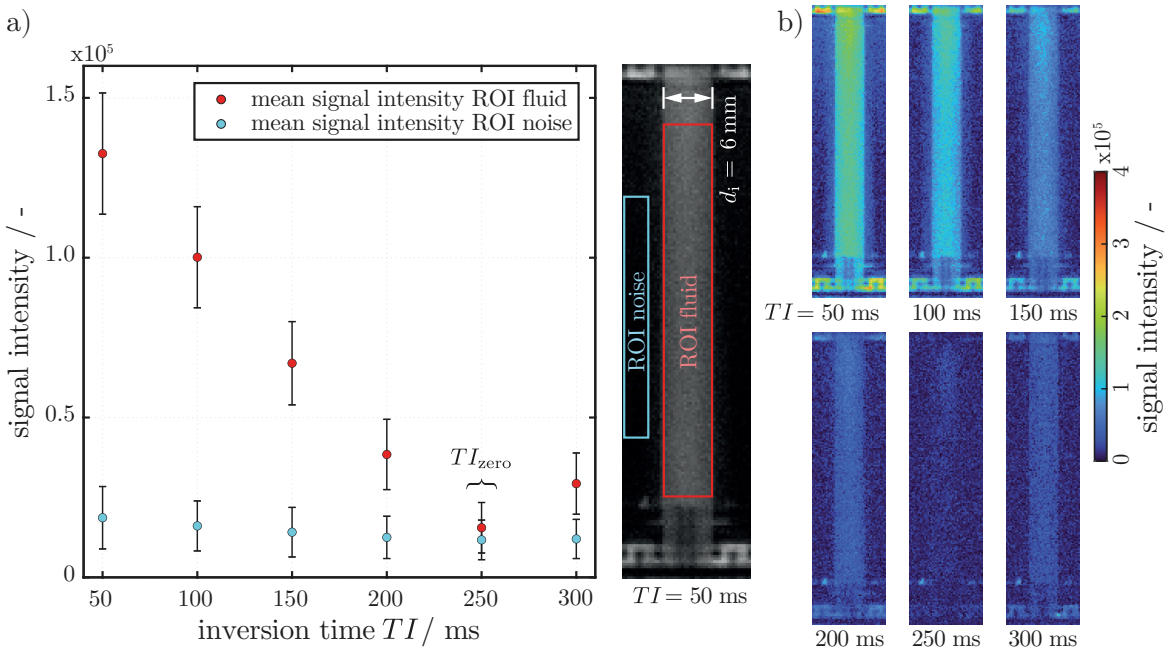

Fig. 7.5.: Inversion time determination by the gradual increment of TI. a) The mean signal intensities of two ROIs are plotted for each MRI image acquired at different TI. The inversion time of the substance TI_{zero} is found where the mean fluid signal intensity equals the mean noise signal intensity, indicating that the reactant's signal is fully suppressed. The corresponding MRI images are shown in b). Calculated values are listed in Tab. 7.2.

even more evident when comparing the average signal intensity to the average noise level of two defined ROIs at different inversion times as listed in Tab. 7.2. The standard deviation relates to all values inside the respective ROI of a single image. The mean signal intensity decreases almost linearly inside the capillary until reaching its minimum at $TI_{zero} = 250\,\mathrm{ms}$. The noise level is slightly amplified near the capillary in the presence of stronger liquid phase signal intensities which is also visible in the MRI intensity images. This signal increase in the noise region is caused by the narrow field of view and the proximity of the noise ROI to the specimen. A constant noise level is expected at a greater distance from the capillary. The mean intensities inside and outside the capillary resemble each other at $TI_{zero} = 250\,\mathrm{ms}$ resulting in a low SNR of 1.7 ± 1.2. Error propagation was used to account for the standard deviation of both ROIs in the SNR calculation.

With the previously determined TI_{zero}, experiments could now be conducted to visualize the formation and distribution of the reaction product inside the wake of a Taylor bubble with maximum contrast. However, the inversion time is set to a slightly larger value for practical reasons. Still, sufficient contrast between the product and unreacted solution is obtained while additional information about the spatial position of both bubble caps can be retrieved. The cap positions provide valuable information about the temporal decrease in bubble length, which is needed to compare the results with the proposed mass transfer model.

Tab. 7.2.: Signal intensities at different TI for $10\,\mathrm{mM}$ Fe^{II}(EDTA) as illustrated in Fig. 7.5.

inversion time TI	mean signal intensity	mean noise intensity	SNR
$50\,\mathrm{ms}$	$(1.326 \pm 0.190) \times 10^5$	$(0.186 \pm 0.098) \times 10^5$	8.9 ± 4.8
$100\,\mathrm{ms}$	$(1.001 \pm 0.158) \times 10^5$	$(0.161 \pm 0.078) \times 10^5$	7.8 ± 4.0
$150\,\mathrm{ms}$	$(0.670 \pm 0.130) \times 10^5$	$(0.141 \pm 0.078) \times 10^5$	5.9 ± 3.5
$200\,\mathrm{ms}$	$(0.384 \pm 0.110) \times 10^5$	$(0.125 \pm 0.066) \times 10^5$	3.9 ± 2.3
$250\,\mathrm{ms}$ (TI_{zero})	$(0.155 \pm 0.079) \times 10^5$	$(0.117 \pm 0.062) \times 10^5$	1.7 ± 1.2
$300\,\mathrm{ms}$	$(0.293 \pm 0.096) \times 10^5$	$(0.120 \pm 0.061) \times 10^5$	3.1 ± 1.9

Since Fe^{II}(EDTA) is extremely sensitive regarding oxygen, it may happen that the Fe^{II}(EDTA) solution will react with traces of air inside the supply vessel during prolonged measurements, even though it is constantly purged with nitrogen. As a result, the inversion time is reduced by possible trace amounts of formed Fe^{III}(EDTA). By choosing a longer initial $TI > TI_{\mathrm{zero}}$, zero crossing of the signal intensity is avoided, and consequently, no signal cancellations occur, which could lead to misinterpretation of the data.

The MRI images for TI determination reveal a slight vertical intensity gradient along the capillary caused by minor magnetic field strength variations inside the resonator. The gradient is visible when looking at the mean signal intensity over the capillary diameter along the y-axis. This effect is shown in Fig. 7.6. The vertical dashed lines in Fig. 7.6 b) show the mean signal of the entire fluid ROI for different TI. The curves represent the in x-direction averaged signal intensities along the capillaries y-axis. Standard deviations are not shown for better readability. The normalized signal intensity is obtained by dividing the averaged local intensity along y by the mean intensity value of the complete ROI and is shown in Fig. 7.6 c).

The effect of a local intensity increase in the upper quarter of the ROI is more pronounced at higher signal intensities. In the range of $TI_{\mathrm{zero}} = 250\,\mathrm{ms} \pm 50\,\mathrm{ms}$ the signal intensities are rather low and noise fluctuations hide the effect. Thus, the influence is negligible if a TI close to the TI_{zero} is selected. For this reason, the three TI values with the largest difference from TI_{zero} were selected to quantify the intensity deviation along y-direction. A third-order polynomial fit well represented the local normalized intensity change. The fitted function indicates a decrease in normalized signal intensity of about $5\,\%$ in the lower half of the capillary, which corresponds to the position of the wake. The maximum increase of approximately $18\,\%$ at the inlet is only valid in case TI is far off TI_{zero}. This valuable information can be extracted from the respective set of TI measurements for each experiment. It could aid in correctly quantifying reaction products, especially when comparing the signal intensities in front of the bubble to those inside the wake region.
During the experiments, the bubble's wake is positioned arbitrarily inside the lower half of the ROI, in which the intensity deviations are relatively small. However, the change in y-position

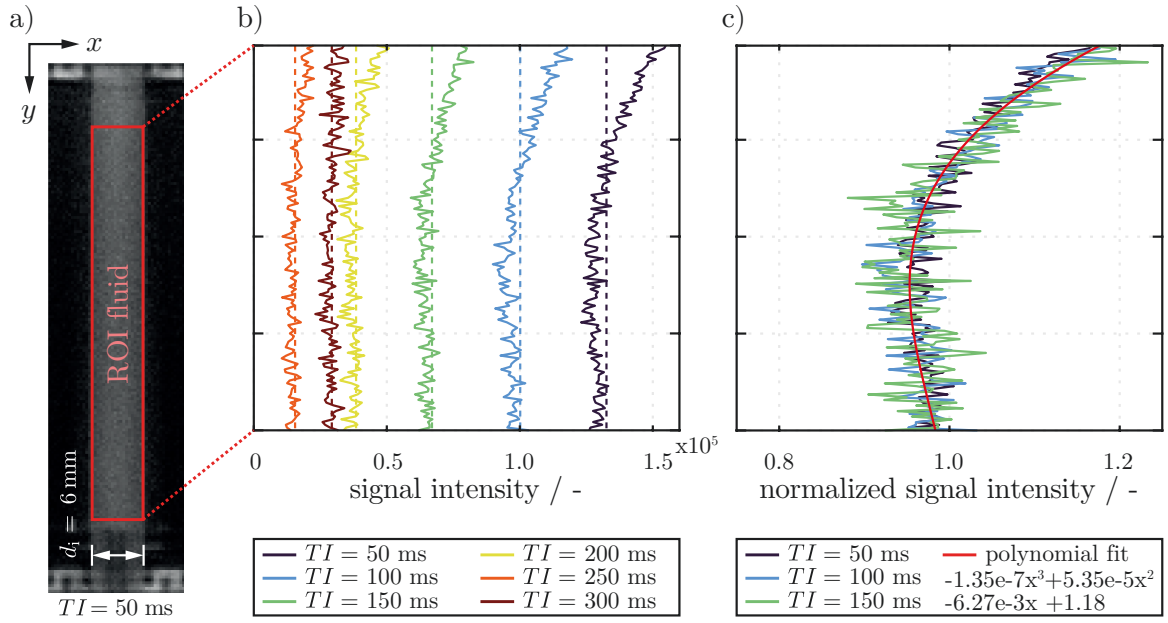

Fig. 7.6.: Visualization of the intensity gradient inside an ROI a) along the capillary (y-direction). b) The in x-direction averaged signal intensities are plotted along the capillaries y-axis and are compared to the ROI's mean signal intensity (vertical dashed line) for various TI. c) The normalized signal intensity is strongest at the top and decreases down the capillary in y-direction. This behavior is well reproduced by a third-order polynomial fit.

of the rear cap caused by the movement of the bubble can impact the signal intensities and should be considered as a possible influence on the obtained data. Since the field homogeneity inside the resonator influences the local signal, this systematic error should always be taken into account. The strength, however, can vary depending on the accuracy of the shimming procedure during the initial setup of the MR scanner before the experiments. The resulting intensity variations along the capillary that originated from the magnetic field variations are in good agreement compared to the fluctuations shown by the B_1 field map of the BC resonator (see Sec. 3.2.2, Fig. 3.12).

7.2.2 Temporal length decrease by mass-transfer and chemical reaction

Next, experiments were repeated, similar to those shown in Sec. 7.1. Here, two Fe^{II}(EDTA) solutions of $10\,\mathrm{mM}$ and $20\,\mathrm{mM}$ were prepared as the liquid phase and two O_2 Taylor bubbles were measured over a prolonged period of time. An inversion time of $TI_{\mathrm{zero}} = 300\,\mathrm{ms}$ was determined for the $10\,\mathrm{mM}$ solution which was increased to $TI = 400\,\mathrm{ms}$ for the experimental investigations. For the higher concentrated $20\,\mathrm{mM}$ solution, the identified $TI_{\mathrm{zero}} = 150\,\mathrm{ms}$ was increased to $TI = 200\,\mathrm{ms}$. The resulting time series are shown in Fig. 7.7. The shrinkage of an $l/d = 2.3$ bubble in $10\,\mathrm{mM}$ Fe^{II}(EDTA) solution over the time of $t = 4\,\mathrm{min}$ is depicted in

Fig. 7.7 a). The temporal evolution of a $l/d = 4.4$ bubble in 20 mM Fe^{II}(EDTA) solution over $t = 9\,\mathrm{min}$ is shown in Fig. 7.7 b).

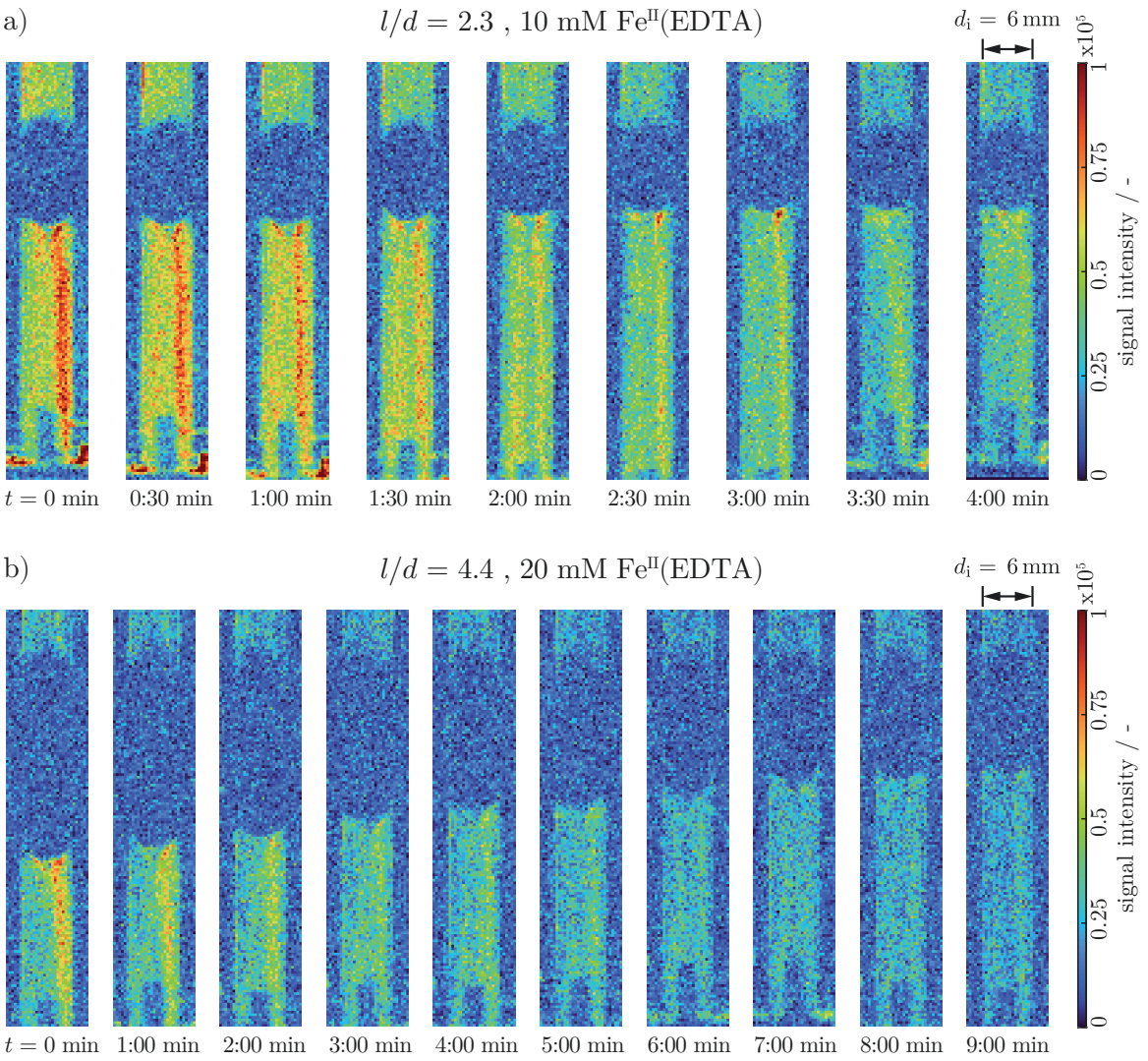

Fig. 7.7.: MRI time series of two single O_2 bubbles in a) 10 mM and b) 20 mM Fe^{II}(EDTA) solution measured over two different time spans. The images are shifted according to their front cap position. Fe^{III}(EDTA) is formed by the superimposed chemical reaction and results in a signal increase inside the wake region. MRI sequence parameters: inversion recovery on, spatial resolution $= (0.3125 \times 0.3125)\,\mathrm{mm}$, slice thickness $= 2.5\,\mathrm{mm}$, $TE = 0.71\,\mathrm{ms}$, $TR = 1.612\,\mathrm{ms}$, flip angle $\alpha = 24°$, scan repetition time $= 3000\,\mathrm{ms}$, a) $TI = 400\,\mathrm{ms}$, $TI_{\mathrm{zero}} = 300\,\mathrm{ms}$, b) $TI = 200\,\mathrm{ms}$, $TI_{\mathrm{zero}} = 150\,\mathrm{ms}$

The images with the lower Fe^{II}(EDTA) concentration (Fig. 7.7 a)) show an overall higher signal intensity, caused by the larger difference of 100 ms between TI_{zero} and TI. The larger difference was chosen to gain a sufficient contrast for manual cap detection. The smaller difference of 50 ms between TI_{zero} and TI of the 20 mM Fe^{II}(EDTA) solution (Fig. 7.7 b)) is still high enough to generate sufficient contrast but already complicates precise manual detection

of the front cap. In both cases, the low SNR renders automatic cap detection unusable. Both bubbles show a temporal length decrease, which seems more pronounced in Fig. 7.7 b). It only appears this way since the time scales are different. The Taylor bubble inside the 20 mM Fe^{II}(EDTA) solution was held steady for over twice as long until it ruptured.

Next, MRI images are compared to the resulting computations from the proposed FDM based mass transfer model (see Sec. 6.3). Discretization and experimental parameters are similar to those listed in Tab. 7.1. Calculations for the reactive case were performed using the same film thickness of $\sigma_{\text{film}} = 80\,\mu\text{m}$ that was previously determined to be the best fit regarding the non-reactive MRI experiments (see Sec. 7.1.1).
Fig. 7.8 shows the resulting decrease in normalized Taylor bubble length over time at two different Fe^{II}(EDTA) concentrations. Experiments and computations are compared for $l/d = 2.3$ in 10 mM Fe^{II}(EDTA) solution and for $l/d = 4.4$ in 20 mM Fe^{II}(EDTA) solution. The MRI data corresponds to the previously shown images of temporal length decrease with superimposed chemical reaction depicted in Fig. 7.7.

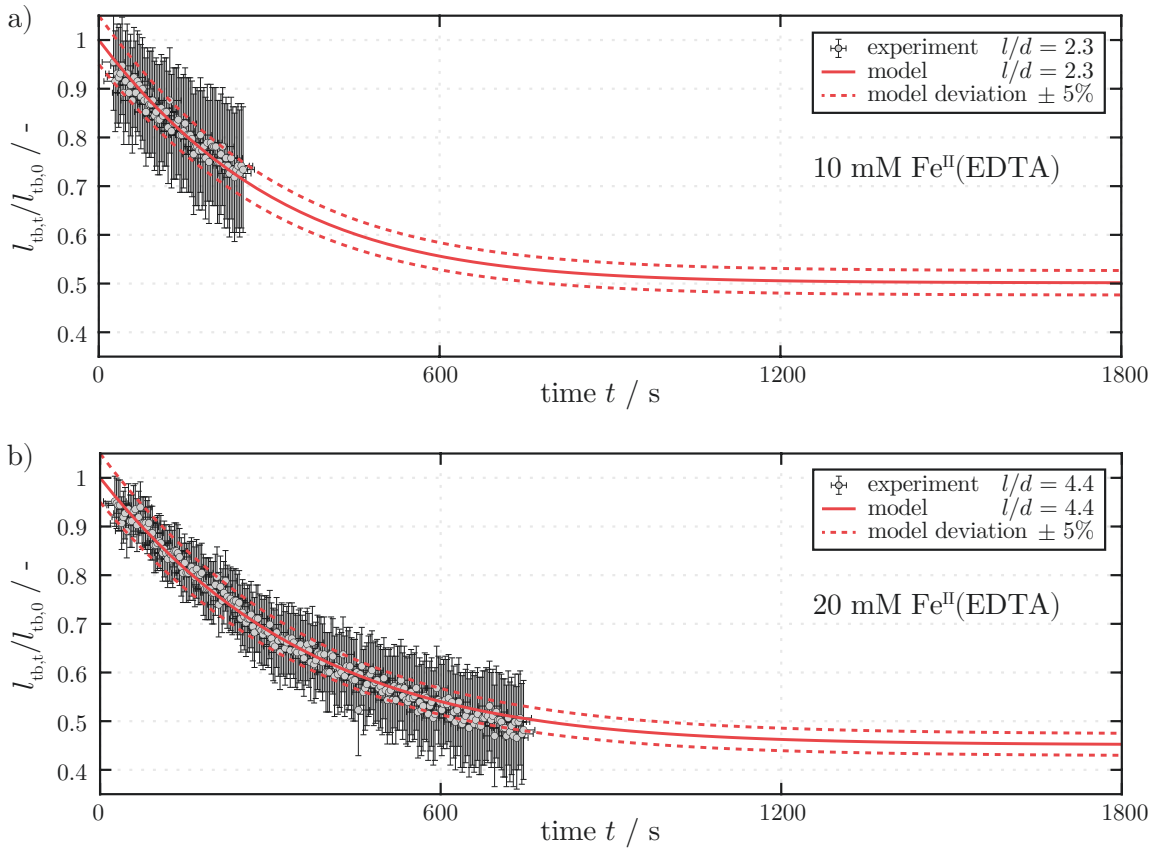

Fig. 7.8.: Comparison of MRI data and computed FDM results with superimposed chemical reaction at different Fe^{II}(EDTA) concentrations. Two Taylor bubbles are investigated: a) $l/d = 2.3$ in 10 mM Fe^{II}(EDTA) solution and b) $l/d = 4.4$ in 20 mM Fe^{II}(EDTA) solution.

Several differences are observable compared to the non-reactive experiments illustrated in Fig. 7.2. What is particularly noticeable is that the bubbles could only be held stable for a significantly shorter time. This phenomenon remained, even after thorough manual cleaning of the capillary. The assumption is that the liquid film between the bubble and the capillary wall breaks, either by contamination due to the presence of the reactants inside the liquid phase or that the product occupies the phase boundary, leading to a local tearing of the film. However, this assumption could not be verified.
Furthermore, a larger error in the normalized bubble length can be identified, mainly caused due to the shorter bubbles, compared to those from the non-reactive experiments. Here, the length deviation is more significant at smaller l/d. Additionally, manual cap detection results in a larger error in the normalized bubble length. The manual cap detection was performed thrice for both datasets, resulting in an average length. Due to the low contrast of the front cap, a deviation of ± 3 voxels can occur. The rear cap is well recognizable and contributes to the error by ± 1 voxel. Thus, a total deviation of ± 4 voxels exists which equals $1.25\,\mathrm{mm}$. As a result, the error in detected bubble length is larger for the reactive experiments. Here, it stays below $19\,\%$ at $l/d = 2.3$ and below $11\,\%$ at $l/d = 4.4$.
As before, the time step error is caused by the way experiments were conducted (bubble generation, position adjustment, start of MRI data acquisition) and is taken into account by $\pm 20\,\mathrm{s}$ (see Sec. 7.1).

A good agreement between the experimental and calculated results is observed for both bubbles within the measured period. The Taylor bubble in the higher concentrated Fe^{II}(EDTA) solution (Fig. 7.8 b)) shows a tendency to drop below the $\pm 5\,\%$ margin of the computed results towards the end of the measurement. This effect can be either caused by the lower signal intensity and, thus, a misinterpretation of the spatial phase boundary position towards the end of the measurement or by a deviation of the Fe^{II}(EDTA) concentration. The latter is likely to occur, attributed to the preparation and handling of the Fe^{II}(EDTA) stock solution under inert conditions. Small amounts of water can boil off during degassing under a vacuum inside an ultrasonic bath which alters the weight ratios during preparation. Working in the absence of oxygen has the highest priority to prevent the chemicals from reacting. That is why the solution is constantly kept inert by bubbling N_2 through the aqueous phase during the weighing and mixing of the substances, which inevitably leads to weighing errors. The stock solution is diluted to the final concentration by transferring it into the reaction vessel with a gas-tight syringe. At this step, dosing errors can occur. All of these errors cannot be exactly quantified. The deviation of the Fe^{II}(EDTA) concentration is estimated to be correct within $\pm 10\,\%$.
Apart from this deviation, the computed values and the experiments agree for both cases with superimposed chemical reaction. Longer measurement times would have been preferable for a more accurate assessment but were not achievable.

7.2.3 Visualization of the reaction product

What strikes most is the increase in signal intensity in the bubble's wake region, visible at both Fe^{II}(EDTA) concentrations in Fig. 7.7. Along with the reduction in bubble length, a signal decrease is observed over time, which is explained by the product formation of Fe^{III}(EDTA). Oxygen is transferred from the bubble into the liquid phase, rapidly oxidizing the Fe^{II}(EDTA). A significant reduction of the T_1 relaxation time and thus, also the TI of the liquid phase, is caused by the formed Fe^{III}(EDTA) (see Sec. 3.4).
Initially, the Taylor bubble consists of pure oxygen, resulting in the highest transfer of O_2 into the liquid phase. Most Fe^{III}(EDTA) is formed at this point, leading to the strongest increase in signal intensity. The driving O_2 concentration gradient between the Taylor bubble and fluid decreases over time as nitrogen enters by two-sided mass transfer and dilutes the gas inside the bubble. Consequently, less Fe^{III}(EDTA) is formed by oxidation as time progresses. A lower reduction of T_1 and respectively TI is caused so that the signal intensity declines.

The total signal inside the wake is increased as the product is partly mixed and distributed within the liquid phase by the hydrodynamics of the system. The distinct maxima behind the bubble are striking. Fe^{III}(EDTA) is formed and mainly flows downwards the capillary in two distinct streaks, with the right one being particularly pronounced. Due to the superposition of the flow field and the chemical reaction, the increased signal denotes a locally higher product concentration. Thus, conclusions about the underlying flow field can be drawn. The streaks indicate a simple vertical downflow without vortices or back mixing inside the wake region. Furthermore, the well-pronounced streaks of high signal intensity fade away rather quickly as time proceeds. The vanishing implies that the chemical reaction partly occurs in the wake region of enhanced fluid flow when high O_2 concentrations are present inside the liquid phase. At low concentrations, a majority of the reaction can already take place along the film.
Compared to the experiments from Kastens et al. [23], one would expect a single streak of product flowing downwards, centered inside the capillary. A slight inclination of the capillary can explain the split-up into two distinct streaks. The Eo number describes the ratio of gravitational and surface tension forces (see Eqn. 1.2). With $Eo = 4.84$, the experimental setup only slightly exceeds the necessary condition of $Eo > 4$ for a buoyancy-driven bubble rise to occur. Thus, the resulting bubble rise velocity v_{rise} is relatively low. Looking at the Ca number (see Eqn. 1.3), the interfacial force is small at low bubble rise velocities, whereas the viscous force dominates. Therefore, even a minor inclination becomes relevant to the flow deflection and alters the local hydrodynamics. Precise vertical positioning of the capillary inside the MR scanner is hardly possible. The flow setup has to be manually aligned within the birdcage resonator before being placed inside the MR scanner (see Sec. 3.2.2, Fig. 3.10). The vertical tilt angles of the flow setup were manually readjusted to stay below $1°$.

A decrease in signal intensity over time is also observed at the fluid region in front of the bubble. This contrasts the expectation of a constant or increasing signal intensity. Ideally, the

intensity would not change over time as the Fe^{II}(EDTA) solution is supplied from a N_2 purged container. However, in case of a reaction with remaining amounts of atmospheric oxygen inside the supply vessel, the produced Fe^{III}(EDTA) will cause a signal increase. This potential source of error has been taken into account by choosing an appropriate $TI > TI_{\text{zero}}$ to avoid zero crossing of the signal intensity.
The observed signal reduction is rather related to the design of the flow setup and can be explained easily. The gas phase is injected into the glass capillary via a small tube. In order to maintain a homogeneous and undisturbed liquid inflow at the top, the tube is integrated into the bottom flow distributor of the setup (see Sec. 3.2.2, Fig. 3.4). When generating a Taylor bubble, a few tiny gas bubbles inevitably emerge from the tube in advance. These bubbles of pure O_2 will get entrapped in the upper flow distributor where they react with the liquid phase and contribute to the overall signal at the inlet. The contribution to the signal decreases rather fast as the bubbles are small and oxygen is consumed by the chemical reaction.

Lastly, the reaction product's temporal behavior is investigated by comparing the mean signal intensity at the inlet to the mean signal intensity in the bubble's wake. Fig. 7.9 shows the resulting time-dependent signal decay. The $l/d = 4.4$ bubble in $20\,\text{mM}$ Fe^{II}(EDTA) solution over $t = 9\,\text{min}$ was chosen here as it offered a better signal contrast due to the higher amount of Fe^{II}(EDTA) and the smaller difference between $TI = 200\,\text{ms}$ and $TI_{\text{zero}} = 150\,\text{ms}$.
For each MRI image, the averaged reference intensity is determined at the inlet ROI (I) of fixed position, indicated by red data points. The mean signal behind the bubble is calculated at the wake ROI (II), which is positioned at a fixed distance of around $3\,\text{mm}$ behind the back cap. Data points of the wake region are indicated in blue. Both ROIs are equally sized at approximately $(6 \times 6)\,\text{mm}$. The average noise is determined from the noise ROI (III) placed outside of the capillary. Black data points indicate the noise data. Three images with the corresponding ROIs are shown at different times, resembling the experiment's start, mid, and end.

As expected, constant background noise is measured over the entire period because a sufficient distance from the capillary was chosen. The mean intensity of the inlet ROI (I) slightly decreases over time by about $40\,\%$ and is caused, as previously discussed, by small entrapped O_2 bubbles inside the top flow distributor. Additionally, the signal in the intake is likely to be slightly amplified due to the coil's B_1 profile which was not considered here, due to the small difference of $50\,\text{ms}$ between TI_{zero} and the chosen TI. The average intensity inside the wake ROI (II) is reduced by more than a factor of two over the entire experiment. The formed Fe^{III}(EDTA) product explains the higher intensity and time-dependent signal reduction inside the wake region. Oxygen transport ceases over time as the driving concentration gradient declines. Consequently, product formation and the resulting contribution to the MR signal is lowered. Bubble movement and manual cap detection contribute to the fluctuations in mean signal strength over time.

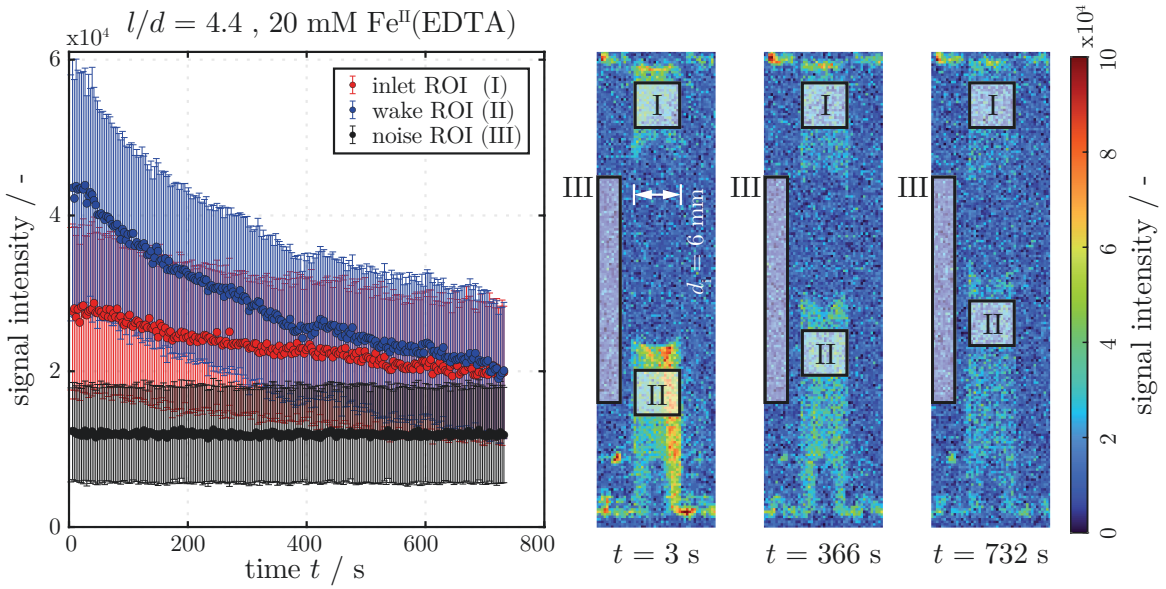

Fig. 7.9.: Comparison of the mean signal intensities at the inlet ROI (I) and the wake ROI (II) of the $l/d = 4.4$ Taylor bubble in 20 mM Fe^{II}(EDTA) solution (see Fig. 7.7 b) and Fig. 7.8 b)). Mean intensities are calculated from two ROIs of approximately (6×6) mm. The noise signal is averaged from an ROI outside the capillary. Three single images with the respective ROIs are shown at different times t.

The mean signal intensities in front of and behind the bubble are of equal size at the end of the experiment, which suggests that all the oxygen has been consumed. However, the computed length reduction in Fig. 7.8 b) indicates that mass transport has not completely ceased at that time, as a further reduction in length is visible from the computed data. At this point, the resulting signal difference is insufficient to distinguish it from the inlet signal. Here, this effect mainly results from the unavoidable difference in TI and TI_{zero}, necessary for front cap detection. Additionally, the detectability of small product quantities can also be limited by the overall signal strength and SNR of the used resonator.

A dilution series of different Fe^{III}(EDTA) product concentrations of fully reacted Fe^{II}(EDTA) is needed to quantify the lower detection limit of the setup. By this, conclusions could be drawn about the resulting product concentration in the wake by mapping the different intensities to the related product concentrations. Unfortunately, due to its complex nature, the dilution series could not be provided for the employed reaction system. Several subsequent (side)reactions may occur [89, 90], which can alter the measured MR signal of the products.

7.3 Conclusion

MRI data of non-reactive and reactive Taylor flows were successfully acquired and evaluated. First, the temporal length reduction of O_2 bubbles in ultrapure water was measured over 30 minutes using a snapshot FLASH sequence. An automatic cap detection algorithm was employed to retain the bubble length from the MR images. These values served as a reference to which the FDM-based mass transfer model was fitted by calculating the coefficient of determination R^2 between the model and the MRI data at different film thicknesses. The best fit was found for a film thickness of $\sigma_{\text{film}} = 80\,\mu\text{m}$. The difference in the computed film thickness to the experimentally obtained $\sigma_{\text{film}} = 130\,\mu\text{m}$ by Haghnegahdar et al. [99] could be related to simplifying the flow profile inside the film as a plug flow. A comparison with a more realistic parabolic flow profile significantly reduced this difference and showed good agreement.

Based on these findings, Taylor flows with superimposed chemical reaction were analyzed. Here, different concentrations of Fe^{II}(EDTA) were added to the liquid phase and served as a reactant for the transferred oxygen species. Mass transfer was enhanced as steeper O_2 concentration gradients at the gas-liquid interface promoted oxygen transfer. The MR signal of Fe^{II}(EDTA) was almost canceled out by the employed inversion recovery method to solely visualize the reaction product Fe^{III}(EDTA). Manual cap detection was applied and the resulting bubble lengths were compared to FDM calculations with superimposed chemical reaction using the same film thickness of $\sigma_{\text{film}} = 80\,\mu\text{m}$. Computed results and experiments were also in good agreement for the reactive case. Here, an even more precise evaluation would have been aided by longer measurement times which, unfortunately, could not be realized with the employed reaction system.

The reaction product was successfully visualized in the vicinity of the bubble. The Fe^{III}(EDTA) followed the hydrodynamics inside the Taylor bubble's wake and appeared as distinct streaks during the beginning of the experiments. A decline in signal intensity over time indicated a reduction in overall Fe^{III}(EDTA) concentration. The consumption and dilution of oxygen inside the bubble resulted in a smaller driving O_2 concentration gradient, leading to a decrease in product and, consequently, a reduced MR signal intensity.
The product concentration was only qualitatively visualized but could not be quantified with the used reaction system. A dilution series of different product concentrations is needed to reference the signal intensities. With the Fe^{II}(EDTA) reaction system, several subsequent (side)reactions may occur [89, 90] that will distort the resulting MRI data and its conclusions. The quantification, however, provides an interesting outlook for further studies.

8 Conclusion and outlook

This work was driven by the initial motivation of combining the two major research fields of magnetic resonance imaging (MRI) and chemical reaction engineering, focusing on the non-invasive investigation of non-reactive and reactive gas-liquid Taylor flows using MRI. Various valuable tools and approaches were developed and interesting insights were gained along the way of finishing this thesis to answer the three research objectives that arose at the start of this journey. Following, the main findings are summarized concerning the research questions.

Initially, the question arose whether MRI allows the evaluation of gas-liquid Taylor flows in pure systems under real flow conditions. Several requirements had to be met to answer this question. Experimental MRI studies of Taylor flows were demanding. The confined space of the horizontal bore MR scanner required a flow setup with defined fluid dynamics. Long-term measurements of single Taylor bubbles were enabled by spatially fixing the bubbles using a countercurrent flow inside a vertically aligned $d_\mathrm{i} = 6.0\,\mathrm{mm}$ glass capillary. Creating an evenly directed vertical flow was especially difficult and only achieved to some extent in the first approach. A loop-gap resonator was tailored around the capillary to gain a good signal-to-noise ratio and sufficient image contrast. A snapshot-FLASH sequence was adapted and improved by a fourfold segmentation during data acquisition to counteract motion blurring during fast image acquisition at a reasonable resolution. Following, the underlying flow dynamics in the Taylor bubble's wake were evaluated by MRI, fulfilling the given prerequisites. Additional 2C-2D PIV measurements inside the identical setup were conducted to analyze the underlying flow fields. The functionality of the adapted pulse sequence was explained and confirmed by a qualitative comparison of MRI and PIV results, which showed a good agreement, indicating that the flow inside the capillary was stationary but not rotationally symmetric. A variable delay time t_d was included in the adapted pulse sequence to acquire additional information on the time-dependent flux into the measurement plane, thus, enabling the mapping of spatial flow progression under stationary conditions. It was successfully demonstrated that MRI could be utilized to examine gas-liquid Taylor flows of a pure system under real flow conditions.

The next issue that had to be addressed was the ability of MRI to analyze reactive flows. Based on the previous findings, an improved flow setup with a sophisticated flow distributor was developed, aided by single-phase flow simulations. The aim was to establish a fully rotationally symmetric flow inside the capillary, fulfilling an essential requirement for accurate mass transport investigations. Further, an inductively coupled birdcage resonator was designed to maximize bore space utilization while providing a uniform B_1 field for accurate measurements

of reactive flows. The resonator was successfully tested under low and high loading conditions. The B_1 field map revealed a homogenous magnetic field inside the resonator with minor alterations near its rungs. A commercial coil was used as a benchmark for qualitative imaging performance. Both devices performed equally well. Long-term measurements of non-reactive and reactive Taylor flows were conducted with the improved flow and resonator setup. MRI experiments of single O_2 bubbles in N_2 saturated water successfully demonstrated mass transfer by the temporal decrease in bubble length. The oxidation of Fe^{II}(EDTA) to Fe^{III}(EDTA) was identified as a suitable reaction system, fulfilling the demanding requirements of a fast reaction rate while exhibiting a strong T_1 contrast between reactant and product crucial for reactive experiments. Inversion recovery measurements of single O_2 bubbles in N_2 saturated water were conducted with varying Fe^{II}(EDTA) concentrations. The reaction system's high T_1 contrast allowed solely visualizing the reaction product Fe^{III}(EDTA) by suppressing the MR signal of Fe^{II}(EDTA) utilizing the inversion recovery method. The temporal decrease in bubble length was employed to visualize mass transfer in reactive flows. Furthermore, inversion recovery measurements successfully revealed the formed reaction product inside the Taylor bubble's wake by a considerable increase in MR signal. A declining signal strength indicated the reaction's temporal progression.

The final question was whether a correlation of the MRI data was possible with a physical model of the temporal length decrease in non-reactive and reactive Taylor flows. A model was successfully developed that physically explains the influence of non-reactive and reactive two-sided mass transfer on the resulting temporal change in Taylor bubble length. A diffusion-advection-reaction equation modeled the 2D concentration profile within the liquid film. The differential equation was discretized and numerically solved using a finite difference method (FDM) with a forward-in-time, centered-in-space (FTCS) scheme. A simplified model was obtained by approximating the Taylor bubble's shape as a cylinder with mass transfer solely taking place over the lateral surface. The impact of this simplified assumption on the results was validated. In addition, the spatial and temporal discretization parameters N_x, N_y, and Δt were subsequently refined to quantify their influence on the accuracy of the computed results. Following this, the effect of various physical parameters on temporal bubble length decrease during two-sided mass transfer with superimposed chemical reaction was investigated. Here, parameters including the l/d ratio, the Fe^{II}(EDTA) concentration c_{EDTA}, and the liquid film thickness σ_{film} were studied. Lastly, the experimental MRI data were compared to FDM results computed at various film thicknesses. The results were discussed regarding the validity of the matching liquid film thickness. A good agreement was found between all experimental MRI results and computed data for non-reactive and reactive Taylor flows for $\sigma_{\text{film}} = 80\,\mu\text{m}$. It was demonstrated that the model's best matching film thickness corresponded to an actual film thickness of $\sigma_{\text{film}} = 130\,\mu\text{m} - 150\,\mu\text{m}$, which was in good agreement to experimental results from the literature. The final issue, about the correlation of experimental MRI data with a physical model, was thus successfully answered.

The tools and methods successfully developed in this thesis offer great potential for future research. They may pave the way for a more in-depth understanding of gas-liquid Taylor flows in pure and opaque systems, previously inaccessible by traditional optical measuring techniques. Applying the methods presented in this thesis in a vertical bore MR scanner would offer various possibilities. The elimination of height limits and, thus, assurance of the required hydrodynamic entrance length enables the experimental investigation of various capillary diameters. The resulting alterations of the fluid dynamics inside the Taylor bubble's wake can be examined by MRI. Furthermore, the proposed Fe^{II}(EDTA) reaction system can be utilized to investigate the effect of altered hydrodynamics on the product formation of the superimposed chemical reaction. Here, it would be particularly interesting to identify a further MRI active reaction system that allows for the visualization of consecutive competitive reactions to assess the influence of fluid dynamics on the reaction's selectivity and yield. Extending the study's focus from single bubbles to bubble trains is also imaginable. Parameter studies over a broader range will help evaluate the proposed model's functionality. An extension of the model to calculate the actual product concentration and compare it to the signal intensity of the MRI data is conceivable.

A

Preparation of the Fe^{II}(EDTA) solution

The preparation of the aqueous Fe^{II}(EDTA) reaction system is described in the following chapter. Since the solution is very air-sensitive (see Fig. A.1 b)), all preparation steps must be followed precisely and it is mandatory to work under a protective N_2 atmosphere the entire time. For this, it is sufficient to continuously displace the air in the reaction vessel by nitrogen. For all experiments, a $50\,\mathrm{mM}$ stock solution of Fe^{II}(EDTA) was prepared, which was later diluted to the desired concentration. The correct amounts of chemicals are given in Tab.A.1. The preparation of the Fe^{II}(EDTA) solution is related to the work of Schneppensieper et al. [87].

First, $500\,\mathrm{mL}$ of ultra-pure water is filled into a $1000\,\mathrm{mL}$ Schott flask and is degassed under vacuum inside an ultrasonic bath for $30\,\mathrm{min}$. After that, stripping with pure nitrogen removes any excess dissolved oxygen by bubbling N_2 through the water under intense mixing with a magnetic stirrer. The dissolved oxygen concentration is monitored by a digital meter (Greisinger GMH 3611, GHM Messtechnik GmbH, Germany). Stripping is performed for at least $15\,\mathrm{min}$ and completed as soon as all the oxygen has been displaced, measured as a dissolved oxygen concentration of $0.0\,\mathrm{mg\,L^{-1}}$.

Next, the correct amount of $Na_2EDTA{\cdot}2\,H_2O$ is added to the freshly stripped water under continuous stirring. After that, the pH value is raised to $10.5 - 11.5$ by adding sodium hydroxide pellets to dissolve the EDTA salt completely. Pellets are preferred over a liquid stock solution, as this prevents the undesired introduction of dissolved oxygen from the liquid. Adding sodium hydroxide causes the turbid solution to turn clear as the entire salt is slowly dissolved. The solution is thoroughly stirred until all visible solids are dissolved and the pH value does not change further. If necessary, the pH is adjusted to $10.5 - 10.9$ by adding concentrated sulfuric acid if this value is exceeded. The final pH value is noted.

In the final step, the iron salt is added. In this critical step, the freshly formed complex immediately and irreversibly binds any excess molecular oxygen from improper preparation. A pale reddish-orange color change directly indicates the reaction. In this case, the solution is discarded and freshly prepared. The right amount of $FeSO_4{\cdot}7\,H_2O$ is added to the EDTA solution under moderate stirring. Here, a ratio Fe : EDTA $= 1 : 1.1\,\mathrm{mol\,mol^{-1}}$ is used so that no free EDTA remains. The pH of the solution has to be in the range of $6.0 - 8.0$ and is lowered by the addition of concentrated sulfuric acid. If a pH< 6.0 is measured, it is increased by adding sodium hydroxide pellets. The final pH value is noted.

A clear to slightly greenish Fe^{II}(EDTA) stock solution (see Fig. A.1 a)) is obtained when the work is carried out very cleanly. A pale reddish-orange color indicates that oxygen was present and part of the solution has irreversibly reacted. In this case, discarding the solution and preparing it fresh is best. For transportation to the MR scanner, the lid of the Schott flask is additionally wrapped with Parafilm to prevent any air from entering.

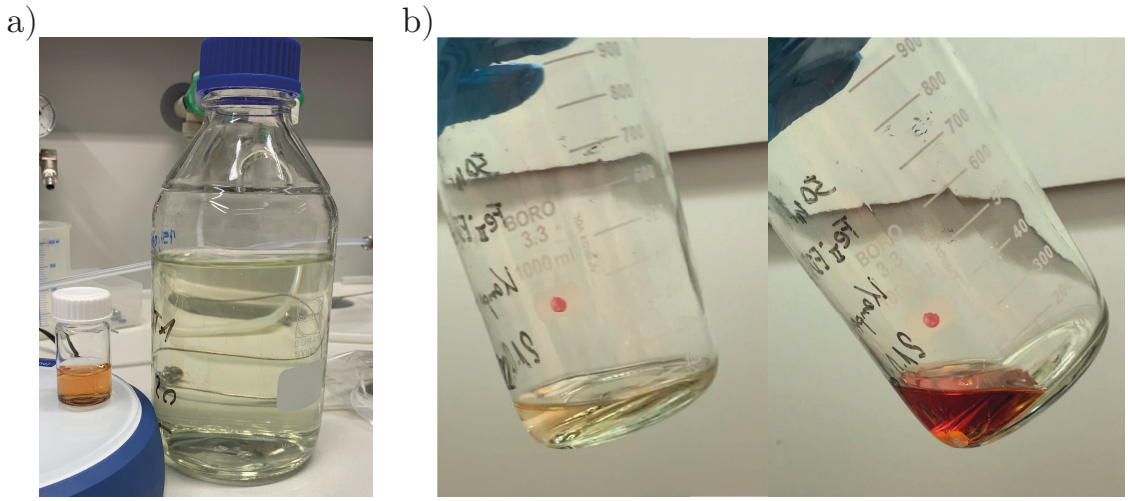

Fig. A.1.: Images of 50 mM Fe^{II}(EDTA) stock solutions under different conditions. a) The slight greenish tint of the cleanly prepared solution inside the Schott flask is visible. Positioned left next to the flask, a small amount of the stock solution was transferred into a vial and exposed to air. The Fe^{II}(EDTA) immediately turned orange after gently mixing the sample with air by shaking. b) Shown in the left picture, a pale reddish-orange coloration of the remaining stock solution at the end of a measuring day indicates a partial reaction with air. The right picture shows the same solution after flushing the protective N_2 atmosphere inside the flask with air and shaking it well for about 15 s. The solution shifted quickly to a dark red color, demonstrating the high reactivity of the Fe^{II}(EDTA) complex to air.

Tab. A.1.: Calculated amounts of chemicals for the preparation of a 50 mM Fe^{II}(EDTA) stock solution, based on the ratio and molar mass of the reactants.

$FeSO_4 \cdot 7\,H_2O$	$278.02\,\mathrm{g\,mol^{-1}}$ [108]
$Na_2EDTA \cdot 2\,H_2O$	$372.24\,\mathrm{g\,mol^{-1}}$ [109]
ratio Fe : EDTA	$1 : 1.1\,\mathrm{mol\,mol^{-1}}$
concentration of the Fe^{II}(EDTA) stock solution	50 mM
volume of H_2O	500 mL
weight of $FeSO_4 \cdot 7\,H_2O$	6.95 g
weight of $Na_2EDTA \cdot 2\,H_2O$	10.24 g

PIV flow measurements

B

The presented information is part of the published work from Kemper et al. [78]. The text and illustrations have been adapted to match the style of this work.

Details on the PIV flow analysis are provided in the following chapter. PIV measurements were performed to subsequently compare them to the flow fields acquired by MRI and thus to verify the function of the MRI pulse sequence. For this purpose, the identical flow setup had to be tested with both measuring techniques. Since the setup was mainly designed for use inside the MR scanner, some additional adjustments had to be made, which are explained below.

A 2C-2D (two-components, two-dimensional) PIV setup, consisting of a single camera and a laser with light-sheet optics, was used for flow quantification inside the experimental setup. Particle imaging was performed with a pco.dimax HS4 (PCO AG, Germany) high-speed CMOS camera. A shallow depth of field (DOF) was archived by a $105\,\mathrm{mm}$ 1:2.8 DG macro-lens (Sigma, Japan) with an additional $475\,\mathrm{nm}$ high-pass filter (Carl Zeiss, Germany) to block the light from laser excitation. Planar illumination was realized using a $12\,\mathrm{W}$ continuous-wave laser with a wavelength of $447\,\mathrm{nm}$ (CNI laser, China) and an adjustable light sheet optic. The capillary was surrounded by a borosilicate glass box and was immersed in a glycerol-water mixture ($n_{\mathrm{ri}} = 1.473$) [110] for refractive index adjustment. Matching the refractive index of the glass allowed for undisturbed optical access at the curved surface of the capillary. All parts were mounted on an optical base plate. Micrometer screws enabled precise positioning of the camera and the light sheet optics. A lab jack was used for height adjustment of the capillary in the optical arrangement. The capillary was rotatable by $90°$ to perform measurements from the front and side plane. Fig. B.1 provides a rendering of the experimental setup.

The liquid phase was seeded with fluorescent particles for the flow experiments. A $0.5\,\mathrm{mL}$ solution of polystyrene particles (Polysciences Fluoresbrite Carboxy YG microspheres, $d = 4.5\,\mu\mathrm{m}$, packaged as $2.5\,\%$ aqueous suspension, excitation maximum at $441\,\mathrm{nm}$, emission maximum at $486\,\mathrm{nm}$) was suspended in $500\,\mathrm{mL}$ ultrapure water. Air was used as the gas phase for Taylor bubble generation. Mass transfer and bubble shrinkage were suppressed through prior saturation of the ultrapure water by bubbling air through the liquid. The investigated Taylor bubbles had an l/d ratio between 2 to 3.

The depth of field describes the thickness of the slice in which particles can be sharply depicted. The total DOF was estimated using the equation stated by Rowlands [111]:

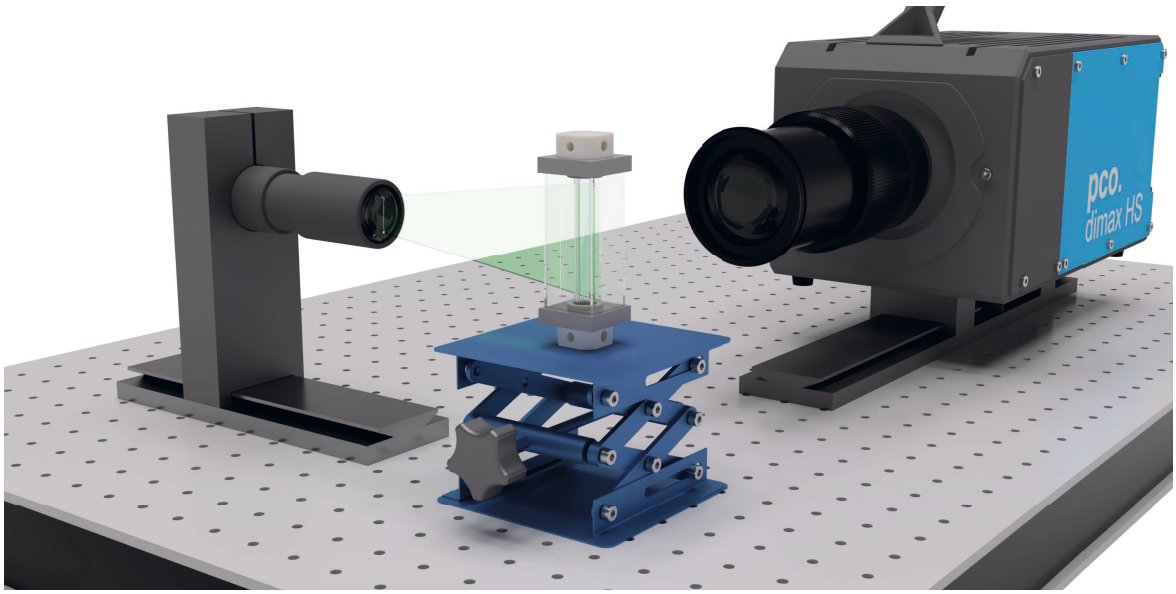

Fig. B.1.: Rendering of the experimental PIV Setup. The high-speed CMOS camera and laser light-sheet optics are aligned with the center planes of the capillary. The flow setup is enclosed by a glass box for refractive index matching and can be adjusted in height using a lab jack. All components are mounted on an optical table.

$$\text{total DOF} = \frac{2\,h_d\,s\,(s - f_l)}{h_d^2 - (s - f_l)^2} \tag{B.1}$$

Here, h_d describes the hyperfocal distance, calculated as $h_d = f_l^2/(\text{CoC} \cdot N_A)$ using the focal length ($f_l = 105\,\text{mm}$) and the numerical aperture of the lens ($N_A = 2.8$) and a calculated value for the circle of confusion $\text{CoC} = \sqrt{w_{\text{CMOS}}^2 + h_{\text{CMOS}}^2}/1500$ which is determined from the width and height of the camera's CMOS sensor ($w_{\text{CMOS}} = h_{\text{CMOS}} = 22\,\text{mm}$). The focus distance s indicates the distance between the imaging plane and the CMOS sensor and is manually measured at the setup ($s = 320\,\text{mm}$). Thus, the total DOF for the given setup was estimated to $0.725\,\text{mm}$.

The limited field of view only permitted imaging of the rear bubble cap and the wake area behind it. A spatial resolution of $(12 \times 12)\,\mu\text{m}$ was achieved with the optical setup. Images were recorded at a frame rate of $300\,\text{Hz}$. All experimental parameters are listed in Tab. B.1.

Before the actual PIV analysis, the raw camera data had to be prepared. Images were cropped and an intensity threshold removed background noise. Bubble drift correction was performed by detecting and shifting the rear cap positions of the complete image series using a 2D cross-correlation algorithm in MATLAB. A maximum displacement of ± 100 pixel around the mean cap position of the image series was tolerated. A video sequence of the shifted images was displayed and manually checked for possible outliers. After passing the manual check, 1200 consecutive shifted images were saved for the subsequent PIV analysis.

Tab. B.1.: Parameters for the PIV experiments and the PIVlab evaluations.

parameters for PIV experiments	
field of view	$(24.2 \times 16.6)\,\mathrm{mm}$
spatial resolution (CMOS sensor)	$(0.012 \times 0.012)\,\mathrm{mm}$
depth of field	$0.725\,\mathrm{mm}$
frame rate	$300\,\mathrm{Hz}$
exposure time	$0.9\,\mathrm{ms}$
slice orientation	x, y (front), y, z (side)
Taylor bubble l/d ratio	$2 - 3$
parameters for PIVlab evaluation	
method	ensemble correlation
number of images	1200
sequencing style	$1 - 2$, $2 - 3$, $3 - 4$, ...
interrogation window size	64×64, 32×32, 16×16
overlap	$50\,\%$
quality setting	normal
calculated values	mean velocity, mean divergence

In-plane flow velocities were determined with an ensemble correlation approach, where the correlation planes from the previously prepared image series are averaged. As the number of images increases, the correlation peaks accumulate and thus indicate the mean displacement of the flow. The spatial resolution of the recovered flow field depends on the so-called interrogation window size (IWS), which is used to compute the correlation planes. [37]

By using an interrogation window size of 64×64 pixel, Vennemann et al. [112] showed that five image pairs were sufficient to obtain $> 90\,\%$ valid vectors. Using 50 image pairs, the number of valid vectors increased to almost $100\,\%$. The information inside the interrogation window decreases proportionally with size. Therefore, the number of images must be accordingly increased to gain reliable data.

This study refined the IWS during the computation of the ensemble correlation from 64×64 over 32×32 to 16×16 pixel. By choosing an overlap of $50\,\%$, a final size of 8×8 pixel resulted, corresponding to approximately $(80 \times 80)\,\mu\mathrm{m}$.

The ensemble correlation was performed in MATLAB using the PIVlab 2.31 toolbox [38]. Calculations of mean vector fields and the divergence were performed directly inside PIVlab. A manually prepared mask helped suppress particle misdetections caused by reflections within the Taylor bubble, so only information on the flow inside the liquid phase is retrieved. All important PIVlab parameters and settings are listed in Tab. B.1.

C MRI resonators

Technical details about the two resonators that were constructed and used in the thesis are provided below.

C.1 Loop-gap resonator

Due to its simplicity, the loop-gap resonator was constructed by a trial-and-error approach to fit around the capillary of the flow setup. Thus, only a brief summary of the geometric parameters and used components is given in Fig. C.1. Adhesive copper tape is glued onto an acrylic cylinder and interconnected by five fixed-value capacitors and one variable capacitor for frequency tuning. The pickup loop is not shown here. It is made up of a $d_\mathrm{i} = 30.4\,\mathrm{mm}$ single turn loop of $d = 1.7\,\mathrm{mm}$ copper wire positioned with adjustable height above the actual resonator.

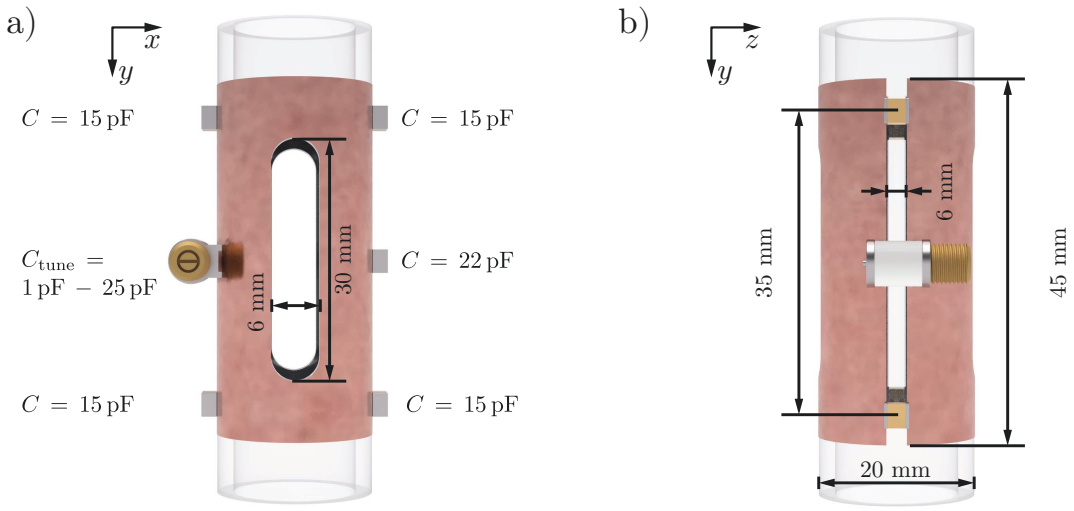

Fig. C.1.: Geometric parameters and component values of the loop-gap resonator shown from the front view a) and from the side view b).

C.2 Birdcage resonator

Results shown in this chapter are published by Kemper et al. [76] with detailed step-by-step instructions on constructing the resonator. The text and illustrations have been adapted to match the style of this work.

During the design phase, a maximum inner coil diameter was aimed to utilize the scanner's entire bore space. The length of the resonator was kept short and was adjusted regarding its diameter. Mispelter et al. [61] point out that a maximized magnetic field amplitude inside the resonator is achieved at $l = d_{\text{coil}} \times \sqrt{2}$ whereas optimum homogeneity is found at $l = d_{\text{coil}} \times 1.661$. A ratio of $d_{\text{shield}}/d_{\text{coil}} = 1.3$ was chosen to avoid excessive concentration of the magnetic field between the shield and the resonator, which would result in a substantial field magnitude decrease inside the coil. A fully enclosed shielding constructed from adhesive copper tape was used to successfully shield the resonator from interfering RF signals of the gradient system. A low-pass design with $N_{\text{leg}} = 12$ legs provided the best compromise between constructability and signal homogeneity. The necessary capacities were calculated using the *pyBirdcagebuilder* [73] based on the geometric demands. Values of the initial calculation and the constructed design are listed in Tab. C.1.

Tab. C.1.: Design and component values calculated using *pyBirdcagebuilder* [73].

	calculation	**construction**
configuration	low-pass	low-pass
resonant frequency f_0	$300\,\text{MHz}$	$300\,\text{MHz}$
type of leg and endring	rectangular	rectangular
number of legs N_{leg}	12	12
coil diameter d_{coil}	$83\,\text{mm}$	$83\,\text{mm}$
leg length l_{leg}	$60\,\text{mm}$	$58\,\text{mm}$
leg width w_{leg}	$5\,\text{mm}$	$5\,\text{mm}$
endring segment width w_{er}	$10\,\text{mm}$	$10\,\text{mm}$
RF shield diameter d_{shield}	$110\,\text{mm}$	$110\,\text{mm}$
capacitance C_{leg}	$2.03\,\text{pF}$	$2.35\,\text{pF}$ $(4.7\,\text{pF} + 4.7\,\text{pF})$

Fig. C.2 a) illustrates the internal structure of the proposed resonator design. The calculated capacitance C_{leg} is split into two capacitors $C_{\text{r}} = 4.7\,\text{pF}$ of approximately twice the capacity, located at both ends of each rung. Field disturbances near the capacitor are thus shifted away from the ROI at the resonator's center. Two capacitors are replaced by variable trimmers $C_{\text{tune}} = 0.6\,\text{pF} - 4.7\,\text{pF}$ for frequency tuning of the resonant structure.

Fig. C.2 b) indicates the rectangular pickup loop placed between the resonator and the shield. The loop consists of $d = 1.7\,\text{mm}$ copper wire. Impedance matching to $50\,\Omega$ is achieved by a

variable capacitor $C_{\text{match}} = 1.5\,\text{pF} - 40\,\text{pF}$, connected in series to a capacitor of fixed value $C_{\text{p}} = 4.7\,\text{pF}$. A directly soldered BNC cable connects the pickup loop to the MR hardware. The copper shield is connected to the ground plane (shielding of the BNC cable) by a copper wire not shown in the picture. Fig. C.2 c) illustrates the electrical schematic of the complete coil assembly with all the associated components.

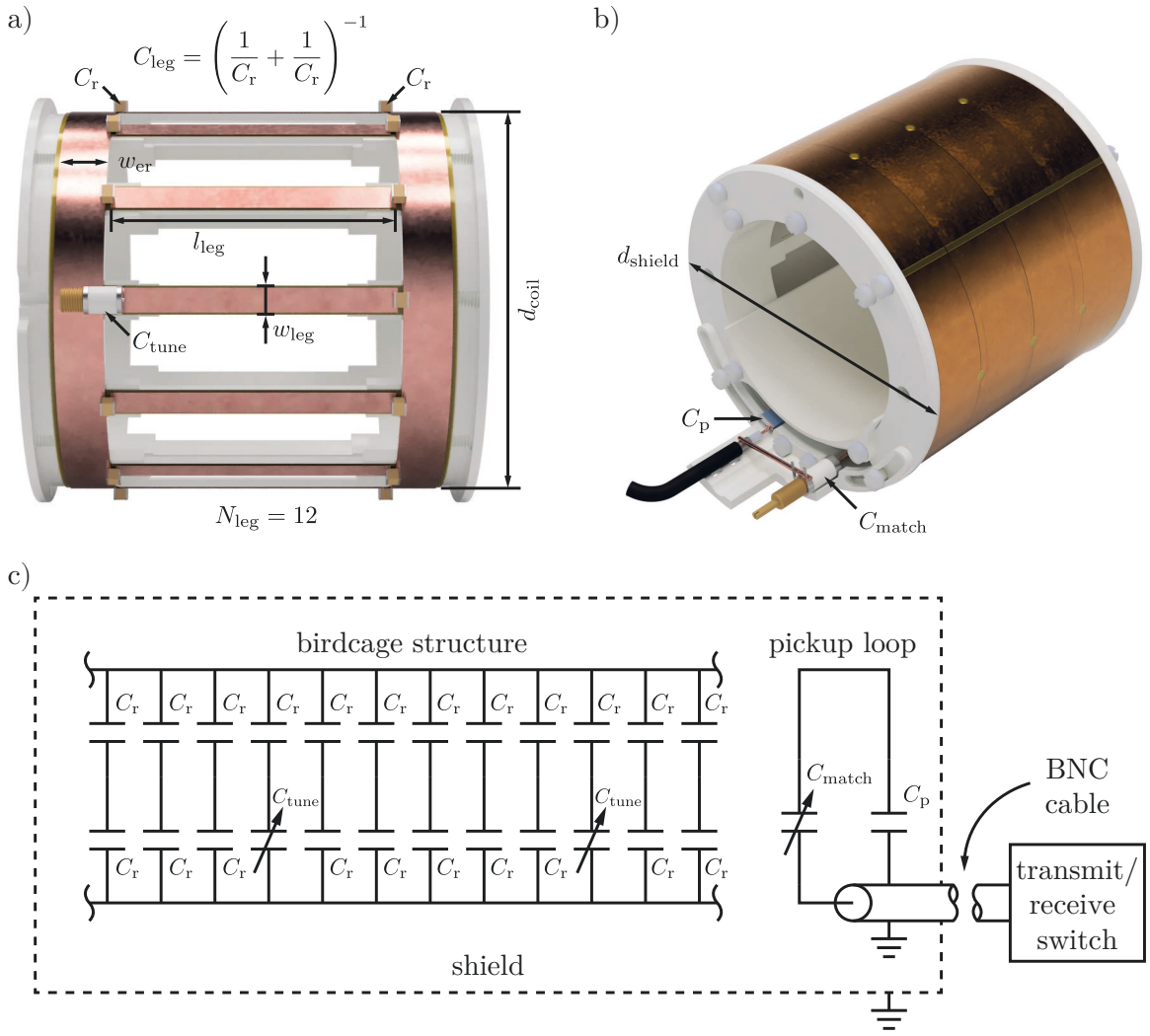

Fig. C.2.: a) Rendering of the internal birdcage structure, showing all important parts and parameters. b) Rendering of the BC enclosed by the copper shield. The pickup loop interfaces the coil to the MR hardware and is located at the bottom between the BC structure and the shield. c) The electrical schematic of the entire coil assembly indicates the fixed value and variable capacitors. Image based on Kemper et al. [76].

Mass transfer modeling

D

Below, a detailed explanation of the mass transfer models from Chap. 6 is given. The chapter is structured identically as Chap. 6 for better clarity.

D.1 Calculation of liquid side mass transfer coefficient using the penetration theory

The liquid side mass transfer coefficient k_L is expressed by Higbie's penetration theory [97] (see Sec. 6.1, Eqn. 6.1):

$$k_L = 2\sqrt{\frac{D_{AB}}{\pi\tau}} \tag{D.1}$$

The residence time inside the film region τ_{film} is defined as the film length l_{film} divided by the fluid velocity inside the film as:

$$\tau_{\text{film}} = \frac{l_{\text{film}}}{v_{\text{film}}} \tag{D.2}$$

v_{film} is determined from continuity between the volumetric flow rate through the capillary and the volumetric flow rate through the narrow film area between the bubble and the capillary wall by:

$$v_{\text{rise}}\frac{\pi d_{\text{i}}^2}{4} = v_{\text{film}}\left(\frac{\pi d_{\text{i}}^2}{4} - \frac{\pi d_{\text{tb}}^2}{4}\right) \tag{D.3}$$

The diameter of the Taylor bubble can be expressed by the capillary diameter minus two times the liquid film thickness:

$$d_{\text{tb}} = d_{\text{i}} - 2\sigma_{\text{film}} \tag{D.4}$$

Each cap's residence time is defined by the circumference of a quarter circle $\pi d_{\text{tb}}/4$, resulting in a total length of half a circle's circumference for both caps [25]. The length is divided by the flow velocity, which equals the bubble's rise velocity v_{rise} in our experiments, resulting in the total cap residence time τ_{cap}:

$$\tau_{\text{cap}} = \frac{\pi d_{\text{tb}}}{2v_{\text{rise}}} \tag{D.5}$$

The liquid side mass transfer coefficients k_L for the film and cap region are obtained by respectively inserting τ from Eqn. D.2 and Eqn. D.5 in Eqn. D.1 (see Sec. 6.1, Eqn. 6.1):

$$k_{L,\text{film}} = 2\sqrt{\frac{D_{AB}\, v_{\text{film}}}{\pi l_{\text{film}}}} \tag{D.6}$$

$$k_{L,\text{cap}} = 2\sqrt{2\frac{D_{AB}\, v_{\text{rise}}}{\pi^2 d_{\text{tb}}}} \tag{D.7}$$

To calculate the total liquid side mass transfer coefficient $k_{L,\text{tb}}$ for the Taylor bubble, the surface ratio of the caps ($A_{\text{cap}} = \pi d_{\text{tb}}^2$) and the cylinder wall ($A_{\text{film}} = \pi d_{\text{tb}} l_{\text{film}}$) on the total surface area ($A_{\text{film}} + A_{\text{cap}}$) must be taken into account since both regions contribute differently to mass transfer (see Sec. 6.1, Eqn. 6.2):

$$k_{L,\text{tb}} = k_{L,\text{film}} \frac{A_{\text{film}}}{A_{\text{film}} + A_{\text{cap}}} + k_{L,\text{cap}} \frac{A_{\text{cap}}}{A_{\text{film}} + A_{\text{cap}}} \tag{D.8}$$

The proportional participation of different regions on mass transport does not apply to $k_{L,\text{cyl}}$ for the cylindrical shape approximation of the presented model since the total surface area solely consists of the cylinder's lateral surface (see Sec. 6.1, Eqn. 6.3):

$$k_{L,\text{cyl}} = k_{L,\text{film}} \frac{A_{\text{film}}}{A_{\text{film}}} = k_{L,\text{film}} \tag{D.9}$$

Tab. D.1.: Calculated percentage deviation of $(((k_{L,\text{cyl}} \,/\, k_{L,\text{tb}}) - 1) \times 100)$ over l/d for two different film thicknesses σ_{film}. Positive values indicate that the cylinder approximation overestimates the actual liquid side mass transfer coefficient. Values are plotted in Sec. 6.1.1, Fig. 6.2 b).

l/d ratio	deviation $k_{L,\text{cyl}}/k_{L,\text{tb}}$ $\sigma_{\text{film}} = 80\,\mu\text{m}$	deviation $k_{L,\text{cyl}}/k_{L,\text{tb}}$ $\sigma_{\text{film}} = 130\,\mu\text{m}$
9.0	$-0.38\,\%$	$-1.99\,\%$
8.0	$-0.01\,\%$	$-1.73\,\%$
7.0	$+0.50\,\%$	$-1.35\,\%$
6.0	$+1.26\,\%$	$-0.77\,\%$
5.0	$+2.43\,\%$	$+0.17\,\%$
4.0	$+4.43\,\%$	$+1.81\,\%$
3.0	$+8.44\,\%$	$+5.19\,\%$
2.0	$+19.54\,\%$	$+14.76\,\%$
1.5	$+37.59\,\%$	$+30.37\,\%$
1.4	$+45.09\,\%$	$+36.82\,\%$
1.3	$+56.03\,\%$	$+46.17\,\%$
1.2	$+73.81\,\%$	$+61.20\,\%$
1.1	$+110.07\,\%$	$+91.19\,\%$
1.0	$+446.36\,\%$	$+330.42\,\%$

D.2 Modeling of two-sided mass transfer with the two-film theory

As stated in Sec. 6.2 the liquid side mass transfer can be modeled using the two-film theory by Lewis and Whitman [100] (see Sec. 6.2, Eqn. 6.4):

$$\frac{dn_i}{dt} = -k_{L,i} A (c^*_{i,\text{liq}} - c_{i,\text{liq}}) \tag{D.10}$$

With the concentration at the gas-liquid interface $c^*_{i,\text{liq}}$ being calculated by Henry's law [99, 102] (see Sec. 6.2, Eqn. 6.5):

$$c^*_{i,\text{liq}} = \frac{c_L p_0 x_i}{H_i^{px} - p_0 x_i} \tag{D.11}$$

Temperature dependence of Henry's law constant is taken into account as stated by Sander [103]:

$$H(T) = H(T_0) \exp\left(\frac{d(\ln(H))}{d(1/T)}\left(\frac{1}{T} - \frac{1}{T_0}\right)\right) \tag{D.12}$$

$H(T)$ is expressed by the Henry solubility constant $H(T_0)$ at a reference temperature $T_0 = 298.15\,\mathrm{K}$ and a constant describing the temperature dependence $\frac{d(\ln(H))}{d(1/T)}$. A large compilation of values is tabulated for various substances by Sander [103]. Values for O_2 and N_2 were taken from the table provided by Sander [103] and originated from the work of Warneck et al. [113]. The respective values are tabulated in Tab. D.2.

Tab. D.2.: Henry's law constants for O_2 and N_2 defined as H^{cp}.

substance	$H^{cp} \mathrel{\widehat{=}} H(T_0 = 298.15\,\mathrm{K})$	$\frac{d(\ln(H))}{d(1/T)}$	reference
O_2	$1.2 \times 10^{-5}\,\mathrm{mol\,m^{-3}\,Pa^{-1}}$	$1700\,\mathrm{K}$	[103, 113]
N_2	$6.4 \times 10^{-6}\,\mathrm{mol\,m^{-3}\,Pa^{-1}}$	$1600\,\mathrm{K}$	[103, 113]

It is important to note that the Henry solubility constants H^{cp} (defined as concentration c / partial pressure p) given by Sander [103] need to be converted to H^{px} using the molar mass and density of water ($M_{\text{water}} = 18.015 \times 10^{-3}\,\mathrm{kg\,mol^{-1}}$, $\rho_{\text{water}} = 997\,\mathrm{kg\,m^{-3}}$ at $T = 298\,\mathrm{K}$, data from Stephan et al. [74]):

$$H^{px} = \left(\frac{M_{\text{water}}}{\rho_{\text{water}}} H^{cp} \right)^{-1} \tag{D.13}$$

The mole fraction of x_i of the component i with regard to the total amount of substance n_{tot} (sum of all n_i) inside the bubble is defined as:

$$x_i = \frac{n_i}{n_{\text{tot}}} \tag{D.14}$$

The total amount of substance n_{tot} inside the bubble of a given volume V is calculated by the ideal gas law:

$$n_{\text{tot}} = \frac{PV}{R_m T} \tag{D.15}$$

P denotes the absolute pressure and $R_m = 8.314\,\mathrm{J\,mol^{-1}\,K^{-1}}$ describes the universal gas constant. Due to the hemispherical caps, the volume V is defined differently for the Taylor bubble and the pure cylinder:

$$V_{\text{tb}} = \frac{1}{4}\pi d_{\text{tb}}^2 (l_{\text{tb}} - d_{\text{tb}}) + \frac{1}{6}\pi d_{\text{tb}}^3 \tag{D.16}$$

$$V_{\text{cyl}} = \frac{1}{4}\pi d_{\text{tb}}^2 l_{\text{tb}} \tag{D.17}$$

The temperature dependence of the diffusion coefficient D for each species is taken into account by the Stokes-Einstein equation:

$$D(T) = D(T_0)\frac{T}{T_0}\frac{\eta(T_0)}{\eta(T)} \tag{D.18}$$

The temperature-dependent dynamic viscosity η for water at atmospheric pressure is tabulated by Stephan et al. [74]. A quadratic polynomial fit is used to interpolate the dynamic viscosity data in the range of $285\,\mathrm{K} \leq T \leq 315\,\mathrm{K}$ as:

$$\eta(T) = 4.5092 \times 10^{-7}T^2 - 2.8926 \times 10^{-4}T + 4.7045 \times 10^{-2} \tag{D.19}$$

The resulting temperature dependency of η is shown in Fig. D.1 a). Viscosity decreases as temperature rises. The literature data are well fitted within the specified range with a squared correlation coefficient of $R^2 = 0.9999$. Fig. D.1 b) illustrates the calculated temperature dependency of D. The diffusion coefficient increases at higher temperatures T. The selected diffusion coefficients D represent those of O_2 and N_2 at $T_0 = 298\,\mathrm{K}$.

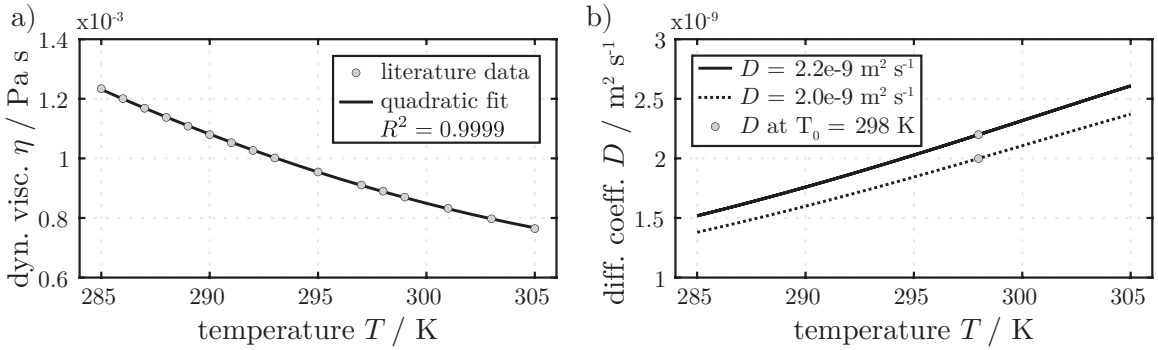

Fig. D.1.: a) Temperature dependency of the dynamic viscosity η of water. The shown literature data points were well fitted by a quadratic polynomial fit with $R^2 = 0.9999$ (see Eqn. D.19). b) Shows the temperature dependency of two diffusion coefficients D (solid and dotted line), with $D(T)$ (see Eqn. D.18) being calculated from the interpolated literature data shown in a). Viscosity data of water at atmospheric pressure were taken from Stephan et al. [74].

Bibliography

[1] C. Fleischer, S. Becker, and G. Eigenberger, "Detailed modeling of the chemisorption of CO2 into NaOH in a bubble column", *Chem. Eng. Sci.*, vol. 51, no. 10, pp. 1715–1724, 1996.

[2] R. A. Meyers, *Encyclopedia of Physical Science and Technology*, 3rd ed. Academic Press, 2001, vol. 18, p. 15 453.

[3] M. Weber, "Large Bubble Columns for the Oxidation of Cumene in Phenol Processes", *Chem. Eng. Technol.*, vol. 25, no. 5, pp. 553–558, 2002.

[4] B. Zhao, Y. Su, and Y. Peng, "Effect of reactor geometry on aqueous ammonia-based carbon dioxide capture in bubble column reactors", *Int J Greenh Gas Con*, vol. 17, pp. 481–487, 2013.

[5] A. I. Stankiewicz and J. A. Moulijn, "Process Intensification: Transforming Chemical Engineering", *Chem Eng Prog*, vol. 96, no. 1, pp. 22–34, 2000.

[6] N. Kantarci, F. Borak, and K. O. Ulgen, "Bubble column reactors", *Process Biochemistry*, vol. 40, no. 7, pp. 2263–2283, 2005.

[7] P. R. Gunjal and V. V. Ranade, *Industrial Catalytic Processes for Fine and Specialty Chemicals*. Elsevier, 2016.

[8] G. Shen and J. A. Finch, "Bubble swarm velocity in a column", *Chem. Eng. Sci.*, vol. 51, no. 14, pp. 3665–3674, 1996.

[9] D. Merker, L. Böhm, M. Oßberger, P. Klüfers, and M. Kraume, "Mass Transfer in Reactive Bubbly Flows - A Single-Bubble Study", *Chem. Eng. Technol.*, vol. 40, no. 8, pp. 1391–1399, 2017.

[10] U. D. Kück, U. Mießner, M. Aydin, and J. Thöming, "Mixing time and mass transfer of rising bubbles in swarm turbulence", *Chem. Eng. Sci.*, vol. 187, pp. 367–376, 2018.

[11] M. T. Kreutzer, F. Kapteijn, J. A. Moulijn, and J. J. Heiszwolf, "Multiphase monolith reactors: Chemical reaction engineering of segmented flow in microchannels", *Chem. Eng. Sci.*, vol. 60, no. 22, pp. 5895–5916, 2005.

[12] T. C. Thulasidas, M. A. Abraham, and R. L. Cerro, "Flow patterns in liquid slugs during bubble-train flow inside capillaries", *Chem. Eng. Sci.*, vol. 52, no. 17, pp. 2947–2962, 1997.

[13] H. Liu, C. O. Vandu, and R. Krishna, "Hydrodynamics of Taylor Flow in Vertical Capillaries: Flow Regimes, Bubble Rise Velocity, Liquid Slug Length, and Pressure Drop", *Ind. Eng. Chem. Res.*, vol. 44, no. 14, pp. 4884–4897, 2004.

[14] S. Nogueira, M. L. Riethmuller, J. B. L. M. Campos, and A. M. F. R. Pinto, "Flow patterns in the wake of a Taylor bubble rising through vertical columns of stagnant and flowing Newtonian liquids: An experimental study", *Chem. Eng. Sci.*, vol. 61, no. 22, pp. 7199–7212, 2006.

[15] P. Angeli and A. Gavriilidis, "Hydrodynamics of Taylor flow in small channels: A Review", *Proceedings of the Institution of Mechanical Engineers, Part C: Journal of Mechanical Engineering Science*, vol. 222, no. 5, pp. 737–751, 2008.

[16] K. Hayashi, R. Kurimoto, and A. Tomiyama, "Terminal velocity of a Taylor drop in a vertical pipe", *Int. J. Multiph. Flow*, vol. 37, no. 3, pp. 241–251, 2011.

[17] F. J. N. Direito, J. B. L. M. Campos, and J. M. Miranda, "A taylor drop rising in a liquid co-current flow", *Int. J. Multiph. Flow*, vol. 96, pp. 134–143, 2017.

[18] A. Kameke, S. Kastens, S. Rüttinger, S. Herres-Pawlis, and M. Schlüter, "How coherent structures dominate the residence time in a bubble wake: An experimental example", *Chem. Eng. Sci.*, vol. 207, pp. 317–326, 2019.

[19] J. J. Heiszwolf, M. T. Kreutzer, M. G. van den Eijnden, F. Kapteijn, and J. A. Moulijn, "Gas-liquid mass transfer of aqueous Taylor flow in monoliths", *Catalysis Today*, vol. 69, no. 1-4, pp. 51–55, 2001.

[20] S. Kastens, S. Hosoda, M. Schlüter, and A. Tomiyama, "Mass Transfer from Single Taylor Bubbles in Minichannels", *Chem. Eng. Technol.*, vol. 38, no. 11, pp. 1925–1932, 2015.

[21] C. Butler, E. Cid, and A.-M. Billet, "Modelling of mass transfer in Taylor flow: Investigation with the PLIF-I technique", *Chem. Eng. Res. Des.*, vol. 115, pp. 292–302, 2016.

[22] S. Boden, M. Haghnegahdar, and U. Hampel, "Measurement of Taylor bubble shape in square channel by microfocus X-ray computed tomography for investigation of mass transfer", *Flow Meas Instrum*, vol. 53, pp. 49–55, 2017.

[23] S. Kastens, J. Timmermann, F. Strassl, *et al.*, "Test System for the Investigation of Reactive Taylor Bubbles", *Chem. Eng. Technol.*, vol. 40, no. 8, pp. 1494–1501, 2017.

[24] F. Kexel, A. von Kameke, J. Tenhaus, M. Hoffmann, and M. Schlüter, "Taylor Bubble Study of the Influence of Fluid Dynamics on Yield and Selectivity in Fast Gas-Liquid Reactions", *Chem. Ing. Tech.*, vol. 93, no. 5, pp. 830–837, 2021.

[25] J. M. van Baten and R. Krishna, "CFD simulations of mass transfer from Taylor bubbles rising in circular capillaries", *Chem. Eng. Sci.*, vol. 59, no. 12, pp. 2535–2545, 2004.

[26] T. Taha and Z. F. Cui, "CFD modelling of slug flow in vertical tubes", *Chem. Eng. Sci.*, vol. 61, no. 2, pp. 676–687, 2006.

[27] N. Shao, A. Gavriilidis, and P. Angeli, "Mass transfer during Taylor flow in microchannels with and without chemical reaction", *Chem Eng J*, vol. 160, no. 3, pp. 873–881, 2010.

[28] L. Rocha, J. Miranda, and J. Campos, "Wide Range Simulation Study of Taylor Bubbles in Circular Milli and Microchannels", *Micromachines*, vol. 8, no. 5, p. 154, 2017.

[29] E. Z. Massoud, Q. Xiao, H. A. El-Gamal, and M. A. Teamah, "Numerical study of an individual Taylor bubble rising through stagnant liquids under laminar flow regime", *Ocean Engineering*, vol. 162, pp. 117–137, 2018.

[30] M. C. F. Silva, J. M. Miranda, J. B. L. M. Campos, and J. D. P. Araújo, "Mass transfer from a Taylor bubble to the surrounding flowing liquid at the micro-scale: a numerical approach", *Microfluid Nanofluid*, vol. 23, no. 4, pp. 1–21, 2019.

[31] T. L. Bergman, F. P. Incropera, D. P. Dewitt, and A. S. Lavine, *Fundamentals of Heat and Mass Transfer*, 8th ed. John Wiley & Sons, 2018.

[32] K. Avila, D. Moxey, A. de Lozar, *et al.*, "The Onset of Turbulence in Pipe Flow", *Science*, vol. 333, no. 6039, pp. 192–196, 2011.

[33] F. P. Bretherton, “The motion of long bubbles in tubes”, *J. Fluid Mech.*, vol. 10, no. 2, pp. 166–188, 1961.

[34] E. T. White and R. H. Beardmore, “The velocity of rise of single cylindrical air bubbles through liquids contained in vertical tubes”, *Chem. Eng. Sci.*, vol. 17, no. 5, pp. 351–361, 1962.

[35] M. D. Giavedoni and F. A. Saita, “The rear meniscus of a long bubble steadily displacing a Newtonian liquid in a capillary tube”, *Phys. Fluids*, vol. 11, no. 4, pp. 786–794, 1999.

[36] J. D. P. Araújo, J. M. Miranda, A. M. F. R. Pinto, and J. B. L. M. Campos, “Wide-ranging survey on the laminar flow of individual Taylor bubbles rising through stagnant Newtonian liquids”, *Int. J. Multiph. Flow*, vol. 43, pp. 131–148, 2012.

[37] M. Raffel, C. E. Willert, F. Scarano, *et al.*, *Particle Image Velocimetry*. Springer International Publishing, 2018, vol. 3.

[38] W. Thielicke and R. Sonntag, “Particle image velocimetry for MATLAB: Accuracy and enhanced algorithms in PIVlab”, *J. Open Res. Softw.*, vol. 9, 2021.

[39] C. Meyer, M. Hoffmann, and M. Schlüter, “Micro-PIV analysis of gas-liquid Taylor flow in a vertical oriented square shaped fluidic channel”, *Int. J. Multiph. Flow*, vol. 67, pp. 140–148, 2014.

[40] A. Dani, P. Guiraud, and A. Cockx, “Local measurement of oxygen transfer around a single bubble by planar laser-induced fluorescence”, *Chem. Eng. Sci.*, vol. 62, no. 24, pp. 7245–7252, 2007.

[41] M. Haghnegahdar, S. Boden, and U. Hampel, “Investigation of mass transfer in milli-channels using high-resolution microfocus X-ray imaging”, *Int. J. Heat Mass Transf.*, vol. 93, pp. 653–664, 2016.

[42] L. F. Gladden and A. J. Sederman, “Magnetic Resonance Imaging and Velocity Mapping in Chemical Engineering Applications”, *Annu Rev Chem Biomol*, vol. 8, no. 1, pp. 227–247, 2017.

[43] L. F. Gladden and A. J. Sederman, “Recent advances in Flow MRI”, *J. Magn. Reson.*, vol. 229, pp. 2–11, 2013.

[44] A. J. Sederman, M. D. Mantle, and L. F. Gladden, “Single excitation multiple image RARE (SEMI-RARE): ultra-fast imaging of static and flowing systems”, *J. Magn. Reson.*, vol. 161, no. 1, pp. 15–24, 2003.

[45] A. B. Tayler, D. J. Holland, A. J. Sederman, and L. F. Gladden, “Applications of ultra-fast MRI to high voidage bubbly flow: Measurement of bubble size distributions, interfacial area and hydrodynamics”, *Chem. Eng. Sci.*, vol. 71, pp. 468–483, 2012.

[46] S. Benders, F. Strassl, B. Fenger, *et al.*, “Imaging of copper oxygenation reactions in a bubble flow”, *Magn. Reson. Chem.*, vol. 56, no. 9, pp. 826–830, 2018.

[47] D. Schurr, F. Strassl, P. Liebhäuser, *et al.*, “Decay kinetics of sensitive bioinorganic species in a SuperFocus mixer at ambient conditions”, *React. Chem. Eng.*, vol. 1, no. 5, pp. 485–493, 2016.

[48] D. W. McRobbie, E. A. Moore, M. J. Graves, and M. R. Prince, *MRI from Picture to Proton*. Cambridge University Press, 2017, p. 400.

[49] W. Gerlach and O. Stern, “Der experimentelle Nachweis des magnetischen Moments des Silberatoms”, *Zeitschrift für Physik*, vol. 8, no. 1, pp. 110–111, 1922.

[50] W. Gerlach and O. Stern, "Der experimentelle Nachweis der Richtungsquantelung im Magnetfeld", *Zeitschrift für Physik*, vol. 9, no. 1, pp. 349–352, 1922.

[51] I. I. Rabi, "Zur Methode der Ablenkung von Molekularstrahlen", *Zeitschrift für Physik*, vol. 54, no. 3-4, pp. 190–197, 1929.

[52] I. I. Rabi, J. R. Zacharias, S. Millman, and P. Kusch, "A New Method of Measuring Nuclear Magnetic Moment", *Phys Rev*, vol. 53, no. 4, pp. 318–318, 1938.

[53] F. Bloch, "Nuclear Induction", *Phys. Rev.*, vol. 70, no. 7-8, p. 460, 1946.

[54] E. M. Purcell, H. C. Torrey, and R. V. Pound, "Resonance Absorption by Nuclear Magnetic Moments in a Solid", *Phys Rev*, vol. 69, no. 1-2, pp. 37–38, 1946.

[55] P. C. Lauterbur, "Image Formation by Induced Local Interactions: Examples Employing Nuclear Magnetic Resonance", *Nature*, vol. 242, no. 5394, pp. 190–191, 1973.

[56] R. W. Brown, Y. C. N. Cheng, E. M. Haacke, M. R. Thompson, and R. Venkatesan, *Magnetic Resonance Imaging, Physical Principles and Sequence Design*. Wiley & Sons, Limited, John, 2014.

[57] C. Westbrook, *MRI at a Glance*. Wiley & Sons, Incorporated, John, 2015, p. 136.

[58] S. Stapf and S.-I. Han, *NMR Imaging in Chemical Engineering*. Wiley & Sons, Incorporated, John, 2006, p. 646.

[59] O. Dietrich, J. G. Raya, S. B. Reeder, M. F. Reiser, and S. O. Schoenberg, "Measurement of signal-to-noise ratios in MR images: Influence of multichannel coils, parallel imaging, and reconstruction filters", *J Magn Reson Imaging*, vol. 26, no. 2, pp. 375–385, 2007.

[60] W. A. Edelstein, P. A. Bottomley, and L. M. Pfeifer, "A signal-to-noise calibration procedure for NMR imaging systems", *Medical physics*, vol. 11, no. 2, pp. 180–185, 1984.

[61] J. Mispelter, M. Lupu, and A. Briguet, *NMR Probeheads for Biophysical and Biomedical Experiments*. IMPERIAL COLLEGE PRESS, 2015.

[62] F. D. Doty, G. Entzminger, J. Kulkarni, K. Pamarthy, and J. P. Staab, "Radio frequency coil technology for small-animal MRI", *NMR Biomed.*, vol. 20, no. 3, pp. 304–325, 2007.

[63] J. Mispelter and M. Lupu, "Homogeneous resonators for magnetic resonance: A review", *C. R. Chim.*, vol. 11, no. 4-5, pp. 340–355, 2008.

[64] J. Link, "The Design of Resonator Probes with Homogeneous Radiofrequency Fields", in *In-Vivo Magnetic Resonance Spectroscopy I: Probeheads and Radiofrequency Pulses Spectrum Analysis*, Springer Berlin Heidelberg, 1992, pp. 3–31.

[65] C. E. Hayes, W. A. Edelstein, J. F. Schenck, O. M. Mueller, and M. Eash, "An efficient, highly homogeneous radiofrequency coil for whole-body MRimaging at 1.5 T", *J. Magn. Reson.*, vol. 63, no. 3, pp. 622–628, 1985.

[66] C. Leussler, J. Stimma, and P. Röschmann, "The Bandpass Birdcage Resonator Modified as a Coil Array for Simultaneous MR Acquisition", in *Proc 5th Scientific Meeting ISMRM, Vancouver*, 1997.

[67] M. C. Leifer, "Resonant Modes of the Birdcage Coil", *J. Magn. Reson.*, vol. 124, no. 1, pp. 51–60, 1997.

[68] S. Crozier, K. Luescher, L. K. Forbes, and D. M. Doddrell, "Optimized Small-Bore, High-Pass Resonator Designs", *J. Magn. Reson. Ser. B*, vol. 109, no. 1, pp. 1–11, 1995.

[69] R. J. Pascone, B. J. Garcia, T. M. Fitzgerald, *et al.*, “Generalized electrical analysis of low-pass and high-pass birdcage resonators”, *Magn Reson Imaging*, vol. 9, no. 3, pp. 395–408, 1991.

[70] J. Tropp, “Mutual Inductance in the Bird-Cage Resonator”, *J. Magn. Reson.*, vol. 126, no. 1, pp. 9–17, 1997.

[71] Y. C. Kim, H. D. Kim, B.-J. Yun, and S. F. Ahmad, “A Simple Analytical Solution for the Designing of the Birdcage RF Coil Used in NMR Imaging Applications”, *Appl. Sci.*, vol. 10, no. 7, p. 2242, 2020.

[72] C.-L. Chin, C. M. Collins, S. Li, B. J. Dardzinski, and M. B. Smith, “BirdcageBuilder: Design of specified-geometry birdcage coils with desired current pattern and resonant frequency”, *Concept Magnetic Res*, vol. 15, no. 2, pp. 156–163, 2002.

[73] D. Welting, *pyBirdcagebuilder - Pthon3 Port of the Original Birdcage Builder*, Accessed: 10.11.2022 (https://github.com/dwelting/pyBirdcagebuilder).

[74] P. Stephan, S. Kabelac, M. Kind, *et al.*, *VDI-Wärmeatlas*, 12th ed., P. Stephan, S. Kabelac, M. Kind, *et al.*, Eds. New York, United States: Springer Berlin Heidelberg, 2019.

[75] M. Kraume, *Transportvorgänge in der Verfahrenstechnik*, 3rd ed. Springer Berlin Heidelberg, 2020.

[76] P. Kemper, J. Thöming, and E. Küstermann, “Tailored birdcage resonator for magnetic resonance imaging at 7T using 3D printing”, *HardwareX*, vol. 12, e00326, 2022.

[77] C. H. Cunningham, J. M. Pauly, and K. S. Nayak, “Saturated double-angle method for rapid B1+ mapping”, *Magn Reson Med.*, vol. 55, no. 6, pp. 1326–1333, 2006.

[78] P. Kemper, E. Küstermann, W. Dreher, *et al.*, “Magnetic Resonance Imaging for Non-invasive Study of Hydrodynamics Inside Gas-Liquid Taylor Flows”, *Chem. Eng. Technol.*, vol. 44, no. 3, pp. 465–476, 2021.

[79] A. Haase, “Snapshot FLASH MRI. Applications to T1, T2, and chemical-shift imaging”, *Magn Reson Med*, vol. 13, no. 1, pp. 77–89, 1990.

[80] É. Tóth, L. Helm, and A. E. Merbach, “Metal Complexes as MRI Contrast Enhancement Agents”, in *Reference Module in Chemistry, Molecular Sciences and Chemical Engineering*, Elsevier, 2015.

[81] P. B. Tsitovich, J. A. Spernyak, and J. R. Morrow, “A Redox-Activated MRI Contrast Agent that Switches Between Paramagnetic and Diamagnetic States”, *Angew. Chem. - Int. Ed.*, vol. 52, no. 52, pp. 13 997–14 000, 2013.

[82] H. Wang, V. C. Jordan, I. A. Ramsay, *et al.*, “Molecular Magnetic Resonance Imaging Using a Redox-Active Iron Complex”, *J. Am. Chem. Soc.*, vol. 141, no. 14, pp. 5916–5925, 2019.

[83] O. Dietrich, J. Levin, S.-A. Ahmadi, *et al.*, “MR imaging differentiation of Fe2+ and Fe3+ based on relaxation and magnetic susceptibility properties”, *Neuroradiology*, vol. 59, no. 4, pp. 403–409, 2017.

[84] B. J. Balcom, T. A. Carpenter, and L. D. Hall, “Spatial and temporal visualization of two aqueous iron oxidation-reduction reactions by nuclear magnetic resonance imaging”, *J. Chem. Soc., Chem. Commun.*, no. 4, pp. 312–313, 1992.

[85] Y. Kurimura, R. Ochiai, and N. Matsuura, “Oxygen Oxidation of Ferrous Ions Induced by Chelation”, *Bull. Chem. Soc. Jpn.*, vol. 41, no. 10, pp. 2234–2239, 1968.

[86] J. F. Demmink, I. C. F. van Gils, and A. A. C. M. Beenackers, “Absorption of Nitric Oxide into Aqueous Solutions of Ferrous Chelates Accompanied by Instantaneous Reaction”, *Ind. Eng. Chem. Res.*, vol. 36, no. 11, pp. 4914–4927, 1997.

[87] T. Schneppensieper, A. Wanat, G. Stochel, and R. van Eldik, “Mechanistic Information on the Reversible Binding of NO to Selected Iron(II) Chelates from Activation Parameters”, *Inorg. Chem.*, vol. 41, no. 9, pp. 2565–2573, 2002.

[88] F. Gambardella, I. J. Ganzeveld, J. G. M. Winkelman, and E. J. Heeres, “Kinetics of the Reaction of FeII(EDTA) with Oxygen in Aqueous Solutions”, *Ind. Eng. Chem. Res.*, vol. 44, no. 22, pp. 8190–8198, 2005.

[89] E. Sada, H. Kumazawa, and H. Machida, “Oxidation kinetics of FeII-EDTA and FeII-NTA chelates by dissolved oxygen”, *Ind. Eng. Chem. Res.*, vol. 26, no. 7, pp. 1468–1472, 1987.

[90] V. Zang and R. V. Eldik, “Kinetics and mechanism of the autoxidation of iron(II) induced through chelation by ethylenediaminetetraacetate and related ligands”, *Inorg. Chem.*, vol. 29, no. 9, pp. 1705–1711, 1990.

[91] H. J. Wubs and A. A. C. M. Beenackers, “Kinetics of the oxidation of ferrous chelates of EDTA and HEDTA in aqueous solution”, *Ind. Eng. Chem. Res.*, vol. 32, no. 11, pp. 2580–2594, 1993.

[92] M. W. Hlawitschka, M. Oßberger, C. Backes, P. Klüfers, and H.-J. Bart, “Reactive Mass Transfer of Single NO Bubbles and Bubble Bouncing in Aqueous Ferric Solutions - A Feasibility Study”, *Oil & Gas Science and Technology - Revue d’IFP Energies nouvelles*, vol. 72, no. 2, F. Augier, Ed., p. 11, 2017.

[93] Air Liquide Deutschland GmbH, *Stickstoffmonoxid, CAS-Nr. : 10102-43-9, Safety Datasheet Rev. 4.0, 2018-08-31*, Accessed: 05.01.2023 (https://gasekatalog.airliquide.de/documents/sm1554800331870.pdf).

[94] S. Pohl, M. Harmjanz, J. Schneider, W. Saak, and G. Henkel, “1,3-Bis(N,N,N′,N′-tetramethyl guanidino)propane: synthesis, characterization and bonding properties of the first bidentate, peralkylated guanidine ligand”, *J. Chem. Soc., Dalton Trans.*, no. 19, pp. 3473–3479, 2000.

[95] N. Šegatin, T. P. Žontar, and N. P. Ulrih, “Dielectric Properties and Dipole Moment of Edible Oils Subjected to ’Frying’ Thermal Treatment”, *Foods*, vol. 9, no. 7, p. 900, 2020.

[96] M. Ladaniya, *Citrus Fruit - Biology, Technology and Evaluation*. Elsevier, 2008.

[97] R. Higbie, “The rate of absorption of a pure gas into a still liquid during short periods of exposure”, *Trans. Am. Inst. Chem. Eng*, vol. 31, pp. 365–389, 1935.

[98] B. I. Morsi and O. M. Basha, “Mass Transfer in Multiphase Systems”, in *Mass Transfer - Advancement in Process Modelling*, InTech, 2015, pp. 189–217.

[99] M. Haghnegahdar, S. Boden, and U. Hampel, “Investigation of surfactant effect on the bubble shape and mass transfer in a milli-channel using high-resolution microfocus X-ray imaging”, *Int. J. Multiph. Flow*, vol. 87, pp. 184–196, 2016.

[100] W. K. Lewis and W. G. Whitman, “Principles of Gas Absorption”, *Ind Eng Chem*, vol. 16, no. 12, pp. 1215–1220, 1924.

[101] Z. Berk, *Food Process Engineering and Technology*. Elsevier Science & Technology Books, 2018, p. 742.

[102] S. Hosoda, S. Abe, S. Hosokawa, and A. Tomiyama, “Mass transfer from a bubble in a vertical pipe”, *Int. J. Heat Mass Transf.*, vol. 69, pp. 215–222, 2014.

[103] R. Sander, “Compilation of Henry’s law constants (version 4.0) for water as solvent”, *Atmos. Chem. Phys.*, vol. 15, no. 8, pp. 4399–4981, 2015.

[104] W. Xing, M. Yin, Q. Lv, *et al.*, “Oxygen Solubility, Diffusion Coefficient, and Solution Viscosity”, in *Rotating Electrode Methods and Oxygen Reduction Electrocatalysts*, Elsevier, 2014, pp. 1–31.

[105] D. S. Christen, *Praxiswissen der chemischen Verfahrenstechnik, Handbuch für Chemiker und Verfahrensingenieure*. Springer-Verlag, 2009, p. 625.

[106] A. C. Hindmarsh, P. M. Gresho, and D. F. Griffiths, “The stability of explicit Euler time-integration for certain finite difference approximations of the multi-dimensional advection-diffusion equation”, *Internat. J. Numer. Methods Fluids*, vol. 4, no. 9, pp. 853–897, 1984.

[107] R. J. LeVeque, *Finite Difference Methods for Ordinary and Partial Differential Equations*. Society for Industrial and Applied Mathematics, 2007.

[108] Carl Roth GmbH + Co. KG, *Iron(II) sulphate heptahydrate, P015, CAS No.: 7782-63-0 print date: 09.06.2022 [online]*, Accessed: 13.12.2022 (https://www.carlroth.com/com/en/ iron-salts-fe/iron(ii)-sulphate-heptahydrate/p/p015.2).

[109] Carl Roth GmbH + Co. KG, *Ethylenediamine tetraacetic acid disodium salt dihydrate, 8043, CAS No.: 6381-92-6 print date: 09.06.2022 [online]*, Accessed: 13.12.2022 (https://www.carlroth.com/com/en/salts-for-complexometry/ethylenediamine-tetraacetic-acid-disodium-salt-dihydrate/p/8043.2).

[110] T. Helmers, P. Kemper, J. Thöming, and U. Mießner, “Modeling the Excess Velocity of Low-Viscous Taylor Droplets in Square Microchannels”, *Fluids*, vol. 4, no. 3, p. 162, 2019.

[111] D. A. Rowlands, *Physics of Digital Photography*, 2nd ed. IOP Publishing, 2020.

[112] P. Vennemann, K. T. Kiger, R. Lindken, *et al.*, “In vivo micro particle image velocimetry measurements of blood-plasma in the embryonic avian heart”, *J Biomech*, vol. 39, no. 7, pp. 1191–1200, 2006.

[113] P. Warneck and J. Williams, *The Atmospheric Chemist’s Companion*. Springer Netherlands, 2012.

List of symbols

Roman symbols		
Symbol	**Description**	**Unit**
A	surface area	m^2
A_{cap}	surface area of the Taylor bubble's caps	m^2
A_{film}	surface area of the cylinder's shell at the liquid film region	m^2
B	magnetic field strength	T
B_0	main (static) magnetic field strength	T
B_1	alternating (RF) magnetic field strength	T
c_i	concentration of component i	$\mathrm{mol\,m^{-3}}$
c_{EDTA}	$\mathrm{Fe^{II}}$(EDTA) concentration	$\mathrm{mol\,m^{-3}}$
$c_{\mathrm{N_2}}$	nitrogen concentration	$\mathrm{mol\,m^{-3}}$
$c_{\mathrm{O_2}}$	oxygen concentration	$\mathrm{mol\,m^{-3}}$
$c_{i,\mathrm{gas}}$	gas phase bulk concentration	$\mathrm{mol\,m^{-3}}$
$c_{i,\mathrm{liq}}$	liquid phase bulk concentration	$\mathrm{mol\,m^{-3}}$
$c^*_{i,\mathrm{gas}}$	gas phase interface concentration	$\mathrm{mol\,m^{-3}}$
$c^*_{i,\mathrm{liq}}$	liquid phase interface concentration	$\mathrm{mol\,m^{-3}}$
c_L	molar water concentration	$\mathrm{mol\,m^{-3}}$
C	capacitance	F
C_{er}	capacitance of the end ring capacitor	F
C_{leg}	capacitance of the leg / rung capacitor	F
C_{match}	capacitance of the matching capacitor	F
C_{p}	capacitance of the pickup loop capacitor	F
C_{r}	capacitance of the rung capacitor	F
C_{tune}	capacitance of the tuning capacitor	F
d	diameter	m
d_{coil}	coil diameter	m
d_{i}	inner (capillary) diameter	m
d_{p}	particle diameter	m
d_{pore}	pore diameter	m
d_{shield}	shield diameter	m
d_{tb}	Taylor bubble diameter	m

Roman symbols		
Symbol	**Description**	**Unit**
D_{AB}	diffusivity of gas A in liquid B	$\mathrm{m^2\,s^{-1}}$
D_i	diffusivity of component i	$\mathrm{m^2\,s^{-1}}$
E	energy	J
$E_{\%}$	percentage error	%
$E_{\%,\mathrm{max}}$	maximum absolute percentage error	%
f	frequency	Hz
f_0	resonant frequency	Hz
f_l	focal length	m
g	gravitational acceleration	$\mathrm{m\,s^{-2}}$
G	magnetic field gradient	$\mathrm{T\,m^{-1}}$
G_{FE}	frequency encoding gradient	$\mathrm{T\,m^{-1}}$
G_{PE}	phase encoding gradient	$\mathrm{T\,m^{-1}}$
G_{SS}	slice selection gradient	$\mathrm{T\,m^{-1}}$
G_x	magnetic field gradient in x-direction	$\mathrm{T\,m^{-1}}$
G_y	magnetic field gradient in y-direction	$\mathrm{T\,m^{-1}}$
G_z	magnetic field gradient in z-direction	$\mathrm{T\,m^{-1}}$
h_{CMOS}	height of CMOS sensor	m
h_d	hyperfocal distance	m
h_x	node distance in x-direction	m
h_y	node distance in y-direction	m
H	Henry's law solubility constant (all variants)	misc.
H_i^{cp}	Henry's law solubility constant (defined as concentration c / partial pressure p)	$\mathrm{mol\,m^{-3}\,Pa^{-1}}$
H_i^{px}	Henry's law solubility constant (defined as partial pressure p / molar fraction x)	Pa
$\tilde{i}$	spatial control variable	
I	spin quantum number	
$\tilde{j}$	spatial control variable	
k_L	liquid side mass transfer coefficient	$\mathrm{m\,s^{-1}}$
$k_{L,\mathrm{cap}}$	liquid side mass transfer coefficient at the bubble's cap	$\mathrm{m\,s^{-1}}$
$k_{L,\mathrm{cyl}}$	total liquid side mass transfer coefficient of the cylinder shape	$\mathrm{m\,s^{-1}}$
$k_{L,\mathrm{film}}$	liquid side mass transfer coefficient at the bubble's film	$\mathrm{m\,s^{-1}}$

Roman symbols		
Symbol	**Description**	**Unit**
$k_{L,\mathrm{tb}}$	total liquid side mass transfer coefficient of the Taylor bubble	$\mathrm{m\,s^{-1}}$
k_{12}	reaction rate constant	$\mathrm{m^6 mol^{-2} s^{-1}}$
k_r	first order reaction rate constant	$\mathrm{s^{-1}}$
k_res	resonant mode	
k_x	k-space coordinate in x-direction	
k_y	k-space coordinate in y-direction	
l	length	m
$l_{h,\mathrm{lam}}$	laminar hydrodynamic entrance length	m
l_film	liquid film length	m
l_leg	BC resonator leg length	m
l_tb	Taylor bubble length	m
$l_{\mathrm{tb},0}$	initial Taylor bubble length at $t = 0\,\mathrm{s}$	m
$l_{\mathrm{tb},t}$	Taylor bubble length at time t	m
l_x	domain / mesh length in x-direction	m
l_y	domain / mesh length in y-direction	m
L	inductance	H
L_coil	inductance of the wire coil	H
L_pickup	inductance of the pickup loop	H
M	net magnetization vector	$\mathrm{A\,m^{-1}}$
M_0	equilibrium net magnetization vector	$\mathrm{A\,m^{-1}}$
M_{xy}	transversal magnetization	$\mathrm{A\,m^{-1}}$
M_z	longitudinal magnetization	$\mathrm{A\,m^{-1}}$
$M_{\mathrm{H_2O}}$	molar mass of water	$\mathrm{kg\,mol^{-1}}$
$\widehat{M}$	mutual inductance between two coils	H
n_i	amount of substance of component i	mol
n_ri	refractive index	
n_tot	total amount of substance of all components	mol
$\tilde{n}$	temporal control variable	
$N_{-1/2}$	number of high energy spins	
$N_{+1/2}$	number of low energy spins	
N_A	numerical aperture	
N_img	number of images	
N_leg	number of legs / rungs	
N_x	number of mesh nodes in x-direction	
N_y	number of mesh nodes in y-direction	

Roman symbols

Symbol	Description	Unit
p_i	partial pressure of component i	Pa
p_0	atmospheric pressure	Pa
P	absolute pressure	Pa
r	reaction rate	$\mathrm{mol\,m^{-3}\,s^{-1}}$
R^2	coefficient of determination / squared correlation coefficient	
s	focus distance	m
t	time	s
t_d	variable delay time	s
t_end	end time / final time step	s
t_p	pulse duration	s
T	temperature	K
T_0	initial or reference temperature	K
T_1	T_1 relaxation time / spin-lattice relaxation	s
T_2	T_2 relaxation time / spin-spin relaxation	s
T_2^*	T_2^* decay / dephasing due to magnetic field inhomogeneities	s
TE	echo time	s
TI	inversion time	s
TI_zero	inversion time at zero crossing	s
TR	repetition time	s
u	flow velocity in x-direction	$\mathrm{m\,s^{-1}}$
v	flow velocity in y-direction	$\mathrm{m\,s^{-1}}$
v_film	liquid film velocity (in y-direction)	$\mathrm{m\,s^{-1}}$
v_p	liquid film velocity with parabolic flow profile (in y-direction)	$\mathrm{m\,s^{-1}}$
v_rise	bubble rise velocity (in y-direction)	$\mathrm{m\,s^{-1}}$
V	volume	$\mathrm{m^3}$
V_cyl	volume of the cylinder geometry	$\mathrm{m^3}$
V_tb	volume of the Taylor bubble	$\mathrm{m^3}$
w	width	m
w_CMOS	width of CMOS sensor	m
w_er	BC resonator end ring width	m
w_leg	BC resonator leg width	m
x	coordinate in x-direction	m
x'	coordinate of rotating reference frame at ω_0	m

Roman symbols		
Symbol	**Description**	**Unit**
x_i	mole fraction of component i	
y	coordinate in y-direction	m
y'	coordinate of rotating reference frame at ω_0	m
z	coordinate in z-direction	m
z'	coordinate of rotating reference frame at ω_0	m

Greek letters		
Symbol	**Description**	**Unit**
α	flip angle	$^\circ$
γ	gyromagnetic ratio	$\mathrm{rad\,s^{-1}\,T^{-1}}$
Γ	reflection coefficient	
ΔE	energy difference	J
Δl	length difference	m
Δt	update time	s
Δt_{step}	single time step for iterative calculation	s
ϵ_{r}	relative permittivity	
ζ	field amplitude (factor)	
η_{liq}	liquid phase dynamic viscosity	$\mathrm{Pa\,s}$
η_{water}	dynamic viscosity of water	$\mathrm{Pa\,s}$
μ	mean value	
ρ_{air}	density of air	$\mathrm{kg\,m^{-3}}$
ρ_{gas}	gas phase density	$\mathrm{kg\,m^{-3}}$
ρ_{liq}	liquid phase density	$\mathrm{kg\,m^{-3}}$
ρ_{water}	density of water	$\mathrm{kg\,m^{-3}}$
σ	standard deviation	
σ_{surf}	surface tension	$\mathrm{N\,m^{-1}}$
σ_{film}	liquid film thickness	m
τ	residence time / contact time	s
τ_{cap}	cap residence time	s
τ_{compute}	residence time for computation	s
τ_{film}	film residence time	s
ω	precession frequency	$\mathrm{rad\,s^{-1}}$
ω_0	Larmor frequency	$\mathrm{rad\,s^{-1}}$

Constants		
Symbol	**Description**	**Unit**
$\widehat{c}$	speed of light $\widehat{c} = 2.997\,924\,58 \times 10^{8}$ [61]	$\mathrm{m\,s^{-1}}$
h	Planck constant $h = 6.626 \times 10^{-34}$ [57]	$\mathrm{J\,s}$
k_{B}	Boltzmann constant $k_{\mathrm{B}} = 1.381 \times 10^{-23}$ [57]	$\mathrm{J\,K^{-1}}$
R_m	universal gas constant $R_m = 8.314$ [74]	$\mathrm{Jmol^{-1}K^{-1}}$

Abbreviations	
Abbreviation	**Description**
^{1}H NMR	proton nuclear magnetic resonance
2C-2D	two-components, two-dimensional
BC	birdcage (resonator)
B.C.	boundary condition
Bo	Bond number (same as Eötvös number Eo)
BP	band-pass (filter)
btmgp	bis(tetramethylguanidino)propylene
BW	bandwidth
Ca	Capillary number
CFD	computational fluid dynamics
CMOS	complementary metal-oxide-semiconductor
CoC	circle of confusion
CSF	continuum surface force
DLP	digital light processing
DNIC	dinitrosyliron compound
DOF	depth of field
DTPA	diethylenetriaminepentaacetic acid
EDTA	ethylenediaminetetraacetic acid
Eo	Eötvös number (same as Bond number Bo)
EPI	echo-planar imaging
FDM	finite difference method
FEP	fluorinated ethylene propylene
FFT	fast Fourier transform
FISP	fast imaging with steady-state precession
FLASH	fast low angle shot
FOV	field of view

Abbreviations	
Abbreviation	**Description**
HF	high-frequency
HP	high-pass (filter)
HPLC	high-performance liquid chromatography
I.C.	initial condition
IFFT	inverse fast Fourier transform
IR	inversion recovery
IWS	interrogation window size
LIF	laser-induced fluorescence
LP	low-pass (filter)
MNIC	mononitrosyliron compound
Mo	Morton number
MR	magnetic resonance
MRI	magnetic resonance imaging
NMR	nuclear magnetic resonance
NMV	net magnetization vector
PDE	partial differential equation
PIV	particle image velocimetry
PLIF	planar laser-induced fluorescence
POM	polyoxymethylene
PTFE	polytetrafluoroethylene
RARE	rapid acquisition with relaxation enhancement
Re	Reynolds number
Re_{crit}	critical Reynolds number
RF	radio frequency
ROI	region of interest
RX	receiver / receive
SNR	signal to noise ratio
TX	transmitter / transmit
VNA	vector network analyzer
VOF	volume of fluid

Students' work

No students were supervised during the development of this work. Hence, this thesis does not include any students' work.

Colophon

This thesis was typeset with LaTeX 2$_\varepsilon$ using the *TeXstudio* environment on MacOS. *MATLAB* was used for data processing and visualization, where the *PIVlab 2.31* toolbox [38] was used for PIV evaluations. Renderings and CAD drawings were created in *Autodesk Fusion 360*. Vector graphics and schematic representations were prepared in *Adobe Illustrator*. Birdcage calculations were performed using the *pyBirdcagebuilder* [73]. Flow simulations were conducted in *Ansys FLUENT*.

This thesis uses the *Clean Thesis* style developed by Ricardo Langner. The design of the *Clean Thesis* style is inspired by user guide documents from Apple Inc.

Download the *Clean Thesis* style at `http://cleanthesis.der-ric.de/`.